Nanoindentation of Bio- and Geo-mineralized Composites: Contribution of Microstructure and Composition

by

S. E. Campbell

B.A., Coe College, 2005

M.S., University of Colorado, 2007

A thesis submitted to the

Faculty of the Graduate School of the

University of Colorado in partial fulfillment

of the requirements for the degree of

Doctor of Philosophy

Department of Mechanical Engineering

2010

This thesis entitled:
Nanoindentation of Bio- and Geo-mineralized Composites: Contribution of Microstructure and Composition
written by S. E. Campbell
has been approved for the Department of Mechanical Engineering

Prof. Virginia L. Ferguson

Prof. Michelle L. Oyen

Date

The final copy of this thesis has been examined by the signatories, and we find that both the content and the form meet acceptable presentation standards of scholarly work in the above mentioned discipline.

Campbell, S. E. (Ph.D., Mechanical Engineering)

Nanoindentation of Bio- and Geo-mineralized Composites: Contribution of Microstructure and Composition

Thesis directed by Prof. Virginia L. Ferguson

Bio-mineralized composite tissues, such as bone and teeth, are heterogeneous in both mineral composition and crystallinity. These tissues are altered throughout life by aging, wear, microfracture, and various disease states (e.g., osteoporosis), and are then further altered geologically after death by fossilization to create geo-minealized tissues. Bone and enamel exhibit a wide range of mechanical responses at nanometer-length scales, where large-scale porosity and macro-structural variation are not factors. Some variability seen in mineralized tissues can be attributed to the amount of mineral; where a general increase in mechanical properties occurs with increasing mineral volume fraction. However, a large range of modulus values for bone is observed at a constant mineral content indicating that both the composition and microstructure play a vital role in the nanomechanical response. This dissertation is aimed at understanding the nanomechanical properties of these heterogeneous mineralized composites in order to elucidate the interplay between composition, microstructure, and tissue mechanical behavior.

A combined approach using nanoindentation testing and complimentary techniques, such as X-ray diffraction, Fourier transform infrared spectroscopy, and quantitative backscattered electron microscopy (qBSE) are used to investigate the effect of variations in crystallography, microstructure, and mineral composition on the nanomechanical properties of these materials. Further, development of novel qBSE glass standards allow for site-matched measurement of mineral volume fraction and nanomechanical properties. Additionally, a finite element analysis (FEA) allows for isolation of individual parameters and their contribution to the nanomechanical properties. The relative contribution of the composition and mi-

crostructure are explored through two experimental model systems of bone fossilization and lemur enamel.

In fossilization, or diagenesis, composition is altered over geologic time as minerals are incorporated into pore spaces within the bone. Fossilized bone samples demonstrate a larger range of mineral composition, mineral volume fraction, and crystallinity than is found in modern samples. Nanoindentation revealed that anisotropy of modern bone can be preserved in fossil bones going back at least to the early Eocene ($\approx$ 50 million years). Further, both increased crystallinity and density correlated with increased modulus values, suggesting that size of bioapatite crystals contribute to the mechanical properties. Nanoindentation is useful in investigating tissue-level diagenesis in bone, and can provide insight into the functional significance of mineralized tissues even after diagenesis has occurred.

Variations in microstructure and mineralization were examined in the enamel of three lemur species *Lemur catta, Lepilemur leucopus, Propithecus verreauxi*, and *Homo sapiens*. Nanoindentation revealed a natural gradation of mechanical properties where a 2-12% increase in modulus and hardness correlated to increased mineral content ($p < 0.001$) measured by qBSE. Enamel microcracking in *Lemur catta* resulted in a 49% reduction in nanomechcanical properties at the occlusal (or chewing) surface of the tooth. FEA modeling demonstrated a similar decrease in modulus values for indentation within 20 microns of a crack. Variations in enamel microstructure and microcracking in lemur species enables study of the interplay between tissue microstructure and nanomechanical properties, and further explores variations with diet.

The investigation of nanomechanical property dependence on microstructure and mineral composition in two experimental model systems combined with FEA is used to understand the fundamental mechanical behavior of biological heterogeneous composite materials. Understanding the interplay between material structure and function in biomineralized composites will help to elucidate the relative contributions of various factors to nanomechanical behavior and will ultimately lead to improved development of biomimetic materials.

Dedication

To my parents, Scott and Leslie Campbell for inspiring my love of science and encouraging me to always chase my dreams.

To my sister and best friend, Emily, may we always jump out of planes together.

Acknowledgements

First and foremost, I would like to thank my advisor Professor Virginia Ferguson for her guidance, encouragement, and support throughout this work. Further, I am deeply grateful to Michelle Oyen, Matt Sponheimer, Jaelyn Eberle, and Jerry Qi who served on my committee and were instrumental in supporting my research and academic development. I would further like to recognize my undergraduate physics advisors, Mario Affatigato and Steve Feller, who both inspired my love for research and material science and whose guidance helped me begin this journey towards a PhD. The financial support for this work was partially provided by NSF Graduate Research Fellowship which is gratefully acknowledged. Special thanks to Roy Geiss, Josesh Smyth, Paul Rice, Michelle Sauther, and Frank Cuozzo for their contributions to this study as well as their support and shared knowledge.

Contents

Chapter

Tables

Table

Figures

Figure

Chapter 1

Motivation and Specific Aims

Biomineralized composite materials, such as bone and teeth, play important mechanical roles in the body during life and postmortem are the primary component of the fossil record. Survival of an animal is dependent on the functionality of its bones to provide locomotion and teeth to provide food via mastication (chewing). Failure and dysfunction of these mineralized tissues may result in death or may degrade quality of life. The mechanical and material properties of these tissues are altered biologically throughout life, by age related changes and disease states such as osteoporosis, and then geologically after death by diagenesis (or fossilization). Understanding the mechanical properties of these heterogeneous mineralized composites is required to elucidate the interplay between structure and function of these materials.

The mechanical response of mineralized tissues varies even at the smallest scale, where large-scale porosity and structural variation are not factors yet other heterogeneities must exist. For example, using the cross-section of a human tooth, the modulus of enamel was shown to vary from less than 70 GPa to more than 115 GPa (Cuy et al., 2002). Some variability seen in mineralized tissues can be attributed to the amount of mineral, as it is well known that mechanical properties generally increase with the mineral volume fraction. However, a large range of modulus values for bone is observed at a constant mineral content and thus mechanical properties cannot be explained by the mineral volume fraction and composites theory alone (Katz, 1971; Oyen et al., 2008). Variation in modulus must also be

related to changes in mineral phase and microstructure of these tissues that occur between type or location of the tissue, different species, with age, and disease state.

Variation in the mineral phase include changes in the amount (volume fraction), the composition, and the crystallinity of the mineral. Further variations exist within the microstructure of these tissue where organization of the mineral and organic phases contribute substantially to the mechanical response. Changes in the microstructure and mineral phase are seen in the numerous diseased states that effect mineralized tissues. For example in osteoporosis, the mineral content is decreased, yet changes in crystallinity are also present which including increased crystal size and decreased lattice strain (Boivin et al., 2000). Furthermore, the composition is altered as carbonate content increases while the phosphate content is decreased (Boskey et al., 2005). Despite all the changes in the mineral phase caused by osteoporosis, the modulus measured by nanoindentation was unaltered (Guo and Goldstein, 2000), demonstrating the complex interaction of these multiple variations. In dentin and enamel a decrease in crystallinity is observed in caries (Spencer et al., 2005) along with a decrease in mineral volume fraction and also modulus measured by nanoindentation (Angker et al., 2004). The size of the crystal also has a clear effect on mechanical properties as seen in the dentin where a decrease in crystal thickness was related to higher modulus values (Low et al., 2008). Clearly changes in mineral crystallinity including crystal size, shape, composition, and perfection may affect the mechanical properties of mineralized tissues. Further, variation in composition has an effect on nanomechanical properties as various minerals found in bio- and geo-mineralized tissues have different mechanical properties (modulus of fluorite= 140, apatite=151, quartz=118 GPa) (Broz et al., 2006). The mechanical contribution of these numerous heterogenities are not well known, but understanding could provide insight into structure-property relationships of mineralized tissues.

The overall goal of this dissertation is to study nanomechanical properties in naturally mineralized biocomposites to investigate the heterogeneities within the mineral phase including variation in mineral composition, crystallinity, and microstructure. The following

specific objectives have been defined:

Specific Aim I: Explore how heterogeneities in mineral composition and content influence the nanomechanical properties of mineralized tissues. Variation in mineral composition likely contributes to the heterogeneous nanomechanical response of mineralized tissues, as different minerals and mineral phases have inherently different mechanical properties. Further as variations in the amount of mineral contributes significantly to mechanical properties, mineral content must be quantified in order to determine the contribution of more subtle changes in the mineral phase. In order to elucidate the connection between mineral content, composition, and mechanical properties the following sub-aims will be considered.

(a) Develop standards to allow characterization of mineral volume content at the microscale using backscatter electron imaging.

(b) Investigate variations in nanomechanical properties over a wide range of mineralized tissues with varying mineral composition and content.

(c) Using a geo-mineralization model, determine variations in mineral composition caused by the highly variable process of diagenesis.

Specific Aim II: Investigate how variations in mineral crystallinity and microstructure affect the nanomechanical properties of mineralized tissues. Wide variations in crystal size, shape, perfection, and orientation are seen in mineralized tissues that exist both in their native states and in those altered by various biological, geological, and other processes. The contribution of these variations to nanomechanical properties is poorly understood. In order to investigate the contribution of crystallinity to the nanomechanical properties of mineralized tissues two model systems will be investigated with the following sub-aims.

(a) Investigate the variation of microstructure and nanomechanical properties within dental enamel, a biological model system with relatively uniform mineral content. Changes in mineral microstructure including prism size, orientation, and micro-cracking will be studied in order to understand their relationship to nanomechanical properties.

(b) Determine the nanomechanical property dependence on nano-scale changes in crystallinity by investigating a series of fossilized bone samples as a geo-mineralization model. Geo-minearlized bone samples provide a uniquely large range of crystallinity not available in modern bone.

Specific Aim III: Using finite element analysis (FEA), model the mechanical properties of mineralized tissues to explore the heterogeneous nature of mineralized tissues. Variations in crystallinity, microstructure, and composition contribute to the nanomechanical response of the material; yet it is difficult to isolate each component's contribution with experimental data alone. The use of modeling will allow the isolation of specific microstructural variations for comparison to the model systems above.

(a) Determine how micro-cracking and damage can affect mechanical properties of mineralized tissues. Specifically, investigate the effect of proximity of damage or micro-cracking to indention testing locations.

Chapter 2

Materials and Processes Background

2.1 Bone

Bone is a complex biocomposite that serves a wide range of structural and biological functions such as mechanical support, protection of vital organs, bone marrow storage, and calcium homeostasis. Bone possesses traits desired by many materials scientists and engineers, as it is both strong and tough. Bone adapts to alterations in mechanical loading by changing its shape, size, and location (or moment of inertia) (Cowin, 1999). As the major structural framework of the body, bone is self-assembling, self-maintaining, and self-repairing. However, much is unknown about how the mechanical behavior of bone relates to its material construction and the physiological processes involved in its dynamic function. A full understanding of bones mechanical properties, at multiple length scales, is essential for a comprehensive understanding of the structure-property-function relationships within healthy and diseased bone as well as for the ultimate success of bone implants and replacement materials.

2.1.1 The Structure of Bone

Bone has a hierarchical structure (Figure 2.1) that requires interpretation of mechanical behavior at multiple length-scales. At macroscopic length-scales bone, exist in many different shapes and sizes such as long bones (i.e., humerus or femur) and flat bones (i.e., scapula). Different structural levels of bone also exist that include visibly dense, cortical (or compact)

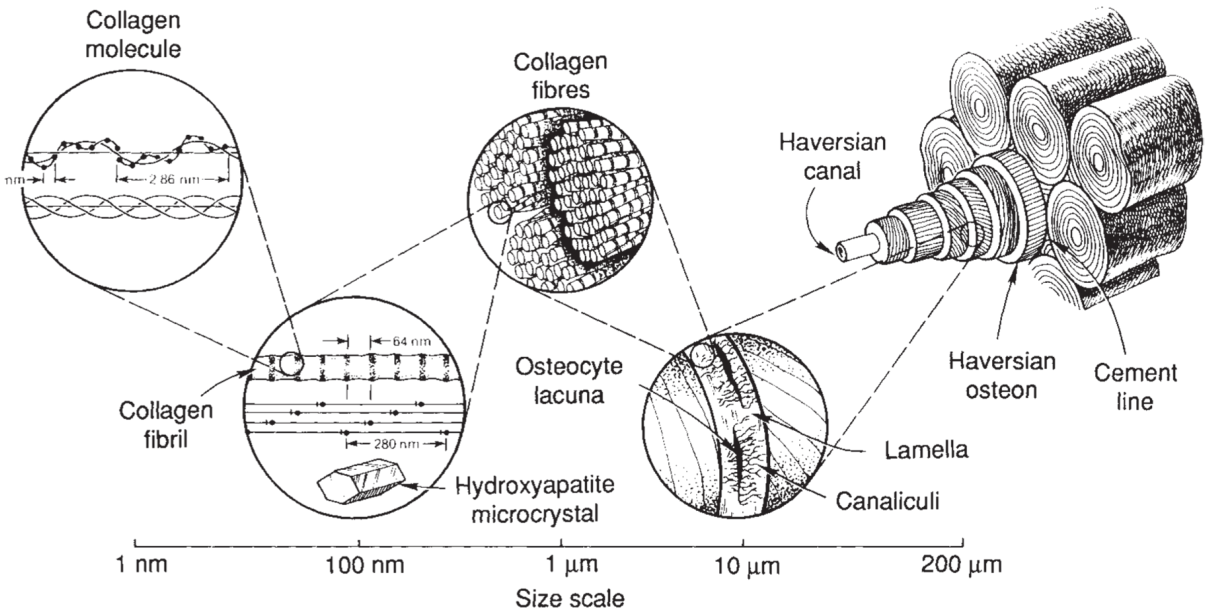

Figure 2.1: Hierarchical structure of human compact bone showing organization from the nanometer scale to the micrometer scale. Figure reprinted with permission from (Lakes, 1993).

bone and trabecular (spongy or cancellous) bone. Long-bones contain a dense cortical bone tissue that surrounds the hollow mid-shaft region (that houses marrow and fatty tissue in adult mammals) and spongy trabecular bone fills in the regions close to the joint surfaces underneath the articular cartilage. Cortical bone provides the bulk of structural support to the skeleton and contains only microscopic pores. In contrast, trabecular bone is made of a network of mostly interconnected plates and rods that reside within the cortical shell or underneath articular joint surfaces. The millimeter-sized spaces in between trabeculae house bone marrow and are much more metabolically active than cortical bone due to their high surface-to-volume ratio (Cowin, 1999). As such, loading patterns within trabecular bone are often visible to the naked eye where trabeculae align along lines of high mechanical loads. Often the structural integrity of trabecular, not cortical, bone is lost in disuse or osteoporosis and results in vertebral or hip fractures.

Bone is a multi-phasic hierarchical composite which consist of an organic, mineral, and water phase (Figure 2.2) that all contribute to the mechanical properties at the multi-scale (Rho et al., 1998). A fully mineralized healthy bone is composed of approximately 50% mineral, 20% water, and 30% organic by volume (Gong et al., 1964; Hayes, 1991). The hierarchical structure of bone (Figure 2.1) is self-assembled from these three nano-scale components creating mineralized collagen fibrils which are arranged into sheet of parallel fibers called lamellae (1-7 μm) (Weiner and Traub, 1992; Rho et al., 1998). The lamellae can be arranged in altering layers of different orientations (0 - 90 $^{\circ}$) with a transition region between each layer creating the rotated plywood structure of lamellar bone (Gebhardt, 1906; Weiner et al., 1997). Concentric layers of lamellar sheets combine to form osteons ($\approx$200-250 μm in diameter) that run parallel to the long axis of the bone and create the primary phase of cortical (or compact) bone. Interstitial lamella exists between primary osteons and the remnants of old osteons.

Woven bone, in contrast to lamellar bone, consists of randomly orientated collagen fibers loosely intertwined giving a woven appearance. Trabecular bone consists of irregularly

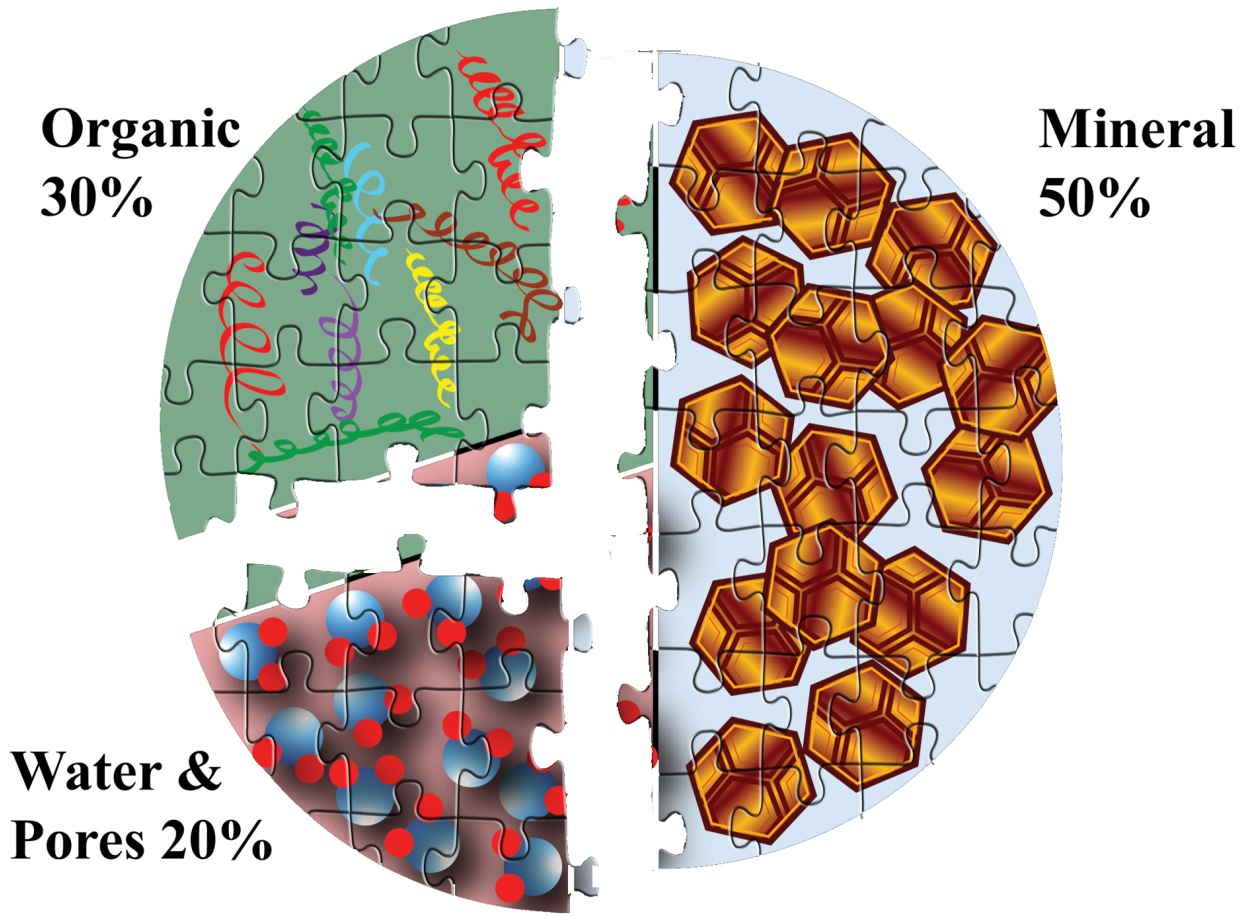

Figure 2.2: Bone is composed of distinct phases: organic (predominately Type I collagen) and mineral (predominately HA with additional forms of calcium phosphates). Water, both bound to the organic molecules and unbound within the interstitial fluid, forms the third constituent phase that acts to plasticize bone and impart viscoelasticity at the tissue (micrometer) level. The nano components and composition of bone are well known, yet how these structures combine to create bones various microstructures is still under debate. The volume percent of each component is reported.

organized struts, which can be made of either lamellar or woven bone. While the macro-scale structure and composition of bone has been widely studied and is well understood, the nano-scale structure proves to be much more elusive.

2.1.1.1 The mineral phase

Bone mineral is composed of extremely impure hydroxyapatite (HA), $Ca_{10}(PO_4)_6(OH)_2$ (Wilson et al., 2006; Elliott, 2002), which forms nano sized crystals. A substantial amount of carbonate (CO_3^{2-}) is commonly substituted into the apatite lattice for OH^- or PO_4^{3-} (Elliott, 2002). Additionally, apatite bone mineral contains a common Ca^+ ion vacancy which often contains sodium, potassium, magnesium, or zinc substitutions. The mineral phase of bone has been widely studied by a variety of techniques including: x-ray diffraction (XRD), infrared and Raman spectroscopy, neutron diffraction, electron microscopy, neutron magnetic resonance (NMR) and atomic force microscopy (AFM) (Rosen et al., 2002; Elliott, 2002; Ivanova et al., 2001; Wilson et al., 2006; Sudarsanan and Young, 1969; Loong et al., 2000; Penel et al., 2005; Arsenault, 1989; Eppell et al., 2001). The collagen-mineral relationship is not fully understood despite this wide range of analysis techniques. The nano-sized minerals in bone (Figure 2.3) are smaller and contain more substitutions that those in enamel (Elliott, 2002). The majority of bone minerals ($\approx 98\%$) appear to exists as small plate like crystals from 6-9 nm in thickness, 20-60 nm in width, and 30-120 nm in length (Ziv and Weiner, 1994; Eppell et al., 2001; Wilson et al., 2006; Rosen et al., 2002). Additionally, AFM techniques have determined that a few larger crystals exist which are approximately 40 x 60 x 90 nm in dimension (Eppell et al., 2001). The size and shape of bone minerals may be caused by the initial formation of crystals between the collagen fibrils in the hole region (Figure 2.3) as originally proposed by Petruska and Hodge (1964). However, the larger crystals, as measured using AFM, are too large to fit within the fibril or hole region and have been observed, via transmission electron microscopy (TEM), to exist in the interfibrillar region (Eppell et al., 2001; Landis et al., 1996; Katz and Li, 1973; Rosen et al., 2002). TEM observations have

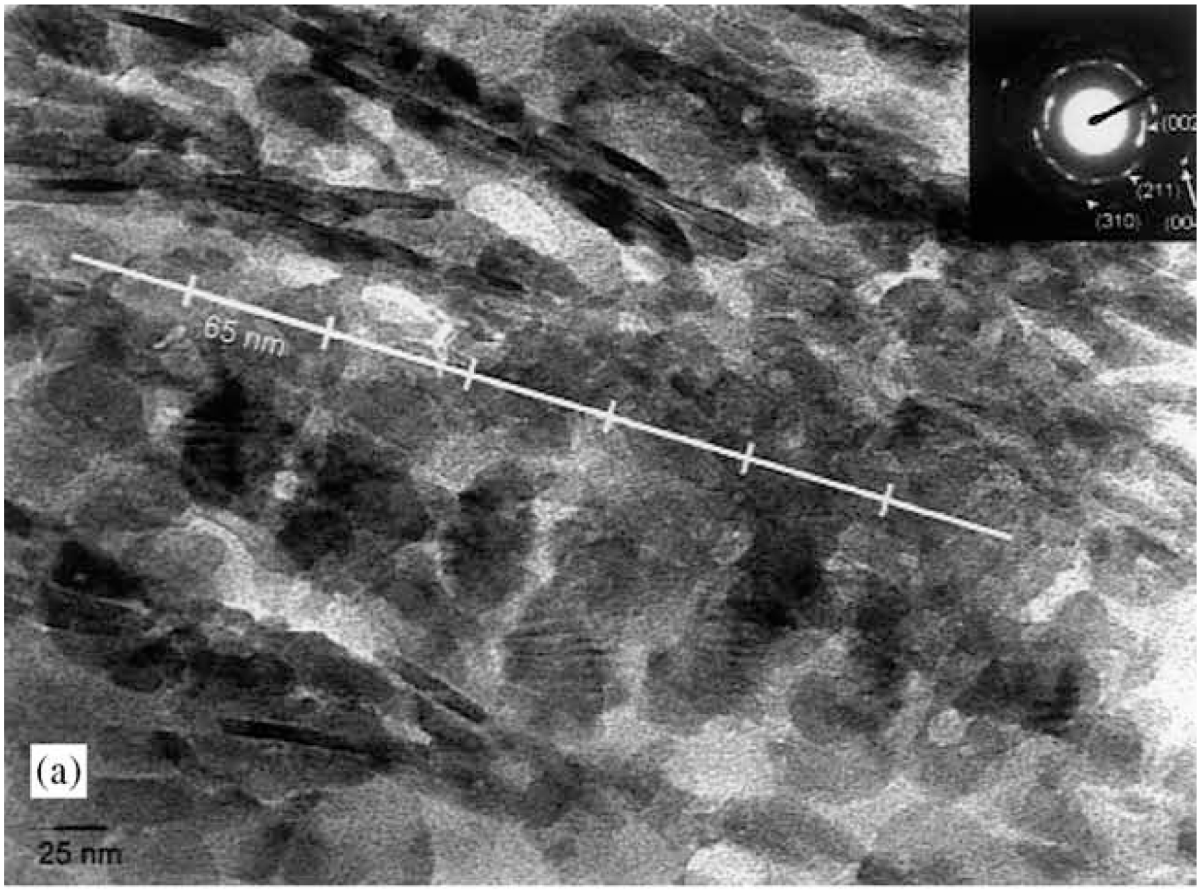

Figure 2.3: A high magnification transmission electron microscopy (TEM) image of bone mineral fibers, where organic portion has been removed. HA crystals contain a plate-like morphology with the long axis of the crystallites (c-axis) is aligned along the longitudinal axis of the fibers. Visible periodic banding 65 nm in length is similar to that of collagen and is consistent with the proposed nucleation sites for apatite crystals between collagen fiber in the hole region. Image is reprinted from Rosen et al. (2002) with permissions.

shown that the majority of bone crystal exists within and on the surface of the collagen fibers within the larger interfibrillar crystals bridging the fibers (McKee et al., 1991). Further, studies of anorganic bone demonstrated that the mineral phase creates a continuous and self-supporting network (Rosen et al., 2002) even after removal of the collagen.

2.1.1.2 The organic phase

The organic phase of bone is primarily (90%) composed of type I collagen fibers. The collagen preferentially aligns and creates a three dimensional network, or scaffold, into and onto which mineral crystals form (Petruska and Hodge, 1964). The collagen fibrils primarily create the viscoelastic response seen in bone and provide toughness to the brittle mineral phase (Bowman et al., 1996). The fibrils are self-assembled from individual tropocollagen molecules, and exhibit characteristic banding every 67 nm (Figure 2.3) due to the quarter-staggering of the 300 nm long triple helices (Alberts et al., 1994). The non-collageneous organic phase in bone is mostly composed of glycoproteins, osteopontin, and proteoglycans. It has been suggested that this non-fibrillar organic matrix can act as a glue which holds mineralized collagen fibers together (Fantner et al., 2005). Additionally, this matrix may serve as a source of sacrificial bonds, thus increasing the energy to fracture.

2.1.1.3 Water and porespace in bone

Porosity and bone fluid plays an important structural and mechanical role as they make up around 20% of bone by volume. The porosity of bone seems to occur in a hierarchical manner, with pore sizes ranging from nanometer to millimeters (Cowin, 1999). The largest pores exist in trabecular bone, then vascular porosity including Haversian canals ($\approx 20\ \mu$m), followed by canaliculi and lacunae ($\approx 0.1\ \mu$m), and finally nanometer-sized pore spaces or matrix micropores (Knothe Tate, 2001) that exist between and within the collagen and mineral crystals. Within these pore spaces, interstitial fluid transports nutrients and wastes throughout the tissue and likely plays a mechanosensory role, whereby physiological strains

result in a shear fluid flow that is detectable by osteocytes (Cowin, 2007). Bone contains two types of water, bound and unbound. Unbound water, which exists mostly in the interstitial fluid within larger (≈ 0.1 μm to millimeter-sized) pore spaces, contributes significantly to the viscoelastic properties of bone (Cowin, 1999). Water may also exists in smaller pore spaces between the mineral crystals and collagen fibrils (Neuman et al., 1956). The collagens and ground substance of the organic matrix contain many charged sites that facilitate interactions with unbound water. Bound water plays an important role in possibly stabilizing the mineral crystallites by occupying OH^- and possibly Ca^{2+} vacancy sites (Wilson et al., 2006). The permeability of bone tissue relies on the degree to which tissue is vascularized and the mineral density of the tissue.

2.1.2 Mechanical Properties of Bone

Bones mechanical properties vary widely at different length scales as the collagen, mineral, and porous water phases combine to form the hierarchical structure of bone. Forces applied to a bone at the macro scale are translated to the cellular level and play a role in the maintenance and adaptation of the bone. Traditional mechanical testing techniques such as tensile or compressive testing and three-point bending have been routinely used to measure the mechanical properties of large bone samples (Reilly et al., 1974; Bayraktar et al., 2004; Choi et al., 1990; Antonio Ascenzi, 1967; Ferguson et al., 2003a). Large hydrated cortical tensile specimens produce modulus values ranging from 14 to 20 GPa (Reilly et al., 1974; Bayraktar et al., 2004), micrometer-sized specimens yield values of 5.4 GPa (Choi et al., 1990), and tensile specimens made from dissected osteons measure at 12 GPa (Antonio Ascenzi, 1967). Additionally, micro-hardness testing has been applied to provides a direct measurement of the resistance to plastic deformation via Vickers hardness. Yet, residual indentation impressions are large and often extend far beyond fifty micrometers in width (Dall'Ara et al., 2007). Nanoindentation provides an advantage that none of these techniques possess: the ability to avoid the influence of bones complicated three-dimensional

geometry on measured properties and to probe bone at the level of the tissue itself.

Nanoindentation can provide valuable nanomechanical data to elucidate insight into tissue-level alterations in bone that are caused by factors including bone diseases, disuse or weightlessness, and even fossilization. Conventional analytical techniques for nanoindentation assume an elastic, isotropic, and homogenous material; yet bone fits none of these criteria. Further, bones complex construction produces time-dependent, or viscoelastic, behavior. This section provides an overview of the our current understanding of bone at the tissue-level that have been enabled by nanoindentation.

2.1.2.1 Microstructural mechanical variation

A large number of nanoindentation studies have investigated the wide range of mechanical properties found in various types and regions of bone. Nanoindentation's high load and displacement resolution is ideally suited to investigate various microstructures in precise anatomical locations. For identical testing methods and anatomical sites, the indentation modulus of interstitial bone is the highest followed by osteonal and then trabecular bone. The nanoindentation modulus of dry trabecular bone samples measured by nanoindentation ranged from 8.2 to 19.4 GPa, whereas cortical (both interstitial and osteonal) bone was significantly higher (18 to 26 GPa) (Zysset et al., 1999; Rho et al., 1997; Hoffler et al., 2005). Osteonal bone is generally reported to have lower modulus values as compared to interstitial bone that has higher mineral content (Gupta et al., 2006). The measured moduli for human bone depend greatly on a vast number of experimental, compositional, structural, and anatomical parameters. Additionally, the values reported above are for dry bone and thus do not represent true in vivo values. Despite the variability, general property relationships between types of bone are maintained and thus may be investigated using nanoindentation.

Nanoindentation tests to shallow depths can be used to test the mechanical properties of smaller structural features such as individual lamellae. For example, using a ramp-and-hold test to 500 mN (100 nm), Gupta et al. (2006) found alternating regions of high

and low stiffness due to the lamellar structure. Mapping with similar spatial resolution of both nanoindentation and Raman data, showed a homogenous distribution of mineral content (Kazanci et al., 2006; Carden and Morris, 2000; Hofmann et al., 2006) suggesting that collagen orientation contributes to the alternating mechanical properties between lamella. However other studies using X-ray microprobe analysis demonstrated that the thick lamellae had 10-15% higher calcium and phosphorus content than thin lamellae (Marotti et al., 1993), indicating that the mineral content may have a profound effect on the mechanical properties. Most likely, both collagen orientation and the degree of mineralization contribute to the mechanical variations seen between thick and thin lamella.

2.1.2.2 Anisotropy

The elastic response of bone is anisotropic, where mechanical properties are dependent on the testing direction. Cortical bone, found within the mid-shaft of a long bone, is transversely isotropic (Reilly and Burstein, 1975; Rho et al., 1997) where the osteons and Haversian canals generally align with the long axis of the bone (Petrtyl et al., 1996). Using millimeter-dimensioned sections of human cortical Haversian bone tested in both compression and tension, revealed that elastic moduli were $\approx 40\%$ greater in the longitudinal versus the transverse direction in tension and $\approx 55\%$ greater in compression (Reilly and Burstein, 1975). Other bone types also possess anisotropy where the properties vary with direction and with the directionality of lamellae, blood vessel networks, and with anatomical site and age (Reilly and Burstein, 1975; Currey, 1984). The functionality of anisotropy is evident within the cortical bone of long bones where the bone is stiffer in the primary direction of applied force.

At smaller scales, bone also possesses anisotropy. The preferential organization of collagen fibrils and mineral crystals within the osteons and lamellar structure creates anisotropy (Pidaparti et al., 1996; Amprino, 1958). Microhardness indentations, sampling areas containing many lamellae and other structures (e.g., osteocyte lacunae), clearly demonstrate

anisotropy using a Knoop indenter tip on selected bone surfaces (Amprino, 1958; Riches et al., 1997).

One key benefit of nanoindentation lies in the ability to measure properties at the level of individual structures within bone, such as within individual lamellae. By conducting nanoindentation testing in different directions, the anisotropy of individual microstructural components can be assessed. Similar to results in bulk sections of bone in compression, (Reilly and Burstein, 1975) Berkovich nanoindentation measurements on dry, cortical bone revealed an elastic modulus for longitudinally-tested interstitial lamellae (25.7 $\pm$ 1.0 GPa) that was $\approx$ 55% greater than that measured in the transverse direction (16.6 $\pm$ 1.1 GPa) (Rho et al., 1999b).

Anisotropy is measureable in both mineral and organic phases of bone. Equine cortical bone samples, experimentally manipulated from a wet, baseline condition to produce five different states: wet, dehydrated (in 100% ethanol), embedded (ethanol dehydration followed by PMMA embedding), decalcified, and deproteinated, showed characteristic anisotropic behavior in all but the wet state (Table 2.1) (Bembey et al., 2005). With the exception of nanoindentation in wet bone, the modulus was significantly elevated in the longitudinal direction for all other conditions. Due to difficulties in sample preparation and testing of wet bone, subtle differences in the longitudinal versus the transverse indentation moduli may have been difficult to discern. That anisotropy was measureable even in PMMA-embedded decalcified bone demonstrates that the organization of the organic matrix may contribute to the overall behavior of bone in nanoindentation.

Nanoindentation is a multiaxial test where the measured modulus is a combination of moduli in all directions and is relatively insensitive to anisotropy (perhaps another reason for the lack of difference in wet bone samples) (Bembey et al., 2005). The measured indentation elastic modulus will vary with anisotropy but will be weighted toward the properties in the direction of the applied load. Swadener et al. (2001) demonstrated that, through integration of measured elastic constants over the indented plane, an anisotropy ratio (based on

Table 2.1: Values [mean (SD), number n =] of plane strain modulus (E') in GPa from nanoindentation on planes that lie transverse and longitudinal to the long axis of the bone. Students t-test between transverse and longitudinal directions results reported as not significantly different (N.S.), significant (*), or highly significant (**). Data are from Bembey et al. (2005).

Condition	**E′ Transverse(GPa)**	**E′ Longitudinal (GPa)**
Wet	11.7 (1.7), 326	11.8 (1.9), 68 (N.S.)
Ethanol Dehydrated	15.0 (2.2), 309	24.8 (2.2), 68**
PMMA Embedded	19.4 (2.1), 283	25.8 (2.1), 74 **
Deproteinated (Embedded)	13.4 (1.0), 62	20.4 (2.2), 62 **
Decalcified (Embedded)	4.9 (0.3), 59	5.5 (0.3), 49 *

elastic modulus E) can be determined that accounts for the indentation modulus (M) ratio in anisotropic materials (Fan et al., 2002; Swadener et al., 2001). For bone, the E ratio of 1.75 (ratio of longitudinal to transverse moduli) corresponds to a M ratio of ≈1.4 (Swadener et al., 2001). This approach, in combination with testing bone of experimentally varied compositions, was used to demonstrate a potential mechanism for anisotropic material behavior (Oyen and Ko, 2005). Bone mineral therefore was implied to have greater connectivity in the longitudinal versus the transverse directions. The longitudinal direction's greater mineral connectivity and strength provide functionality in the direction of primary loading in long bones.

2.1.2.3 Viscoelasticity

Bone behaves in a time-dependent manner due in part to its organic phase (Sasaki and Enyo, 1995) and its water content with a corresponding poroelastic flow through the bone material (Cowin, 1999). Viscoelasticity in bone has been shown to correlate with hydration state (Bembey et al., 2006a; Sasaki and Enyo, 1995; Yamashita et al., 2001) and mineral content (Sasaki and Enyo, 1995). Historically, the general approach for nanoindentation of bone has been to employ a range of techniques to minimize creep effects, rather than to

complicate nanoindentation data analysis with time-dependent behavior. A long creep hold at maximum load can minimize time-dependent behavior on unloading and thus permits measurement of elastic properties (Briscoe et al., 1998; Chudoba and Richter, 2001). Rapid unloading following no hold at peak load enables determination of the unrelaxed modulus (Cheng et al., 2005). A third method attempts to eliminate viscoelastic effects by correcting the unloading stiffness (Tai et al., 2005) with the creep rate at max contact depth (measured during a hold at max load) (Feng and Ngan, 2002).

Rather than eliminate viscous effects during indentation, more recent works have embraced nanoindentation as a tool to explore the viscous behavior of bone. For more detailed explanation of the viscous behavior of bone see appendix B. The use of indentation to study the elastic and viscous responses of biological materials is well established. Further, while nanoindentation was initially developed to study stiff, elastic-plastic engineering materials, its use for examining polymers is becoming widespread (Oyen and Cook, 2003; Briscoe et al., 1998; Oyen, 2006b; Zhang et al., 2005). Early work on the viscoelasticity of dry bone, included in a noninfiltrating epoxy resin, examined the role of loading rates or holding times (at max applied load) (Fan and Rho, 2003). The use of various loading rates (with a constant 180 s creep hold) demonstrated that elastic modulus was overestimated at fast indentation rates and that an extended hold time (at least 30 s) was required to eliminate the time-dependent effect. Additional testing on dry bone specimens used a viscoelastic correction procedure (Feng and Ngan, 2002) to produce a corrected elastic modulus. Both of these studies utilized a pointed, Berkovich tip and employed a multiple loading protocol at each indentation site prior to collecting data. The pointed tip may complicate the interpretation of the bone materials response by causing an immediate plastic deformation upon loading (Oyen and Cook, 2003). Single loading indentations made into a bone-dental implant interface using a pointed tip, analyzed using a viscous-elastic-plastic model, (Oyen and Ko, 2007), produced modulus and hardness results that were comparable to those obtained by using traditional elastic-plastic analysis techniques. Recently, the viscous-elastic-plastic model has

been extended to include analysis of the common trapezoidal testing condition (see Appendix B).

Several studies utilizing a spherical tip have evaluated the viscous behavior of bone via creep testing following a finite-rate ramp loading (Oyen and Ko, 2008; Bembey et al., 2006c,b). Analytical expressions, based on curve-fits to the load-time or displacement-time data during a creep hold at maximum load, were used to calculate measurements of the creep or stress relaxation functions. This approach was used to examine the role of hydration in the viscous behavior of bone, where cortical bone soaked in varying concentrations of ethanol demonstrated a loss of viscosity with increasing dehydration (Bembey et al., 2006c). Similarly, bone soaked in solvents possessing varying degrees of polarity (and Hansens solubility parameter for Hydrogen bonding) revealed a similar dependence on hydration and a distinct role of hydrogen bonding in their viscous response (Bembey et al., 2006b). A poroelastic analysis of the same data set revealed that bones intrinsic permeability increased with increasing values of the solubility parameter (Oyen and Ko, 2008). Correlation of these results to the fundamental porosity length scale indicated that a characteristic pore size of ≈ 1.6 nanometers describes the intrinsic permeability of water in bone at the scale of the collagen-apatite interactions. While such analyses are simplified and preliminary in nature, they demonstrate the applicability of nanoindentation for the exploration of time-dependent and molecular level interactions in bone.

Analysis of viscoelasticity in bone is well within the reach of available analytical tools. In particular, approaches for analysis of polymers with viscous behavior are well-developed (Oyen and Cook, 2003; Feng and Ngan, 2002; Oyen, 2006b; Zhang et al., 2005; Oyen, 2005) and are applicable to the study of biological tissues' including bone (Bembey et al., 2006c,b; Fan and Rho, 2003; Oyen and Ko, 2007). Such analytical formulations are ideal for the analysis of local variations in tissue properties. These analytical methods are easily applied and can provide insight into the viscous behavior at the tissue-level of bone. Finally, such analyses may add to our ability to better understand many research and clinical problems

as the mechanical response is inherently viscoelastic *in vivo*.

2.2 Tooth Enamel

Enamel, as the hardest biological tissue in the human body, forms the crown of the tooth and makes it possible to cut, grind and tear food during mastication. Immediately below the enamel surface (around 1 mm thick in humans) is a softer, yellow tissue called dentin (Figure 2.4). The extremely brittle enamel would crack under standard masticatory loading without the support of the compliant dentin (Boyde, 1989). During mastication the tooth is exposed to normal and shear forces ranging from 28 N to more than 1200 N (Ferrario et al., 2004; Fernandes et al., 2003), which can result in wear of the enamel surface. Further, fracture and micro-damage that accumulate in enamel are not repaired by cellular processes as in bone. Raised functional surfaces, called cusps, are generally the first to display signs of wear and tend to have the thicker enamel than the fissures (or valleys) . Not all mammals have enamel, the order Edentata (including anteaters, armadillos, and sloths) is distinguished by having none, but in those that do the thickness can range from microns up to 4 mm in elephants (Boyde, 1989).

2.2.1 Enamel as a material

Enamel is a composite material that consists of 89-91% mineral by volume with the remaining proportion composed of organic tissue and water (Boyde, 1989). The mineral phase is composed of hexagonal HA crystals that are much larger then those in bone at sizes of approximately 50 x 100 nm and up to a 50 μm in length (Bres et al., 1993; Boyde, 1989; Jongebloed et al., 1975). The HA in enamel contains fewer substitutions that those in bone and is chemically homogenous (Elliott, 2002). These crystals fuse laterally together to form enamel rods, which run perpendicular from the enamel-dentin junction (EDJ) toward the tooth surface. The enamel rods, 4-7 μm in diameter (Boyde, 1989; Ge et al., 2005), combine to form highly ordered 3D arrays or prism patterns (Figure 2.5). The prisms vary

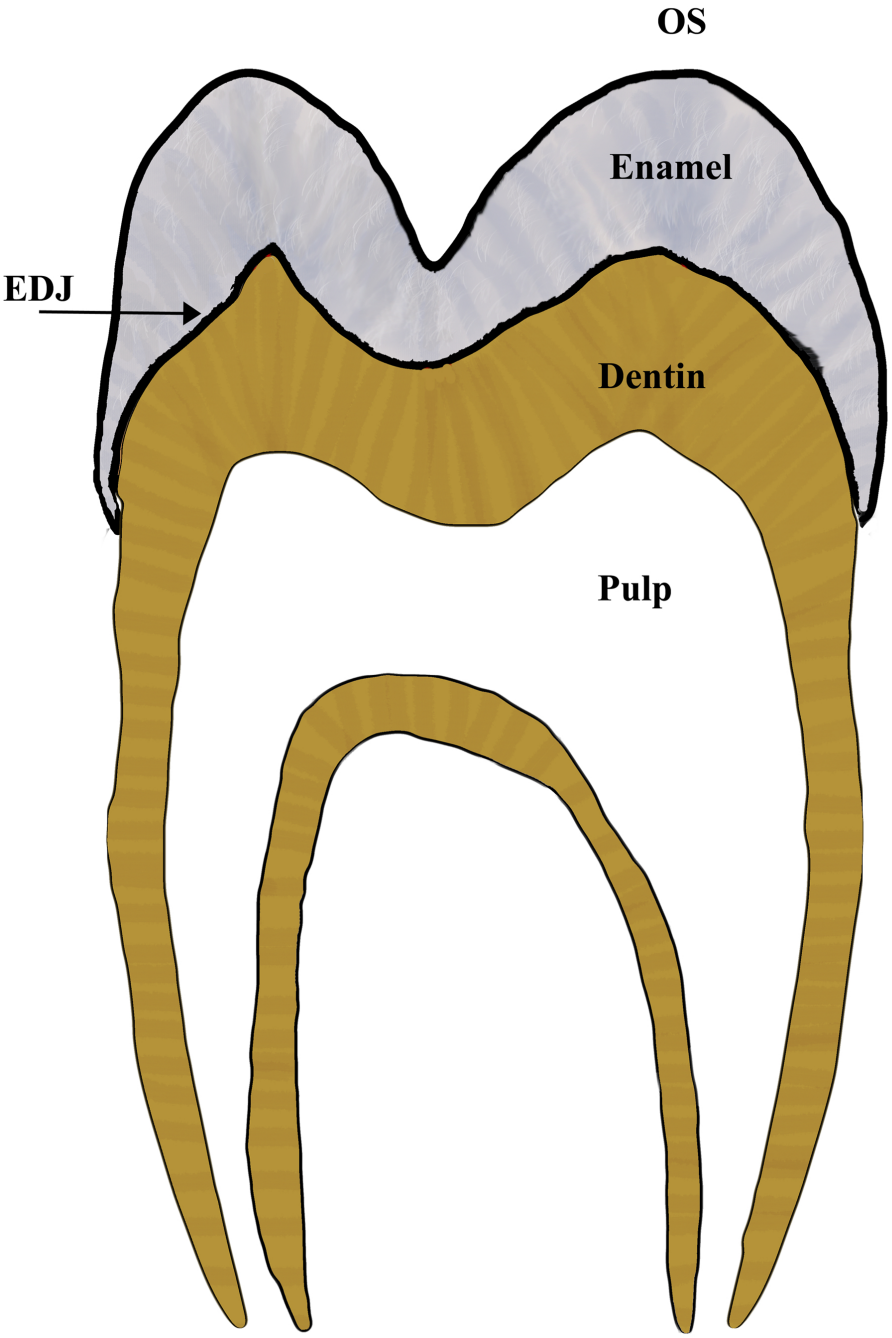

Figure 2.4: Schematic of the cross-section of a tooth with enamel, dentin, pulp, occlusal surface (OS), and enamel-dentin junction (EDJ) labeled.

in orientation throughout the enamel. Near the occusal surface, the prisms are generally perpendicular to the surface, while near the EDJ, the prisms are randomly oriented (Boyde, 1997). Enamel connects to the underlying more compliant dentin at the EDJ, and plays a vital role in the functionality of the tooth. The EDJ has a complex scalloped structure with 25-40 μm convexities directed towards the dentin that helps to create a graded region that have been suggested to play a significant role in the EDJs unique crack resistance (Constantino et al., 2009).

The organic phase of enamel is composed of a noncollagenous protein matrix which begins to mineralize within minutes of it secretion by ameloblasts. The enamel crystals increase in diameter, but not in number, as the percent mineral content increases rapidly during development (Boyde and Fortelius, 1986). As the minerals continue to mature, the matrix is resorbed to allow the crystals to thicken (Boyde, 1997). In mature enamel, the organic phase primarily exist in the prism boundaries and serves as both crack stoppers and propagators as enamel tends to break at these boundaries (Boyde, 1989). Due to the extremely small concentrations of the organic and water phase, enamel behaves in an approximately time independent manner.

2.2.2 Mechanical properties of enamel

As the functional layer of the tooth, enamel allows mammals to prepare food for digestion and plays a large evolutionary role in survival of the animal. Enamel has demanding functional requirements such that it must sustain a wide range of loads without failure as it is non-reparible. As such, the mechanical properties of enamel have been widely investigated. In many early studies, compression testing and microhardness were used to investigate fracture toughness, elastic modulus, and strength (El-Mowafy and Watts, 1986; Craig et al., 1961; Imbeni et al., 2005). These large scales test often measure a combined mechanical effect of dentin and enamel and are further complicated by tooth geometry. For example, Stanford et al. (1958) determined the modulus of enamel to be 47.5 $\pm$ 5.5 GPa, which is

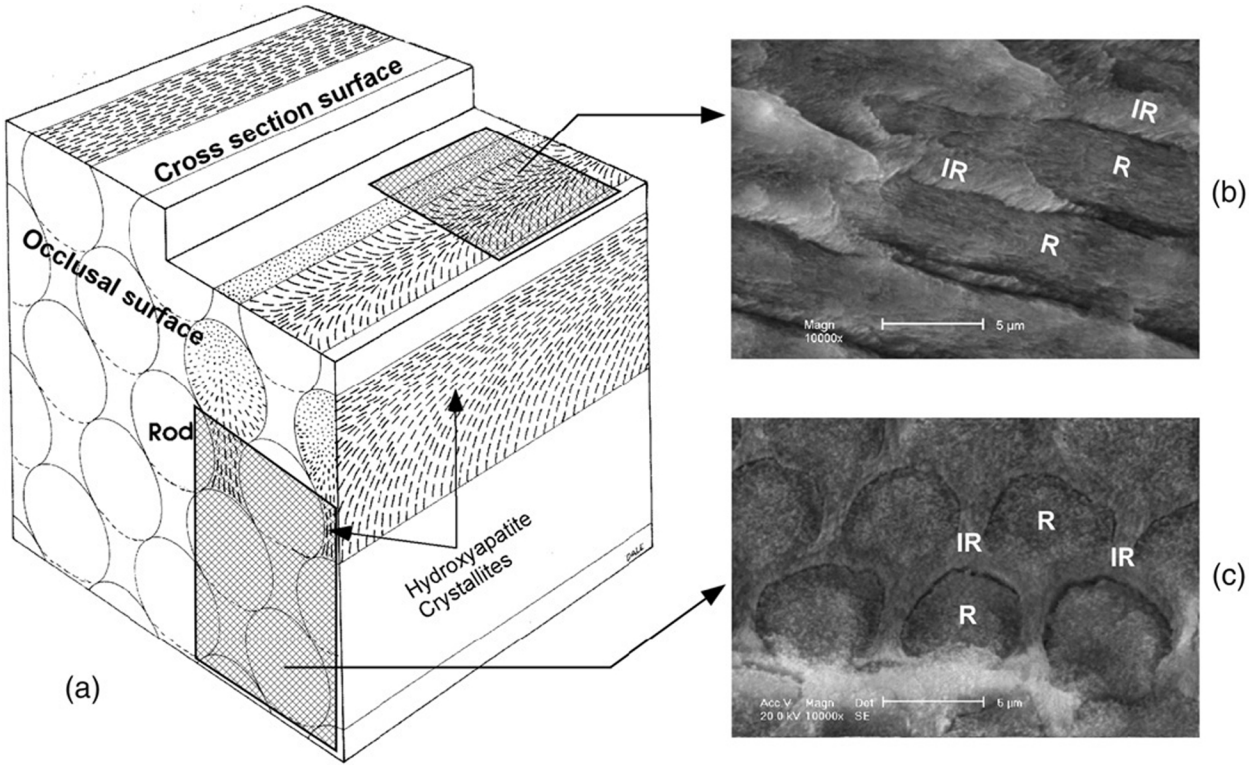

Figure 2.5: (a) Schematic illustration of human enamel's microstucture showing keyhole shaped prisms of about 5 μm diameter. Enamel prisms or rods (labeled R) are constructed from apatite crystals with different orientations in the head and tail area. The sheath or inter-rod region (labeled IR) surounds each prism and is enriched in organic matter. SEM images of the axial (b) and occlusal (c) surface of acid etched human enamel. Reprinted from (He and Swain, 2008) with permission.

substantially lower than values measured using nano- or micro-scale test. Nanoindentation allows the isolation of the mechanical properties of individual fundamental microstructures and has become the primary enamel mechanical testing tool (Cuy et al., 2002; Straines et al., 1981; Habelitz et al., 2001; Ferguson et al., 2005). Investigation of the nanomechanical properties of enamel can provide insight into on a number of factors ranging from microstructure and prism orientation (Shimizu et al., 2005) to mineralization and composition (Weatherell et al., 1974; Tesch et al., 2001; Svalbe et al., 1984; Cuy et al., 2002; Darnell et al., 2010). Knowledge of mechanical properties of enamel is important to understanding disease states, functional adaptations to diet, and ultimately lead to the development of improved dental replacement materials. This section provides an overview of the our current understanding of enamel at the tissue-level that have been enabled by nanoindentation.

2.2.2.1 Microstructural mechanical variation

Recently nanoindentation has emerged as the primary investigation method to study the mechanical behavior of human enamel (Table 2.2). Hardness and modulus values have been commonly reported as averaged values (Willems et al., 1993; Habelitz et al., 2001; Mahoney et al., 2000; Marshall et al., 2001) where it is assumed that enamel is a homogenous material. However, enamel is extremely heterogeneous as the mechanical properties have been shown to vary drastically across the crown of the tooth (Figure 2.6). Modulus values ranged from more than 115 GPa on the occlusal surface to less than 70 GPa at the EDJ (Cuy et al., 2002). Additionally, chemical composition has been shown to vary in a similar manner where mineral content, CaO and P_2O_5 was highest at the hard occlusal surface and lower toward the softer EDJ (Cuy et al., 2002). While enamel's mechanical properties are known to depend on mineral content and composition (Weatherell et al., 1974; Tesch et al., 2001; Svalbe et al., 1984; Cuy et al., 2002; Darnell et al., 2010), the heterogeneity of modulus and hardness values have further been linked to microstructural variations such as prim orientation (Spears, 1997; Jiang et al., 2005) and prism size (He et al., 2006).

Table 2.2: Mechanical properties of human enamel measured by nanoindentation reported by a range of investigators. Modulus and hardness are reported at mean ± SD (when available) or as the range of reported values.

Literature	**Test location**	**Test load or depth**	**Modulus (GPa)**	**Hardness (GPa)**
Braly et al. (2007)	at cusp tip	200 nm	120 to 130	6 to 7
Cuy et al. (2002)	axial (occlusal to EDJ)	400 & 800 nm	120 to 47	6.4 to 2.7
Zhou and Hsiung (2007)	occlusal surface	100 - 2000 nm	104 to 70	5.7 to 3.6
He et al. (2006)	occlusal surface	up to 450 mN	100 to 60	5.0 ± 0.45
He et al. (2006)	axial surface	up to 450 mN	80 to 40	4.5 ± 0.45
Willems et al. (1993)	occlusal surface	10 mN	90.59 ± 16.13	3.39 ± 0.18
Habelitz et al. (2001)	occlusal surface	1.5 mN	87.2 ± 2.2	3.9 ± 0.3
Habelitz et al. (2001)	axial surface	1.5 mN	72.7 ± 4.5	3.8 ± 0.4
Ge et al. (2005)	occlusal (inter prism)	1 mN	83.4 ± 7.1	4.3 ± 0.8
Ge et al. (2005)	occlusal (prism sheath)	0.3 mN	39.5 ± 4.1	1.1 ± 0.3
Mahoney et al. (2000)	axial (occlusal to EDJ)	10 & 150 mN	80.35 ± 7.71	4.88 ± 0.35
Marshall et al. (2001)	axial (near EDJ)	up to 14 mN	63.55 ± 1.46	3.51 ± 0.13

Recently using AFM-based nanoindentation, Ge et al. (2005) reported that the modulus and hardness of the prism sheaths were about 73.6% and 52.7% lower than those of the prisms. The prism sheath or inter-rod region (labeled in figure 2.5) is enriched in organic matter which leads to its reduced mechanical properties. As human enamel prisms are approximately 5 μm in diameter a single indentation test to low depths and placed at the center of a prism will test only the HA crystals within a single prism. As the depth of the indent increases a larger volume may include both prism and sheath and thus the resultant mechanical properties will be reduced compared to a test which only samples the HA crystals. This concept has been demonstrated in human enamel where the mechanical properties have been shown to decrease with an increase in indentation depth (He et al., 2006; Zhou and Hsiung, 2007). In a similar fashion, changes in mechanical properties have also been related prism size where indentation test to a constant depth incorporated more organic sheath in smaller prisms and resulted in reduced mechanical properties compared to larger prisms (Angker et al., 2004).

2.2.2.2 Anisotropy and Prism Orientation

HA crystals are inherently anisotropic in nature and combine to create enamel prisms which also display directionally dependent mechanical properties. Numerous nanoindentation and microhardness studies have shown that modulus values measured on the occlusal surfaces (with prism aligned perpendicular to the surface) are higher than that measured in the axial direction (Habelitz et al., 2001; Meredith et al., 1996; Craig et al., 1961; Jiang et al., 2005). When force is applied in the direction of long axis of the HA crystals most of the load is carried by the prism and not the sheath. However, when load is applied perpendicular to the HA crystals the smaller thickness of the crystals in that direction require that more of the load be distributed within the organic component. In addition, several finite element models have confirmed the anisotropic nature of enamel in both indentation simulations and under uniaxial loading (Spears, 1997; Xie et al., 2009).

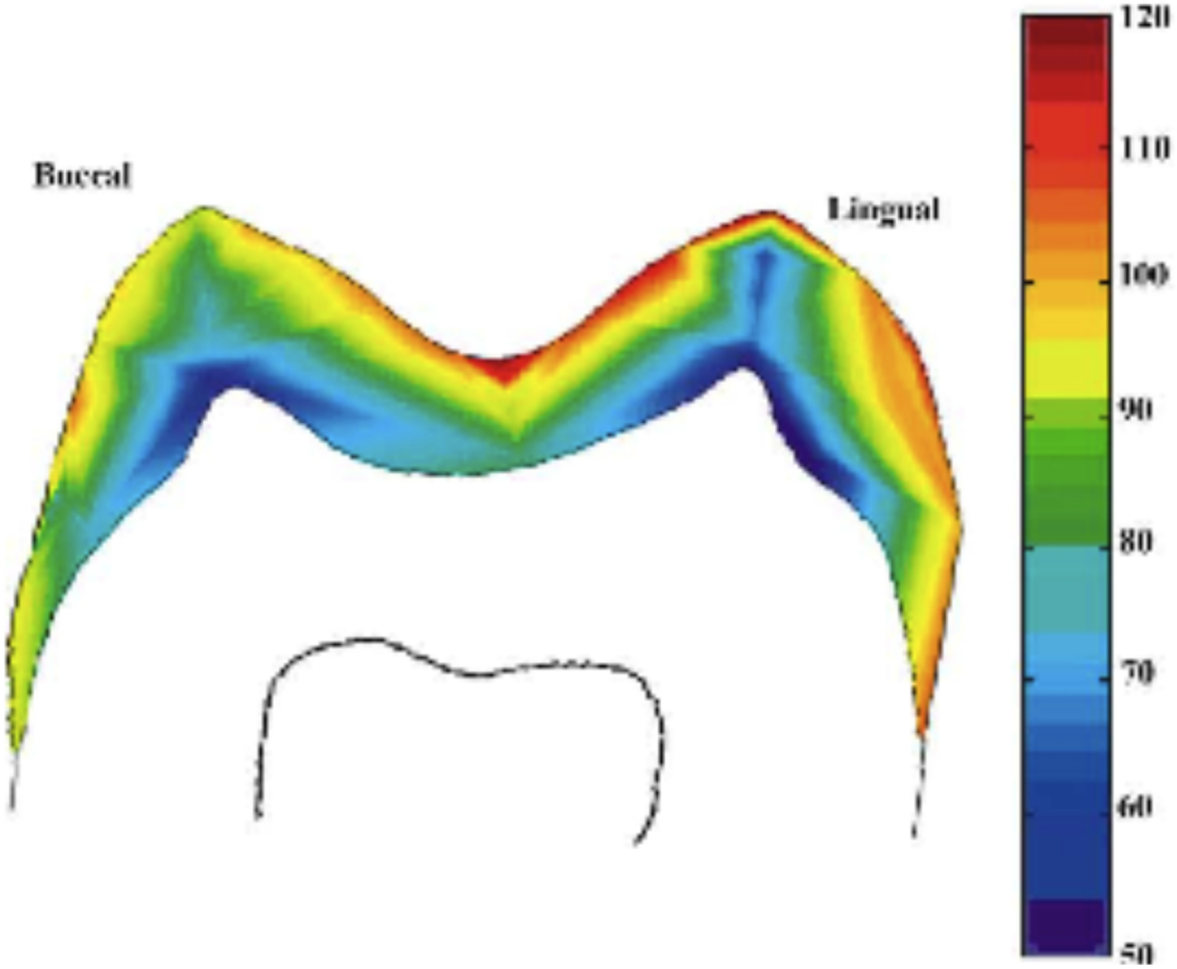

Figure 2.6: Enamel nanoindentation modulus (E, GPa) values mapped over a human M^2 tooth. Notice the decrease in mechanical properties from the enamel surface to the EDJ (with permission from (Cuy et al., 2002)).

The effect of anisotropy of enamel prisms is an even more complex issue at locations that an not near the occlusal surface. While prisms near the occlusal surface are generally aligned perpendicularly, or radially, prism near the EDJ generally have more random orientation (Boyde, 1997). Additionally decussation, or variation in the orientation of groups of prisms, exists in the majority of primates > 2000 g in mass (Maas and Dumont, 1999). Decussation provides a crack propagation barrier and is thought to increase the toughness of the enamel.

While is has been well established that enamel is an anisotropic and heterogeneous material many studies have assumed enamel to be homogenous and isotropic (Lucas et al., 2008; Lawn et al., 2009; von Koenigswald et al., 1987; Rensberger, 1995). Furthermore loading conditions are variable throughout mastication and rarely run perpendicular from the cups to the EDJ (Macho and Spears, 1999). Rather cusp tips become rapidly worn and teeth are then loaded (near) perpendicular to the wear facets (Rensberger, 1995; Macho et al., 2005; Shimizu and Macho, 2008). These complicated conditions and material properties variations need to be considered in order to appraise the functional significance of primate enamel and further determine the implication for evolutionary biology.

2.3 Composites Theory

A composite material consist of two distinct phases that combine to create a single material with superior properties over those of the individual components. Common to both engineering and nature, a composite material is often composed of a compliant matrix phase and a stiff filler phase. A wide range of mineral composites exist in the natural world from mineralized cartilage, dentin, nacre, bone, and enamel where the mineral-filler phase (often HA but occasionally other minerals such as aragonite in nacre) provides stiffness to an organic matrix substantially increasing the strength of the material. Numerous studies have used composite theory to relate mineral content to mechanical property variations in bone and enamel (Jager and Fratzl, 2000; Kotha and Guzeslu, 2002; Oyen et al., 2008; Currey,

1964; Katz, 1971).

In simple composites theory the mechanical response of the material is a weighted combination of the properties of the individual components (Chawla, 1987). This simple rule of mixtures is applied in both the Voigt model of uniform strain and the Reuss model of uniform stress. The Voigt-Ruess bounds have been widely applied to model material properties of fiber reinforced composites. The Voigt model is an assembly of alternating layers of two materials equally strained where the displacement length is the same in both materials. Using the Voigt equation the upper limit of the elastic modulus E_U of the composite is a mixture of multiple phases with elastic modulus E_i and a volume fraction V_i and is given below for a two phase composite:

$$E_U = V_2 * E_2 + (1 - V_2) * E_1 \tag{2.1}$$

Similarly the Reuss model can be visualized as alternating layers with force applied across the layer such that each experiences equal stress to described the lower bound as:

$$E_L = \left[\frac{V_2}{E_2} + \frac{1 - V_2}{E_1}\right]^{-1} \tag{2.2}$$

A more physically realistic representation of mineralized composites consist of a compliant matrix phase reinforced by a particle filler phase as in the Hashin-Shtrikman bounds. The Hashin-Shtrikman bounds are derived in terms of the shear (G) and bulk moduli (K) which are related to Poisson's ratio (ν) and elastic modulus (E) for isotropic materials by:

$$G = \frac{E}{2(1+\nu)} \text{ and } K = \frac{E}{3(1-2\nu)} \tag{2.3}$$

The lower bounds are given by (Hashin and Shtrickman, 1963):

$$K_L = K_1 + V_2 \left[\frac{1}{K_2 - K_1} + \frac{3(1 - V_2)}{3K_1 + 4G_1}\right]^{-1} \tag{2.4}$$

$$G_L = G_1 + V_2 \left[\frac{1}{G_2 - G_1} + \frac{6(K_1 + 2G_1)(1 - V_2)}{5G_1(3K_1 + 4G_1)} \right]^{-1} \tag{2.5}$$

$$E_L = \frac{9K_L G_L}{3K_L + G_L} \tag{2.6}$$

And the upper bounds are given by:

$$K_U = K_2 + (1 - V_2) \left[\frac{1}{K_1 - K_2} + \frac{3V_2}{3K_2 + 4G_2} \right]^{-1} \tag{2.7}$$

$$G_U = G_2 + (1 - V_2) \left[\frac{1}{G_1 - G_2} + \frac{6(K_2 + 2G_2)(V_2)}{5G_2(3K_2 + 4G_2)} \right]^{-1} \tag{2.8}$$

$$E_U = \frac{9K_U G_U}{3K_U + G_U} \tag{2.9}$$

Both large scale pioneering work on bone as a composite tissue (Katz, 1971) and more recent tissues level studies using nanoindentation (Oyen et al., 2008) have determined that no simple relationship exists between modulus and mineral content (Figure 2.7). Composite theory merely predict bounds on elastic behavior and describe the positive correlation between modulus and mineral content (Katz, 1971; Oyen et al., 2008). This relationship is not exact and at a single mineral content a wide range of modulus values can be observed indicating that other factors must inherently contribute to the mechanical response. Understanding the mechanical properties of mineralized composite tissues is impressively complex as and numerous factors including microstructure and composition create extremely heterogeneous materials where properties vary substantially at even the nanoscale. Additionally variations in both the mineral and organic phases are influenced by factors including age (Hoffler et al., 2000b), type and location of the tissue (Zysset et al., 1999; Rho et al., 1997, 1999a; Hoffler et al., 2000a; Zysset et al., 1998), and disease state (Ferguson et al., 2003a). More advanced paradigms are required to fully incorporate all sources of heterogeneity within mineralized tissues that include mineral content, composition, and orientation, crystallinity,

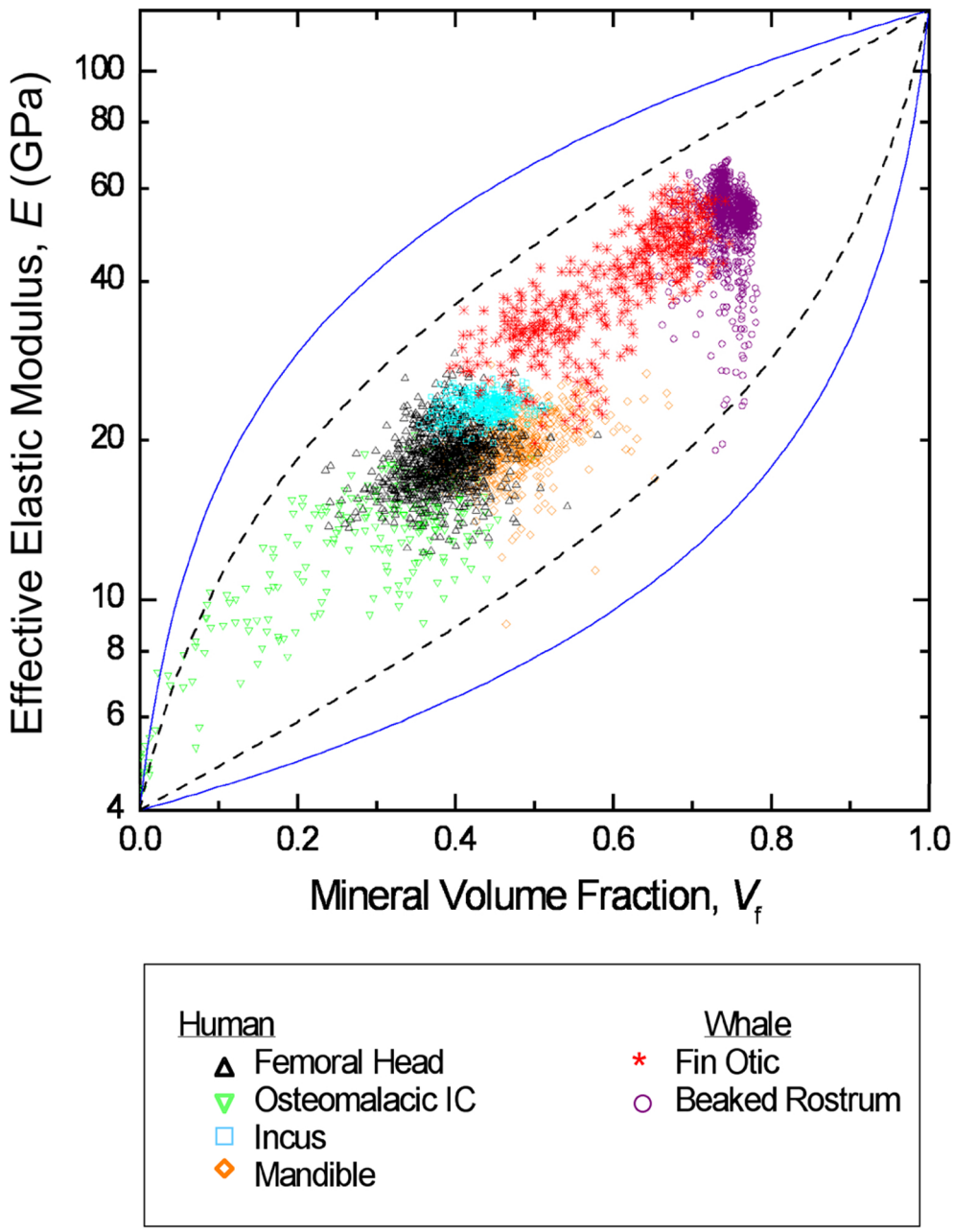

Figure 2.7: Elastic modulus (E) versus mineral volume fraction (V_f) of PMMA-embedded bone samples: human femoral head; human osteomalacic iliac crest (IC); human incus; human mandible; fin whale otic bone; and dense beaked whale rostrum. The solid lines are Voigt-Reuss bounds and dashed lines are the Hashin-Shtrikman bounds. From Oyen et al. (2008) with permission.

collagen content, anisotropy, porosity, and the level of hydration in order to understand the functional significance of mineralized tissues such as bone and teeth.

2.4 The Process of Diagenesis

Mineralized tissues are the main components of the fossil record, and can provide valuable information to paleontologists and archaeologists on the biology, ecology and the environment of ancient vertebrates. An understanding of alteration and preservation of bone and teeth are vital to studies of chemical signals and histology of ancient bones and teeth that are used to investigate paleodiet, physiology, migration, age, and paleoclimate (Ambrose et al., 1997; Cerling and Sharp, 1996; Lee-Thorp and Sponheimer, 2003; Lubell et al., 1994; Price et al., 2002; Wang and Cerling, 1994; Zazzo et al., 2002). While diagenesis is widely documented throughout the geologic record, the actual processes are not well understood. Significant chemical and structural alterations occur at scales ranging from the nanometer to the macroscopic. Furthermore, the degree of alteration is highly variable and can include loss of organic material, partial or complete dissolution of minerals, recrystallization, collagen loss, uptake of trace elements, and changes in porosity (Hedges and Millard, 1995; Reiche et al., 2003; Badone and Farquhar, 1982; Elliott and Grime, 1993; Kohn et al., 1999; Trueman et al., 2004; Nielsen-Marsh and Hedges, 2000).

2.4.1 Diagenesis of Bone

Histological changes that occur during diagenesis of bone have been well documented using light and SEM microscopy (Bell et al., 1996; Hackett, 1981; Hedges and Millard, 1995). Particularly common, are destructive foci described by Hackett (1981). These circular nodes are a result of microbial action; often occurring within the first few years of burial (Bell et al., 1996). Additionally, the histological preservation of bone seems to occur in a bimodal fashion, where histological destruction occurs to completion, if it occurs at all (Hackett, 1981). During diagenesis, bone crystals grow in size and tend to obtain a more needle-like

morphology, similar to pure HA (Trueman et al., 2004; Reiche et al., 2002). While poorly understood, an increase in crystallinity has been observed through peak broadening measured by X-ray diffraction and increased infrared splitting factor (IRSF) as measured by infrared (IR) spectroscopy (Weiner and Bar-Yosef, 1990; Sillen and Parkington, 1996; Bartsiokas and Middleton, 1992). Measurements on South African specimens showed an increase in the IRSF with age through 20 ka, with little increase in older samples (> 40 ka) suggesting that the increase in crystallinity is time-dependent, yet finite (Sillen and Parkington, 1996). In contrast, other studies report no correlation of increased IRSF with time (Hedges and Millard, 1995; Person et al., 1996) suggesting that the commonly observed increase in crystallinity is highly dependent on the burial environment. The nature of crystallinity increase is not well known as it is unclear if crystals simply grow in size or if new crystals are deposited. Growth of a single crystal may occur as in dental enamel where an increase in crystal size is related to an increase in mineralization (Ferguson et al., 2005). Alternatively, new crystals may form from HA that is presumably dissolved locally and re-precipitated or from foreign minerals that are incorporated or substituted into the mineral matrix (Hedges, 2002).

Loss of organic content is also highly variable and dependent upon the burial environment. Bones in burial sites exposed to fluctuating water levels tend to have lower protein content and a high percentage of porosity(Hedges, 2002). Loss of organic matter has been correlated with an increase in crystallinity (Person et al., 1995), indicating that the mineral and organic phases of bone are intimately linked and changes in one phase will inherently affect the other. While many digenetic effects have been widely documented, a true understanding of the process remains nebulous and further investigation is needed.

2.4.2 Diagenesis of Tooth Enamel

Enamel, as a non-porous mineralized tissue, is thought to be much more resistant to the process of diagenesis (Wang and Cerling, 1994). While there have been numerous studies

on the diagenesis of bone, very few have focused on the diagenesis of enamel. Modern enamel is 90% mineral by weight and thus very resistant to microbial attacks and dissolution of the organic phase which permits the excellent preservation of histology seen in fossilized enamel (Wang and Cerling, 1994; Budd et al., 2000). Additionally, minimal changes in crystal size, shape, and phase have been recorded (Budd et al., 2000; Sponheimer and Lee-Thorp, 1999; Rink and Schwarz, 1995). However, changes in chemistry have been noted in many cases; for example using Fourier Transform Infra-Red (FTIR) spectroscopy changes in the proportion of carbonate ions occupying hydroxyl and phosphate sites have been detected with little alteration in the crystallinity (Sponheimer and Lee-Thorp, 1999). While it is generally thought that tooth enamel does not undergo diagenesis, clearly, some changes in composition (Sponheimer and Lee-Thorp, 2006) and crystallinity (Michel et al., 1995) do occur and caution is should be taken for studies of isotope measurements for paleodiet and paleoclimate studies.

Chapter 3

Testing methodologies

Nanoindentation is an ideal tool for mechanically testing at the"tissue-level", yet unique challenges exist in both testing methods and analytical approaches. Mineralized tissues are heterogeneous in composition and structure. Further, hierarchical organization, typical of many biological tissues, implies that multiple structural levels may influence a single nanoindentation site. The degree of organization and mineral infilling varies with factors including the age, type, and location. This chapter reviews practices for the collection of high quality data where the organization of multiple phases complicate our ability to prepare samples, visualize 3-D structure, and obtain exact measurements of material properties at small length scales. Nanoindentation, in combination with additional independent measures of the tissue, enable the detailed study of poorly understood 3-D construction, material properties, compositional information, and mechanical behavior at sub-micrometer scales. Surface imaging techniques, such as quantitative backscattered electron (qBSE) imaging and polarized or plain light microscopy, are used to image indent sites for location or composition and to visualize pile-up, sink-in, or cracking. Other characterization techniques, such as x-ray diffraction (XRD) allow investigation of the mineral to determine chemical compositional and structural information. The correlation of nanoindentation data with any such assay enables an advanced interpretation of tissue-level properties.

3.1 General sample preparation

Small-scale mechanical testing is complicated by the need to prepare samples for analysis. The mere process of removing tissues from *in vivo* physiological conditions triggers a series of events that potentially alter tissue properties. These include altered pH and ionic environment, dehydration, temperature, enzymatic degradation, and cell death. Further processing to prepare samples for analysis may involve storage over time; handling in the form of cleaning, sectioning, and polishing; decalcification (in some cases); and mechanically stabilizing the sample via embedding or through the use of a fixture. Throughout collection, sample preparation, and testing processes, the maintenance of physiologically relevant conditions is often desired. However, more important is the uniform treatment, or control, of variables that may skew results in ways that are often difficult to recognize or interpret.

While some have attempted to mechanically probe (Hansma et al., 2006) or measure strains (Goodship et al., 1979; Rubin and Lanyon, 1985, 1984) *in vivo*, the bulk of mechanical bone measurements are performed *ex vivo*. Depth-sensing indentation testing of bone in live human subjects is under development and may have great clinical potential (Hansma et al., 2006); however, the challenges of obtaining high quality and repeatable data are immense. Testing bone samples *ex vivo* provides such advantages as the ability to selectively test specific locations or orientations within the 3-D structure, and couple indentation testing with other analysis methods to enable a multi-factor interpretation of the nanomechanical results (Ferguson et al., 2003b).

The key to success lies in tight experimental control of potentially influencing factors. That is, consistently ensuring the preservation of relevant properties during tissue collection, attending to conditions during subsequent storage, and selection of optimal techniques to preserve the condition of the tissue prior to and during nanomechanical testing. Because nanoindentation occurs at very small length scales, consideration must be given to alterations in the surface and near-surface properties of the sample. Further, the influence of collection,

storage, and sample preparation on the three phases of mineralized tissues are critical. Each of bone's components contributes to the mechanical response of the tissue, and thus alteration of any single phase will affect the nanoindentation response.

3.1.1 Storage and preservation methods

While storage and preservation of mineralized samples beyond the day of collection is often necessary, it is critical to consider the benefits and limitations of each storage method on tissue-level properties. Other more comprehensive reviews of storage and preservation methods exist (Martin and Sharkey, 2001). A brief overview here examines preservation methods from the perspective of tissue-level alterations that may influence nanomechanical testing results.

Dehydration is a cheap and simple approach that can be employed to store bone samples over long durations. Following removal of nonosseous (non-bony) tissue, samples can be dried in ambient air or under an applied vacuum and stored for extended durations. Mechanical properties of dry bone are significantly different than for hydrated samples due to the formation of microfractures, decreased elasticity of the collagen, and possibly increased packing density of the mineral platelets (Lu et al., 2004; Lee and Glimcher, 1991). Water may also serve to plasticize bone tissue (Bembey et al., 2006c; Bushby et al., 2004). Subsequent mechanical testing performed on rehydrated samples demonstrated little measureable effect at the scale of the whole bone (Broz et al., 1993). However, the effects of dehydration in air followed by rehydration on nanomechanical behavior at the tissue-level are unknown.

Air-dried surfaces are readily polished and easy to test, yet substantial microstructural damage occurs through shrinking of the high watercontaining organic phase. This is readily seen in tooth tissues, where large cracks typically separate the dental enamel from the underlying dentin in air-dried samples. Volumetric shrinkage measured by dimensional changes has been reported to be $\approx 6-7\%$ (Lees et al., 1984; Finlay and Hardie, 1994). However true volumetric changes may be significantly larger as shrinkage measured by helium pycnometer

and the Archimedes principle decrease by 15-16% (Lievers et al., 2007).

Water is a main constituent of bone, thus the hydration state of the sample plays a vital role in the measured mechanical properties. Dehydration can cause increased modulus of elasticity, tensile and bending strengths along with reduced values of fracture toughness (Hoffler et al., 2005; Broz et al., 1993; Evans and Lebow, 1951). Nanoindentation experiments have shown that dehydration increased modulus values up to 50%, yet most studies found an average increase of 15-25% (Bushby et al., 2004; Hengsberger et al., 2002; Rho et al., 1999b). While the magnitude of mechanical properties is increased with dehydration, the inherent material relationships (e.g., variations in type of bone) are maintained.

Chemical fixation is another method where samples are dehydrated via chemical means through submersion in solvents, such as ethyl alcohol (ethanol, C_2H_5OH), which are commonly used to dehydrate tissues in preparation for histology (Bembey et al., 2006c). Ethanol is pH neutral and avoids mineral dissolution, and may be most effective at storage temperatures of 4 to 7°C (Schenk et al., 1984). Such solvents simultaneously displace the water molecules and preserve the tissue from bacterial invasion and significant enzymatic degradation. It is thought that recovery from this form of dehydration is possible through rehydration in an isotonic saline solution (Guidoni et al., 2006). However microcracks often form with such histological preservation methods. The extent of permanent alterations within the tissue that may occur following chemical dehydration and that affect nanomechanical behavior remain unknown.

Also, the replacement of unbound water by ethanol has been shown to increase the modulus of bone by more than 20% (Bushby et al., 2004). This substantial increase is more than expected of a simple fluid substitution and emphasizes the importance of water as a key component of bone. Unbound water may fill fine pore spaces and contribute to the stability of the collagen, while dehydration can cause stiffening of the fiber (Saito and Yokoi, 1992). Storage of dental tissues in ethanol resulted in no significant change in indentation modulus or hardness (Malek et al., 2003). While the ability of bone tissue to fully recover

from ethanol dehydration is unclear, chemical fixation in other common solutions such as formalin or glutaraldehyde, is irreversible.

Freezing is one of the most common approaches to preservation of mineralized tissue and has the potential to preserve water content, bone structure, cells, proteins, and even genetic material. However, freezing and thawing is known to cause significant damage when done improperly. A rapid transition to the frozen state minimizes the damage to the tissue by ice crystals. Use of a cryoprotectant, to replace water and reduce the amount of ice formed, also prevents destruction by the formation of large ice crystals (Pegg, 2007). However the cryoprotectant is only as effective as its ability to penetrate into the tissue–a process that is likely inhibited by small pore spaces and complicated microstructural geometries.

The rate and temperature at which tissue samples are frozen will determine, in part, their quality of preservation. The rate at which the tissue passes through temperatures of $\approx$ 0°C to -10°C is critical, as this is the temperature range where large, destructive ice crystals may form if given a sufficient period of time. A rapid transition through this region is achieved by the use of small samples and a freezing temperature that is much less than -10°C. The ultimate storage temperature, for temperatures less than -10°C, has little effect on the size of the ice crystals. Rather it is the time that it takes to undergo the transition through this critical temperature range that is the key factor. One complication is that uncharacterized changes often occur within the tissue, and cause micro- or macroscale fractures, during transition from room temperature to very cold temperatures–such as during immersion in liquid nitrogen at -196°C. Attention must therefore be paid to artifacts caused by the freezing process in any experiment.

In general, a conventional refrigerator operates at +4°C and its companion freezer unit at -4°C. Damage to hard and soft tissues following freezing at -4°C is extensive. Further, such units typically include a self-defrosting feature, which cycles the temperature to eliminate the build-up of excess ice, and will rapidly destroy the microstructure of any tissue contained within. Bone structure and cells are reasonably well maintained when frozen at -20°C (the

temperature of a typical 'chest freezer'). However the significant thermal mass of bone, especially for large sections, causes the exterior of the sample to freeze much more rapidly than the internal region. It is not uncommon to find small, microscopic fractures within a bone sample that has been frozen at -20°C. Storage at -85°C, the temperature of a typical lab freezer used to preserve proteins and genetic material, will also preserve bone samples for a long period of time.

Mechanical consequences of freezing and thawing on properties of whole or large machined sections of bones are not profound. In a survey of seventeen studies, bone structural variables, rather than material properties, were the most affected (Martin and Sharkey, 2001). Overall, strength tended to increase and stiffness decrease. It was concluded from the survey that freezing bone samples at a temperature of -20°C, while maintaining moisture content, was sufficient to preserve mechanical properties of whole bones or large, machined bone specimens. Nanomechanical properties of dental tissues weaken significantly with freezing (Malek et al., 2003) and thus should be avoided. Further enamel storage in deionized water or calcium chloride buffered saline solution have been shown to demineralize tooth tissues resulting in decreased nanomechanical properties (Habelitz et al., 2002). Alternatively storage in Hanks balanced salts solution preserves tissues and mechanical properties (Habelitz et al., 2002).

3.1.2 Mechanical stabilization of samples

The form of mechanical stabilization needed depends on the intended testing condition (e.g., wet, dry, or embedded) as well as the size and 3-D structure of the tissue sample. Bone samples can be machined using conventional tools, polished in manners similar to conventional ceramics or metals, and glued to glass slides or indenter stubs to prevent movement during nanomechanical testing. During sample preparation, it is critical to exercise caution in preserving the surface of the sample by avoiding high temperatures, due to excess friction during cutting and polishing, and through modification by exposure to lubricants (including

various forms of water) that might alter the bone or tooth material. In general, a band saw can be used to cut large blocks, followed by a low-speed diamond blade saw for machining surfaces with minimal friction. The form of lubrication during cutting or polishing must also be considered to avoid significant leaching or deposition of minerals (see Section 3.1.3).

Dehydrated samples are generally infiltrated with, or included within, various types of epoxies. These epoxies are highly viscous, prior to curing, and only fill large void spaces but not smaller pores (e.g., Haversian canals or canaliculi). As the epoxy does not infiltrate into small pore spaces within the bone material, the measured mechanical properties remain unaltered for indent sites that are sufficiently far away from the epoxy bone interface (Rho et al., 2002). Inclusion in epoxy resin permits the testing of dry or rehydrated bone samples following surface preparation using conventional (e.g., metallographic) sectioning and polishing methods.

A commonly used alternative to including dry bone in epoxy resin is to, instead, embed bone samples in a low viscosity, infiltrating resin or polymer (e.g., PMMA). Embedding facilitates complete infiltration of the embedding medium into pore spaces to preserve cells, maintains tissue morphology, and permits excellent surface preparation. High quality tissue embedding is time-consuming and typically requires that the samples are dehydrated in a series of ethanol, 'cleared' with a solvent such as acetone or xylene that is miscible with the monomer, and then slowly infiltrated with the embedding medium (unpolymerized monomer). As rapid curing or polymerization often results in incomplete infiltration into smaller pore spaces, the infiltration process may be prolonged over many days or weeks prior to encouraging polymerization with the addition of a chemical initiator (e.g., benzoyl peroxide) and/or low heat ($\approx 37 - 40°$C).

Tissue embedding is useful for stabilizing the porous 3-D architecture of mineralized tissues. Additionally, PMMA can stabilize delicate bone samples such as fossilized, demineralized, or deproteinated specimens. PMMA, with a low modulus of ≈ 5 GPa, is thought to minimally contribute to the measured mechanical properties of PMMA-embedded bone

(Oyen et al., 2005). This is demonstrated by the similarity between measured values between dry bone and PMMA-embedded bone (Hoffler et al., 2005).

3.1.3 Surface preparation

Surface preparation for nanoindentation is generally achieved by mechanical polishing or with microtome sectioning. Preparation of dried, included, or embedded samples may follow conventional polishing methods whereby the surface is smoothed by progressively finer grit silicon carbide paper and then polished with diamond suspension paste (Rho et al., 2002). Between each step, samples are ultrasonically cleaned in an appropriate solution. Preparation of wet samples is possible, yet the fine polish afforded by pastes or slurries finer then ≈1200 grit paper appears to add little benefit. A simple approach to preparing surfaces of wet bone tissue is cryopolishing via placing polishing paper over a frozen metal surface (Bushby et al., 2004). When comparing small structural features (e.g., lamellae) at low depths the surface roughness of the sample can have significant effect on the measured mechanical properties. Mechanical polishing of bone selectively removes thin lamellae more quickly and creates a topographical profile of high and low regions which have been observed to vary by about 200 nm (Gupta et al., 2006). In the valleys created by the thin lamellae the contact area function A_c is underestimated, thus the modulus is over estimated (Gupta et al., 2006). When comparing the difference in modulus of thick and thin lamellae, a greater difference was seen with samples prepared via microtome due the superiorly flat surface preparation (Xu et al., 2003).

Nanoindentation studies of bone have been shown to generate standard deviation values upward of 50% (Oyen and Cook, 2003; Hengsberger et al., 2002). This large variability is partially a reflection of bones natural tissue structure and heterogeneous nature, yet some sample preparation and experimental variation must also contribute to high standard deviation values. In order to probe individual bone microstructures (e.g., individual lamellae) indentations must be sufficiently shallow to only probe the microstructure of interest, yet

sufficiently deep as to avoid influence of surface roughness.

Physiological conditions are ideal for testing any biological material. Bone and enamel are no exception. Many researchers have attempted to determine the relevance of determining properties of bone *in vivo* and live bone *ex vivo*. However the benefits of testing under the ideal conditions must be weighed with the practicality and the advantages of collection of high-quality data from well-controlled tests that lack degrees of physiological relevance. On macroscopic samples, mechanical testing of bone is often performed in an environment that mimics critical physiological conditions of hydration, ionic solution, and temperature. The accessibility of some nanoindentation systems to controlling such variables is limited, but adaptations to the systems can be made to enable testing under wet or temperature-controlled conditions.

3.2 Nanoindentation

In order to understand the mechanical properties of mineralized tissues at multiple scales, the basic structural building blocks must also be investigated. Nanoindentation is the ideal tool as it allows testing of small volumes of tissue and excludes the effect of large-scale porosity on mechanical property measurements. The three-dimensional structure and composition of bone and enamel are impressively complex. Nanoindentation is an ideal tool for studying the mechanical behavior within individual millimeter-scale structures, such as in trabecular bone, or micrometer-sized tissue-level features, such as lamellae. Further, probing at the nanometer scale permits the study of compositional heterogeneity at the tissue-level and the relationships between organic and mineral phases of bone material.

Nanoindentation overcomes many of the difficulties that exist in accurately mechanically testing small volumes of material. Attempts have been made to isolate individual osteons, lamellae, and single trabeculae for micromechanical testing (Mente and Lewis, 1994; Ascenzi, 1988; Ascenzi et al., 1987; Ramasamy and Akkus, 2007). Such examinations are complicated by our inability to accurately dissect tissues at very small scales without causing

damage to the test specimen. Testing is also complicated by the geometry of the structural features of interest, such as in the case of a single trabeculae, where the cross-section varies in diameter and geometry along its length (Mente and Lewis, 1994). Further, early attempts to measure the mechanical properties of enamel were made using macro-scale compression of a whole tooth resulting is extremely low modulus values (Stanford et al., 1958). In addition to sample preservation and preparation, micromechanical testing is complicated by adequately gripping the sample, slippage, edge effects, and high measurement uncertainty–especially for custom-built mechanical testing systems. Such factors may profoundly influence testing results. Nanoindentation avoids such complications by providing a means of testing the bone material *in situ*.

Due to these unique advantages, nanoindentation testing has recently become the primarily method to measure the mechanical properties of mineralized tissues. In a standard nanoindentation test a small diamond tip (often spherical or pyramidal) is pressed into a material to determine the elastic modulus and hardness. While nanoindentation traditionally provides the mechanical elastic (modulus, E) and plastic (hardness, H) response of the material, more recently nanoindentation has been used to determine viscoelastic parameters (Olesiak et al., 2010a; Oyen, 2006b) and even poroelasticity and hydraulic permeability (Galli et al., 2009). A typical test usually involves an elastic-plastic loading procedure followed by an elastic unloading during which the load-dispalcment response is recorded (see Figure 3.1). The forces involved are in the millinetwon (10^{-3} N) range and the depth of penetration ranges from hundreds of nanometers (nm) to a few microns (μm). At these measurement scales every aspect of the nanoindentation test can have an effect on the measured mechanical properties. Tip selection, loading rate, maximum load and other variables can play a significant role in the type of data that can be extracted from the test. This section provides an overview of contact mechanics and nanoindentation test parameters as they relate to and influence the measured properties of mineralized tissue.

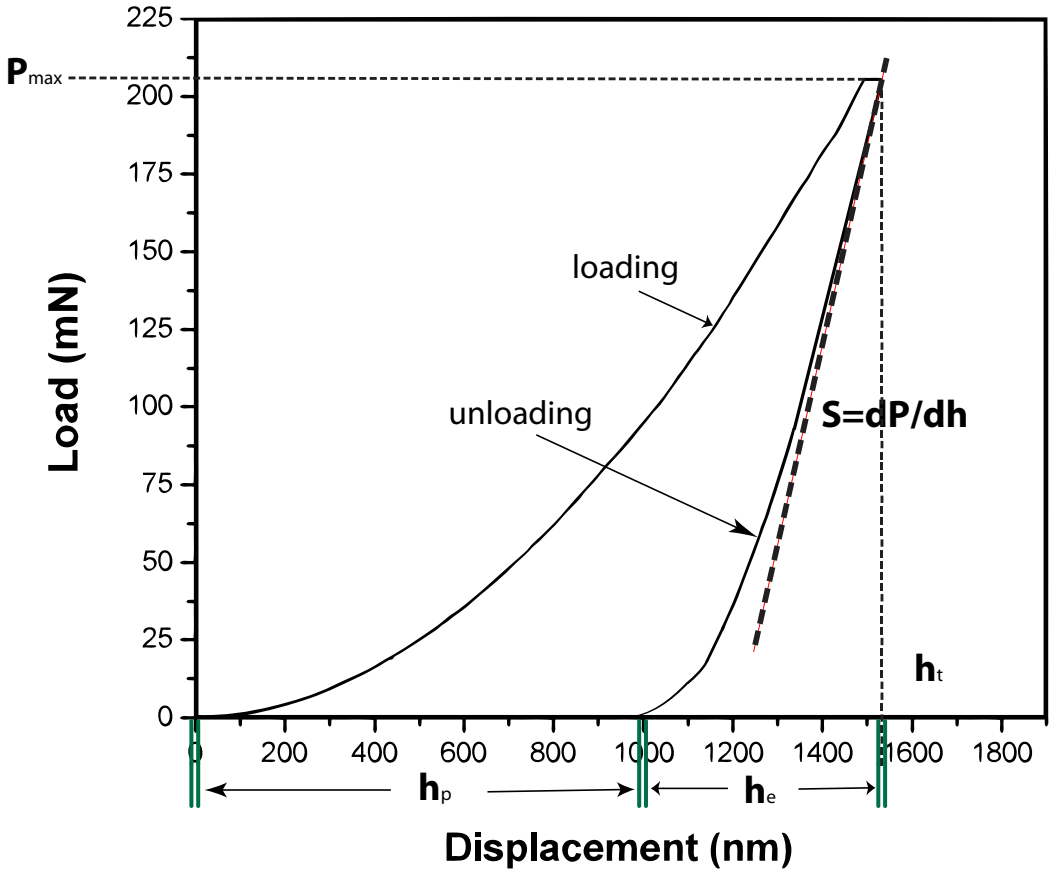

Figure 3.1: A schematic of typical nanoindentation load-displacement data with max load P_{max}. The total displacement depth h_t consist of both plastic deformation (h_p) and elastic deformation (h_e) which is recovered upon unloading. The slope of the elastic unload S=dp/dh is used with the Oliver-Pharr (Oliver and Pharr, 1992) method to calculated the modulus of the material.

3.2.1 Contact Mechanics

Hertzian contact mechanics is used to describe the stresses and deformations involved when two frictionless, elastic surfaces are brought into contact (Johnson, 1985). Two non-confoming surfaces initially touch at a single point or line contact. As the surfaces deform more material connects to create an area of contact. For indentation we consider the elastic contact of a sphere (radius = R) to a flat half-space where the area of contact can be described by a circle of radius = a. Hertz determined that radius of the circle is related to the total deflection (δ) of the half-space in the vicinity of the indenter by (Fischer-Cripps, 2002):

$$a^2 = R\delta \tag{3.1}$$

The applied indenter load (P) is related to the total deflection (δ) of the half-space by:

$$\delta^{3/2} = \frac{3P}{4E_R\sqrt{R}} \tag{3.2}$$

For a conical indenter with opening angle of 2α, similar equations were determined by Sneddon (1948) for the radius of contact as related to the indenter load:

$$P = \frac{\pi a^2}{2} E_R \, cot(\alpha) \tag{3.3}$$

The total indent depth (δ) at the vertex of the cone is related to the indenter load by:

$$\delta^2 = \frac{P\pi}{2E_R \, tan(\alpha)} \tag{3.4}$$

For a non-rigid indenter tip the elastic displacement of the tip forces the true contact displacement, h_c, to be smaller than the total indent depth, δ. The majority of indentation tests uses either spherical or conical diamond tips. As diamond is a relatively stiff material the elastic deformation of the tip is minimal, thus when testing very compliant materials the tip is often approximated as rigid (e.g. $E_i >> E_s$). The above contact equations describe both spherical and conical contact with a half-space. Additionally the use of pyramidal tips is common in indention testing. While contact solutions exist for pyramidal contact,

these tips are treated as a cones with the same opening angle. The conical solution provides the same area to depth relationship as the pyramidal and further allows application of the axis-symmetric contact equations.

Elastic-plastic contact occurs during many indention test on a wide variety of materials. In brittle materials plastic deformation most commonly occurs when testing with at sharp-pointed tip where as in ductile materials even spherical tips can induce plastic deformation. In Figure 3.2, the load-displacement curve for a variety of materials is show for nanoindentation test with both a small (5 μm) and a large (65 μm) spherical tip. Spherical tips produce an initial, primarily elastic response with a detectable transition to plastic deformation (as seen in the aluminum load-displacment curve from the 65 μm tip). Larger spherical tips, such as the 65 μm tip, elicit an elastic response over larger depths than small tips as evident in the fused silica and soda-lime glass data. Smaller spherical tips such as the the 5 μm tip act similarly to a pointed tip in which the onset of plastic deformation is almost instantaneous. For comparison the load-displacement curve from a Berkovich (a conical tip) indent on fused silica is shown in figure 3.1, where both elastic (h_e) and plastic (h_p) deformation occurs during loading. Upon unloading the elastic displacement recovers leaving a residual impression caused by the plastic deformation. A measurement of plasticity in nanoindentation is the contact hardness (H_c) which is calculated as the mean pressure (P_m) divided by the contact area (A_c):

$$H_c = \frac{P_m}{A_c} \tag{3.5}$$

Contact hardness is not an independent measure and has been shown to correlate to E' (Olesiak et al., 2010a), therefore it is often of interest to calculate the more commonly known hardness (H) or resistance to plastic deformation (Oyen, 2006c).

For elastic-plastic indentation, Johnson (1985) developed the expanding spherical cavity model to examine the stress and deformation caused by plastic flow. The basis of the model is that the stress-strain relationship maintains a spherical symmetry as a rigid inden-

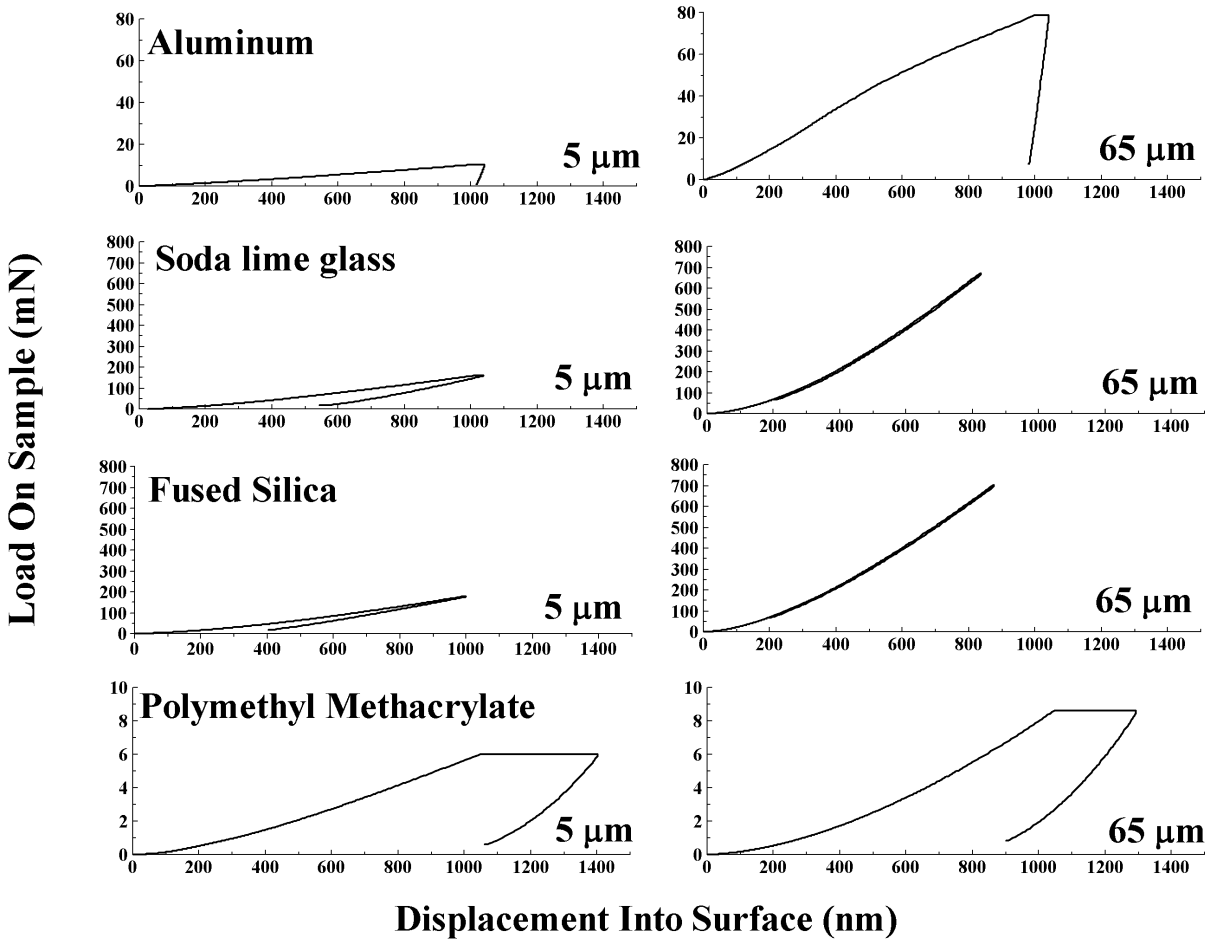

Figure 3.2: Load-displacment curve for a variety to materials using both 5 and 65 μm spherical tips. Samples were tested under load control with a constant indentation strain rate to a maximum depth limit of 1000 nm, where the current indenter load was held for 120 s prior to unloading. Higher loads are required to displace the 65 μm tip to 1000 nm than the 5 μm tip.

ter tip is driven into the material. Figure 3.3 depicts the hydrostatic core near the indenter tip which exerts outward pressure on the plastic flow region that is surrounded by elastically deforming material. The radius of the plastic zone (c) is dependent on the load (P) and the yield strength (σ_o) of the material, and is given by (Harvey et al., 1993; Johnson, 1985):

$$c = \sqrt{\frac{3P}{2\pi\sigma_o}} \tag{3.6}$$

As demonstrated in Figure 3.3, an incremental increase in depth of the indenter (dh) results in expansion of the hydrostatic core (da), which in turn causes an increase in the radius of the plastic zone (dc). For geometrically similar indentation tips, such a with Berkovich tip, the radius of the plastic zone increases at the same rate as that of the core or da/dc=a/c (see Figure 3.3). Geometrical similarity will discussed further in section 3.2.3.

3.2.2 Oliver-Pharr Method

With the commercialization of nanoindentation testing systems the majority of test seek to extract the elastic modulus and hardness of the material from the load-displacement measurement. In microhardness testing measurement of the size of the residual plastic impression at a specific load is required in order to determine the hardness of the material. However, physical measurement of the impression is both tedious and extremely difficult for nanoindentation as residual imprints are only a few microns or less. The Oliver-Pharr method of analysis (Oliver and Pharr, 1992) allows direct extraction of both contact hardness and modulus though measurement of the load and displacement of a tip with a known geometry. The acceptance of the Oliver-Pharr method propelled nanoindentation to the forefront of micro-mechaincal testing rendering microindentation essentially obsolete.

The elastic response of the material is determined through the known tip contact area (A_c) and the stiffness (S) or slope of the unloading portion of the load-displacement curve (Figure 3.1). It is assumed that the unloading curve exhibits a purely elastic response

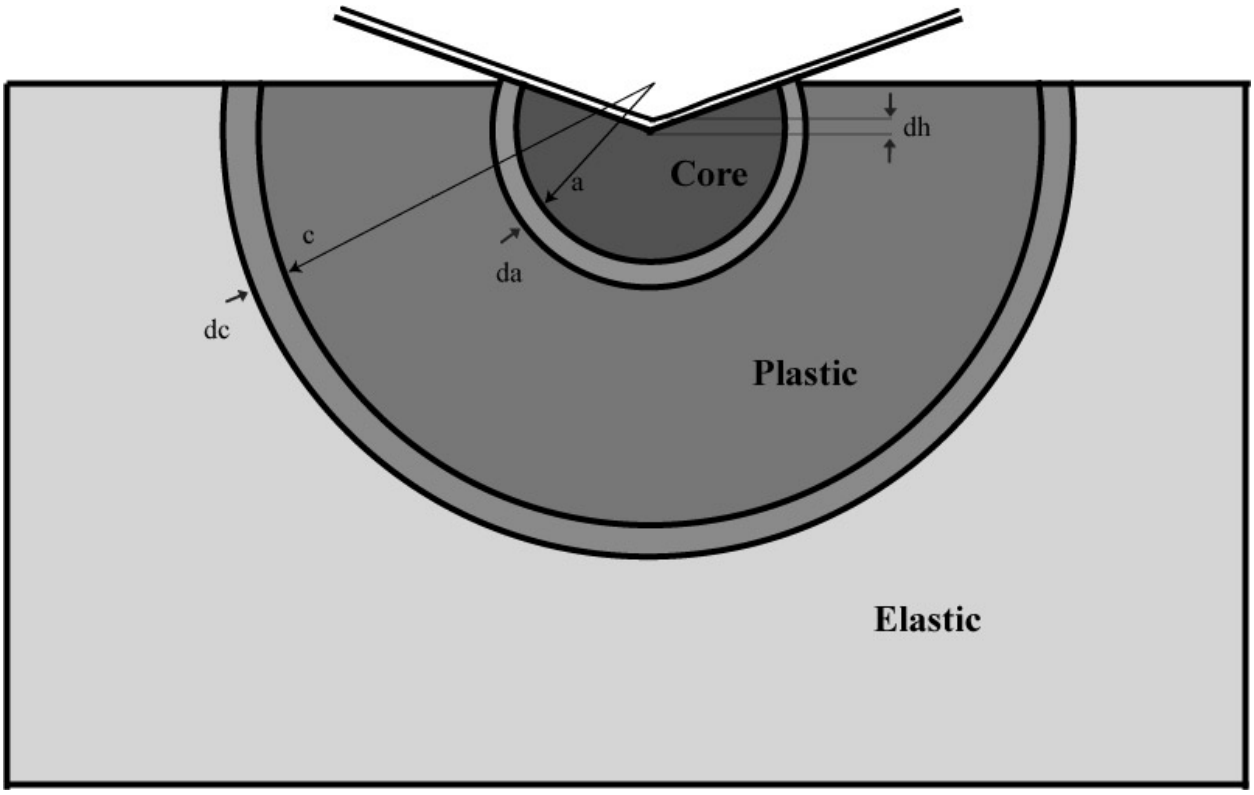

Figure 3.3: Schematic of the expanding spherical cavity model. The contacting surface of the indenter tip is surrounded by a hydrostatic core of radius a. Upon loading this core exerts outward pressure on the plastic flow region of radius=c that is surrounded by elastically deforming material. A small incremental penetration of the tip, dh, results an increase in the radius of both the core (da) and plastic (dc) regions. After (Johnson, 1985).

allowing calculation of the reduced modulus (E_r) as:

$$E_R = \frac{\sqrt{\pi}\, S}{2\sqrt{A_c}} \tag{3.7}$$

The reduced modulus is a result of the combined elastic response of the indenter (given by the Youngs modulus and Poissons ratio of diamond: 1140 GPa and 0.07, respectively) and the test surface (given by the plane strain modulus E').

$$\frac{1}{E_R} = \frac{1}{E'} + \frac{1+\nu_i^2}{E_i} \tag{3.8}$$

Throughout this work the plane strain modulus (referred to as modulus or E') of the material will be reported, which eliminates error in assuming the Poissons ratio of the sample. Further the contact hardness can be determined at the max load as:

$$H_c = \frac{P_{max}}{A_c} \tag{3.9}$$

The contact area A_c (Equation 3.10) is a function of the contact displacement (h_c) and is determined by calibration tests on a well characterized reference material, often fused silica. As a homogenous-isotropic material fused silica makes an ideal standard material as it exhibits a very elastic response with high hardness values.

$$A_c = C_o h_c^2 + \sum_{n=0} C_{n+1} h_c^{\frac{1}{2^n}} = C_0 h_c^2 + C_1 h_c + C_2 h_c^{\frac{1}{2}} + C_3 h_c^{\frac{1}{4}} + \ldots \tag{3.10}$$

Further the contact displacement (h_c) is not equal to the full contact displacement (h_{max}) which is combination of both elastic and plastic deformation of the sample and elastic deformation of the tip (see figure 3.4). For the Berkovich tip the contact deformation is given by:

$$h_c = h_{max} - \epsilon \frac{P_{max}}{S} \tag{3.11}$$

where $\epsilon = 0.75$ is typically used (Oliver and Pharr, 1992).

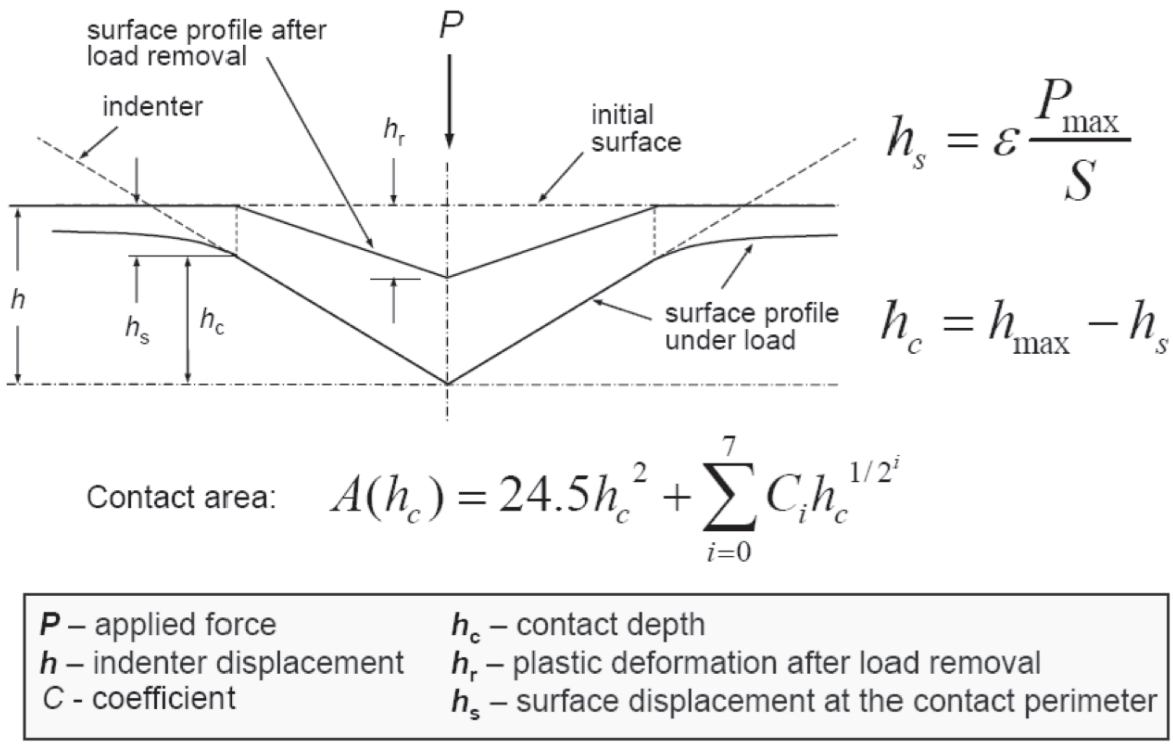

Figure 3.4: The geometry of Berkovich contact with a half-space. Modified after (Oliver and Pharr, 1992).

3.2.3 Tip geometry

The selection of the optimal tip geometry is critical for obtaining high quality indentation data. The biggest limitation in tip selection lies in our limited understanding of what occurs within the collagen, mineral, and pore spaces within the bone material, at nanometer length scales, during an indentation event. For example, plastic deformation under an indenter tip likely results in compaction of the mineral platelets, possible generation of microcracks within the material of bone, pore collapse, and permanent displacement of water (for bone in a hydrated state). The mechanics of how each tip contacts and indents into the material is therefore of critical importance and should be considered when determining the experimental approach to testing elastic, plastic, or viscous behaviors. Yet, nanoindentation measurements in bone sample a three-dimensional volume of material, where Berkovich and spherical tips produce roughly comparable values of modulus for bone (Bushby et al., 2004). Selection of tip geometry may be more important to the underlying contact mechanics and subsequent deformation mechanisms than to the measured material properties.

Berkovich: The majority of bone and enamel indentation experiments have been carried out with a Berkovich tip, which is supplied with most commercially available testing systems. The typical Berkovich tip, possessing a contact radii that is similar in size to a lamella (R $\approx$100-200 nm), has been effectively used to determine mechanical properties of such individual structural features in bone (Rho et al., 1999b; Zysset et al., 1999). Berkovich tips are often preferred for indentation testing as they are geometrically similar and thus the indentation process is length-scale independent for a monolithic material. All conical indenters are geometrical similar as the ratio of the radius of the circle of contact (a) to the depth of the indent (δ) remains constant for increasing loads (see Figure 3.5). Therefore the strain within the material is independent of the load resulting in a constant measurements of hardness for all indention depths for a homogenous material. Berkovich tips are sharp and cause significant plastic deformation at the onset of indentation. While the contribution

of plastic (and elastic and viscous) deformation to the overall indentation depth can be analytically determined (Oyen, 2006a), the nature of this plastic deformation in bone and enamel remains unclear. Consideration should be thus given to the effects of indenting a viscoelastic material with a sharp indenter tip.

Spherical: Spherical tips of various radii serve as a powerful tool to study both elastic and viscoelastic properties in mineralized tissues (Bushby et al., 2004; Bembey et al., 2006b; Ferguson et al., 2003a). The cross-sectional area of contact increases with the indentation load, unlike the geometric similarity of the Berkovich tip. The the ratio of the radius of the circle of contact to the contact depth (h_c) increases with increasing load (see Figure 3.5). However with the use of multiple spherical tips of different nominal radius values (R) geometric similarity can be maintained while the indentation strain a/R is maintained constant. Alternatively the use of a range of tips with varying radii provides the unique ability to explore the elastic-plastic response of a variety of microstructural features in within a limited load and depth range (Bushby et al., 2004; Bushby, 2001). Spherical tips possess the advantage of producing an initial, primarily elastic response with a detectable transition to plastic deformation (Bushby, 2001). The spherical tip allows exploration of the full range of elastic-plastic behavior resulting in the indentation stress-strain curve (Tabor, 1951). In contrast, Berkovich tips have an immediate onset of plasticity at very small displacements due to the high stress concentration near the materials surface.

Unlike Berkovich tips, the geometry of spherical tips is less uniform from one tip to another and therefore require time-consuming and careful characterization of the tip area function. For example, spherical tips may flatten slightly or deviate from a perfect spherical geometry (Field and Swain, 1993). The radius of a spherical tip remains the major factor in producing high quality data.

Cube corner: Fracture toughness of human tibial cortical bone (Mullins et al., 2007) and enamel (Myoung et al., 2009) have been investigated by using a cube corner tip to induce fracture. Crack lengths likely vary with material anisotropy, compositional variations, and

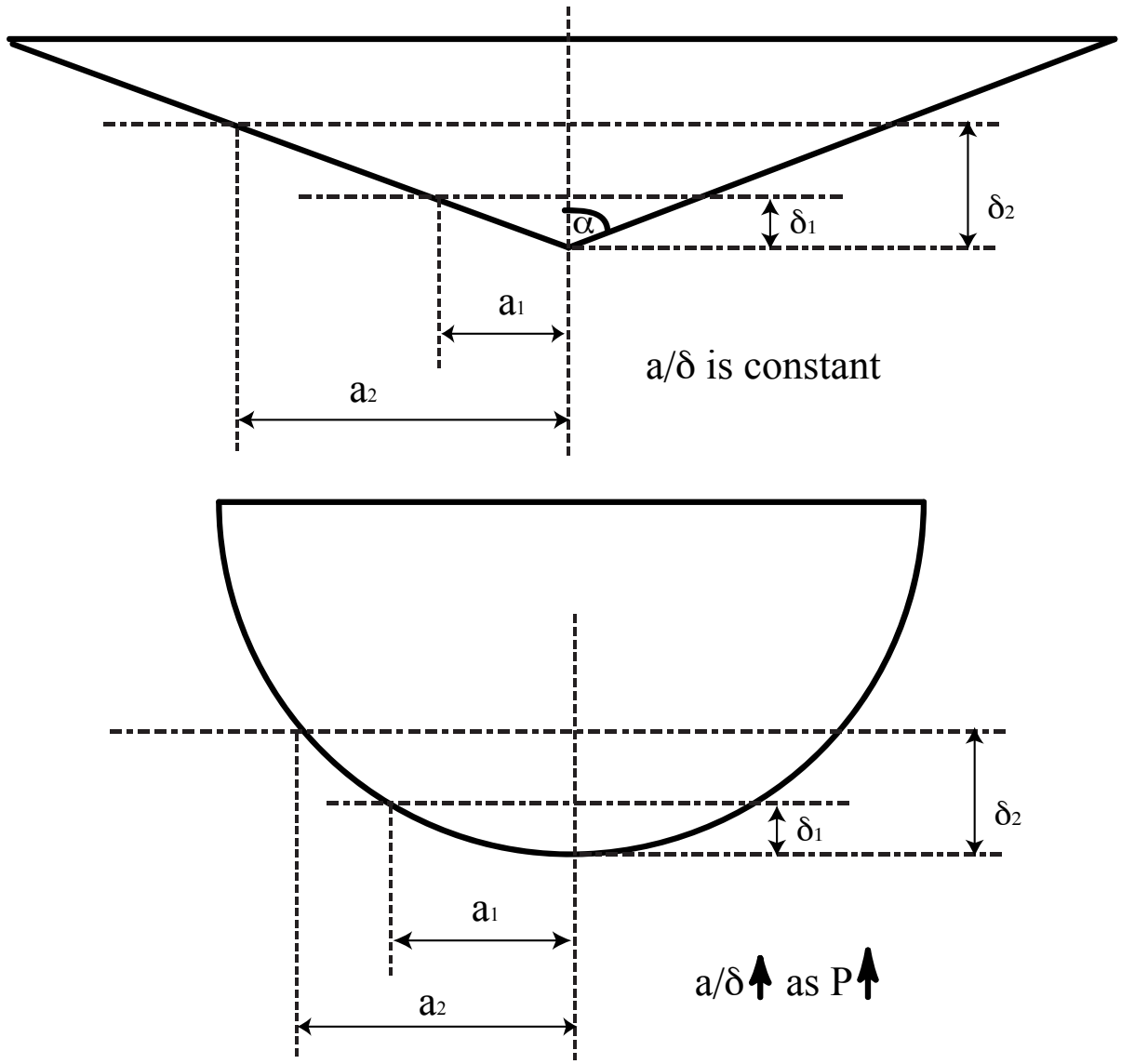

Figure 3.5: Schematic demonstrating the geometric similarity of the Berkovich tip where the ratio of the circle of contact (a) to the depth of the indent (δ) remains constant with increasing load. For spherical tips the ratio of a/δ increases with increasing load.

microstructural organization. Scratch testing, also using a cube corner tip, may also prove to be a useful tool for studying variations in bone quality (Wang et al., 2007) and enamel wear resistance (Alarcon et al., 2009).

3.2.4 Testing methods

A variety of testing procedures have been used for the nanoindentation of bone. Three of the most commonly used methods include ramp-and-hold, constant stain-rate testing with continuous stiffness mode (CSM), and a partial-unloading technique. Figure 3.6 demonstrates the load-time histories for two loading procedures used in this work, ramp-and-hold and constant stain-rate testing. Both methods involve five main test sections: 1) load, 2) creep hold, 3) unload (to 90% max load, 4) pre-hold, and 5) drift measurement. The pre-hold and drift measurement are preformed at 90% the max load to measure the thermal drift which is then subtracted from the entire load-displacement curve. Caution must be used when applying this method to viscoelastic materials as creep displacement will be included in the thermal drift measurement. This can lead to substantial error and thus drift correction should not be preformed on highly time-dependent materials. As many mineralized tissues (e.g. bone and dentin) exhibits time-dependent behavior and properties are often sensitive to strain rate and dynamic testing frequency testing methods and loading rates need to be considered carefully.

Ramp-and-Hold: While the monotonic ramp-and-hold approach is likely the most commonly used test for nanoindentation of bone, variations in its implementation have produced varied results. The viscoelastic nature of bone creates a significant dependence of the modulus values on the unloading rate and the creep hold at maximum load (Bembey et al., 2006c; Oyen, 2006b; Oyen and Cook, 2003; Oyen and Ko, 2007). Not permitting the creep displacement to saturate enables further displacement to occur during the unloading period, causing the unloading curve to demonstrate a characteristic “bowing out”. In this case, the tip continues to sink deeper into the test material even while during unloading (Bushby et al.,

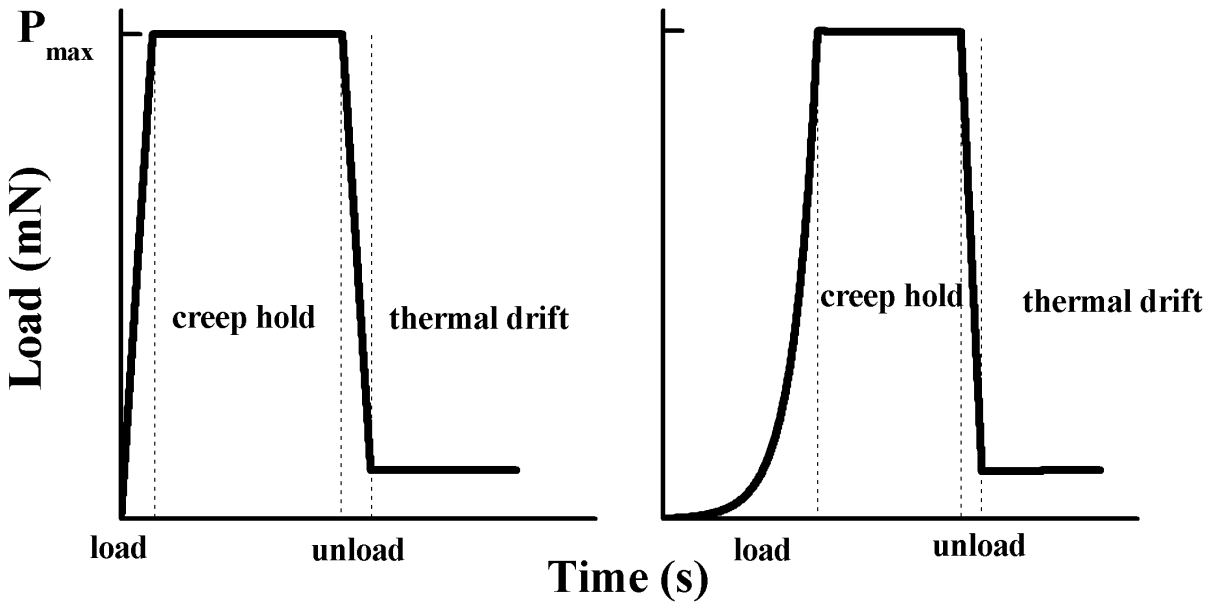

Figure 3.6: Load-time curve for the ramp and hold (left) and constant strain rate loading (right) testing methods used in this research. Each test consists of five segments including: loading, creep hold, unload, settling period, thermal drift measurement.

2004). Such behavior increases the elastic recovery rate (dP/dh) and the apparent depth of contact (h_c), thereby overestimating the calculated value for indentation modulus (Oliver and Pharr, 1992). It is therefore common practice to minimize viscous behavior through an extended creep hold (Feng and Ngan, 2002; Briscoe et al., 1998; Chudoba and Richter, 2001). As proposed by (Feng and Ngan, 2002) the calculation of the creep factor, C, equation 3.12, can be used to determine if the unloading rate for an indentation test is sufficiently fast to minimize the viscous behavior.

$$C = \frac{\dot{h_c} S}{|\dot{P}|} \tag{3.12}$$

Where $\dot{h_c}$ is the creep displacement rate at the end of the holding period, S is the stiffness measured for the unloading curve, and $\dot{P}$ is the unloading rate. As long as C $<$ 0.10 then the contribution of creep to the unloading curve is sufficiently minimized (Feng and Ngan, 2002). The measured modulus of bone has been shown to increases with the loading rate using a triangular loading-unloading profile (0 s creep hold) with loading rates ranging from 10 to 1000 mN/s, indicating the significant presence of viscoelasticity and time-dependent plasticity (Fan and Rho, 2003). In practice, the loading rate and creep hold time can, and should, be determined experimentally as the viscoelastic response of bone varies tremendously with many factors (Bushby et al., 2004). For example, Berkovich indentations in equine cortical bone, dehydrated in 100% ethanol and tested to a 5 mN maximum applied load, show creep on unloading with no hold (0 s) at maximum applied load. However a complete superposition of the unloading responses occurs following unloading after both 120 and 240 s creep hold times thus indicating that a 120 s hold is sufficient for these samples and testing conditions (Bushby et al., 2004).

A limitation of many commercially available nanoindentation systems is that they permit only creep, and not stress-relaxation, testing. Because many systems are designed for testing stiff materials with no time-dependence, they are instrumented to control for load and not displacement. Advancements in instrumentation would assist in a sophisticated

analysis of viscoelastic, biological materials.

Partial Unloading: Unlike the ramp-and-hold approach, the indentation modulus can be determined at a discrete number of contact depths via a multiple partial unloading technique that is described in detail elsewhere (Ferguson et al., 2003a; Field and Swain, 1993; Bushby, 2001). In brief, the indenter tip is incrementally loaded and unloaded into a material over a preselected number of intervals. As the initial unloading response of most materials is elastic, each loading event (to a force, P1) is followed by a partial unloading to a fraction of that force (P2) and enables a calculation of modulus at a specific contact depth. Successive loading continues, to a higher value of P1, and is again followed by partially unloading to the same fraction of P1. The net effect is that each successive loading event causes the applied load to increase until the maximum desired applied load is attained. A new value for modulus is collected for each pair of load-unload increments, thus permitting modulus to be collected as a function of contact depth. Typical values for partial unloading of bone using a small (R $\approx$ 5 μm spherical indenter tip) might be a 5 mN maximum load with unloading to 75% of the applied load at each of 40 incremental loading events (Ferguson et al., 2003a). The partial unloading approach is advantageous in that the separation of the loading and corresponding unloading points can be used to indicate the yield point of the material. This method readily permits the generation of an indentation stress-strain curve and analysis of modulus as a function of contact depth (for each incremental loading step). However, due to the viscoelastic nature of bone, the rates of loading and unloading are of critical importance to once again avoid a creep response from being superimposed on every partial unloading event. Similar to the ramp-and-hold method, such creep behavior results in an overestimation of the measured indentation modulus at each incremental depth.

Constant Strain Rate with continuous stiffness measurement: The continuous stiffness measurement technique utilizes a small sinusoidal oscillation that is superimposed over the main loading function. The loading function is generally exponential loading with a constant unload rate (see Figure 3.6). Continuous stiffness measurement, a standard feature

on many nanoindentation systems, enables the continuous determination of stiffness from before making contact with a surface to the maximum contact depth at each indent site. Measurements of continuous stiffness enable the collection and analysis of modulus data as a function of contact depth as a resolution that is much higher than in multiple partial unloading. In the literature covering nanoindentation of bone, the effect of using various oscillation amplitudes and frequencies is generally unexplored. With continuous stiffness measurement, an increase in mechanical properties seen with increased strain rate is similar to the increase seen with increased loading rate (Vanleene et al., 2006). Even for identical experimental procedures, continuous stiffness measurement tests performed at a constant strain rate take variable amounts of time during the loading portion of the test and depend on the exact material response at each specific indent site, and consequently may vary in loading rates. Mineralized tissues varies significantly in its inherent structural and material heterogeneity; therefore, continuous stiffness measurement testing will naturally vary from site to site. In addition, variable loading times introduce greater complications when testing a viscoelastic material. The use of continuous stiffness measurement for extracting nanomechanical property information is also complicated due to bones natural resonant frequencies and its viscoelasticity (Mencik et al., 2005).

3.2.5 Influence of contact depth

The volume of material that contributes to a materials overall nanomechanical response depends on factors that include the indenter contact depth and the size of the tip. The effective volume contributing to elastic modulus measurement can be described by a paraboloid of revolution with radius 3a and depth 5a (where a = radius of circle of contact between the tip and the surface) (Bushby, 2001). It is a simple matter, therefore, to optimize the tip selection and experimental parameters to enable testing of the microstructures or regions of tissue and, conversely, to avoid testing volumes that extend beyond the regions of interest.

The length-scale of bones microstructural features of interest, for example a lamellae

$\approx$ 5 micrometers thick, is critical to selecting the appropriate tip shape, tip size, maximum indenter penetration depth and corresponding maximum applied load. A wide range of indentation depths, from 100 nm to 3000 nm (Hengsberger et al., 2002; Vanleene et al., 2006; Habelitz et al., 2001; Cuy et al., 2002), have been used to extract bone and enamel's modulus and hardness. The volume of material deformed is laterally seven times the depth of the indent (Johnson, 1985), thus the deeper indents test a larger volume of bone. Larger testing volumes include the influence of heterogeneities such as pore spaces of various sizes, changes in the degree of mineralization, increased numbers of lamellae, and multiple types of bone or other structural features. In addition, the maximum depth on loading may produce an effective volume that lies within the boundaries of the region of interest, yet further penetration upon a creep hold at maximum load may further expand the contact volume.

In general, the measured modulus of bone and enamel has been shown to decrease with increased max load ranging (He et al., 2006; Zhou and Hsiung, 2007; Zhang et al., 2008). As the contact area and plastic deformation increase at higher loads, in bone it is likely that more pores and regions high in organic volume fraction are incorporated into a test volume to create a softening influence (Zhang et al., 2008, 2010). Similarly in enamel more organic sheath is incorporated into the deformation volume at higher loads (He et al., 2006). The consideration of the maximum depth of penetration with regards to the 3-D microstructure is clearly of great importance. Indentation to various depths can be used to probe enamel and bones hierarchical structure. For example, shallow indents (<1000 nm) have been commonly applied to investigate microstructural features– such as individual lamella (Rho et al., 1999b; Gupta et al., 2006; Hengsberger et al., 2002) or single enamel prisms(He et al., 2006; Zhou and Hsiung, 2007). These shallow indents, often performed with an AFM-based indentation system, are more sensitive to heterogeneities as less material volume contributes to the overall mechanical response within a single indentation. Surface roughness, porosity, polishing relief, and other near-surface characteristics may cause a high degree of variability in measured indentation properties (Donnelly et al., 2006). Deeper

indents sample large volumes of material and measured mechanical properties are averaged properties of the multiple heterogeneities. Using both experimental results and finite element models, nanoindentation modulus values have been shown to converge to a single value as the depth of the indent, and consequently the effective volume of measurement, increases (Oyen and Ko, 2008).

3.3 X-ray Diffraction

X-ray powder diffraction (XRD) has been commonly applied to mineralized tissues and allows for phase identification, measurements of crystallinity, and determination of lattice parameters (Fujisaki and Tadano, 2007; Michel et al., 1996; Person et al., 1995). In powder diffraction, the sample is sufficiently ground, to insure random orientation of the crystals, and then exposed to monochromatic x-rays. If the orientation of the crystalline particles is truly random, then for each family of planes, with its characteristic interplanar spacing (d), there will be enough correctly oriented particles to satisfy Braggs law (Equation 3.13). Different families of planes will satisfy Braggs law for different values of θ and the intensity of the reflection is measured as the detector is rotated though the angle 2θ (Klein and Dutrow, 2008).

$$n\lambda = 2dsin(\theta) \tag{3.13}$$

For x-ray diffraction analysis of mineralized tissues, samples are mechanically crushed often in a mechanical shatter box or hand ground with a mortal and pestle to a very fine powder (particle size $\approx 10\mu m$). For best results this powder is packed into a special rectangular sample holder to ensure that a sufficient number of approximately equally sized crystals are available with random orientation. The XRD spectra are most commonly obtained using Cu Kα radiation (wavelength, $\lambda = 1.5428\mathring{A}$). The XRD detector moves though a 2θ range in order to measures the intensity of the reflected x-ray by the crystalline lattice according to Bragg's law. Assuming a perfect crystal lattice the diffraction pattern of HA

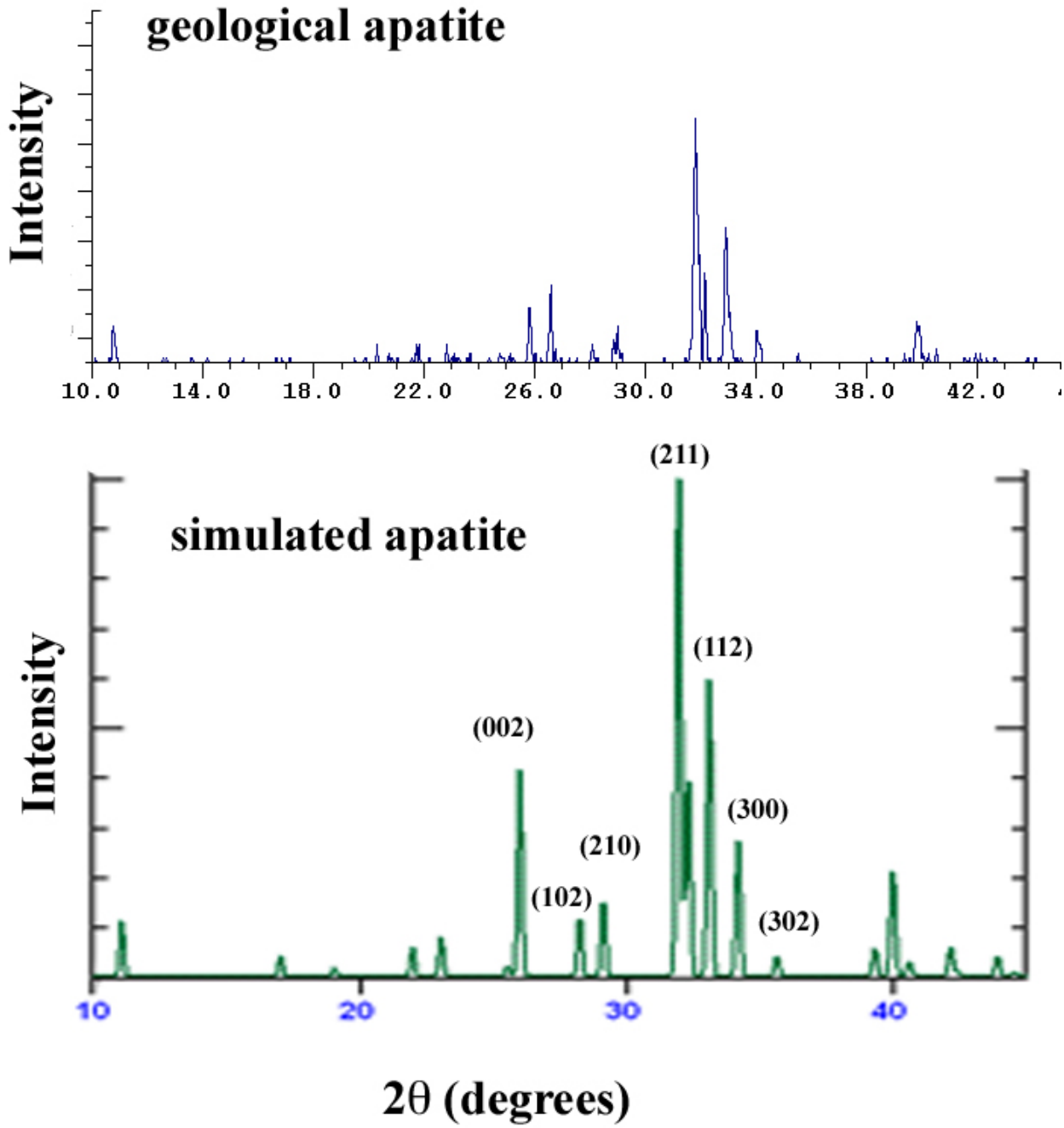

Figure 3.7: XRD spectra for geological apatite compared to the calculated powder diffraction pattern for HA using the program XPOW.

can be simulated using the XPOW (Mineralogical Society of America) software (Figure 3.7). Collected XRD spectra are generally used for chemical analysis though comparison of peaks to a national database complied by the Joint Committee on Powder Diffraction Standards (JCPDS). This national data base contains diffractions peaks for most materials with peak intensity and location for each crystal plane listed, for example JCPDS number 09-0432 is the HA spectra (Sudarsan and Young, 1969).

Measurements of XRD peak location, area, and width provide insight into alterations in the crystal structure caused by substitutions, vacancies, or even changes in lattice volume. Specifically, changes in crystallinity can be investigated by measuring the full width at half maximum (FWHM) of diffraction peaks. The FWHM has been commonly used as a measurement of crystallinity in bone samples and reflects changes in crystal size, number of defects, and overall crystal perfection of the mineral phase (Hubert et al., 1996; Price et al., 2002; Hedges and Millard, 1995). Using the FWHM (B) of a given XRD peak, the crystal size (t) in a direction perpendicular to the miller plane can be estimated by the Scherrer formula:

$$t = \frac{57.3K\lambda}{Bcos(\theta)} \tag{3.14}$$

Where 57.3 is a conversion from degrees to radians, K is the shape factor (K=0.9 for the crystal habit of apatite), λ is the wavelength of the X-rays, and θ is the diffraction angel of the peak. From Equation 3.14 it is clear that as the diffraction peak narrows (i.e., B decreases), the size of the crystal perpendicular to that direction increases. While, numerous experimental factors and variations in lattice strain can effect the measurements of B, crystal size changes contributes the most substantially (Sudarsan and Young, 1969).

3.4 Scanning Electron Microscopy

Scanning electron microscopy (SEM) is one of the most versatile instruments available as can provides high resolution ($\approx$ 1- 5 nm for commercial instruments) information about the

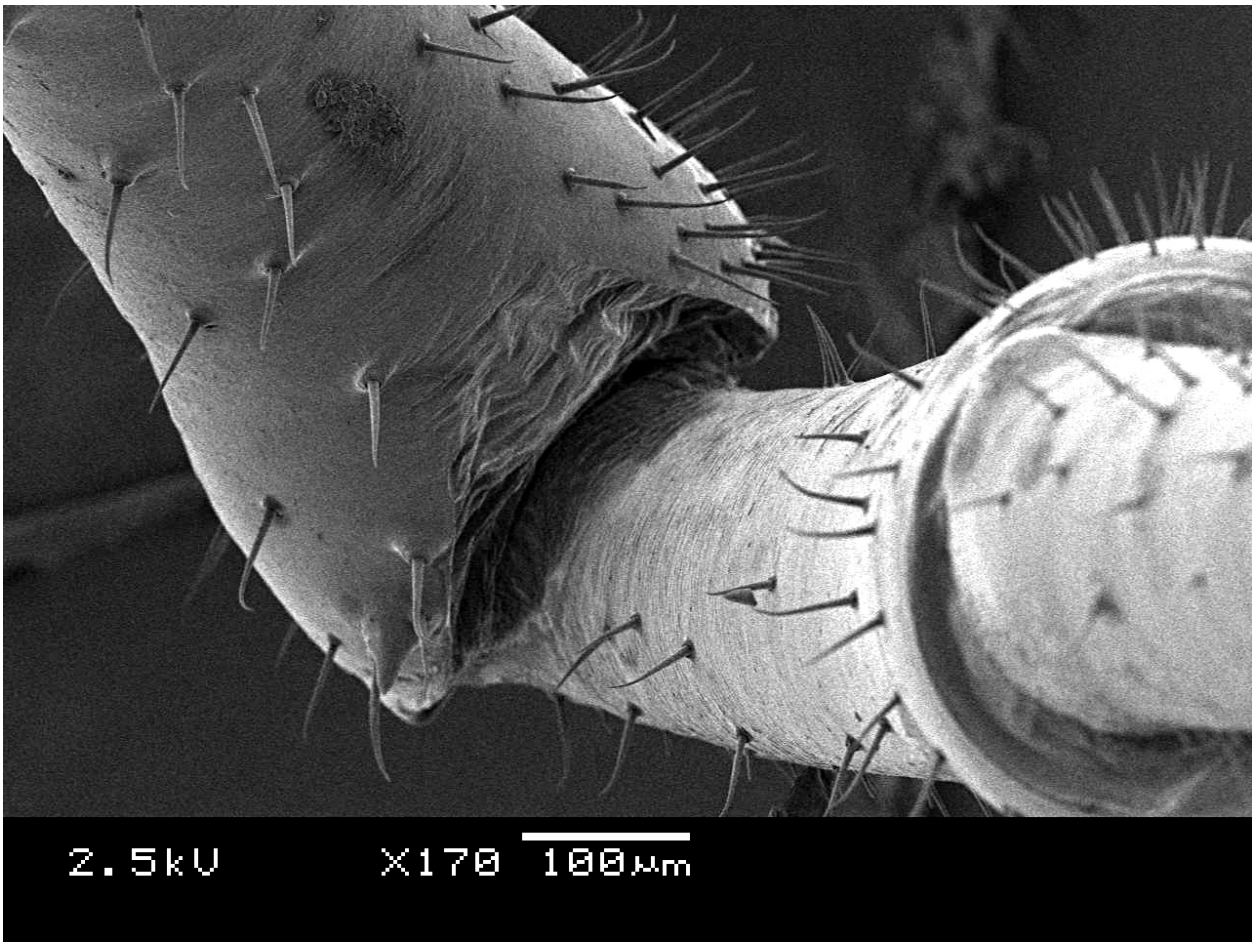

Figure 3.8: SEM image of a spider leg demonstrating the depth of field in SEM images. Image taken as part of a Science Discovery class, Nanoworlds, for 8th graders.

nature of the sample including: shape, composition, crystal structure, and even electronic conductivity. Additionally, the large depth of field of SEMs creates a 3D-like image for analysis of the surface structure of a sample (see Figure 3.8). In a standard SEM electrons are generated by heating a tungsten filament which is focused onto the sample surface in a raster scan pattern. The electron beam typically has energy ranging from 0.5 keV to 40 keV is focused in the microscope column (see Figure 3.9) though a combination of condenser lenses and apertures (Goldstein et al., 1981). The beam, about 0.4 nm to 5 nm in diameter, is deflected in x and y by the scanning coils to create the classic raster scanning of the SEM.

The versatility of the SEM for the study of materials is provided primarily by the diverse range of interactions the electron beam can undergo. Electrons interacts with the sample though either elastic or inelastic scattering events. Elastic scattering alters the trajectory of the electron but does not alter the energy and creates the backscattered electron signal. Alternatively inelastic scattering results in energy transfer to the sample leading to the generation of secondary electrons, Auger electrons, x-rays, and numerous other sources of energy absorption. While the diameter of the incident electron beam is about 5 nm the actual interaction volume is much larger due to electron scattering which alters the trajectories of the electrons. Upon consideration of electron scattering the probability of a scattering event occuring is defined as the cross section (Q) (Goldstein et al., 1981):

$$Q = N/n_i n_t \tag{3.15}$$

where N is the number of events per unit volume, n_t is the number of target sites per unit volume, and n_i is the number of incident particle per unit area. The cross section has units of area and can be consider as the effective size of an atom for a given interaction. From the cross section of a particular event (e.g., the elastic scattering of an electron off an atom) the average distance a particle travels between interactions can be defined as the mean free path (λ):

$$\lambda = A/N_o \rho Q \tag{3.16}$$

where A is the atomic weight, N_o is Avogadro's number (6.02 X10^{23} atom/mol), and ρ is the density. With the knowledge of the mean free path, Monte Carlo simulations can be used to determine the interaction volume of an indent electron beam. For example, a 20 keV electrons have been shown to penetrate up to 5 μm in depth in PMMA (Everhart et al., 1972). The interaction volume is teardrop-shaped and is highly dependent upon the electron energy, atomic number (Z), and sample density. In Monte Carlo simulation of electron interactions with bone the interaction volume has been shown to significantly increases with increased electron energies from 20 keV to 30 keV (see Figure 3.10). Additionally these simulations demonstrate that backscattered electron (elasticity scattered) are generated from a much smaller volume than secondary electrons (inelasticity scattered) as represented by the black area (backscattered, BSE) compared to the gray area (secondary electrons) in Figure 3.10.

3.4.1 Backscattered Electron Imaging

It was determined experimentally that about 30% of the incident electrons in SEM are not absorbed by the sample and are instead scattered out of the sample (Goldstein et al., 1981). These electrons are collectively termed backscattered electrons (BSE) and are most commonly the result of one or more elastic scattering events. The number of backscattered electrons (η_{BS}) divided by the total number of incident on the sample (η_{total}) is defined as the backscattered coefficient (η):

$$\eta = \frac{\eta_{BS}}{\eta_{total}} \tag{3.17}$$

During an elastic scattering event kinetic energy is conserved and the direction is altered from the original path by ϕ, ranging from 0° to 180°. Elastic scattering events are the results of the electron's "collision" or interaction with the nuclei of the atom as described by the Rutherford model. The cross section probability for elastic scattering at an angle greater than ϕ_0 is given by:

$$Q(> \phi_0) = 1.62x10^{-20}\frac{Z^2}{E^2}cot^2\frac{\phi_0}{2} \tag{3.18}$$

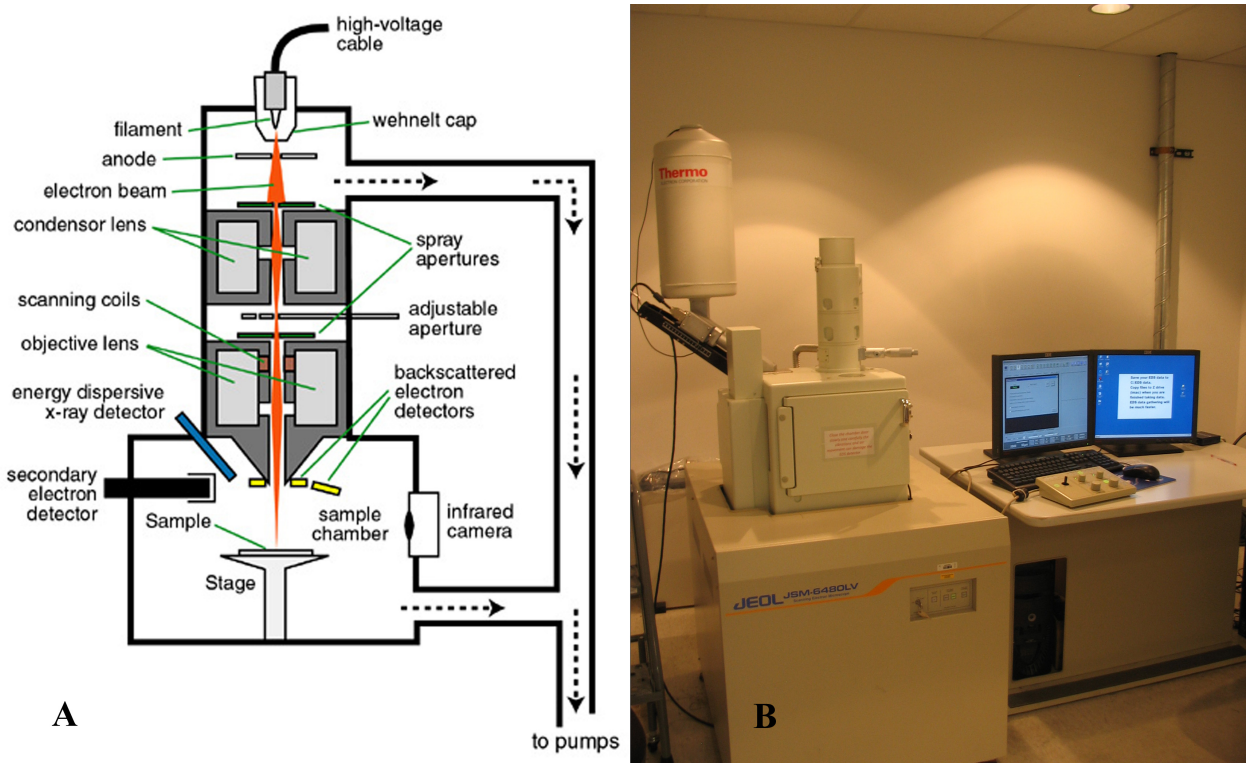

Figure 3.9: (A) schematic of the SEM column which focuses the electrons emitted from a heated tungsten filament into a small nanometer sized spot. The electron beam is raster scanned across the sample to create an image. From http://www4.nau.edu/microanalysis/Microprobe-SEM/Instrumentation.html. (B) Picture of JEOL-6480LV low vacuum SEM (LVSEM) located in the Nanomaterials Characterization Facility at the University of Colorado-Boulder

where E is the electron energy. Equation 3.18 revels that electron scattering is more probable in high atomic number (Z) materials at low electron energies (E).

The dependence of backscattered electrons on the atomic number provides an extremely useful signal for imaging with an SEM. The backscatter coefficient has been found to increase as a function of the atomic number (Z) (Joy, 1995). Several equations have been proposed, based on curve fitting to experimental data, for interpolation for missing values (Arnal et al., 1969; Herrmann and Reimer, 1984; Lloyde, 1987). However all these formula except the equation by Arnal et al. (1969) (Equation 3.19) give negative BSE coefficients for low atomic number elements.

$$\eta = 2^{-9/\sqrt{Z}} \tag{3.19}$$

For a compound the backscatter coefficient η_{comp} is simply the weighted mean of the individual constituents (Casting, 1960) given by:

$$\eta_{comp} = \sum (c_i \eta_i) \tag{3.20}$$

where c_i denotes the weight fraction of the ith constituent and η_i is the backscatter coefficient for each element. A corresponding Z_{comp} for a composite material, similar to equation 3.20, can be determined though a weighted average of the atomic numbers of the individual constituents (Lloyde, 1987):

$$\eta_{comp} = \sum (c_i Z_i) \tag{3.21}$$

where Z_i indicated the atomic number of the of the ith atom respectively.

The backscatter coefficient's atomic number dependence has lead to quantitative backscatter electron imaging (qBSE) to investigate the mineral content of calcified tissues, especially bone (Bloebaum et al., 1997; Boyde et al., 1993; Ferguson et al., 2003b; Skedros et al., 1993). As the electron beam is scanned across the sample the backscatter coefficient intensity of each portion of the image is recorded for each pixel in the form of the gray level intensity (0-255). The BSE gray level is thus dependent on the atomic number of the sample (Lloyde, 1987; Howell and Boyde, 2003) and has been shown to correlate to the mineral content of

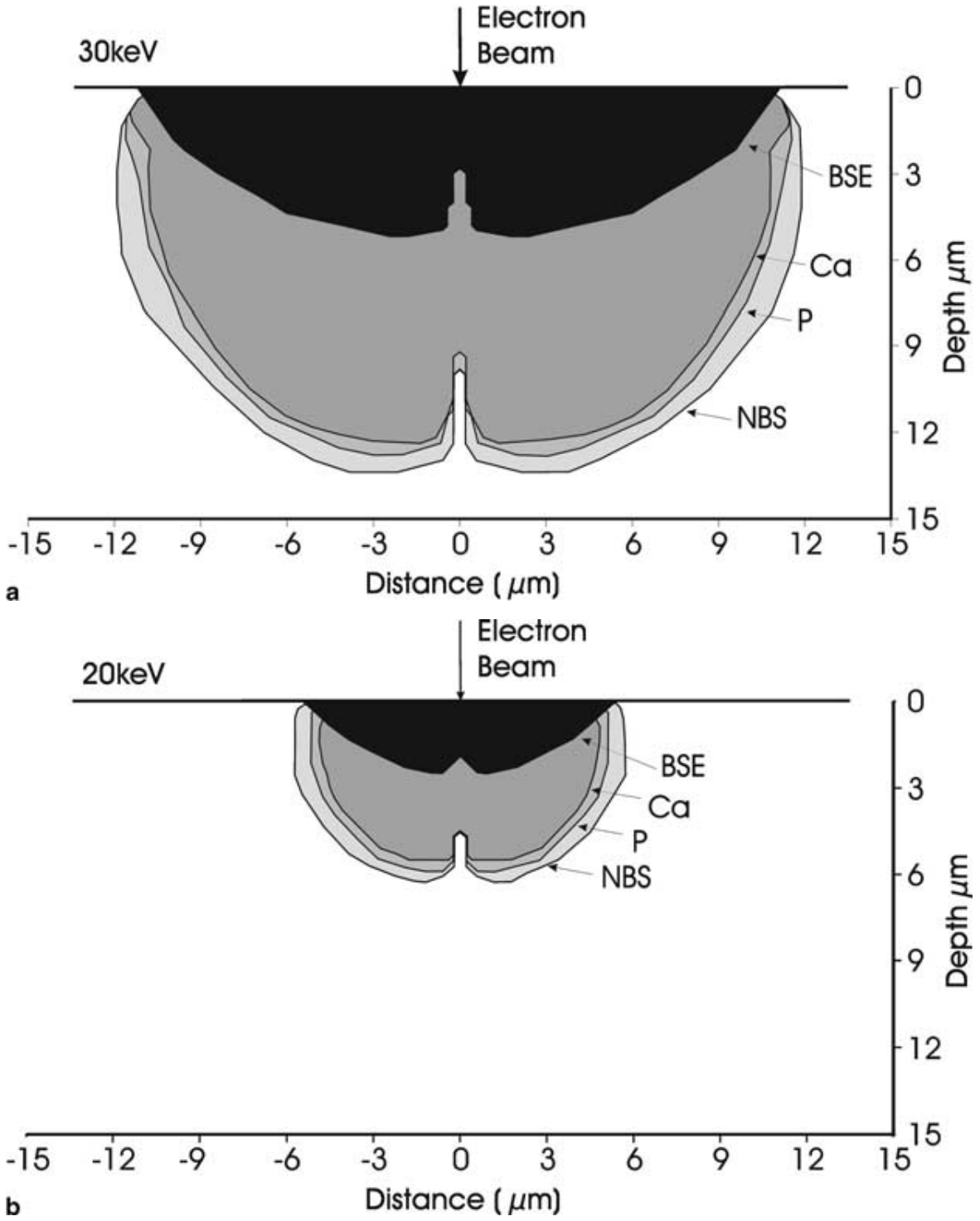

Figure 3.10: Monte Carlo simulations of the volumes from which phosphorus and calcium x-rays and backscattered electrons (BSE) arise in bone mineralized to 40% by volume at (a) 20 kV and (b) 30 kV accelerating voltages. Absorbed, non-backscattered electrons designated NBS. Image from (Howell and Boyde, 2003) with permissions.

bone (Boyde and Jones, 1983; Skedros et al., 1993). The use of standards allows for the mean gray level of multiple samples to be compared between different BSE imaging sessions, in which the gray level can drastically fluctuate from variations in beam current and image collection settings (this will be discussed in detail in Chapter 4). qBSE imaging of bone provides a high resolution technique in which small, localized variations in mineralization can be identified. qBSE has previously been used to investigate mineral content variations with age related changes (Kingsmill and Boyde, 1999; Reid and Boyde, 1987; Skedros et al., 1993), between different types of bone (Bloebaum et al., 1997; Oyen et al., 2008), and with bisphosphonate treatment (Burr et al., 2003). Additionally, because backscattered electrons originate from a tissue depth approximately 1- 5 μm depth (see Figure 3.10), thick samples with complex geometries (e.g. cancellous bone) can be used for mineral content analysis. Further, qBSE has been combined with complementary techniques such as confocal microscopy (Doube et al., 2005) or nanoindentation (Ferguson et al., 2003b). Nanoindentation has been used with qBSE imaging and allows for linked analysis of mechanical and mineral content within a small tissue volume (Oyen et al., 2008).

3.5 Fourier-transform infrared Spectroscopy

Fourier-transform infrared Spectroscopy (FTIR) has been commonly applied for more than a half-centry to probe the composition and crystallinity of bone and enamel (Posner and Duyckaerts, 1954; Mcconnel et al., 1967; Boskey et al., 2005). FTIR has been used to identify the presence and nature of (CO_3, HPO_4) substitutions in the HA lattice (Posner and Duyckaerts, 1954), compositional variations with diet (Grynpas and Rey, 1992), aging, space flight and even osteoporosis (for a review of the numerous applications see Boskey et al. (2005)). Several useful parameters that can be extracted from FTIR analysis include: mineral/matrix ratio, carbonate/phospahte ratio, crystallinity, collagen maturity, and acid phosphate content (Boskey et al., 2005; Elliott, 2002). Mineral to matrix ratio is calculated from the ratio of integrated areas of the phosphate ν_1, ν_3 band at 900–1200 cm^{-1} to the amide

I band at 1585–1725 cm^{-1} and correlats to the ash weight precent mineal (Pienkowski et al., 1997). The total carbonate (based on the ν_2 band at $\approx 850 - 900 cm^{-1}$) to phosphate ν_1, ν_3 ratio gives a measure of compositonal variations within the minearlized tissue (Paschalis et al., 1996).

Chapter 4

Development of Quantitative Backscatter Electron Microscopy Standards

Quantitative backscatter electron imaging (qBSE) has been used to investigate the mineral content of calcified tissues, especially bone (Bloebaum et al., 1997; Boyde et al., 1993; Ferguson et al., 2003b; Skedros et al., 1993), but also enamel and dentin (Angker et al., 2004). The BSE imaging method allows visualization of local changes in mineral concentration within cortical and trabecular bone structures and other mineralized tissues. The BSE image gray level (0-255) is a measure of the number of backscatter electrons (measured by the backscatter coefficient, η) that directly related to the atomic number of the sample (Howell et al., 1997; Lloyd, 1987). While mineralized tissues contain both organic (C, H, N, O, P, S) and mineral (Ca, P, O, H, Mg) components, the mineral with higher atomic numbers contributes significantly more to the backscatter signal. Because of the direct atomic number dependence, the gray level has been shown to correlate to the mineral content of bone (Boyde and Jones, 1983; Skedros et al., 1993). Further, the BSE signal originates from 1- 5 μm in depth which allows for tissue-scale measurements in which small, localized variations in mineralization can be identified. The BSE signal has been widely used to investigate variations in mineralization with age and sex (Kingsmill and Boyde, 1999; Reid and Boyde, 1987; Skedros et al., 1993), type and location (Bloebaum et al., 1997; Oyen et al., 2008), and disease states (Burr et al., 2003; Roschger et al., 1995).

Application of qBSE imaging to numerous samples necessitates multiple imaging sessions over days and weeks and requires the use of standards. Large fluctuations in beam

current, detector brightness and contrast, accelerating voltage, working distance, filament fatigue, and electronic drift may influence the BSE detector output voltage and also the gray-level of the image. To ensure reproducible gray-level values two standards, one of low atomic number set to a gray level value of zero and one with high atomic number set to 255, are selected to encompass the range of mineral volume fraction of the sample. Most commonly the use of pure metallic standards of magnesium and aluminum and sometimes carbon standards have been applied to qBSE of bone (Roschger et al., 1995; Boyce et al., 1990; Skedros et al., 1993). While these pure standards are easily obtained, both the applied standardization methods and materials are problematic. Metallic standards are macrocrystalline, display channeling contrast effects, and can further oxidize over time and thus cannot be used as long term standards. The use of Mg and Al (Vajda et al., 1995; Bloebaum et al., 1997; Skedros et al., 1993) as standards creates an extremely narrow atomic number range (Z = 12-13) compared to mineralized tissues which typically span a much larger range (Z = 9-14). Ideally a set of standards should encompass the whole range Z values of the material of interest to prevent backward interpolation of the standardization curve. Further use of gold coating, while common (Bloebaum et al., 1997; Skedros et al., 1993; Boyce et al., 1990) can interfere with the calibrated gray level due to its high atomic number. Rather, a carbon coating should be used because of its low atomic number.

The use of polymeric standards have been suggested as an alternative to the problematic metallic standards (Boyde and Jones, 1983; Boyde et al., 1995; Howell et al., 1997). These polymers posses no long-range order or crystallinity that may induce channeling contrast. The composition of these polymers is customizable and can be specifically selected to cover a range of atomic numbers. Further, polymeric materials are not subject to oxidation and have been shown to maintain long term stability (Howell et al., 1997). However the creation of these polymers require advance understanding of organic chemistry (Boyde et al., 1995; Davy, 1994) and their fabrication is quite expensive and technically difficult thus not readily available to the typical laboratory.

In this work we created a set of novel (lithium-rubidium borosilicate) glass standards with known mean atomic numbers. By varying the composition we can create a range of standards that span the atomic numbers of interest which can be used to quantify a large range of mineral content. Calibration of the mean gray-level of these standards to the backscatter coefficient was achieved with a wide variety of materials, including both engineering materials (e.g. aluminum) and geological minerals (e.g. quartz). These glasses are simple and straight forward to make and very cost effective. Further adjustments of composition are simple allowing for customizable standards for a specific range of atomic numbers.

In this dissertation, these standards were used to investigate a range of mineralized tissues from young mouse femur (poorly mineralized bone) to whale tympanic bulla (highly mineralized bone). These tissues were used to further verify this method's ability to quantify the mineral volume faction to gray level. The mineral compositional (using FTIR), density (using μCT), and nanomechanical properties (using nanoindentation) of these tissues were further investigated to access their relationship to mineral volume fraction.

4.1 Study Objectives

The qBSE imaging technique provides a valuable tool to assess the mineral volume fraction (or content) at the tissue level. However, currently used crystalline calibrations standards have numerous limitations. **This study seeks to develop novel qBSE amorphous standards to relate backscattered gray level to mineral volume fraction.** The use of these glass standards for calibration of BSE images of mineralized tissues was validated by comparison of measured qBSE mineral volume fraction of a wide range of tissues including cartilage, bone, and enamel. This work formed the basis to study the role that additional factors may play in contributing to heterogeneity in bone including mineral volume fraction, composition, density, and nanomechanical properties. The following sub-goals have been defined.

(a) Develop and calibrate novel glass standards to quantify mineral composition using qBSE imaging.

(b) Investigate a wide range of mineralize tissues from shark cartilage to whale bulla for changes in mineral content using newly developed standards.

(c) Further explore the relationship of mineral volume fraction, density using μCT, composition using FTIR, and nanomechanical properties using nanoindentation of these mineralized tissue.

4.2 Materials and Methods

4.2.1 Creation of glass standards

The glass system $(0.25 - X)Li_2O \cdot XRb_2O \cdot (0.30)B_2O \cdot (0.45)SiO_2$ with (0<X <0.25) was selected to span the compositional range of mineralized tissues. Following the methods of Feller et al. (2010) and Stentz et al. (2001), the glasses were made from starting materials of: lithium carbonate (Li_2CO_3, SigmaAldrich 99.9+%), rubidium carbonate (Rb_2CO_3, SigmaAldrich 99.9+%), silica (SiO_2, Alfa Aesar 99.9%), and boric acid (H_3BO_3, SigmaAldrich 99.9+%). Stoichiometric combinations of the starting materials were thoroughly mixed in a platinum crucible for five minutes to create eight gram batches. Each batch mixture was then heated in the range 1000°C to 1200°C (for high Rb_2O content) for about 25 min. Weight loss measurements taken after 15 minutes of heating, indicate that the compositions are accurate in X to $\pm$ 2%. Bulk glasses were obtained by splat quenching the melt between two brass plates with an estimated cooling rate of about 103 K/s (Feller et al., 2010). Two batches of each composition were combined and crushed using a mortal and pestle. This mixture was heated for 10 minutes, splat quenched, crushed, and mixed and repeated two times though before final glass formation. Final glasses were then annealed for 4 hours at about 50°C below Tg (475-500°C) as measured by differential Scanning Calorimetry (DSC) and finally

slow cooled overnight. Small section of each glass we placed side-by-side and embedded in epoxy to form one glass standard block in which all glasses could be viewed in a single image.

4.2.2 Reference Materials

A wide range of engineered and geological materials were obtained for calibration of the glass standards. Materials included geological quartz (Boulder county, Colorado), soda lime glass (Corning glass microscope slide, $(0.73)SiO_2 \cdot (0.14)Na_2O \cdot (0.07)CaO \cdot (0.04)MgO \cdot (0.02)Al_2O_3$), geological aragonite (Cairns Bay, Flinders, Victoria, Australia), Mg ribbon (Mg, SigmaAldrich 99.5+%), aluminum wire (Al, SigmaAldrich 99.99+%), and geological fluorapatite (Cedar City, Iron county, Utah). Samples were embedded together in epoxy to form a reference sample block. Both the glass standards and reference sample block were polished to a 0.25 μm finish and coated with a thin layer of carbon before imaging.

4.2.3 BSE imaging capture

The BSE-imaging was preformed on a field emission scanning electron microscope (Gemini LEO 1525 FEG-SEM, Carl Zeiss) equipped with consistent settings for each imaging session with an accelerating voltage of 20 kV along with a constant working distance of 15 mm. The microscope was run for a minimum of a one hour warm-up period to ensure constant operating conditions for each imaging session. Beam current remained stable at 435 ± 15 pA over a four hour imaging session. Each captured image had a resolution of 1024 x 768 pixels with grayscale pixel values ranging from 0 (black) to 255 (white). The nominal magnification was set to $\approx$ 90x for images of standards and calibration materials, and 500 or 800x for images of mineralized tissues.

At the beginning of a typical imaging session, brightness and contrast setting were adjusted to include the gray-level range of the samples and glass standard within the 0 to 255 grayscale. All imaging setting, including brightness and contrast were held constant throughout each imaging session. Topological contrast contributes significantly to BSE gray-

level values and thus all samples, while loaded into the sample tray at different heights, were imaged at the same working distance ± 0.01mm. Standards were imaged at the beginning, end, and every 20 minutes during each imaging session. Post-processing of the qBSE images was preformed using the software package NIH ImageJ (Bethesda, Maryland, USA, http://rsb.info.nih.gov/ij/). The glass X = 0 was selected as the low standard whose raw gray-level is mapped to 0 and the glass X =0.15 as the high standard whose raw gray-level is mapped to 255. Extrapolation of gray-level values for high and low standards were pulled from images of the glass standards from both before and after a given sample image. Linear mapping of raw gray-level of the low and high standards to 0 and 255, respectively, ensures comparable gray-level values between images taken at different times and with operating conditions. Using this mapping technique gray-level values of the middle standards (X = 0.02, 0.05, and 0.1) taken over multiple imaging sessions and weeks varied at most by six graylevels.

Before evaluation of the weighted mean gray-level (WMGL) of each image, the background (PMMA and any soft tissue or void space) was discriminated by a threshold routine and set to zero. The weighted mean gray-level (WMGL) of a selected region is given by (Vajda et al., 1995):

$$WMGL = \sum_{i=1}^{255} \frac{P_i GL_i}{P_{total}} \tag{4.1}$$

where: i = index of a single gray-level ranging from 0 (black) to 255 (white), P_i = number of pixels at each gray-level (GL_i), and P_{total} = total number of pixels. Black pixels with i=0 can artificially influence the WMGL and are thus excluded from calculation.

4.2.4 Calibration of WMGL

The relationship of experimental WMGL to η and Z was determined through the use of the reference materials and glass standards with known compositions. The Z_{comp} and η_{comp} of the reference materials and glass standards were calculated using equations 3.19,

3.20, and 3.21. The use of the calibration curve for WMGL allows determination of η_{comp} or Z for an unknown material, through measurement of WMGL. In the case of a composite material the weight fraction of each component (with known chemical compositions) can be determined from a simple rule of mixtures (equations 3.20, or 3.21). For mineralized tissues we can assume a two constituents composite consisting of organic matrix (OM, Z= 6.833, η_{OM} =0.0907) and hydroxyapatite (HA, Z= 14.06, η_{HA} = 0.1818) to allow for calculation of weight mineral fraction (WT_{min}) given by equation 4.2.

$$\eta_{comp} = WT_{min}\eta_{HA} + (1 - WT_{min})\eta_{OM} \tag{4.2}$$

Volume mineral fraction (VMF) can then be calculated from the weight fraction and the density of the OM (ρ_{OM} = 1.285) and HA (ρ_{HA} = 3.18) using equation 4.3.

$$VMF = \frac{WT_{min}}{WT_{min} + ((1 - WT_{min})(\frac{\rho_{HA}}{\rho_{OM}}))} \tag{4.3}$$

4.2.5 Mineralized Tissues

Calibrated standards were applied to investigate a series of mineralized tissues in order to validate and quantify mineral volume fraction at the micron scale. The samples included a unique range of mineralized tissues from high mineral content: whale bulla, bobcat bulla, and bobcat periotic to samples with low mineral content: 2 week old mouse femur, carp dermal bone, and shark cartilage, as well as the mid-diaphysis of several femurs from a range of species including cow (obtained from an abattoir: Arapahoe Packing, Lafayette, CO), lamb (obtained from an abattoir: Mountain Meadow Lamb Corporation, Denver, CO), and 20 week old mice (C57). All fresh samples were cleaned to remove all non-osseous tissue and dehydrated in a series of ethanol solution. Two small neighboring samples from each mineralized tissues were cut using a low-speed diamond wafering saw (Isomet: Buehler, Lake Bluff, IL). One section of each sample was used with microCT to measure the density and then ashed to measure mineral weight percent. The remaining section was utilized

for nanoindentation and then qBSE site matched measurements. The second section was embedded into PMMA and ground with a series of silicon carbide paper (300, 400, 600, 1200 grit) and then polished with successfully finer diamond suspension paste (Buehler) of particle size 6, 3, and 0.25 μm. Each sample was ultrasonically cleaned after each suspension paste step and finally coated with carbon.

4.2.6 Evaluation of Mineral Content

In order to determine the mineral content of each sample both MicroCT and ash mineral volume fraction measurements were preformed on the first section of each tissue, on average 25 mm^3 in size. Each tissue was evaluated for volumetric bone mineral density using MicroCT (microCT 80, Scanco Medical AG; Bassersdorf, Switzerland), with isotropic voxels of 10 $\mu m/side$. Additionally, the same section was first defatted (in chloroform, 24 h) and then analyzed for dry mass (Dry-M, 105°C drying for 24 h), mineral content (Min-M, 800°C drying for 24 h) to ultimately determine weight percent mineral (ASH-WT_{Min} = Min-M/Dry-M x 100%). Ash mineral volume percent is reported as determined by ASH-WT_{Min} and equation 4.2.

FTIR in reflectance was used on bulk samples to get a measure of compositional variations. Mineral to matrix ratio is calculated from the ratio of integrated areas of the phosphate ν_1, ν_3 band at 900–1200 cm^{-1} to the amide I band at 1585–1725 cm^{-1} and correlates to the ash weight precent mineral (Pienkowski et al., 1997). The total carbonate (based on the ν_2 band at $\approx 850 - 900 cm^{-1}$) to phosphate ν_1, ν_3 ratio gives a measure of compositional variations within the mineralized tissue (Paschalis et al., 1996). Reference samples of geological hydroxyapatite and gelatin powder (collagen) were tested, see figure 4.1

4.2.7 Nanoindentation and site-matched qBSE

Nanoindentation tests were performed using a ramp-and-hold method (Nanoindenter XP; MTS Systems Corp, Oak Ridge, TN) in continuous stiffness mode. Indentation tests

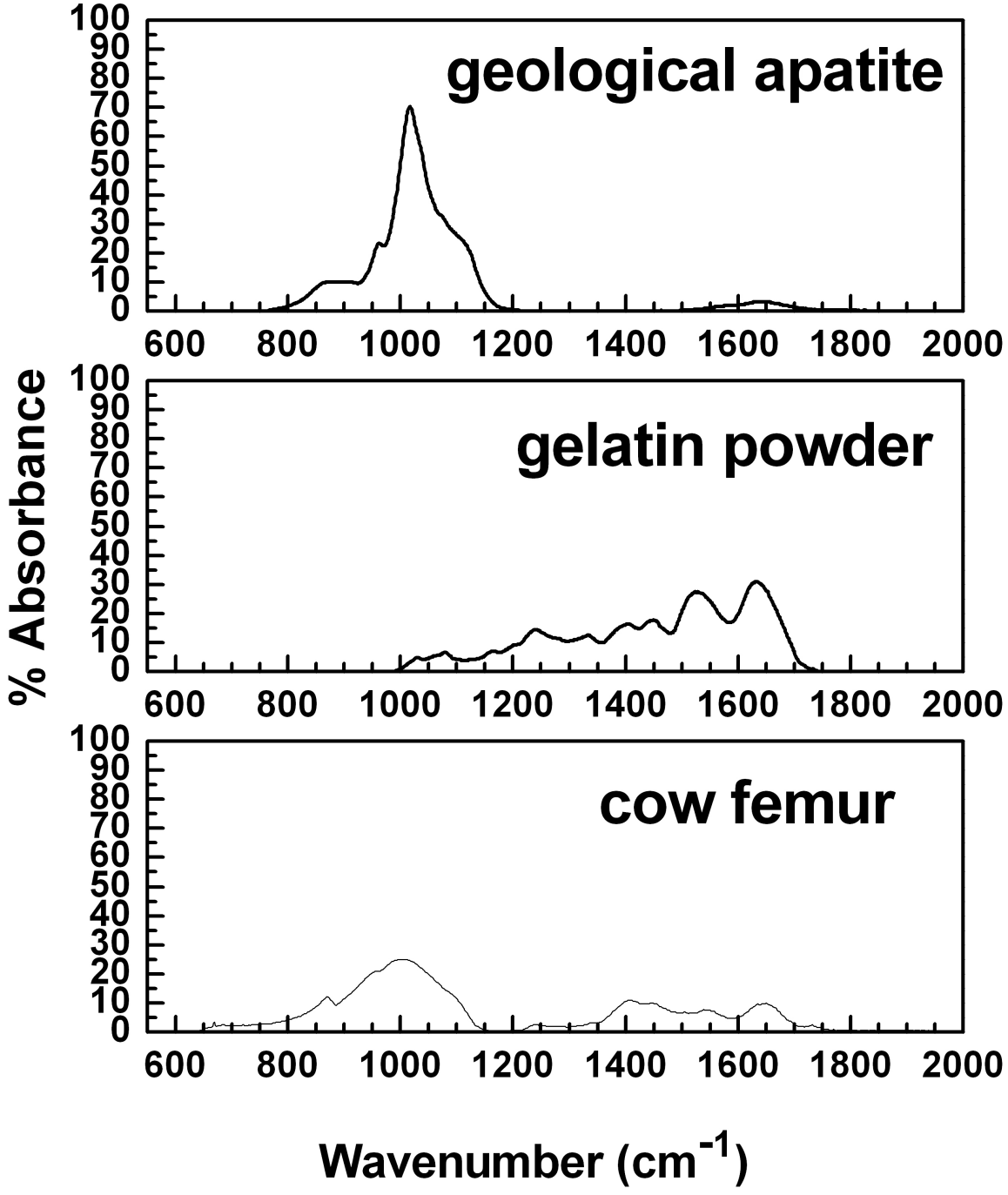

Figure 4.1: FTIR spectra of the components of bone: apatite (geological), collagen (gelatin powder), and a representative spectra of bone (cow femur).

utilized a constant loading and unloading rate of 0.5 mN/s to a maximum load value of 20 mN, where a 120 s hold time of maximum load was used to minimize the contribution of creep to the unloading curve. On each mineralized sample, 20 test were run using a Berkovich indenter tip. Reduced modulus (E_R) and hardness (H) was calculated using the Oliver-Pharr method (Oliver and Pharr, 1992) from the slope or stiffness (S) of the unloading curve, max load (P_{max}), and tip area function (A_c). The Berkovich indenter tip was calibrated using fused silica reference material to determine A_c. Here, we report the plane strain modulus (E'), which is related to E_R through equation 3.8 and eliminates error in assuming the Poissons ratio of the sample.

The effective volume of material contributing to the overall mechanical response depends on factors that include the indenter contact depth and the size of the tip, and can be described by a paraboloid of revolution with radius 3a and depth 5a (where a = radius of circle of contact between the tip and the surface) (Bushby, 2001). The contact radius, a, was calculated from the calibrated tip area function (A_c) assuming a circular contact at the maximum depth of contact. For each sample the depth of contact was taken as the average value over all 20 indentation sites.

Site matched measurements of qBSE WMGL were preformed on each nanoindentation site. Within a circular region, radius = 3a, around each indentation imprint the WMGL was measured. Using NIH ImageJ (Bethesda, Maryland, USA, http://rsb.info.nih.gov/ij/) the residual indentation imprint, cracks, osteocyte lacuna, and any other void spaces were removed from analysis though a threshold routine.

4.3 Results and Discussion

4.3.1 Standards and Calibration

The glasses (X = 0, 0.02, 0.05, 0.10, 0.15) successfully encompassed the WMGL range of mineralized tissues from bone to enamel (Figure 4.2). The two extreme compositions

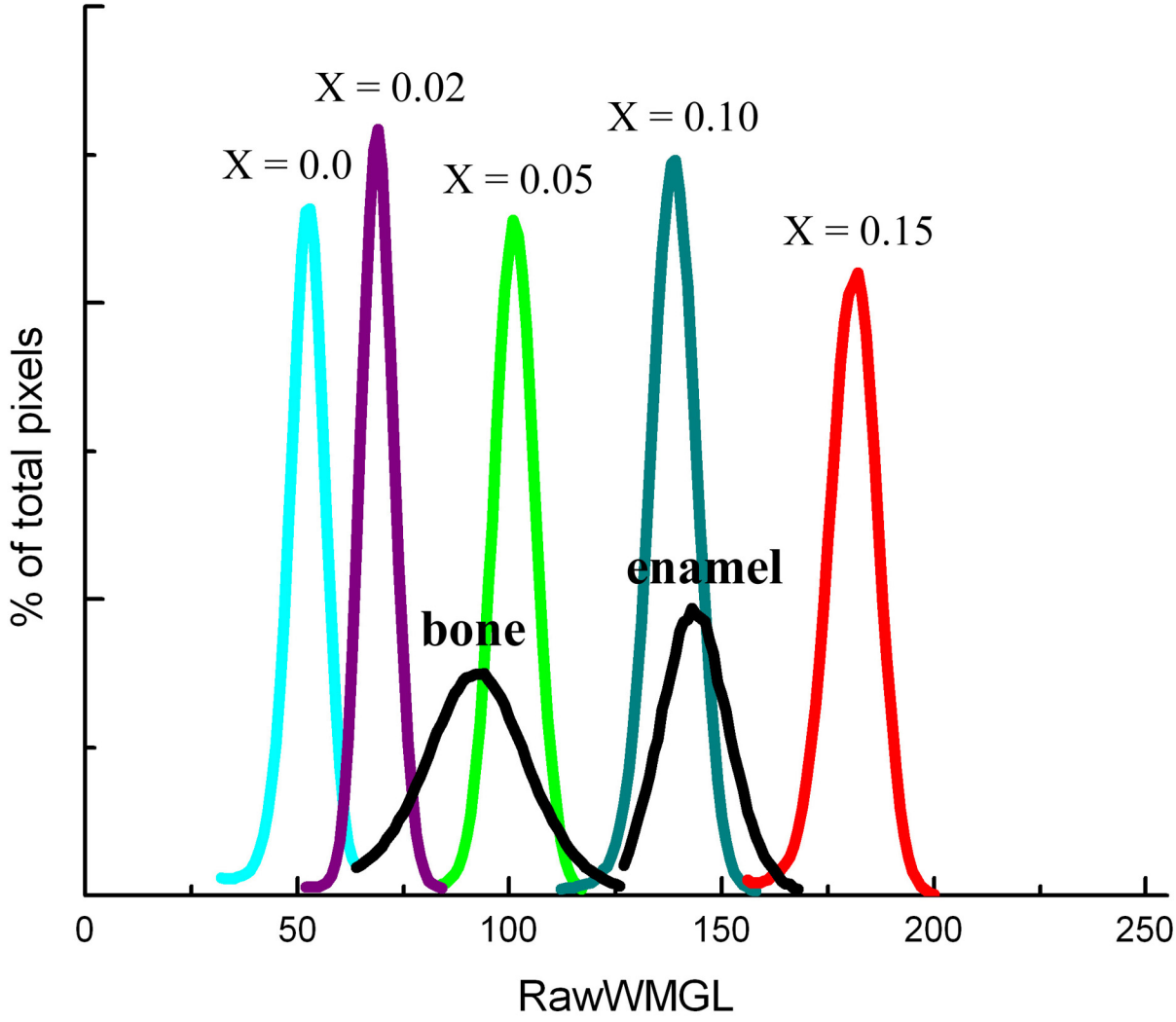

Figure 4.2: Raw gray-level histograms of the five most relevant glass standards along with those from bone and enamel. Glass standard x =0 and x = 0.15 were selected as they completely encompass the pertinent range of gray-levels.

(X = 0 and 0.15) were selected as the standards for this study as they completely encase the gray-level histogram of a large range of mineralized tissues. Alternatively, a narrow range of composition and WMGL is easily obtained by selecting other standards between the extremes giving better resolution contrast for samples with more uniform composition. These tunable glass standards are ideal qBSE standards as they are amorphous and have no long-range order which may induce channeling contrast and further these glasses possess long term stability (Islam et al., 2008), overcoming the main limitations of metallic standards.

The WMGL correlated to both Z and η for both reference standard materials and glass standards (Figure 4.3). However, the correlation for Z of the standard materials and the glasses did not correspond, displaying two distinctive, non-corresponding linear fits. For pure elements the WMGL relates directly to Z through Arnals formula (equation 3.19). However, it has been shown that for composite materials, especially those with significant amount of low atomic number elements, that Z_{comp} (equation 3.21) does not correctly predict WMGL values (Howell and Boyde, 1998). As mineralized tissues contain substantial amounts of low atomic number elements, quantification of mineral volume fraction with Z should not be used, yet this is still common practice in the literature (Roschger et al., 1995; Boyce et al., 1990; Skedros et al., 1993; Vajda et al., 1995; Bloebaum et al., 1997). The correlation of WMGL to η for both glass standards and reference materials matched with similar linear fits (Figure 4.3) indicating that η can be used for both pure elements and composite materials to correctly relate measured WMGL to composition.

Using the rule of mixtures (equation 4.2), η_{comp} for a range of mineralized tissues was calculated from known η_{HA} and η_{OM} to determine the equivalent value of MVF for the range of η_{comp}. Using a polynomial fit of the WMGL of the glass standards and their equivalent value of MVF, the final calibration curve was determined (Figure 4.4). The glass standards encompass the range of MVF from 20% to 180% allowing a quantification of even the high mineral content for example in enamel ($\approx$ 98% mineral). The X = 0.10 had an equivalent MVF around 96% and thus its gray-level histogram fell slightly lower than

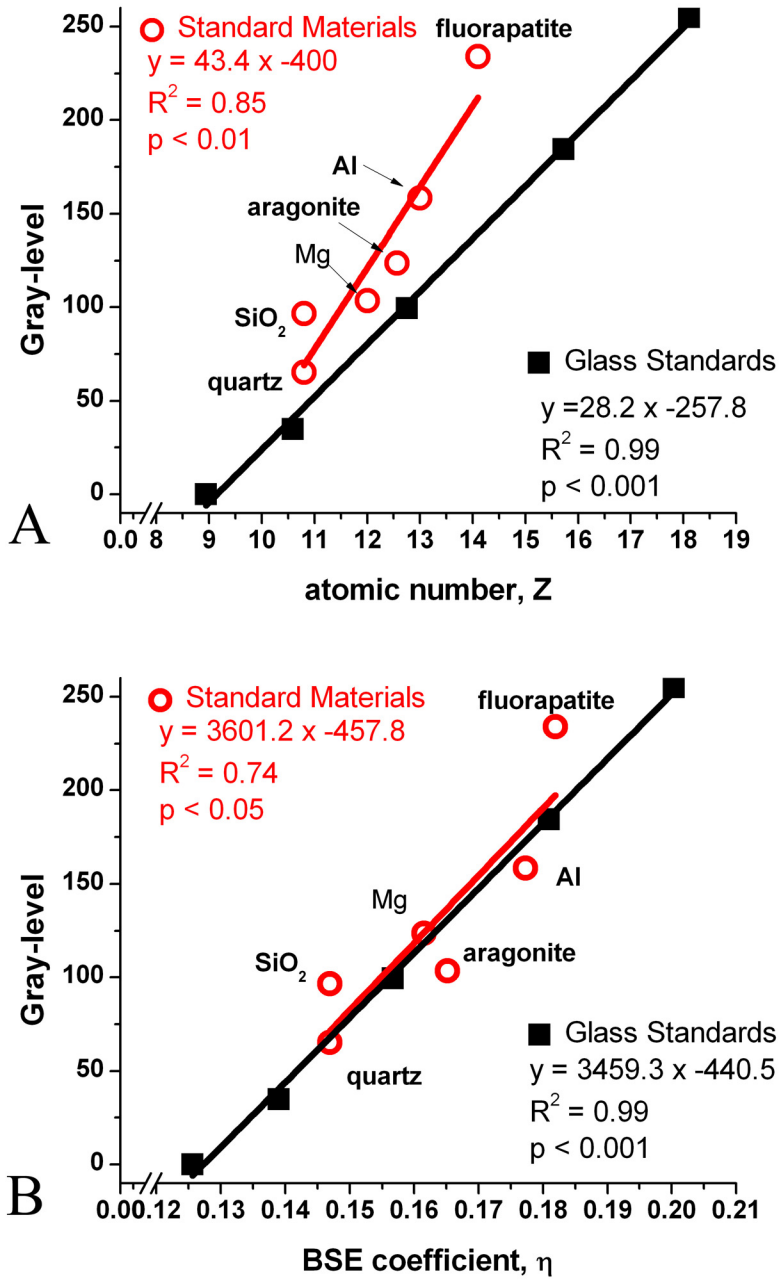

Figure 4.3: Gray-level of calibration materials plotted against (A) mean atomic number, Z and (B) qBSE coefficient, η. Theoretical calculations for mean Z of composite materials gives incorrect backscatter behavior as seen in A, thus calibration should be achieved using the qBSE coefficient, η.

the enamel histogram, making X = 0.10 an invalid high standard for studies that include enamel. However, the X = 0.10 standard can be used to studies only involving bone in order to achieve better image contact, and thus WMGL resolution.

4.3.2 qBSE images of mineralized tissues

Calibrated BSE images of the wide range of mineralized tissues analyzed in this study demonstrated both local and inter-sample variations in mineral content (Figure 4.5). The BSE images of the more highly mineralized samples (whale bulla, Figure 4.5F) appear distinctly brighter (e.g. higher values of gray-level) than samples with lower mineral content, such as the 2 week old mouse femur (Figure 4.5A). Additionally, local variations within one sample are evident as the with the immature lamb femur (Figure 4.5B) where older, more highly mineralized interstitial bone has a distinctly higher WMGL than the newly formed, poorly mineralized osteon.

The qBSE MVF of each mineralized tissue was determined from average of the measured WMGL value over all 20 indentation sites per sample. The mean qBSE MVF was significantly correlated with both microCT density ($p < 0.01$, $R^2 = 0.52$) and ash MVF ($p < 0.001$, R^2=0.74)(Figure 4.6), thus validating MVF values measured by qBSE. However these correlations are not perfect and the errors are likely result of drastically different length scales of these measurement techniques. The volume of material investigated differs drastically as qBSE considers a volume about 74 μm^3 (for 20 keV accelerating voltage) (Howell and Boyde, 2003) where as microCT and ash MVF measured values from an average volume of about 25 mm^3 in this study. The micro-scale variations captured by qBSE are averaged out by microCT and even more so by ash mineral volume fraction. The strong correlation of qBSE MVF to ash MVF ($R^2 = 0.74$, $p < 0.001$) validate qBSE measurement to MVF using tunable glass standards.

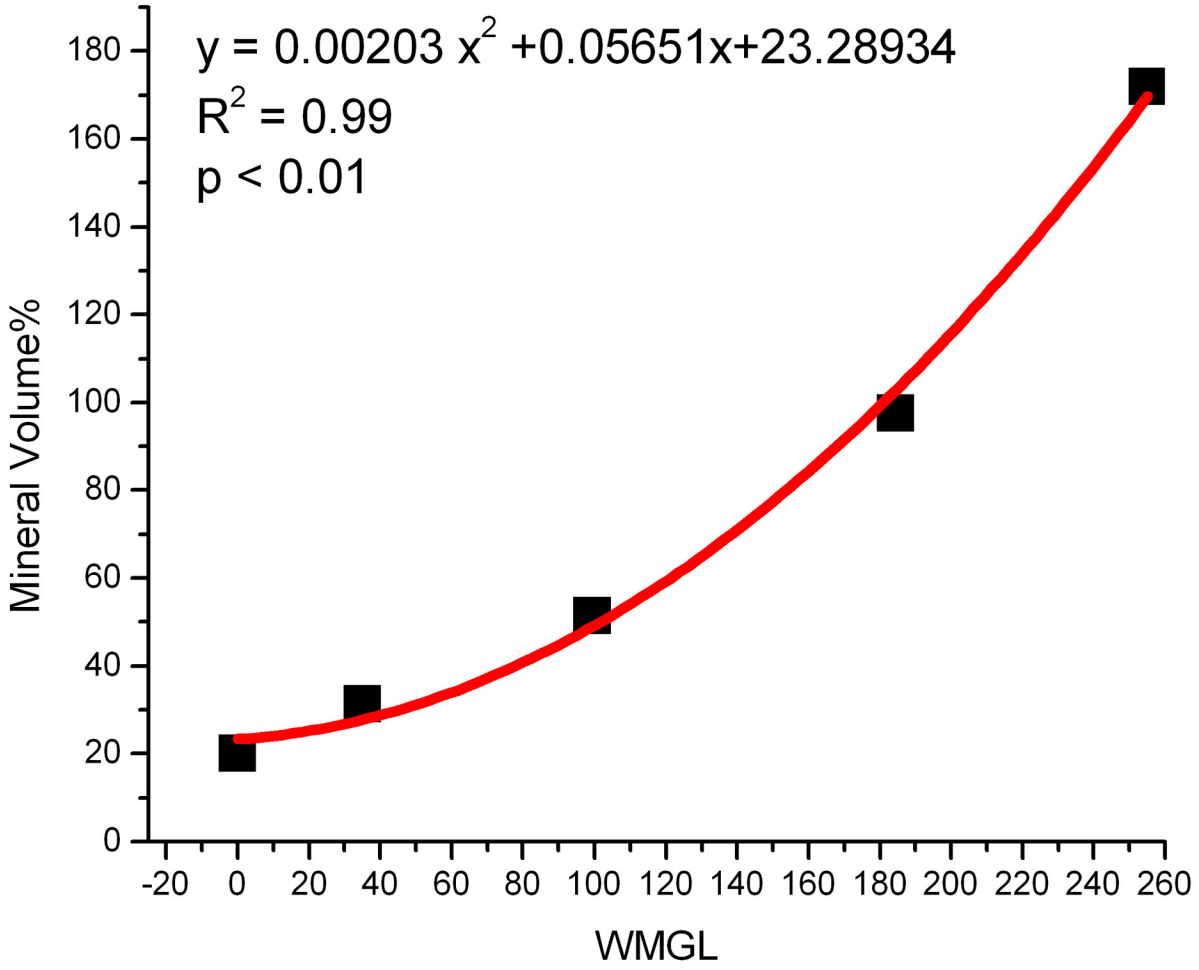

Figure 4.4: Calibration curve for conversion of gray-level values to mineral volume fraction.

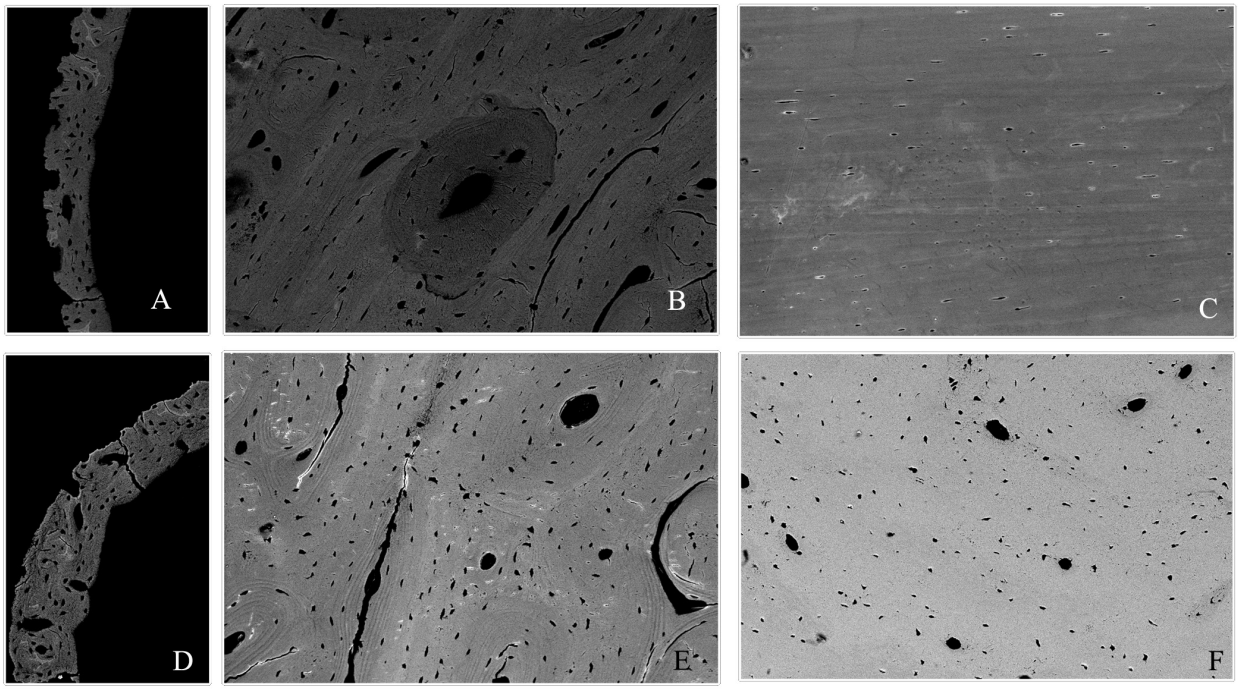

Figure 4.5: Calibrated qBSE images of representative samples displaying variation of mineral content within and between samples (increasing mineral content from A to F). All images were taken at 500X at 20 keV with a 15 mm working distance. A) mouse femur 2 weeks old, B) lamb femur, C) carp dermal bone D) mouse femur 20 weeks old, E) cow femur, F) whale bulla

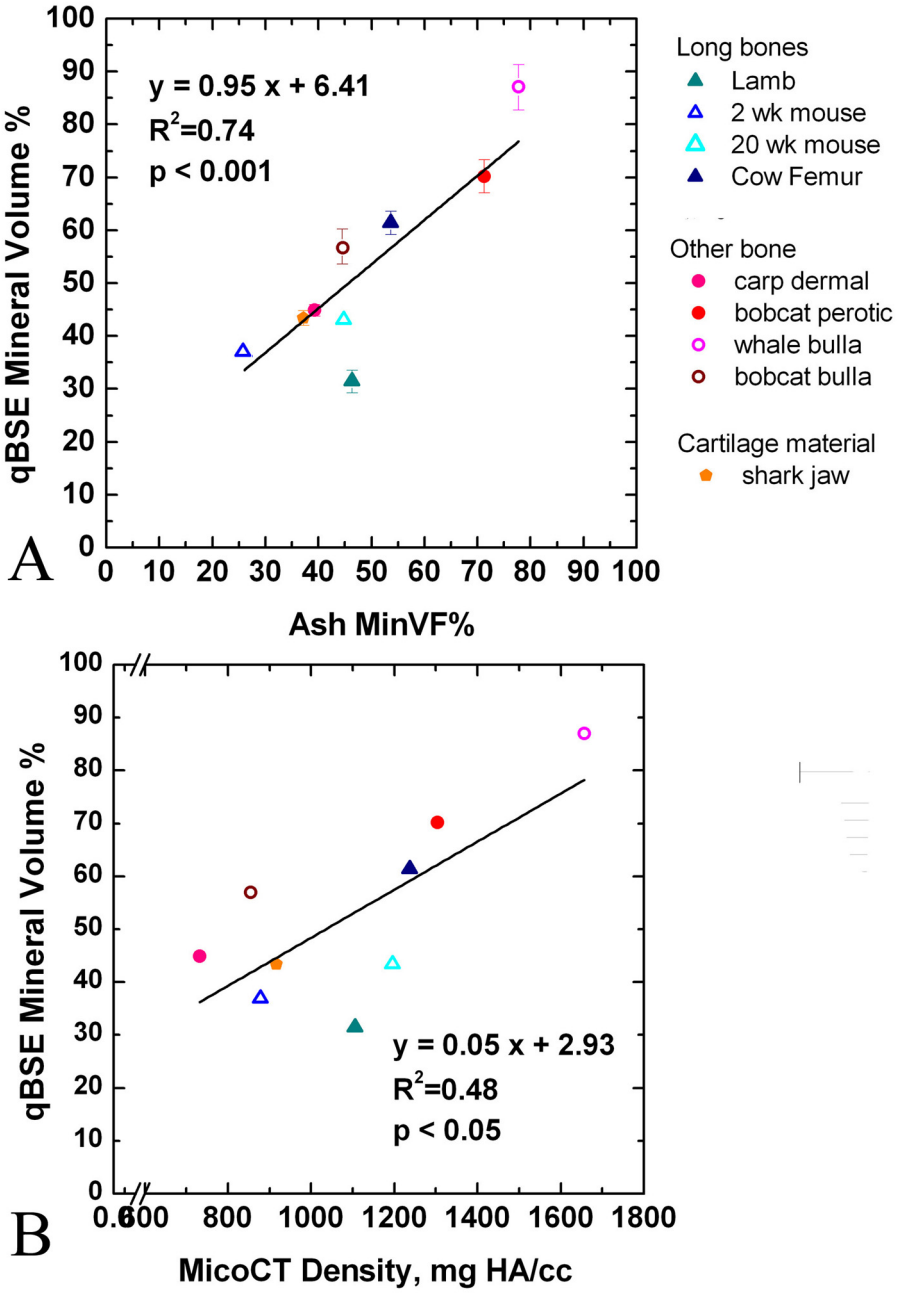

Figure 4.6: Mineral volume fraction measured by qBSE correlated to (A) ash mineral volume percent and (B) microCT density. Correlation is not perfect as qBSE considers a volume of material with radius of 1-5 μm where as μCT considers a volume of hundreds of mm^3.

4.3.3 Nanoindentation of mineralized tissues

Nanoindentation plane strain modulus (E') of the mineralized tissues ranged from carp dermal bone (E' = 15.50± 1.02 GPa) to whale bulla (E' = 74.73± 3.19 GPa). Site matched measurement revealed a positive correlation between qBSE MVF and nanomechanical properties. This unique strength of the qBSE imaging technique is demonstrated on a representative sample, the lamb femur (Figure 4.7). Indentation sites were grouped as either falling on osteonal or interstitial bone. The newly formed osteonal bone had lower values of both qBSE MVF (33.80 ± 0.54%) and indentation modulus (E'= 24.52 ± 1.60 GPa) than the older interstitial bone with MVF = 37.96 ± 0.73% and E'= 25.31 ± 2.02 GPa. The increase MVF of the interstitial bone resulting in higher mechanical properties has been previously observed in the literature (Rho et al., 1999b).

Increased modulus values with qBSE MVF were observed across the range of mineralized tissues (Figure 4.8). While this correlation of mineral content to mechanical properties has been previously observed (Currey, 1964; Oyen et al., 2008) it is not exact and the mechanical response at a single value of MVF can be highly variable. This inherent variability indicates that other factors, such as heterogeneities in composition of mineral or organic phase, mineral crystallinity, and microstructure connectivity must contribute to the nanomechanical response.

Further insight into this variability is possible by considering mineralized tissues as two phase composites of an organic and mineral phase which combine together to create the mechanical response (Oyen et al., 2008; Currey, 1964; Katz, 1971). In traditional composites theory these two phases can be combined as discrete particles in a matrix (Hashi-Shtrikman) (Hashin and Shtrickman, 1963) or as stiff fiber composites (Voigt-Reuss) (Chawla, 1987). In figure 4.8, all mineralized tissues data falls within the particle composites lines as previously observed (Oyen et al., 2008; Katz, 1971). The amount and connectivity of mineral phase and organic phase within the tissues contributes to where modulus values fall within the

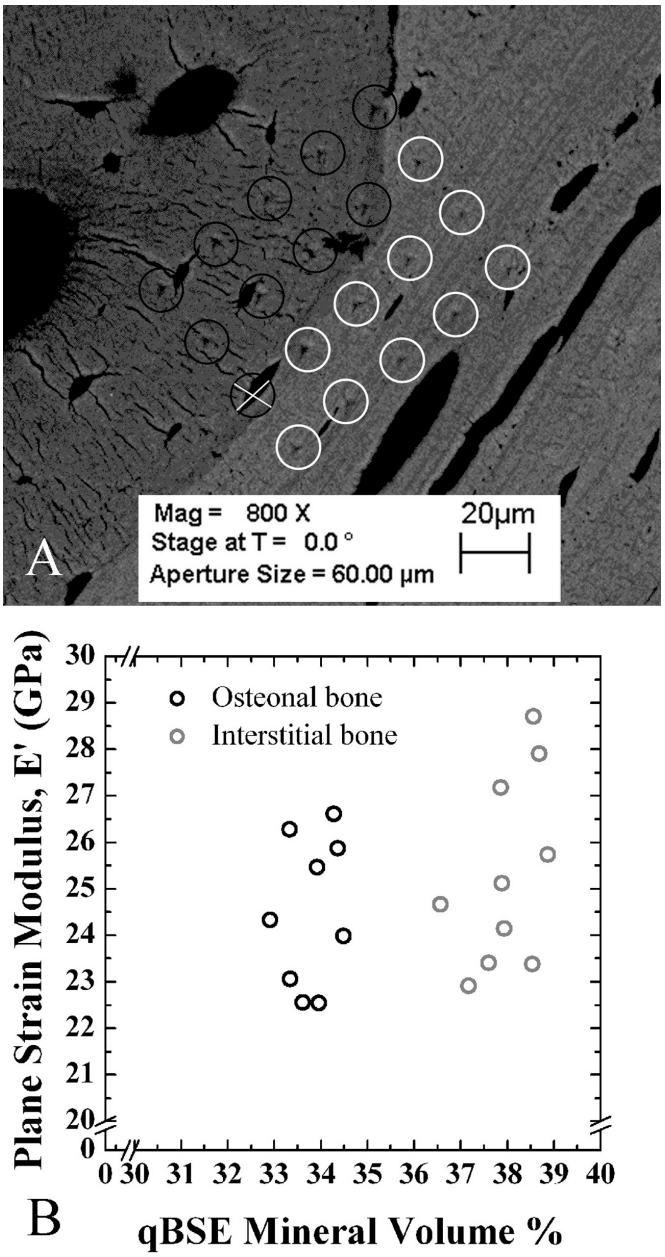

Figure 4.7: Site matched measurements on lamb femur of nanoindentation test and qBSE MVF measured within a corresponding circle of radius 6 μm. (A) qBSE image showing an indentation array of 5 x 4 indents with 20 μm spacing between test sites. Where test sites are categorized to interstitial bone (white circles) or osteonal bone (black circles). The test site with an X though the circle was removed from analysis as the indenter tip landed on an osteocyte lacuna. The corresponding nanoindentation modulus for each test site is plotted versus qBSE MVF in B.

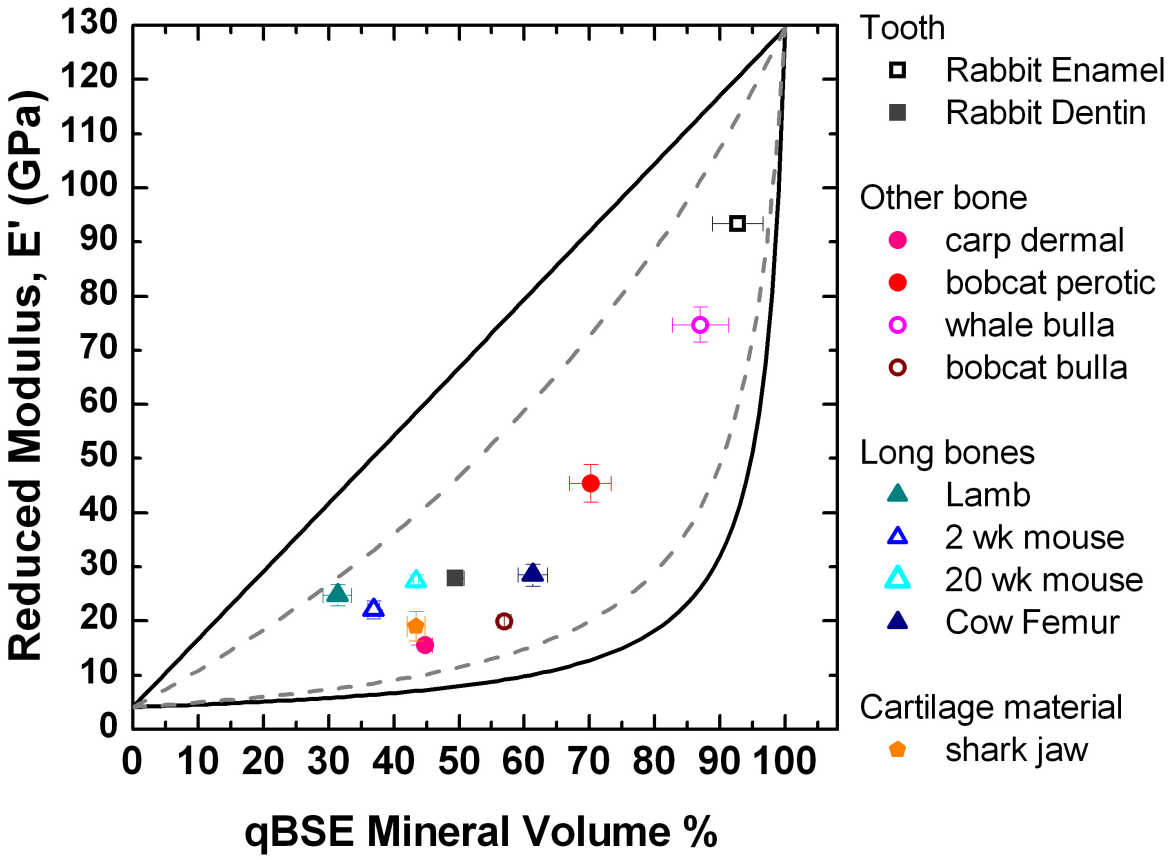

Figure 4.8: Elastic modulus (E') versus mineral volume fraction (V_f) of PMMA-embedded mineralized tissues. The solid lines are Voigt-Reuss bounds and dashed lines are the Hashin-Shtrikman bounds.

composite bounds. A more highly connected mineral phase will fall near the top of the composite range as a stiff matrix with soft particles and a less connected mineral phase would fall near the bottom of the composites range. In this study shark cartilage, carp dermal bone, and bobcat bulla were all near the lower composite bound suggesting less connected mineral phase. Further, the degree of alignment of the collagen fibers within these tissues plays and important role in the process of mineralization and the resulting alignment and connectivity of the mineral phase (Currey, 1964). During bone formation, the mineral initial forms within the collagen "hole" region having little effect on the stiffness. However, once the mineral increases to where overlap regions become mineralized, the elastic modulus along with the connectivity increases rapidly (Miller et al., 2007). For example carp dermal, the bullas, and perotic all have less highly organized collagen networks as a result fall on the lower composites bound of a hard particles in a matrix. Where as, the more highly organized network present in fully mature long bones (*i.e.,* lamb, cow, and mouse) fall from the middle to upper region of the composites bounds. The arrangement and connectivity of mineral and organic phases within a tissues contributes significantly to where its modulus value falls within the composite bounds.

4.3.4 FTIR

FTIR spectra are shown in figure 4.9 demonstrate significant variations in the composition between tissues though differing peak height and areas for carbonate, phosphate, and amide I and II peaks. Both bulla and perotic displayed significantly less amide I signal compared to long-bones reflecting the low collagen content of these samples. Additionally, shark jaw had a significantly increased signal for amide I and II peaks reflecting its primarily organic content. FTIR integrated peak areas for mineral/matrix and carbonate/phospate ratios are plotted versus microCT density and qBSE mineral volume fraction in figure 4.10. A positive increasing trend for mineral/matrix and carbonate/phospate ratios is evident with microCT density and qBSE MVF. However, correlation to qBSE WMGL was not significant

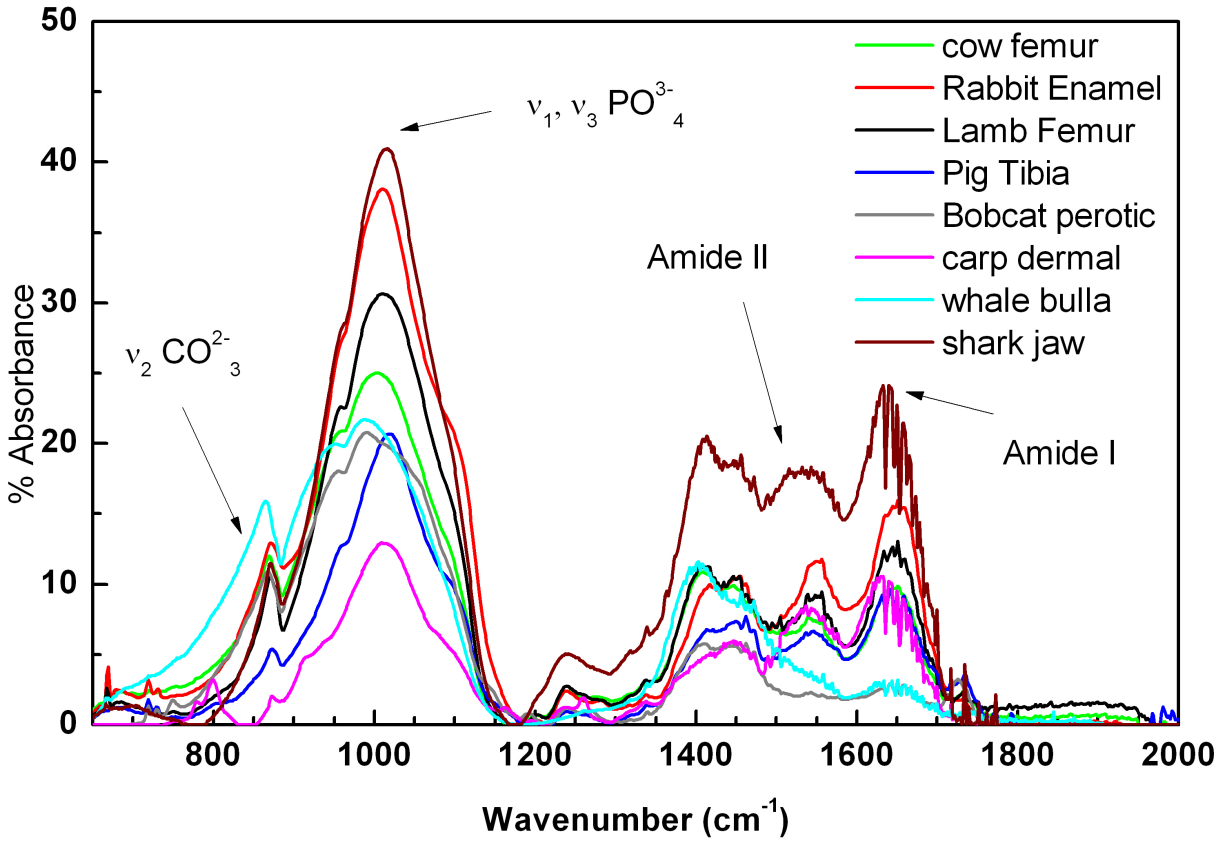

Figure 4.9: FTIR spectra of mineralized tissues.

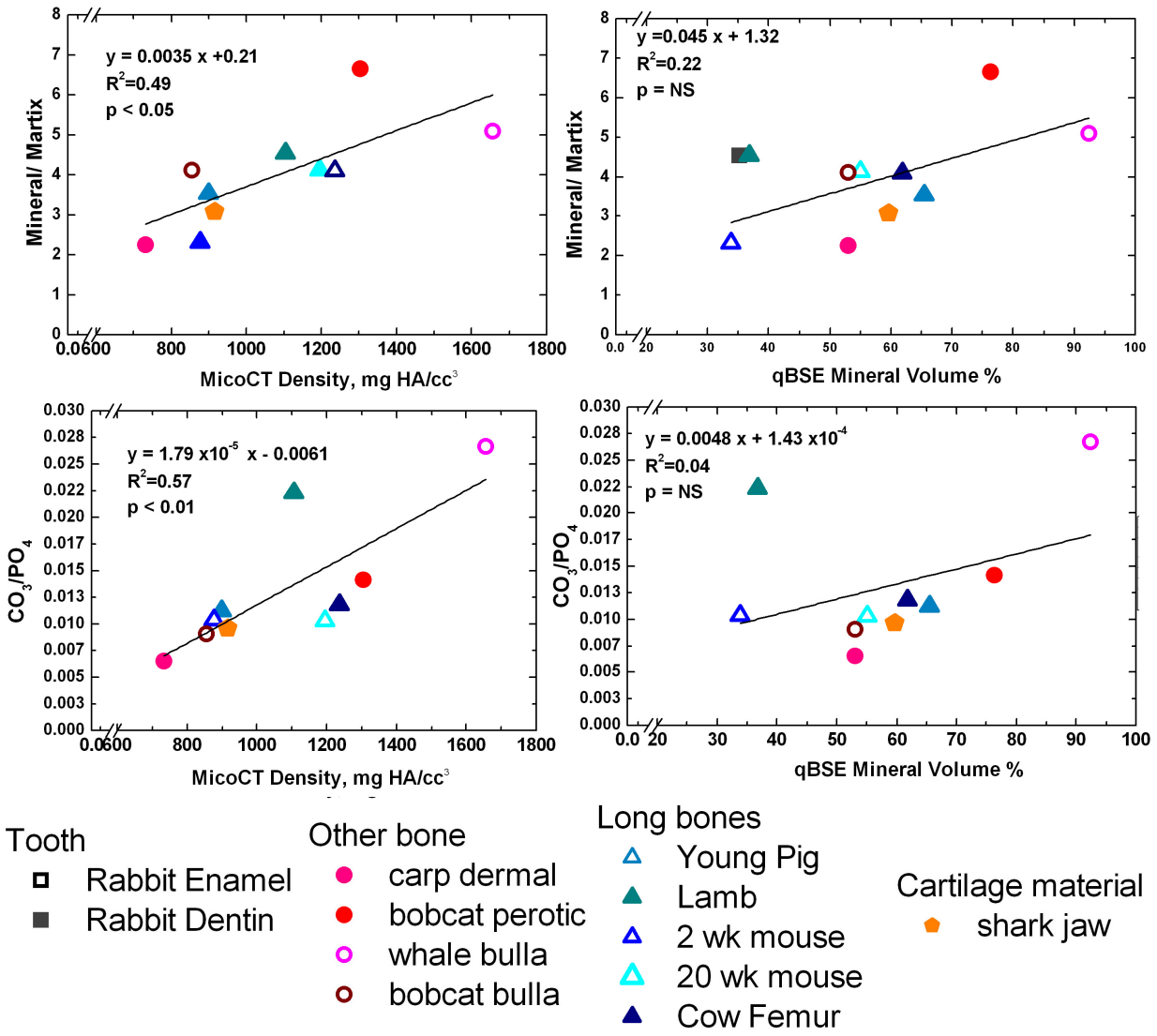

Figure 4.10: FTIR measurements of composition as compared to micro-CT density and qBSE mineral volume fraction. Linear correlation fit equations are listed in the upper left of each plot.

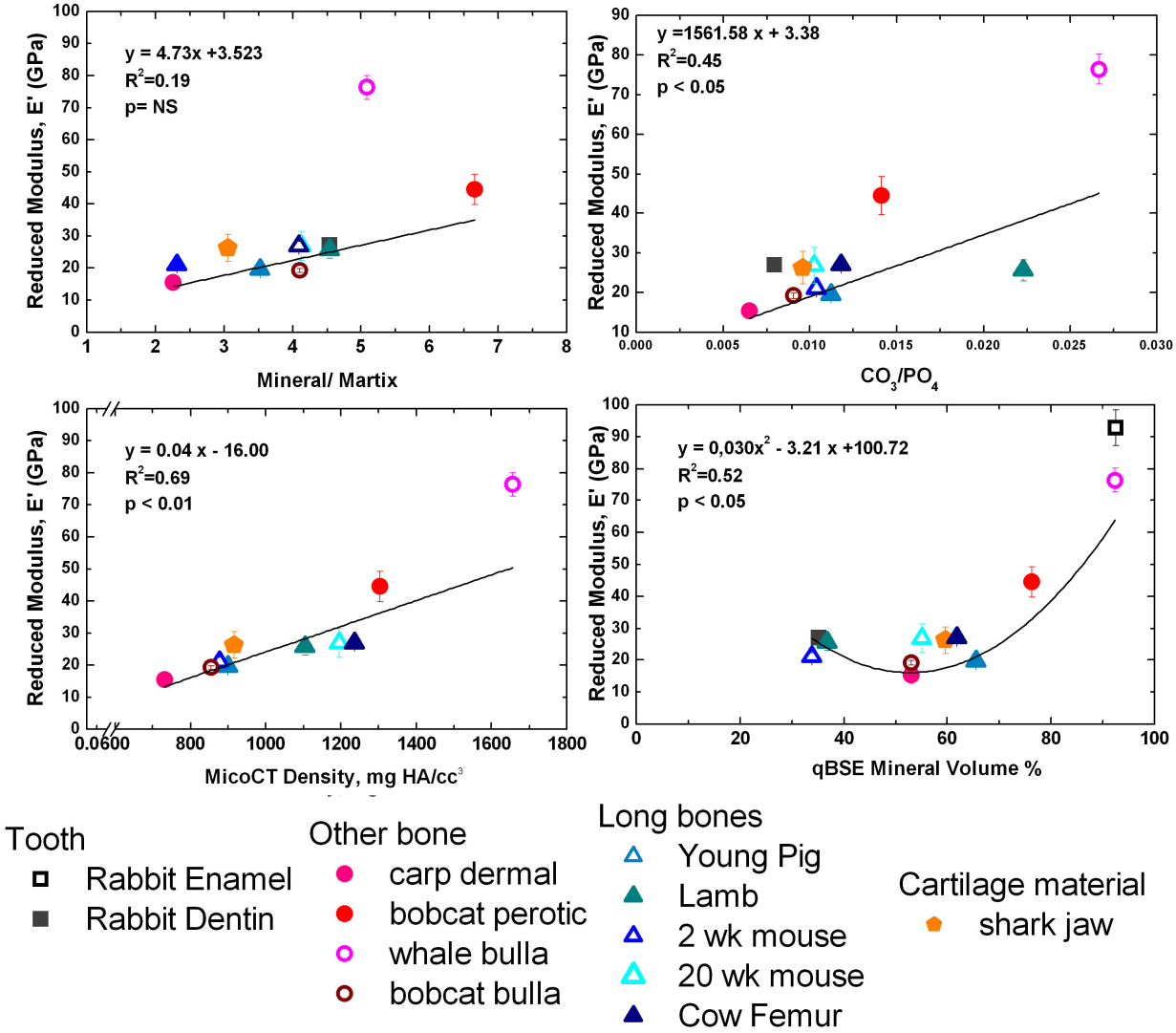

Figure 4.11: Relationship of measured modulus values to mineral content and composition parameters measured by FTIR, microCT, and qBSE. Correlation fit equations are listed in the upper left of each plot.

and thus may reflect the diffrences in the volume of material tested in these techniques. As qBSE considers a much smaller volume of material than FTIR testing (μm compared to mm) it is more sensitive to variations in the mineral contact. Both FTIR and microCT reflect average measurements over mm sized regions, these techniques are more likely to have higher correlation of properties to each other.

The dependance of modulus on the measurements of mineral content and composition parameters measured by FTIR, microCT, and qBSE is shown in figure 4.11. It was no surprise that modulus was, most significantly correlated to bSEM mineral volume fraction and microCT density measurements which directly relate the amount of mineral in each tissue. Both parameters measured by FTIR had an increasing trend relating them to the modulus values of the tissue. The carbonate/phospate ratio was significantly correlated to modulus values, suggesting a relationship between composition and mechanical properties. However, as previously discussed above better resolution, using techniques such as microRaman and mircroFTIR, are needed to further understand the relationship between mechanical properties and compositional changes.

4.4 Conclusions

I successfully developed tunable amorphous standards which are easily produced in any material science lab and overcome the numerous limitations of the commonly used metallic standards. The standards encompass a wide range of MVF from 20 to 180% allowing quantification of mineral in a wide range of mineralized tissue. The adjustable composition of these standards further allows selection of a narrower range of MVF for study of more uniform tissue in order to increase resolution. Measurements of qBSE MVF were validated by good correlation to measurements of microCT density and ash MVF. Finally, the utility of the qBSE technique was demonstrated through investigation of a wide range of mineralized tissues and their mechanical properties. Site-matched measurements of nanomechanical properties and qBSE MVF can provide insight into structure-property relationship of these

tissues during normal conditions, aging, diseased states, or even near implantable materials. These tunable glass standards significantly increase the availability of the qBSE imaging technique by providing cost effective and easily reproduced standards.

Exploration of the uniquely wide range of mineralized tissues permitted investigation of the dependence of mechanical properties on mineral composition and content. Through analysis using composites theory it is clear that the amount of mineral and mineral connectively play significant roles in mechanical properties. As the amount of mineral reaches a connectivity threshold the modulus increases very sharply as the mineral matrix forms a more fully connected networks. Further, variation is chemical composition, observed with FTIR, might also play a role is mechanical properties but are secondary as these measurements are also linked to the amount of mineral. Carefully controlled future studies with length scale matched measurements are needed to further explore the role of composition.

Chapter 5

Nanomechanical Properties of Modern and Fossil Bone

Nanoindentation is a relatively nondestructive tool that can be used to assess the mechanical properties and functional significance of a wide range of materials including archeological and paleontological bones and teeth. Nanoindentation can determine mechanical properties with less than one-micron resolution, allowing for investigation of individual microstructural features (e.g., bone lamellae $\approx 5\mu m$) (Rho and Pharr, 1999). Nanoindentation has previously been used to provide insight into the functional significance of a wide range of modern materials including: tooth enamel (Cuy et al., 2002; Guidoni et al., 1998; He and Swain, 2008), fruit seeds (Lucas et al., 2006), nacre (Barthelat et al., 2006), insect cuticle (Barbakadze et al., 2006), gecko seta (Huber et al., 2008), fish scales (Bruet et al., 2008), and bone (Bushby et al., 2004; Oyen, 2006b; Rapoff et al., 2008; Rho et al., 1997). However, no nanoindentation testing has been performed on fossilized tissues. Nanomechanical behavior of fossilized tissues such as bone and teeth may provide information on tissue structure and function of ancient vertebrates. Further, nanoindentation provides an innovative approach to investigate the complex nature of diagenesis at the tissue-level.

Bone is a living tissue that undergoes growth and remodeling through biomineralization during its lifetime. Following an organisms death, diagenesis occurs in bone at scales ranging from the nanometer to the macroscopic, and includes postmortem physical, chemical, and biological modifications. An understanding of specimen preservation and tissue-level diagenetic alteration is vital to paleontologists and archaeologists. For instance, studies of

chemical signals provide information on the paleodiet, physiology, and behavior of ancient vertebrates as well as paleoclimate (Ambrose et al., 1997; Cerling and Sharp, 1996; Croft and Anderson, 2008; Koch, 1998; Lee-Thorp and Sponheimer, 2003; Lubell et al., 1994; Price et al., 2002; Sponheimer et al., 2006; Wang and Cerling, 1994; Zazzo et al., 2002). These studies rely on the assumption that diagenesis has occurred but does not interfere with the desired signal (e.g., isotopic signature). While poorly understood, post-mortem alteration is known to occur over a wide range of scales and clearly affects all components of bone, including mineral, collagen, and the porous water phase.

Diagenetic alterations can include collagen loss, histological alterations, changes in porosity, partial or complete dissolution of minerals, recrystallization, and uptake of trace elements (Badone and Farquhar, 1982; Bell et al., 1996; Berna et al., 2004; Elliott and Grime, 1993; Favre-Quattropani et al., 1999; Hedges and Millard, 1995; Kohn et al., 1999; Lee-Thorp, 2002; Nielsen-Marsh and Hedges, 2000; Reiche et al., 2003; Trueman et al., 2004; Turner-Walker and Jans, 2008). Importantly, an increase in crystallinity with geologic time has been observed through peak broadening measured by X-ray diffraction (XRD) and increased infrared splitting factor (IRSF) measured by infrared (IR) spectroscopy (Bartsiokas and Middleton, 1992; Sillen and Parkington, 1996; Weiner and Bar-Yosef, 1990). The increase in crystallinity is often correlated with the loss of the organic phase (Person et al., 1995; Sillen and Parkington, 1996), demonstrating the dynamic link between the various constituents of bone. However, it is unclear whether increased crystallinity implies alteration of isotope compositions, suggesting that crystallinity may be a poor indicator of chemical alteration in some instances (Munro et al., 2008). Further, these techniques observe only the whole bone properties while small-scale variations, which can be observed by nanoindentation, are averaged out and potentially missed.

Bone is a composite material and its mechanical behavior is dependent upon the relative volume fractions of mineral, organic, and pore space (filled with water in physiological conditions) (Katz, 1971; Oyen et al., 2008). During a vertebrates life, increased

bio-mineralization of bones and dental tissues occurs through increasing crystal size (e.g., in enamel) or infilling of available pore space with additional mineral, which corresponds to an increase in mechanical properties measured by nanoindentation (Ferguson et al., 2005, 2003a). A similar phenomenon is likely to occur postmortem during diagenesis where ample pore space, at nanometer and micrometer scales, exists to permit additional geo-mineralization. Generally, there is a positive correlation between increased mineral volume fraction and the elastic modulus, or stiffness, in mineralized tissues (Katz, 1971; Oyen et al., 2008). The microstructure, mineral phase, and organic phase of bone are all affected by diagenesis and contribute to the mechanical properties of the tissue.

Nanoindentation combined with complimentary techniques can be used to investigate the functional significance of a wide range of archeological and paleontological materials even after fossilization. For this study we employed nanoindentation, XRD, density measurements, and scanning electron microscopy (SEM) to investigate the nanomechanical, histological, density, and crystallographic properties of fossilized and modern bone samples with the goal of providing insight into the complex processes of diagenesis.

5.1 Study Objectives

While the organic phase is primarily removed during diagenesis, the mineral phase is altered by changes in crystallinity and infilling of foreign minerals. The process of diagenesis creates a heterogeneous geo-mineralized material with large variations in crystallinity and composition. **The goal of this study is to investigate alterations to the mineral phase of bone caused by diagenesis as a tool to understand the structure-property relationships of crystallinity, composition, and nanomechanical properties.** Nanoindentation of fossilized bone has never before been investigated, and further provides a unique models system that encompasses wide ranges of composition and crystallinity not found in *in vivo*. The following sub-goals have been defined to :

(a) Use nanoindentation to investigate the nanomechanical response of fossilized bone of various ages ranging from modern to 50 million years old.

(b) Investigate changes in crystallinity and its relationship to nanomechanical properties though x-ray diffraction peak broadening.

(c) Explore how variations in composition measured using XRD and FTIR contribute to the nanoindentation response.

5.2 Materials and Methods

5.2.1 Samples, localities, and ages

Mammalian long bones (all from ungulate taxa, with exception of a single carnivore - the nimravid specimen; Table 5.1) ranging in age from modern to early Eocene ($\approx$ 50 Ma) were investigated for mineral, mechanical, and histological variations utilizing nanoindentation, XRD, density measurements, and scanning electron microscopy (SEM) (Table 5.1). Samples were tested at or as near as possible to mid-diaphysis of each long bone sampling only cortical bone. Three to four bone fragments were sampled from each of four different localities in the Western Interior (Wyoming, Colorado, and Nebraska) (Table 5.2). Fossils were provided by the University of Colorado Museum of Natural History (UCM), where detailed locality information is on file. The specimens' approximate ages are listed in Table 5.1, and are correlated to epoch as well as North American Land Mammal 'Age' (NALMA).

The 15 fossilized bone samples were compared to three modern long bone samples (Table 5.1). One modern (Artiodactyla, indet.) femur was collected by VLF on the surface near Golden, Colorado ($\approx$ 3 ya). The other two modern samples (Bos taurus (cow) and Ovis aries (sheep) femurs) were frozen fresh, and later dehydrated in a series of ethanol solutions.

Table 5.1: Basic fossil and modern bone sample information including and nanoindentation data. Approximate age of each sample is listed as MD=modern, P=Pleistocene, M=Miocene, O=Oligocene, E=Eocene. Non HA minerals found in XRD patterns are indicated by # = quartz, * = calcite. Bone type listed with: LBF=long bone fragment, MT=metatarsal, H=humerus, F=femur. Parametric data from values plotted in figure 3 (mean (SD, n=)) for plane strain modulus, E' (GPa), determined by nanoindentation in cortical bone tested in both the longitudinal (L) and transverse (T) directions. Longitudinal vs transverse ratio (L/T) is reported for each sample. P-values, or significance (sig), are listed from a Students t-test that was used to determine statistical significance of higher modulus in L vs T testing directions within each sample; NS = not significant (also when T>L), S = significant (<0.01), HS = highly significant (p<0.001).

UCM #	Age ~(Ma)	Species	Type	Location	HI	E' (GPa) Long	E' (GPa) Trans	L/T ratio	Sig
	MD ~0	*Bos Taurus*	F	Fresh	5	24.27(3.14, 72)	20.41 (2.57, 36)	1.19	HS
	MD ~0	*Ovis aries*	F	Fresh	5	25.71 (2.45, 70)	19.96 (1.04, 36)	1.29	HS
	MD ~0	Artiodactyl	F	On surface, CO	5	23.87 (2.04, 70)	21.80 (1.66, 36)	1.10	HS
101385	P ~0.01	Mammal indet.	LBF	Little Box Elder	4	33.05 (2.31, 69)	30.56 (1.34, 36)	1.08	HS
101387	P ~0.01	Mammal indet.	LBF	Little Box Elder	2	34.73 (4.35, 69)	34.35 (4.81, 33)	1.01	NS
101389	P ~0.01	*Ovis*	LBF	Little Box Elder	2	26.87 (2.48, 69)	26.76 (4.81, 33)	1.00	NS
100371	P ~0.01	*Odocoileus*	LBF	Little Box Elder	4	41.41 (4.09, 67)	15.38 (2.66, 35)	2.70	HS
36609#	M ~15	Ungulate indet.	LBF	Verdigre Quarry	2	96.78 (5.95, 65)	85.52 (3.12, 36)	1.13	HS
36607	M ~15	*Merychippus*	R 4 MT	Verdigre Quarry	4	80.24 (9.72, 66)	65.53 (2.60, 36)	1.23	HS
36611*	M ~15	*Merychippus*	L 4 MT	Verdigre Quarry	2	93.77 (5.41, 65)	91.23 (3.30, 31)	1.03	HS
100373*	M ~15	*Merychippus*	R 3 MT	Verdigre Quarry	5	86.30 (5.42, 72)	71.51 (4.36, 36)	1.21	HS
101383	O ~33.3	Nimravidae	Dist H	Hirsh small jaw	2	68.55 (6.52, 66)	74.08 (2.20, 35)	0.93	NS
101382*	O ~33.3	Ungulate indet.	LBF	Hirsh small jaw	3	57.37 (5.29, 72)	54.19 (3.72, 31)	1.06	S
101384#	O ~33.3	Ungulate indet.	LBF	Hirsh small jaw	0	80.78 (7.80, 62)	72.92 (3.72, 31)	1.11	HS
69498	E ~50	Mammal indet.	LBF	Green River Basin	1	95.20 (4.33, 61)	85.20 (3.00, 36)	1.12	HS
101214	E ~50	Ungulate indet.	LBF	Green River Basin	2	92.30 (9.37, 62)	75.07 (7.04, 36)	1.23	HS
101213	E ~50	*Hyrachyus*	MT	Green River Basin	4	91.81 (5.31, 62)	98.49 (3.73, 36)	0.93	NS
100372#	E ~50	*Hyrachyus*	MTI	Green River Basin	4	97.77 (3.42, 63)	81.39 (7.67, 31)	1.20	HS

Table 5.2: Basic locality information for the fossilized samples including: locality name, formation, UCM number, country and state, and approximate age of the samples for each locality.

Locality	**Formation**	**UMC #**	**County, State**	**Age**
Little Box Elder Cave		77021	Converse County, WY	Rancholabrean ≈ 10 ka
Verdigre Quarry	Valentine Formation	84016	Knox County, NE	Miocene (Barstovian or Clarendonian ≈15 Ma)
Hirsch Small Jaw	Brule Formation, White River Group	77271	Sioux County, NE	early Oligocene (late Orellan ≈ 33 Ma)
Hickey Mountain Limestone	Twin Buttes Formation, Green River Basin	93026, 94028, 94129	Uinta County, WY	Eocene (Bridgerian ≈ 50 Ma)

5.2.2 Sample preparation

Each sample was embedded in poly methylmethacrylate (PMMA) under vacuum to stabilize the pore spaces within bony or fossilized material. The low modulus of PMMA contributes minimally to the measured mechanical properties of the samples (Oyen et al., 2005). Bones were sectioned as close as possible to the assumed mid-diaphysis based upon gross morphology, using a low-speed diamond wafering saw (Isomet: Buehler, Lake Bluff, IL). Surfaces were prepared for testing in both the transverse and longitudinal directions on each sample; the orientation was confirmed with microscopic analysis of structural features. The transverse direction lies perpendicular to most Haversian canals and the long axis of the bone, whereas the longitudinal direction lies parallel to the Haversian canals (Petrtyl et al., 1996). Each surface was ground with a series of silicon carbide paper (300, 400, 600, 1200 grit) and then polished with successfully finer diamond suspension paste (Buehler) of particle size 6, 3, and 0.25 μm. The specimens were ultrasonically cleaned with deionized water to remove debris between each step. As a final preparation, samples were air dried after ultrasonic cleaning for a minimum of 72 hours prior to analysis.

5.2.3 Bone Histology

A combination of scanning election microscopy (SEM) and reflective optical microscopy were used to assess the general histological preservation of each bone. Hedges and Millard (1995) used a histological index (HI) scale from zero to five to describe the state of histological preservation of archaeological bone. A zero indicates that no distinct structural features are visible other than Haversian canals, whereas a five indicates perfect preservation in which the bone appears indistinguishable from fresh bone (Hedges and Millard, 1995). Using a blind test, two independent observers assigned a HI for at least three optical images per specimen. The values for all of the images of each sample were averaged and rounded to obtain a single HI value for each sample.

5.2.4 Nanoindentation

Nanoindentation testing was used to investigate variations in nanomechanical properties of bone caused by diagenesis. In a standard nanoindentation test, a small diamond tip ($\approx$100 nm) is pressed into the material of interest while measuring the load and displacement; from unloading data the mechanical properties of each testing site are extracted (Oliver and Pharr, 2004). Depth-sensing nanoindentation tests (NANO Indenter XP, MTS Systems Co., Oak Ridge, TN) were performed on the PMMA-embedded bone samples with a three-sided pyramidal Berkovich indenter tip. Bones were tested under load control with a constant indentation strain rate (0.05 s^{-1}) to a maximum depth limit of 1500 nm, where the current indenter load was held for 120 seconds prior to unloading. This extended creep hold minimizes the creep contribution (Feng and Ngan, 2002) from the unloading curve allowing measurements of a purely elastic response. A maximum depth test was used in order to maintain constant contact volume as samples varied significantly in modulus. Using a slightly modified version of the Oliver-Pharr method (Oliver and Pharr, 1992) the stiffness is calculated as the slope of a line drawn tangent to the first 50% of the unloading curve.

Following section 3.2.2 the contact hardness (H) and plane strain modulus (referred to as modulus or E) were calculated from the stiffness and max load on each sample.

On each sample, two nanoindentation arrays (at least 6 x 6 indents with 20 μm spacing between indent sites) were placed in the longitudinal direction and were located over distinct osteons. The first indent in each square array was positioned in a Haversian canal such that the array sampled one quarter of the circular osteonal region to cover both osteonal (O) and interstitial (I) bone (Figure 5.1A). In order to investigate tissue anisotropy, the variation of properties in different testing directions, indent arrays placed in the transverse direction (4 x 9 arrays, 20 μm spacing) were located in osteonal bone. Measurements falling on cracks, flaws, edges or other voids were discarded from the primary analysis.

5.2.5 X-ray Diffraction

In order to investigate the crystallinity and composition of modern and fossilized bone, x-ray diffraction (XRD) was performed on all samples. Cortical bone samples were mechanically crushed in a shatter box for three minutes and then hand-ground with a mortar and pestle to a very fine powder. XRD spectra were obtained for each sample using Cu Kα radiation with an accelerating voltage of 40 KeV. Data were collected over a 2θ range of $20-38°$ with a 0.02° step size. All spectra were checked for the presence of contaminate minerals. In order to investigate changes in crystallinity, the full width at half maximum (FWHM) of the (002) reflection was measured for each sample and defined as the crystallinity index (CI). The CI has been commonly used as a measurement of crystallinity in fossilized bone samples and reflects changes in crystal size, number of defects, and overall crystal perfection (Hedges and Millard, 1995; Hubert et al., 1996; Sillen, 1989).

5.2.6 Density Measurements

Density of each sample was measured using Archimedes principle on a digital scale (Denver Instruments) using a method modified after (Keenan et al., 1997). Small samples

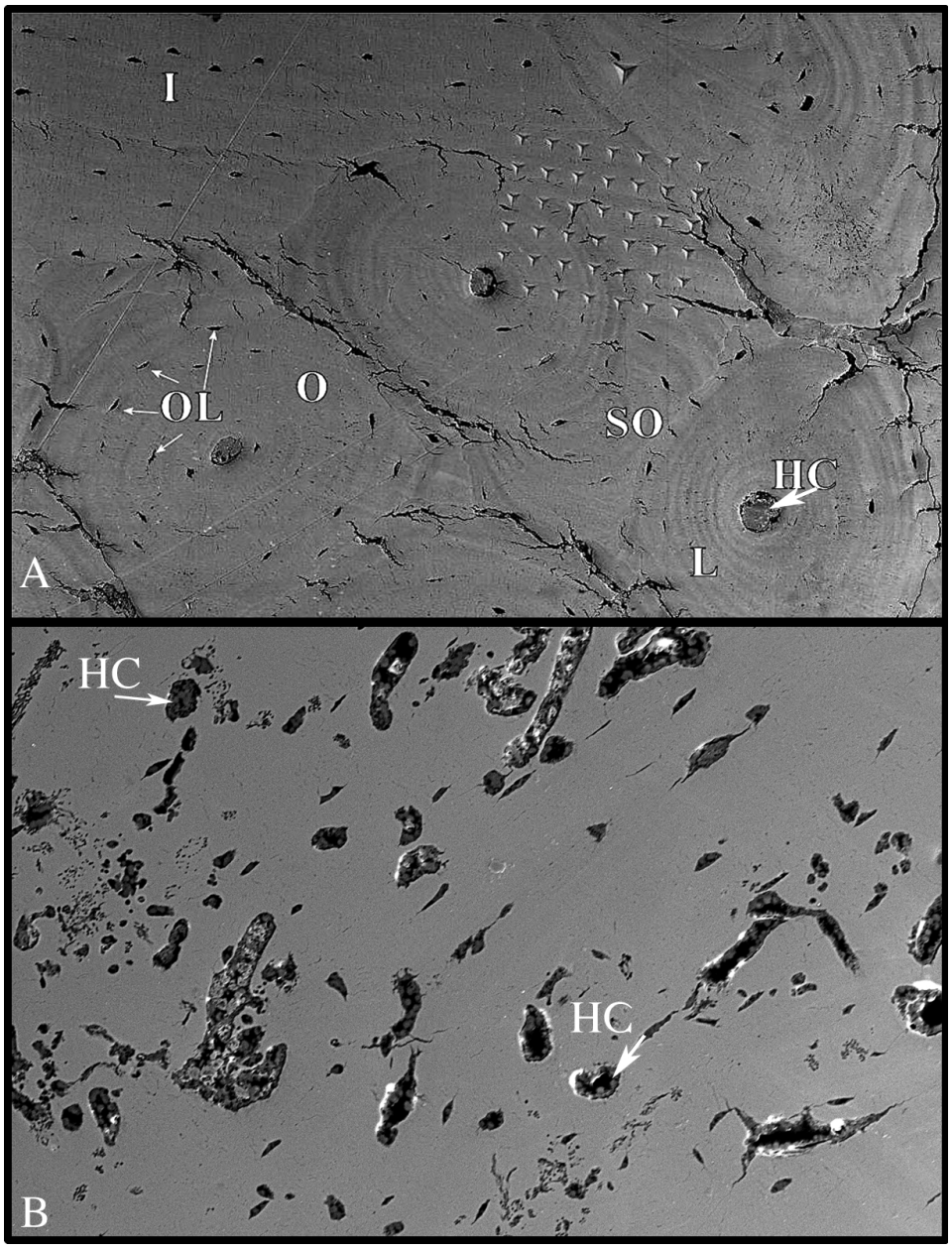

Figure 5.1: SEM-BSE images (15 KeV) of a histological well preserved sample (A) and a poorly preserved sample (B). Image A has a field width of 650 μm and shows the longitudinal surface of the UCM 100373 (≈15 Ma) sample with 6x6 indent array over secondary osteonal (SO) bone showing distinct regions of osteonal (O) and interstitial (I) bone. The Haversian canal (HC) and osteocyte lacuna (OL) are clearly visible in this histologically well-preserved sample. Image B has a field width of 350 μm and shows the poorly histologically preserved sample UCM 101384 (33.3 Ma); potential Haversian canal (HC) are the only visible bone structures remaining

of each bone were taken near the to nanoindentation section with caution to only include cortical bone. Samples were dried for 72 hours under vacuum before measuring the dry weight (DW). Samples were then submerged in deionized water for 1 hour under vacuum and the wet weight (WW) was recorded with sample suspended and entirely submerged under water. Both WW and DW were measured three times with low variability between measurements. The density (ρ) was determined by equation 5.2 and ρ_{water} was assumed to be 1 g/cm^3.

$$\rho = \frac{DW}{DW - WW} * \rho_{water} \tag{5.1}$$

5.3 Results

5.3.1 Bone Histology

Observation with SEM and reflective optical microscopy revealed a wide range of preservation conditions of the fossilized samples. The histological index (HI) ranged from poorly preserved (0) to excellent preservation (5), with no clear trend with geologic age of the specimen or other measured properties (i.e., CI or E', Table 5.1). In histologically well-preserved samples (HI = 5, 4), such as UCM number 100373 (Miocene), distinct osteons (O), interstitial bone (I), and osteocyte lacuna (OL) were clearly visible (Figure 5.1A). In poorly preserved samples (HI = 0), such as UCM number 101384 (Oligocene), Haversian canals (HC) were the only visible structural feature (Figure 5.1B). Some samples, even well preserved samples, had a scattering of small holes or destructive foci (DF) that have been-described by others as the probable result of bacterial alteration (Bell et al., 1996; Hackett, 1981; Turner-Walker and Jans, 2008).

5.3.2 Nanoindentation

In the modern specimens, the modulus (or stiffness) in the transverse direction was 9-22% lower than that measured in the longitudinal direction (Table 5.1), which compares

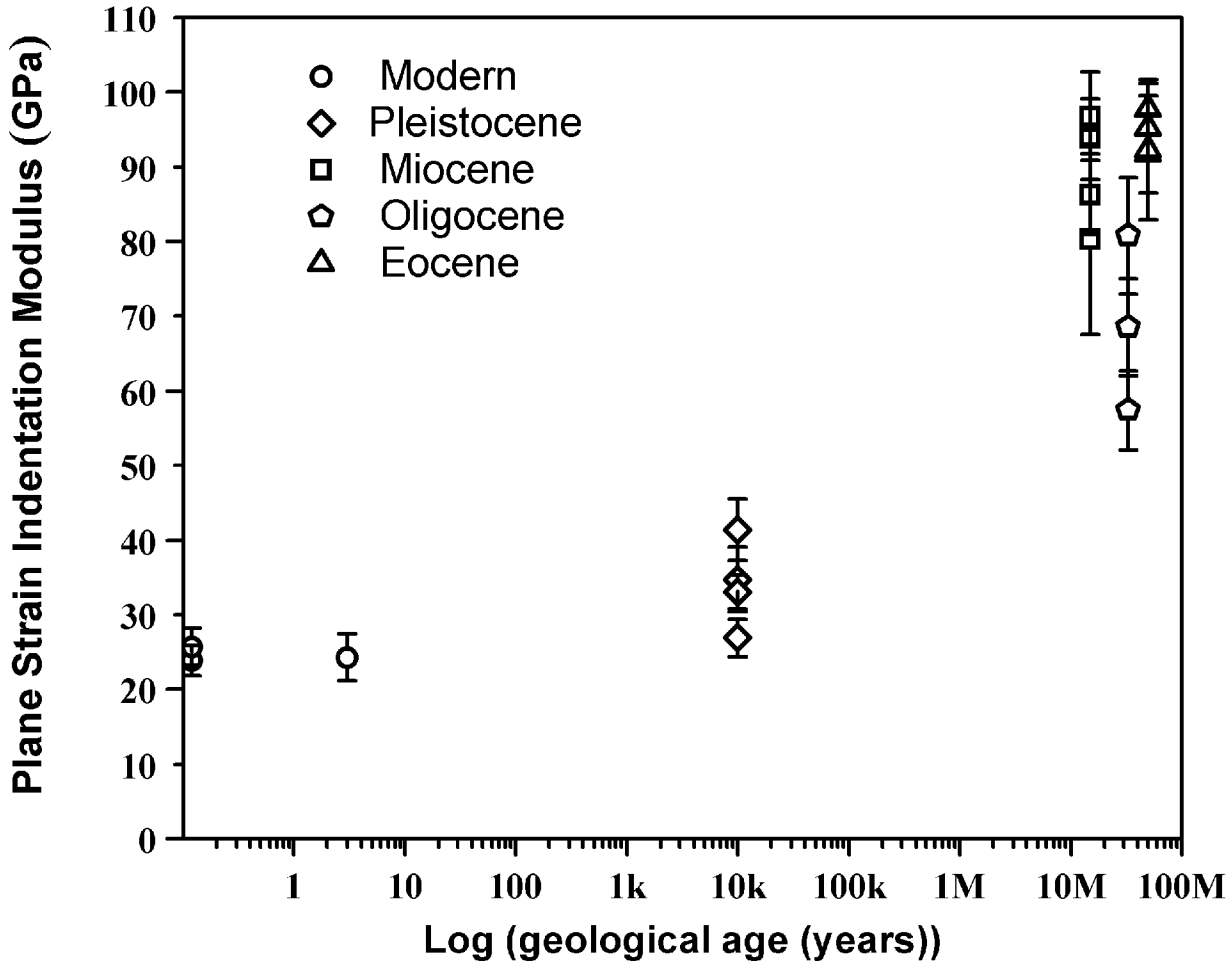

Figure 5.2: Longitudinal modulus values vs. the log of geological age. Data plotted as mean value of each sample ± STD. There is a clear increase of modulus values with the geologic age of the sample.

well with previously measured anisotropy of ≈25% in human and horse (Fan et al., 2002; Rho et al., 2001). Anisotropy was shown in two-thirds (67%) of fossilized samples by significantly higher modulus values in the longitudinal direction than those in the transverse direction (p-values from t-test, Table 5.1). A two-way ANOVA demonstrated a significant difference ($p < 0.05$) in longitudinal and transverse modulus values that was independent of the geologic age of the sample. The mechanical properties of fossilized bone are significantly increased from their modern counterparts in both longitudinal and transverse testing directions (Table 5.1). In general, the modulus increased with the geologic age of the sample (Figure 5.2). The mean longitudinal modulus values of the Pleistocene samples were 25% higher compared to the mean of the modern bone samples. A dramatic increase (114%) in modulus was present between the Pleistocene and Miocene samples, with an additional small increase of 3.1% between the Miocene and early Eocene-aged fossils. The early Oligocene-aged bones had modulus values that were significantly increased from modern bone (64%), but were reduced compared with the Miocene bones.

5.3.3 XRD and Density

All bone samples were identified as primarily containing carbonated HA (JCPDS-09-0432) by comparison to standard diffraction patterns reported by the JCPSD (Joint Committee of Powder Diffraction). Additionally, calcite was identified in three samples and quartz was identified in one (Table 5.1). All samples containing contaminant minerals were Miocene or older in age, and the presence of contaminate minerals had no clear association with histology, CI, density, or modulus. The modern and Pleistocene samples displayed nearly amorphous XRD spectra (Figure 5.3), while a general increase in crystallinity was found in older samples (Miocene, Oligocene, and Eocene in age) as peaks narrowed to more closely resemble the diffraction pattern of pure HA. The CI showed a general decrease with the geologic age of the sample (Figure 5.4A), which indicates an increase in crystallinity that in turn, reflects an increase in crystal size with less lattice strain and a more perfect

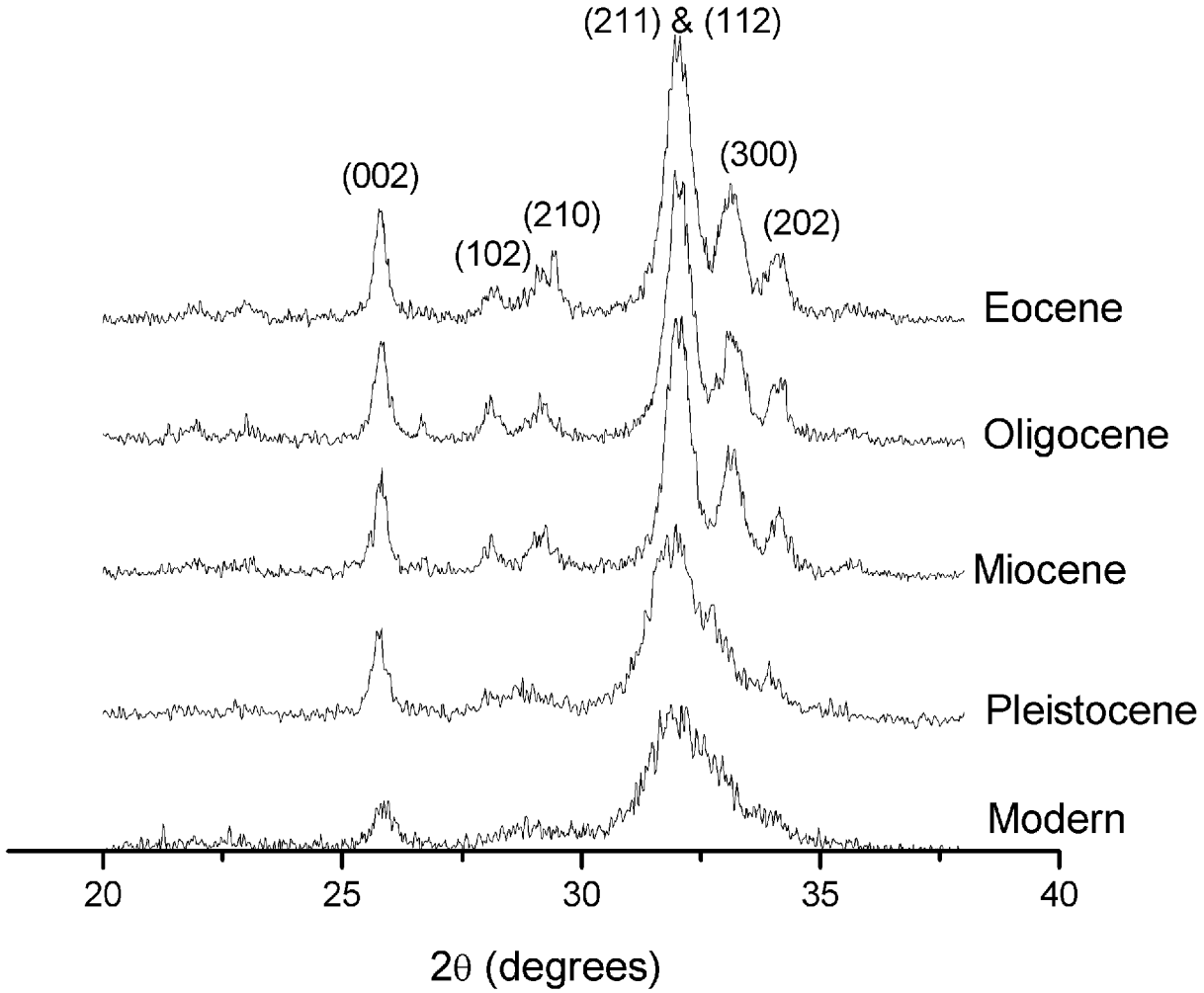

Figure 5.3: Representative x-ray diffraction spectra from each locality of different geologic ages. The modern and Pleistocene spectra are nearly amorphous where as the much older samples (Miocene, Oligocene, and Eocene) have a significantly higher degree of crystallinity that is evident from peak narrowing.

crystal structure. Additionally, a decrease in CI was strongly correlated with an increase in modulus (Figure 5.5A), indicating a link between the crystallinity and mechanical properties of the samples. Further, the density of the samples increased with the age of the specimen (Figure 5.4B) and correlated to the modulus of the samples (Figure 5.5B). CI and density were linearly correlated (CI = -0.19ρ+0.83, R^2=0.63, p<0.001) indicating that the increase in crystallinity is strongly linked to increase in crystal size.

5.4 Discussion

The goal of this study was to provide insight into the complex processes of diagenesis by comparing the nanomechanical, histological, and crystallographic properties of fossilized and modern bone. Further, we seek to elucidate the potential of nanoindentation to investigate the functional significance of paleontological materials even after diagenetic alteration.

Nanoindentation revealed that nanomechanical properties of fossil bone increased with the geological age of the samples, yet the directional differences (anisotropy) that exist in modern bone were still evident in the fossilized bone samples, regardless of their geologic age. Preservation of the anisotropic nature of bone suggests that the original bone provided a scaffold onto which diagenesis occurs, preserving the original structure. Further, evidence of modification of the mineral phase was demonstrated by an increase in crystallinity and density with the geological age of the sample. Both increased crystallinity and density correlated with an increase in modulus, indicating a link between the crystal structure to the mechanical properties of these samples.

5.4.1 Anisotropic Preservation

In the modern samples, the ratio of longitudinal to transverse modulus (L/T ratio) ranged from 1.10 to 1.29, which compared well, yet was slightly reduced to previous nanoindentation measurement of the anisotropy of modern bone 1.33-1.7 (Fan et al., 2002; Rho et al., 2001). Nanoindentation is a multiaxial test where the measured properties are a

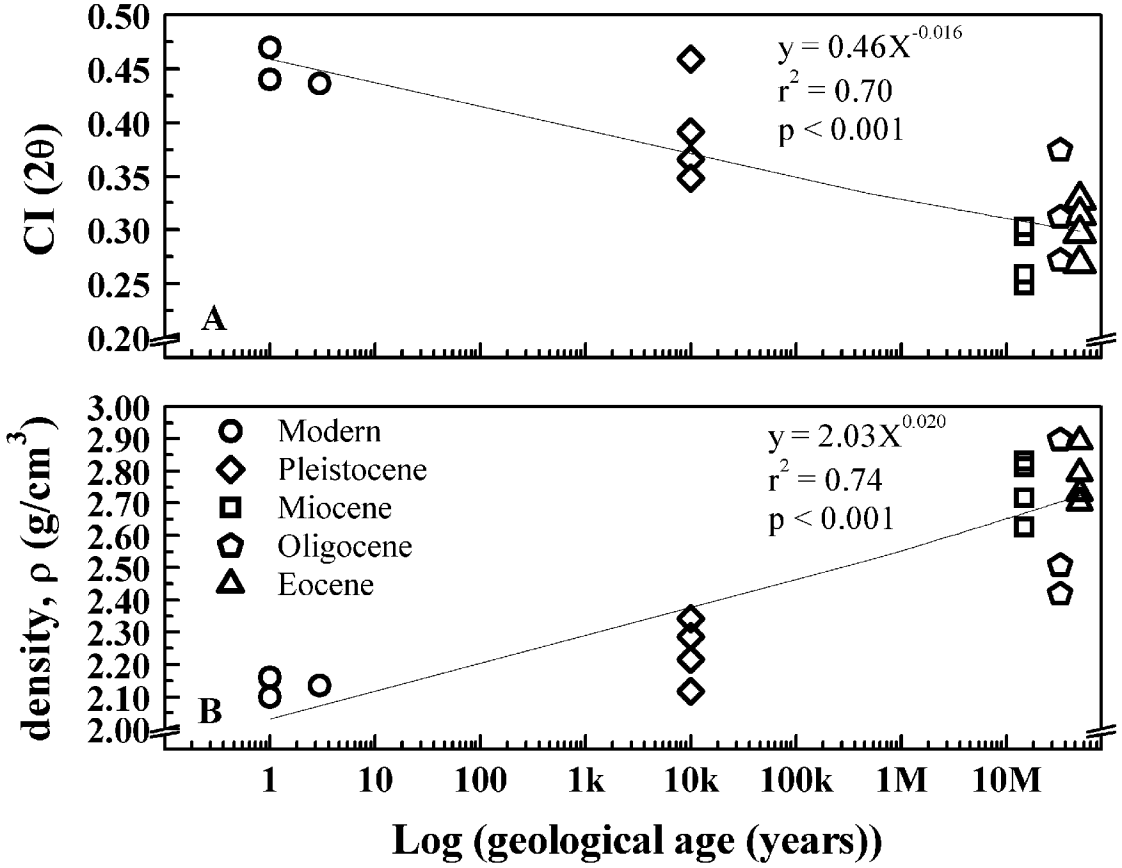

Figure 5.4: A: The crystallinity index (CI) and B: the density plotted against the log of geological age. Data were fit to a power law curve with the equations given in the figure. A clear increase in crystallinity and density are seen with an increase in geologic age of the sample.

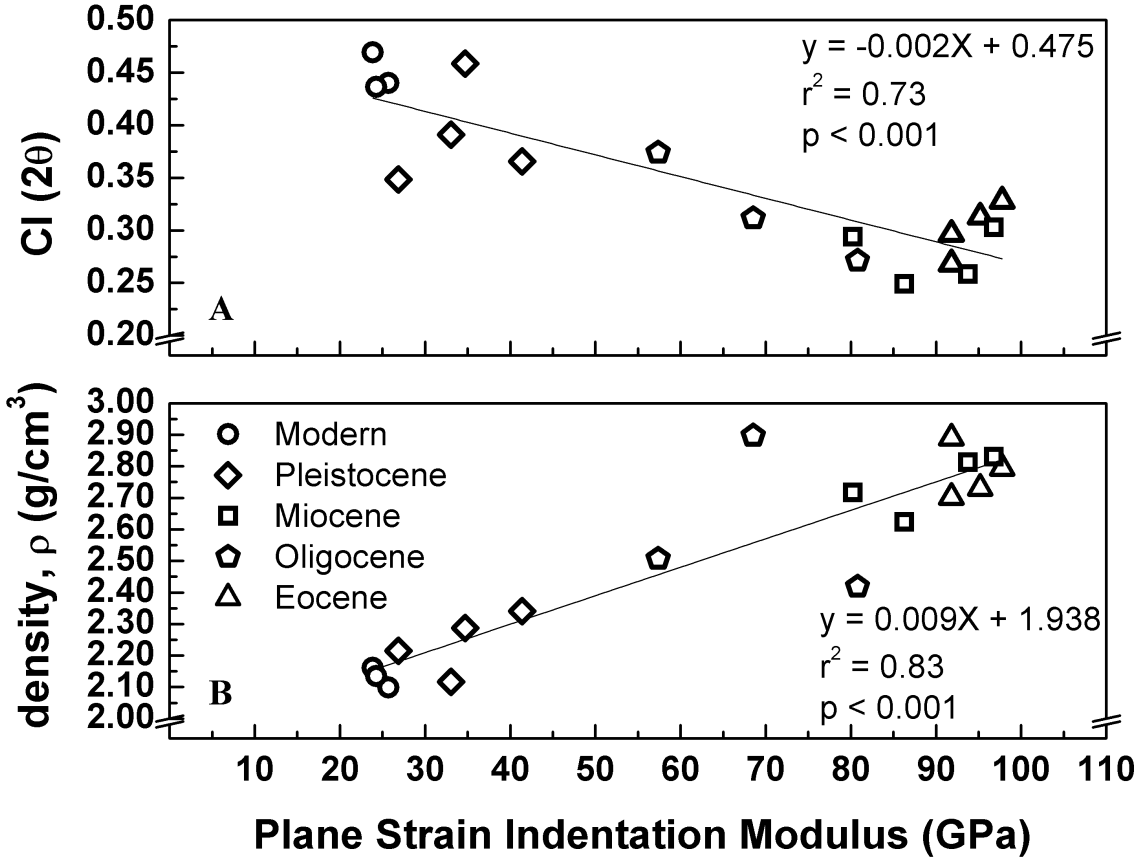

Figure 5.5: The A: crystallinity index (CI) and B: the density plotted against the longitudinal modulus. A linear fit was applied to data with the equations given in the figure. A clear correlation is displayed between the crystallinity and density of the bone sample and its mechanical properties.

combination of the properties in all directions, but are weighted toward the properties in the direction of the applied load (Bushby et al., 2004). The anisotropy ratio was slightly lower than previous published values (Fan et al., 2002; Rho et al., 2001) a likely combined result of digenesis and natural variability between species. Bone within the body is naturally anisotropic as it is formed around longitudinally aligned collagen fibrils onto which mineral crystals grow. This creates a structure that is mechanically stronger in the longitudinal and primary load-bearing direction.

Despite the different depositional environments from which the fossils were recovered, the basic mechanical anisotropy of modern bone is preserved in the fossil record going back at least to the early Eocene ($\approx$ 50 Ma), with L/T ratios ranging from 1.06 to 1.23 (Table 5.1). Although four samples had no preservation of anisotropy and one had an outlying L/T ratio of 2.70, this large range of L/T ratios suggest that while anisotropy is generally preserved in the fossil record, the state of preservation is highly variable and must depend on the postmortem environment. Studies have recognized that bone preservation is dependent upon a variety of factors that include hydrology of the depositional environment, soil pH, geologic age and tissue type, presence of microbes, state of burial, and sediment composition (Hedges and Millard, 1995; Nielsen-Marsh and Hedges, 2000; Weiner et al., 1993). Such factors have a direct impact on the mineralogical and organic components of fossilized bone that contribute to its mechanical behavior.

The anisotropic preservation seen in fossilized bone reflects the original structure of bone. It is possible that as the collagen is dissolved, the original bone crystals increase in size as smaller crystals are dissolved and re-precipitated onto the larger crystals, which maintain their anisotropic nature and original chemical composition. Alternatively, new minerals may be deposited into anisotropic pore spaces, thereby creating a chemically-altered bone with contaminate minerals; XRD analysis revealed several samples with contaminate minerals (Table 5.1), yet all samples primarily contained HA indicating a combination of contributing processes. In a pilot study, we noted the preservation of the mechanical relationship between

different types of bone (i.e., osteonal versus interstitial)(Olesiak et al., 2006), further pointing to maintenance of the original structure of bone during diagenesis. Here, it was impossible to analyze variations between osteonal and interstitial bone, as many samples lacked clearly defined boundaries between the two types of bone (Figure 5.1B).

5.4.2 Modulus increase

The mean longitudinal indentation modulus of our modern artiodactyl bone samples was 24.6 ± 0.97 GPa, which compares well to other nanoindentation data on modern ungulates, including equine bone (≈ 20 GPa) (Rho et al., 2001) and bovine bone (≈ 24.4 GPa) (Rho et al., 1999b). Additionally, the tensile modulus of many ungulate long bones has been shown to range from 15.6 GPa (donkey) to as high as 26.8 GPa (fallow deer) (Currey, 1999). While there is some taxonomic dependence upon the mechanical properties of bone, the variation due to postmortem alteration or diagenesis demonstrated in this paper is much larger and ranged from 26.9 to 97.8 GPa.

The longitudinal modulus was shown to increase with the log geologic age of the sample (Figure 5.2). Additionally, the indentation hardness of these samples has previously been shown to increase with the geologic age of the sample (Olesiak et al., 2008). Increased mechanical properties are likely due to mineral infilling of pore space, as a general increase of density with age was observed. It is well known that increase in the amount of mineral (or mineral volume fraction) is directly related to an increase in Youngs modulus (Katz, 1971; Oyen et al., 2008). Additionally, there was little further increase in the mechanical properties in fossil bones that are older than Miocene in age suggesting that mineral infilling is limited by spatial saturation. Further, little increase in density was observed in samples older than Miocene as density also approached that of apatite ($\rho = 3.19 g/cm^3$) and exceeded that of quartz ($\rho = 2.65 g/cm^3$).

A composite material is generally composed of two or more phases that combine together to create enhanced mechanical properties that are different from the two elements

alone. Bone can be approximated as a composite material, with the collagen phase as a soft compliant matrix that is reinforced by a stiff mineral phase. As the organic component is replaced by mineral (at low mineral content), the mechanical properties of the composite bone will increase. With further mineral infilling, the mineral volume fraction approaches 100% mineral (i.e. 0% organic) and the mechanical properties will approach the properties of the fully dense mineral phase (Ferguson et al., 2003a; Katz, 1971; Oyen et al., 2008). Mineral infilling is evident with in the density increase with the age of the sample (Figure 5.4B). These measured density values were converted to approximate mineral volume fractions V_f using a simple rule-of-mixtures and an organic phase density of $\rho_o = 1g/cm^3$ and mineral density of apatite of $\rho_a = 3.19g/cm^3$:

$$\rho = \rho_o(1 - V_f) + \rho_a V_f \tag{5.2}$$

The contribution of the mineral volume fraction to the mechanical properties is clearly evident in Figure 5.6. A strong increase in modulus values occurs with increasing mineral volume fraction. Hashin-Shtrikman (H-S) and Voigt-Reuss (V-R) composite bounds were calculated (Herakovich, 1997; Hashin and Shtrickman, 1963) using modulus values from indentation test on mineralogical apatite E = 129.5 GPa and in unmineralized osteoid embedded PMMA E = 4.1 GPa (Oyen et al., 2008) and a Poissons ratio of 0.3 for both phases. Using the same composite bounds Oyen et al. (2008) found that all bone samples fell within the H-S bounds for a wide range of bone types of bone with mineral volume fractions ranging from $\approx 20 - 80\%$. The fossilized bone sample did not follow this trend as many samples that were Miocene and older in age fell outside the H-S bound but still within the V-R bounds. The H-S bounds represent a particle composite as is typical of most types of bone where small nanometer sized crystals reinforce the organic matrix. The V-R bounds represent a fiber composite with the mineral phase occurring in the form of connected fibers. It is possible that during fossilization as mineral replaced the organic material a more connected fiber type composite is formed. Alternatively, infilling with other lower density minerals

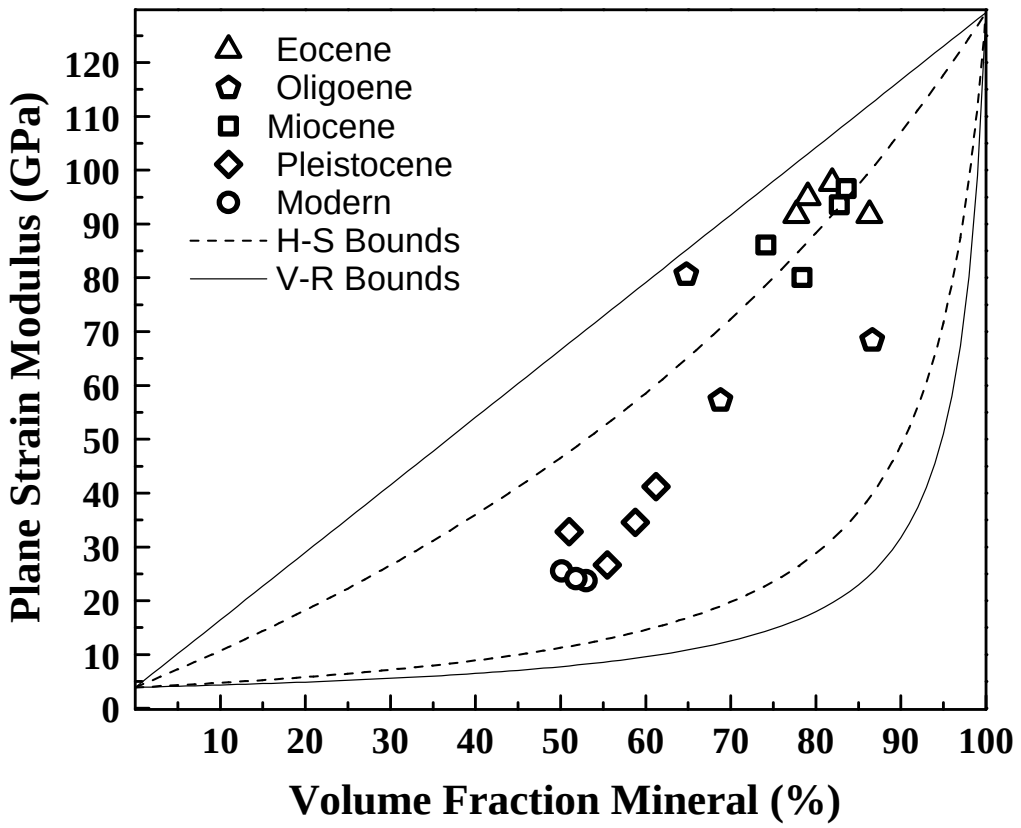

Figure 5.6: The longitudinal modulus plotted against the calculated mineral volume fraction from the measured density. Additionally the Hashin-Shtrikman (H-S) and Voigt-Reuss (V-R) composite bounds are plotted for comparison.

with such as quartz ($\rho = 2.65g/cm^3$) (Broz et al., 2006) would shift the calculated mineral volume fraction such that the fossilized samples would all lie within the H-S bounds.

While there is a clear increase in mechanical properties with the geologic age of the fossil, the diagenetic environment also plays a role. For example, that the early Oligocene samples have reduced mechanical properties compared to the Miocene and Eocene samples (Figure 5.2) may be related to the rock lithology, that in turn, has affected the diagenetic environment. Specifically, the fossil-bearing strata at Oligocene-aged UCM locality 77271 contain volcanic ash which has been shown to dissolve bone mineral (Harris and Vancouvering, 1995) a plausible cause for the decreased mechanical properties of the Oligocene samples.

5.4.3 Crystallinity

The Crystallinity Index (CI) from the samples in this study ranged from 0.46 to 0.26, which falls within the range of previously observed CI values for fresh and fossilized bone samples (Hubert et al., 1996; Sillen, 1989). The previously observed CI of synthetic HA, with a very sharp (002) peak, is 0.18 whereas fresh cow, sheep, pig, and rabbit bones have much broader peaks with a CI = 0.41-0.54 (Sillen, 1989). The decrease in CI, or increase in crystallinity, in the fossilized samples correlates with an increase in the geological age (Figure 5.4).

Our results corroborate the correlation of crystallinity and geologic age of fossilized bone that has been previously documented in many studies by XRD peak narrowing (Bartsiokas and Middleton, 1992; Sillen, 1989) and IRSF (Sillen and Parkington, 1996; Weiner and Bar-Yosef, 1990). This general increase in crystallinity is attributed to a larger crystal size, with less defect and less lattice strain (Daculsi et al., 1991). Yet other studies reported no correlation of increased crystallinity within individual archeological sites over smaller time ranges, (thousands of years) (Hedges and Millard, 1995; Person et al., 1996, 1995). While Person et al. concluded no correlation between crystallinity and age of the sample, con-

sideration of only the samples from the paleontological sites ranging from 68 ka to 218 Ma (Person et al., 1995) indicated a general increase.

The nature of the general increase in crystallinity is not well known, as both an increase in crystal size and a decrease in lattice strain contribute to peak narrowing of XRD spectra. Bone crystals have been shown to grow in size and obtain a more needle-like morphology during diagenesis (similar to pure HA) (Reiche et al., 2002; Trueman et al., 2004), which could result in XRD peak narrowing due to the increased size of the single crystals. Alternatively, new crystals may form from HA that is presumably dissolved locally and re-precipitated (Hedges, 2002), creating more perfect crystals (with less lattice strain) that could result in an increase in crystallinity. As CI and density were correlated, it is likely that the increase in crystallinity primarily reflects an increase in the crystal size and therefore also the density of the sample.

Nanoindentation modulus was correlated to both the CI (R^2=0.73, p $<$ 0.001, Figure 5.5A) and the density (R^2=0.83, p $<$ 0.001, Figure 5.5B). The increase in the crystal size (related to both CI and density) is linked to the mechanical properties of the sample. The increase in crystal size both result in increased mineral volume fraction and thus increased mechanical properties following composites theory (Oyen et al., 2008).

We demonstrate clear correlations of the modulus (stiffness), CI, and density with the age of the sample that is related to diagenetic processes. However, the continued increase in modulus and CI values needs to be interpreted with caution because our data are collected from distinct samples that have undergone diagenesis for variable amounts of time, rather than a single bone specimen that has undergone continuous diagenesis measured at controlled intervals. Little alteration appears to occur in samples older than Miocene in age as the largest changes in modulus, CI, and density occurred earlier in time. While diagenesis is dependent on the burial site, a better understanding of diagenetic processes may be elucidated with further testing of younger aged samples (especially $<$ 20 MA) when fossils appear more prone to change. Additionally, this technique may provide information on vari-

able burial conditions such as observed in the Oligocene samples. Further, XRD and density measurements are bulk analysis tools, while nanoindentation provides site-specific nanomechanical properties of a specimen. The benefits of the nanoindentation technique could be further utilized when combined with additional tools such as high resolution laser ablation mass spectroscopy (Brady et al., 2008; Felicissimo et al., 2004; Lu et al., 2000; Sponheimer et al., 2006), micro Raman and infrared spectroscopy (Akkus et al., 2004; Cardell et al., 2009; Colomban and Treppoz, 2001), and quantitative backscatter SEM (Ferguson et al., 2003a, 2008; Oyen et al., 2008) to better characterize diagenetic alterations at the tissue-level.

5.5 Conclusion

The mechanical properties of fossilized bone were significantly altered from modern bone, yet key anisotropic relationships were maintained. For example, the consistently lower modulus values measured in the transverse direction, as compared to those in the longitudinal direction, reflect preservation of the anisotropy of bone in its native biological state. The modulus and crystallinity values of fossil bones generally increased with geologic age of the sample, although the diagenetic environment in which the fossils occur also plays a role in modifying its nanomechanical properties. Additionally, a structure-property relationship of each sample is apparent from the correlation between modulus values to the crystallinity and density of the sample. Nanoindentation is sensitive to alteration of the mineral phase and may help to further understand this complex process. Nanoindentation combined with complementary techniques such as XRD and SEM provides a novel approach to investigate diagenesis in mineralized tissues.

Chapter 6

Nanoindentation of Lemur Enamel

Mammalian teeth must function under a wide range of imposed normal loads and sheer stresses that occur during mastication. Yet failed functionality is demonstrated in the ring-tailed lemurs (*Lemur catta*) of Beza Mahafaly Special Reserve where extreme enamel wear and tooth loss is the likely result of thin enamel combined with the consumption of a hard fallback food (Cuozzo and Sauther, 2004, 2006; Sauther et al., 2002). The complex structure of the tooth has been suggested to adapt to the demanding functional requirements through alteration of tooth shape, size, and enamel thickness (Crompton and Sita-Lumsden, 1970; Gregory, 1922; Kay and Hiiemae, 1974; Maas and Dumont, 1999). In addition to the morphology of the tooth, the mechanical and material properties of enamel must also inherently contribute to the functionality. However only recently have investigators explored the mechanical properties at the micro- or nano- length scale (Constantino et al., 2009; Currey and Abeysekera, 2003; Darnell et al., 2010; Ferguson et al., 2005; Fong et al., 2009), see Table 6.1. In this study we compare the nanomechanical and material properties of enamel with failed functionally in *Lemur catta* to successfully functioning enamel of *Lepilemur leucopus, Propithecus verreauxi*, and *Homo sapiens*.

It has been hypothesized that variations in primates diet play an adaptive evolutionary role on the shape of the tooth (Crompton and Sita-Lumsden, 1970; Gregory, 1922; Kay and Hiiemae, 1974; Kay, 1975). Additionally, enamel thickness has been linked to hard object feeding in primates (Dumont, 1995; Kay, 1981), and has been further suggested to provide

greater wear potential (Macho and Spears, 1999) or resistance to fracture (Kay, 1981; Lucas et al., 2008). However, the relationship between thick enamel and hard object consumption is not direct (Maas and Dumont, 1999; Martin et al., 2003; Teaford and Ungar, 2000). For example *pitheciins* primates have thin enamel with considerable prism decussation and are able to successfully consume hard objects, indicating that enamel microstructure plays a vital role in the function of the tooth (Macho and Shimizu, 2010; Martin et al., 2003). Similarly, the ring-tailed lemurs (*Lemur catta*) have extremely thin enamel compared to other primates, (Godfrey et al., 2005; Martin et al., 2003; Shellis et al., 1998), yet rely heavily on a hard, tough fallback food from the tamarind tree, Tamarindus indica, (Cuozzo and Sauther, 2004, 2006; Sauther, 1998; Sauther and Cuozzo, 2009; Simmen et al., 2006; Yamashita, 1996, 2002, 2003). Consumption of this hard fallback contributes to extreme tooth wear and loss (Cuozzo and Sauther, 2004, 2006; Sauther et al., 2002). This failed functionally in *Lemur catta* suggest ill-adapted enamel where mechanical and material properties are not equipped to handle the high stresses caused by their diet. Tooth functionality and wear are dependent a number of complex factors which include morphology and enamel thickness but also microstructure and mechanical properties. Investigation of the material and nanomechanical properties will help elucidate the functional adaptation of the ring-tailed lemurs' thin enamel.

Investigation of the nanomechanical properties of enamel can provide insight into on a number of factors including: prism orientation (Shimizu and Macho, 2008), mineralization (Ferguson et al., 2005), microstructure, and composition (Cuy et al., 2002). Nanomechanical properties functionally vary across the enamel cap and increase from the enamel dentin junction (EDJ) to the occlusal surface (OS) in humans (Braly et al., 2007; Cuy et al., 2002) (see Figure 2.6). Mineral volume fraction correlates to mechanical properties as mineral content (P_2O_5 and CaO) is highest at the hard occlusal surface and decreases toward the softer EDJ (Cuy et al., 2002). A similar gradation of the mechanical and material properties have been demonstrated in other primates (Darnell et al., 2010) and are likely to exist in all mammalian teeth, yet few studies investigate the mechanical properties in addition

Table 6.1: Comparison of mehcanical properties of enamel for a range of mammalian species measured using either Vickers hardness or nanoindneation test. Values are listed for each test type with acending hardness values. * = Vickers hardness numbers (VHN) have been converted from kgf/mm^2 to GPa by multiplying by 0.009807. a (Currey and Abeysekera, 2003), b (Marcondes et al., 2009), c (Xu et al., 1998), d (Ferguson, 2004), e (Cuy et al., 2002), f (Fong et al., 2009), g (Darnell et al., 2010), h (Mahoney et al., 2000)

Taxa	**Tooth**	**Modulus** ± **STD (GPa)**	**Hardness** ± **STD (GPa)**	**Test**
Vickers				
Delphinus sp.[a] (dolphin)	Tooth		2.84 ± 0.14*	0.49 N
Bos taurus[a] (bovine)	Molar		3.00 ± 0.34*	0.49 N
Homo sapiens[b]	M3		3.02*	1.96 N
Ovis aries [a] (sheep)	Molar		3.04 ± 0.18*	0.49 N
Cervus elaphus[a] (red deer)	Molar		3.13 ± 0.11*	0.49 N
Equus caballus[a] (horse)	Premolar		3.27 ± 0.14*	0.49 N
Homo sapiens[c]	M3	80.0 ± 4.0	3.37 ± 0.15	1.96 N
Rattus rattus[a] (rat)	Incisor		3.52 ± 0.15*	0.49 N
Macaca mulatta[a] (macaque)	Incisor		3.68 ± 0.87*	0.49 N
Nanoindentation				
Equus caballus[d] (horse, 2 yrs)	M_2 (root to OS)	20 – 80		20 mN
Homo sapiens[e]	M^2 (EDJ to OS)	47- 120	2.7 - 6.4	800 nm
Mus musculus[f] (mice)	M_1	87 ± 3.0	3.1 ± 0.3	100 nm
Alouatta palliata[g] (howler monkey)	M^3 (buccal cusp, EDJ)	85.2 ± 9.7	4.13 ± 0.3	600 nm
Alouatta palliata[g] (howler monkey)	M^1 (buccal cusp, EDJ)	77.3 ± 7.4	4.75 ± 0.7	600 nm
Homo sapiens[h]	M^1	80.4 ± 7.7	4.88 ± 0.35	50 mN

to morphology. Numerous evolutionary and dietary studies often disregard the mechanical properties and assume homogenous, isotropic enamel (Mahoney et al., 2000). A complete understanding of the functional adaptations of mammalian teeth requires knowledge of the variations in the mechanical and material properties of enamel within individual teeth and between species and further provide insight into the process of wear and evolutionary adaptation of the tooth.

6.1 Study Objectives

In this study we investigate variations in nanomechanical properties, microstructure, and mineralization within the infraorder Lemuriformes as compared to *Homo sapiens* in order to understand how mineralization and microstructure combine to create a successful enamel surface. We further explore variations in these properties in the functionally failed enamel of *L. catta* where extreme wear causes tooth loss or even death. The variability provided by this biological model system will be used to investigate the nanomechanical property dependence on crystallinity and composition variations. The nanomechanical properties of lemur teeth have never been investigated and many questions still remain about the structure-function relationship of enamel and the wear process. Variations in crystallinity and composition will be investigated in a single animal and between species by the following sub-goals:

(a) Use nanoindentation to investigate the nanomechanical property variation from the occlusal surface to the EDJ in lemur enamel within and between species.

(b) Determine the relationship of nanomechanical properties variation in microstructure and mineral content in lemur dental enamel.

(c) Explore the nanomechanical response of damaged enamel as compared to intact enamel.

(d) Create a finite element model of the nanoindentation of enamel in-order to explore how micro cracking and microstructure contribute to the nanomechanical response.

6.2 Methods and Materials

6.2.1 Sample Preparation

The maxillary second molar (M^2) was sampled from two individuals from each of three lemur species (*Lepilemur leucopus, Lemur catta, Propithecus verreauxi*) and *Homo sapiens*. Lemur samples were collected on the surface from previously deceased animals at Beza Mahafaly Special Reserve, Madagascar of Beza Mahafaly Special Reserve, southwestern Madagascar (23° S latitude, 44 (23°E longitude). Additionally, two *Homo sapiens* M^2 were supplied by the dental school at the University of Colorado-Boulder. Each tooth was embedded in poly methylmethacrylate (PMMA) under vacuum and then sectioned along the buccal-lingual direction though the mesial cusps, using a low-speed diamond-wafering saw (Isomet: Buehler, Lake Bluff, IL). The mesial half was then polished with a series of silicon carbide paper (300, 400, 600, 1200 grit) and then polished with successfully finer diamond suspension paste (Buehler) of particle size 6, 3, and 0.25 μm. The specimens were ultrasonically cleaned with deionized water to remove debris between each step. As a final preparation, samples were air dried after ultrasonic cleaning for a minimum of 72 hours prior to analysis.

6.2.2 Mechanical testing

Investigation of the nanomechanical properties of enamel within teeth and between species was performed by Nanoindentation tests (NANO Indenter XP, MTS Systems Co., Oak Ridge, TN). The enamel of each PMMA-embedded sample was testing using a Berkovich indenter tip using a constant load rate of 1.667 mN/s to a maximum load of 50 mN ($\approx$ 800nm), where the indenter was held for 30 seconds to minimize the creep response during

unloading. Data were analyzed using a modified version of the Oliver-Pharr method (Oliver and Pharr, 1992) to determine contact Hardness (referred to as hardness or H) and plane strain modulus (referred to as modulus or E'). Plane strain modulus is calculated from the slope of the first 80% of the unloading curve, the tip area function (calibrated using a fused silica standard), and the known elastic parameters of the Berkovich tip (given by the Youngs modulus and Poissons ratio of diamond: $E_i = 1140$ GPa and $\nu_i = 0.07$, respectively). The indentation hardness (H) can be determined from the maximum load and the tip area function.

Indent arrays were four indents wide for all lemur samples (with 20 μm spacing) and placed perpendicular to and covering the area from the EDJ to the OS. Indent arrays were placed on the two mesial cusps (or nearby when cusps had been worn away) and though the central valley (Figure 6.1). To cover the entire area from the EDJ to OS lemur teeth required 6 -19 rows of indents depending on enamel thickness at the location of the array. Arrays placed on *Homo sapiens* samples had 50 μm spacing and with only 3 indents per rows due to the substantially thicker enamel, and still required 28-44 rows of indents to cover the complete area from EDJ to OS. In order to further understand the variation in mechanical properties each nanoindentation array was spatially divided into halves, the half of enamel thickness adjacent to the OS and the half adjacent to the EDJ half, based on the percent distance of the enamel thickness at each array location. Data taken from the EDJ half allows comparison of properties between species within unworn and undamaged enamel.

6.2.3 Quantitative Backscatter Electron Imaging

Quantitative backscatter electron imaging (qBSE) was used to analyze the relative mineral content of each indentation location. Following nanoindentation testing, the PMMA-embedded teeth were coated with carbon and each indentation array was imaged using an SEM with backscatter detector (JEOL 6480LV) operated at 20kV with a 15mm working distance and a spot size of 60. Gray-level images, with pixel values ranging from of zero

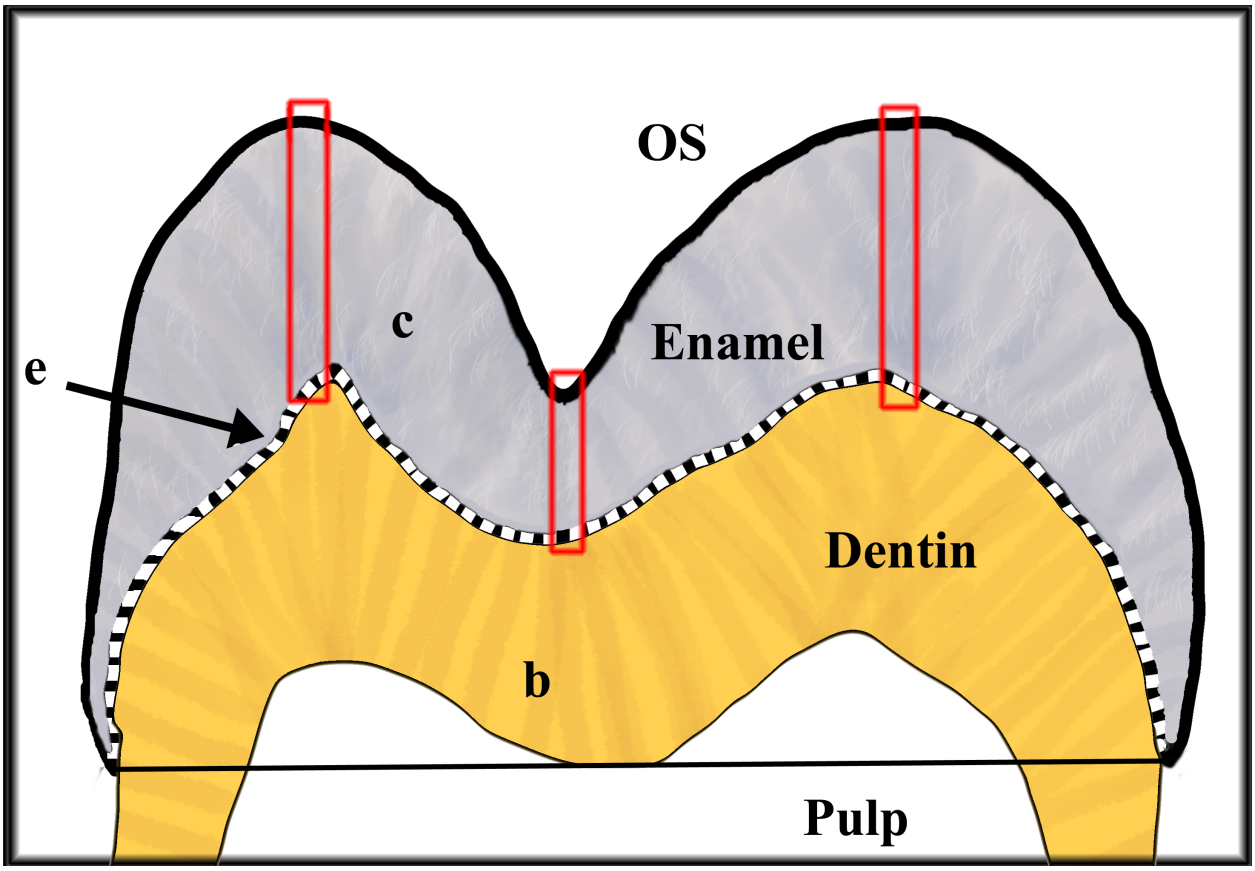

Figure 6.1: Schematic of the cross-section of a tooth with enamel, dentin, pulps, occlusal surface (OS), and EDJ (e) labeled. Red rectangles indicate the approximate location of indentation testing arrays placed on each tooth. Additionally this images shows the measurements recoded in this study used to calculate the RET: c the cross-sectional area of the enamel cap, b the cross-sectional area of the dentin enclosed by enamel cap, and e the length of the EDJ.

for black to 255 for white, of each indentation array were taken at 500X after an hour of SEM warm up time to insure stabilized conditions. The number of backscattered electrons and hence the gray level value of an individual pixel is based on the mean atomic number of the sample at that location. To permit comparison between imaging sessions, novel lithium-rubidium borosilicate glass standards of known composition were imaged at the start and every 20 minutes, and again at the end of each imaging session. The histogram for each image of enamel was stretched over the 256 gray levels where the glass standard x = 0.05 was set to zero and x = 0.15 was set to 255 to encompass the range of gray scale values of enamel. Similar methods of qBSE analysis have been employed often with the use of polymeric and metallic materials (Boyde and Jones, 1983; Boyde et al., 1995). The weighted mean gray level (WMGL) of each indentation site was determined as the average gray level of the pixels within a R= 5 μm circle around the center of the indent site. The radius of this circle was determined using contact mechanics principles (Johnson, 1985) where the radius of the volume of deformed material was approximated by an indentation test to 800 nm in depth. Additionally, the residual plastically deformed imprint left from the Berkovich tip was removed by threshold from the image and not included in the WMGL measurements.

6.2.4 Scanning Electron Imaging

Backscatter electron images (BSE) of each indentation array were further used to bin each indent location into four cracking classifications based on the distance of the test site to the nearest crack. Each indent was grouped into one of four categories: category 1 = ideal indent location with no visible damage within 3 indent widths of test site, category 2 = indent site is > 1 and ≤ 3 indent widths from a crack, category 3 = indent site is ≤ 1 indent width of a crack, category 4 = indent is directly on a crack of crack or visible damage. Figure 6.2 demonstrates the categories assigned to indents in an example array. All analysis only included category 1 or ideal indent locations except where specifically stated to include categories 2-4 additionally. The extent of cracking in each sample was defined as the number

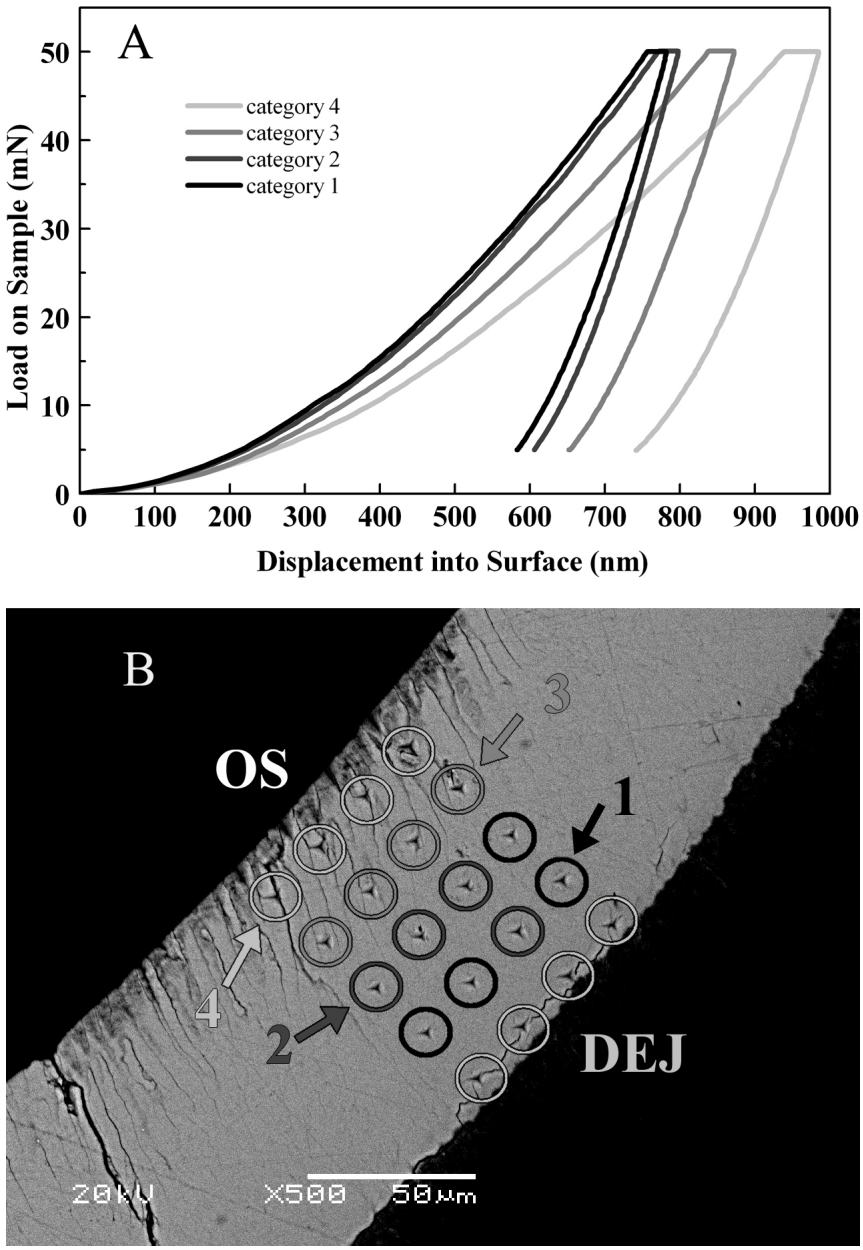

Figure 6.2: Nanoindentation data was classified into 4 categories based on location of indent test site to a micro crack. Category 1 = prefect indent location with no visible damage, category 2 = crack distance greater than one to three indent widths away from indent location, category 3 = crack located within one indent width of a test site, category 4 = indent on top of crack or visible damage. Image A provides the load-displacement nanoindentation curves for representative indents in each cracking category. Image B is a BSE image of substantial cracking present in *L. catta* 2 sample demonstrating cracking category classification on an indentation array.

of indentation sites within three indent-widths of a crack (the sum of group 2, 3, 4) divided by the total number of indentation sites x100%.

BSE compilation images of the cross-section of each sample were used to measure the enamel thickness (Figure 6.3) using Image J (U. S. National Institutes of Health, Bethesda, Maryland, USA). The measurement of the relative enamel thickness (RET), a dimensionless index, allows for comparison of enamel thickness independent of the size of the tooth (Martin, 1985). Calculation of the RET is given by the area of the enamel cap (c) divided by the length of the EDJ (e) and then divided by the square root of the area of the dentin (b) multiplied by 100. For each sample, the lengths and areas (c, e, and b) were measured (Figure 6.1) three times and averaged to reduce measurement error. Differences in measured values were minimal where the mean coefficient of variance was 1.8%. While RET measurements are generally made on unworn samples, measurement on our samples allowed for a quantitative assessment of gross wear. The *L. leucopus* 2 sample was fractured and missing a portion of the tooth (Figure 6.3), therefore RET measurements were made using only half the tooth to the midline and then doubled. Measured values were similar to *L. leucopus* 1.

After all other analysis, one sample from each species was etched following the method of (Boyde et al., 1986) with 0.5 % H_3PO_4 for 60 s and then coated with a conductive carbon coating. Samples were reimaged using secondary electron (SE) imaging with a JEOL 6480LV SEM operated at 10kV with a 18mm working distance and a spot size of 30. SE images were used to determine prism pattern and orientation at the EDJ and OS of one representative sample from each species. Average prism width for each species was measured near the OS on 10 randomly selection prisms from an SEM image taken near the cusps of each sample.

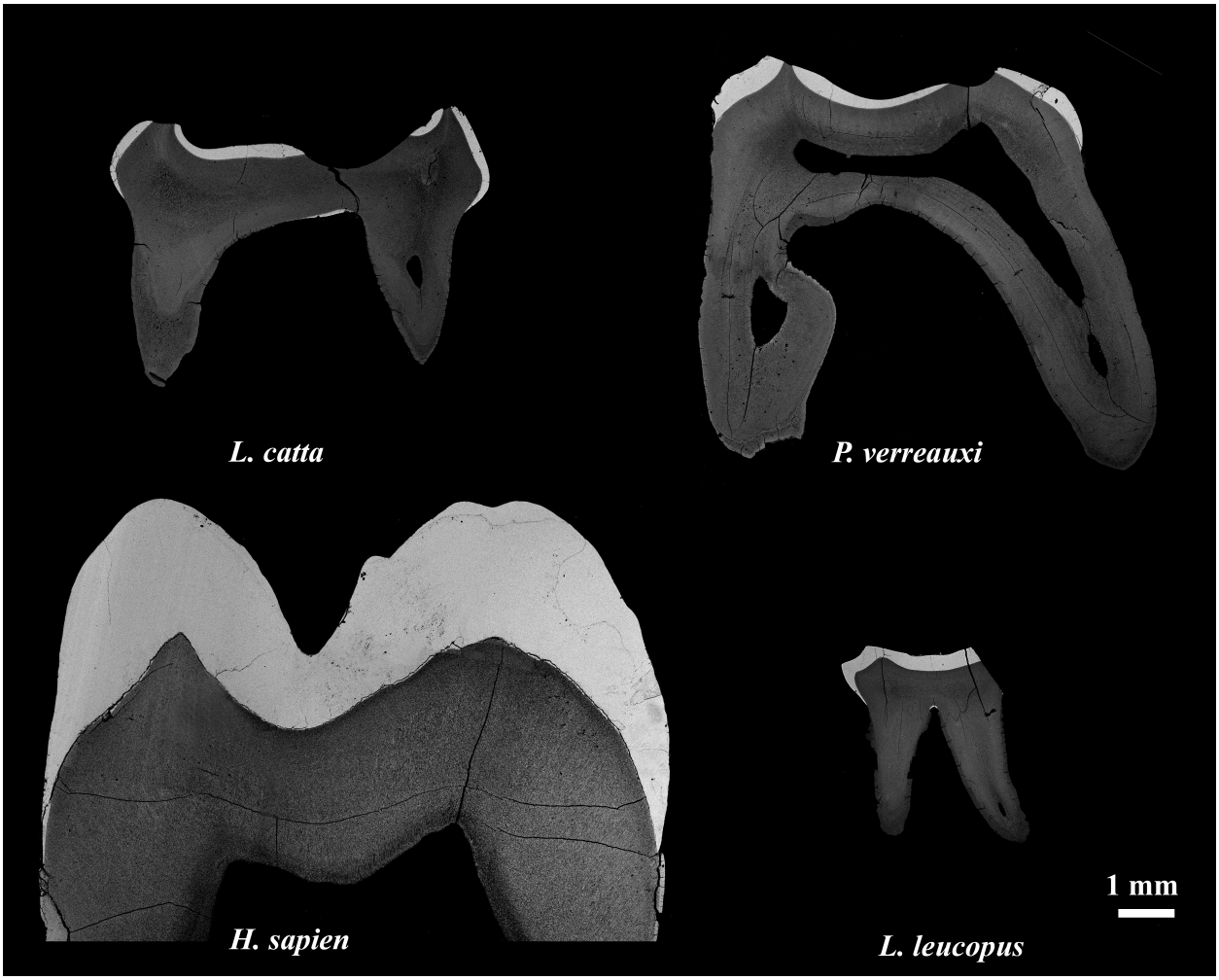

Figure 6.3: BSE image compulations of example cross section for each species at the same scale. Images were taken in backscatter mode at 20 kV, with 15 mm working distance, and a spot size of 60. Enamel wear is clearly present on *L. catta* and *P. verreauxi*.

Table 6.2: Indentation modulus and hardness values are presented along with qBSE data for all lemur species and human enamel. Data were divided into two groups based on the longest array on each species: an EDJ and OS half. For each of these groups data are presented as the mean standard deviation (n-value). Additionally the difference between the EDJ and OS was determined as [diff = (OS-EDJ)/((EDJ+OS)/2) *100]. § indicates statically significant $p < 0.05$ using a students t-test.

Sample	H (GPa), EDJ half	H (GPa), OS half	H %diff	E'(GPa), EDJ half	E' (GPa), OS half	E %diff	WMGL, EDJ half	WMGL, OS half	WMGL, %diff
H. sapiens 1	4.05 ± 0.25 (143)	4.58 ± 0.47 (155)	12.40 §	91.12 ± 3.76 (143)	97.43 ± 4.90 (155)	6.70 §	170.45 ± 3.72 (143)	173.19 ± 5.20 (155)	1.59 §
H. sapiens 2	4.04 ± 0.29 (133)	4.60 ± 0.45 (155)	12.97 §	86.34 ± 4.59 (133)	94.82 ± 4.70 (155)	9.36 §	167.79 ± 3.18 (133)	170.35 ± 4.08 (155)	1.51 §
Mean of *H. sapiens*	4.04 ± 0.00 (2)	4.59 ± 0.02 (2)	12.68	88.73 ± 3.38 (2)	96.13 ± 1.85 (2)	8.00	169.12 ± 1.88 (2)	171.77 ± 2.01 (2)	1.86
P. verreauxi 1	4.12 ± 0.27 (44)	4.39 ± 0.34 (84)	6.39 §	86.00 ± 3.02 (44)	90.55 ± 2.72 (80)	5.15§	173.48 ± 4.18 (44)	174.80 ± 2.95 (84)	0.76
P. verreauxi 2	4.13 ± 0.29 (30)	4.21 ± 0.30 (57)	1.99	88.89 ± 3.72 (30)	89.96 ± 4.59 (57)	1.23	169.23 ± 1.44 (30)	170.10 ± 1.30 (57)	0.53
Mean of *P. verreauxi*	4.13 ± 0.01 (2)	4.30 ± 0.13 (2)	4.21	87.44 ± 2.04 (2)	90.23 ± 0.39 (2)	3.18	171.87 ± 2.91 (2)	172.20 ± 2.46 (2)	0.64
L. *catta* 1	4.42 ± 0.18 (25)	4.55 ± 0.25 (21)	2.81	87.95 ± 2.40 (25)	86.32 ± 9.02 (21)	-1.87	168.18 ± 9.16 (25)	171.57 ± 8.76 (21)	2.00
L. *catta* 2	4.43 ± 0.19 (22)	4.52 ± 0.71 (24)	2.03	88.59 ± 3.18 (22)	87.93 ± 5.03 (24)	-0.75	170.43 ± 5.14 (22)	170.86 ± 4.25 (24)	0.25
Mean of L. *catta*	4.43 ± 0.00 (2)	4.54 ± 0.17 (2)	2.42	88.27 ± 0.45 (2)	87.12 ± 1.14 (2)	-1.31	169.31 ± 1.59 (2)	171.22 ± 0.50 (2)	1.12
L. leucopus 1	4.30 ± 0.32 (58)	4.83 ± 0.56 (90)	11.77 §	77.88 ± 4.91 (58)	79.33 ± 5.38 (90)	1.84	168.56 ± 1.94 (58)	170.33 ± 2.49 (90)	1.66 §
L. leucopus 2	4.20 ± 0.30 (36)	4.63 ± 0.32 (77)	9.84 §	78.48 ± 4.91 (36)	79.34 ± 7.69 (77)	1.08	170.29 ± 7.09 (36)	173.78 ± 7.98 (77)	2.03 §
Mean of *L. leucopus*	4.25 ± 0.07 (2)	4.73 ± 0.14 (2)	10.82	78.18 ± 0.42 (2)	79.33 ± 0.00 (2)	1.41	169.43 ± 1.22 (2)	172.06 ± 2.43 (2)	1.54

6.3 Results

6.3.1 Nanomechanical Measurements

Nanomechanical data for each sample divided into OS and EDJ half are reported in Table 6.2. Mechanical property trends for were similar in all species, except *L. catta*, where E' and H values significantly increased ($p < 0.001$) from the EDJ toward the OS, while *L. catta* showed decreased values (Figures 6.4 and 6.5). Similarly, the modulus and hardness values from the OS-half were 1.08% to 12.97% greater than that of the EDJ-half (significance shown in Table 6.3) for all species except *L. catta*. Comparison of the unworn enamel within the EDJ-half demonstrated little species variation, as the mean modulus was 88.15 ± 0.65 GPa for all of the species except *L. leucopus* which had a mean modulus of 78.18 $\pm$ 0.42 GPa (Table 6.2) which was 11.9 % reduced from human. Variations of mechanical properties between species were evident in the mechanical properties of the OS-half as the mean modulus of *L. catta* and *P. verreauxi* were similar yet reduced 6-9% from that of human enamel and for *L. leucopus* was reduced by 17.5% from that of human (Table 6.2).

6.3.2 Mineralization and Microstructural variations

Figure 6.3 contains SEM images of the whole enamel surface for one sample of each species investigated. Severe wear was clearly visible on both *L. catta* and *P. verreauxi* 2 teeth, minor amounts of wear were evident on *L. leucopus* 1 and *P. verreauxi* 1 (not pictured), and the remaining samples had little evidence of wear. Measurement of RET clearly reflect the severe wear present on both *L. catta* samples and *P. verreauxi* 2 with reduced values compared to those reported previously in the literature (Table 6.3).

Using qBSE-imaging WMGL, a relative measure of mineral content, was calculated for each indentation point and grouped into OS and EDJ halves (Table 6.2). WMGL remained relatively constant from the EDJ to the OS with a mean increase of 1.3% for all species. However, significant increases in WMGL was observed in human and *L. leucopus*, the two

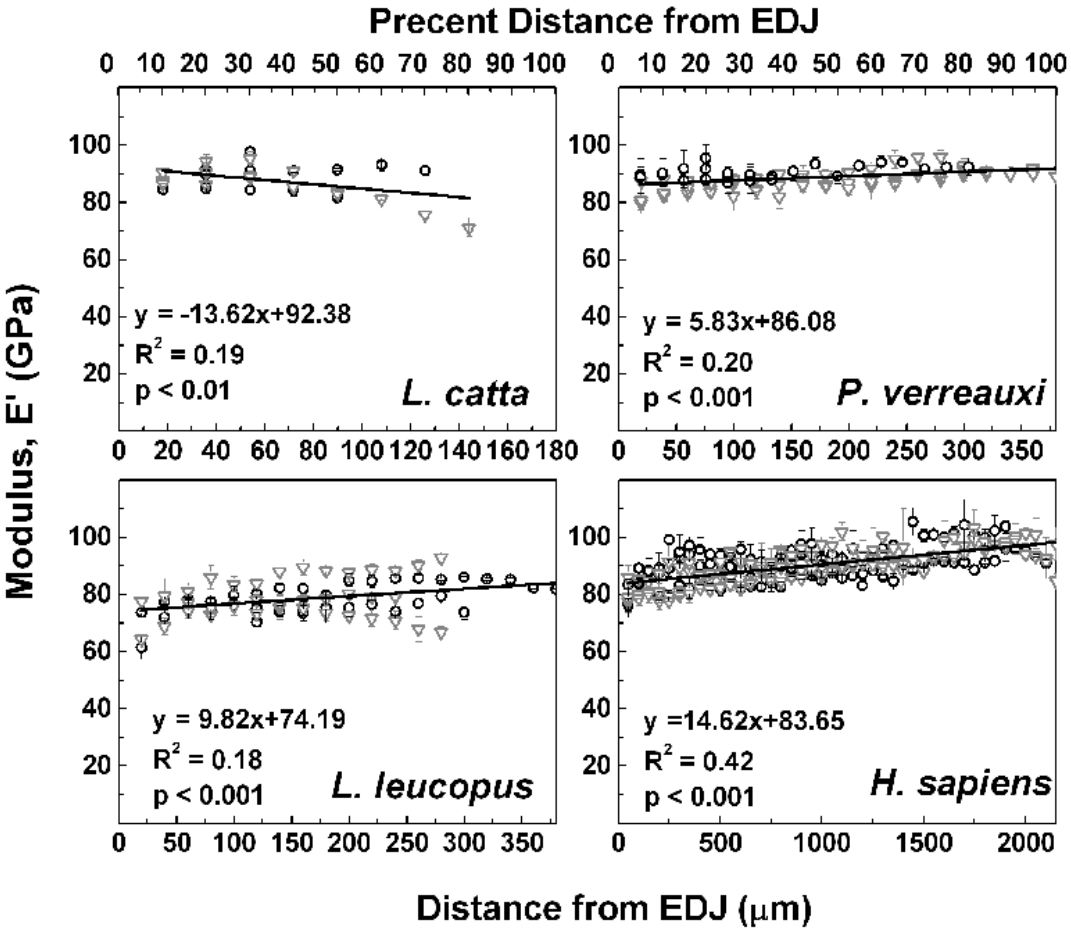

Figure 6.4: Nanoindentation modulus of dental enamel of three lemur species plus human. Open circles and triangles each represent an individual sample. Three indentation arrays were placed on each samples perpendicular to and covering the area from EDJ to the OS. Each data point represents the mean ± standard deviation of four (3 for human sample) indentations taken in a row at equal distance from the EDJ (distance = 0) to OS. Rows were spaced 20 μm apart in lemur species and 50 μm in human sample. Linear fit equation for all data points are listed.

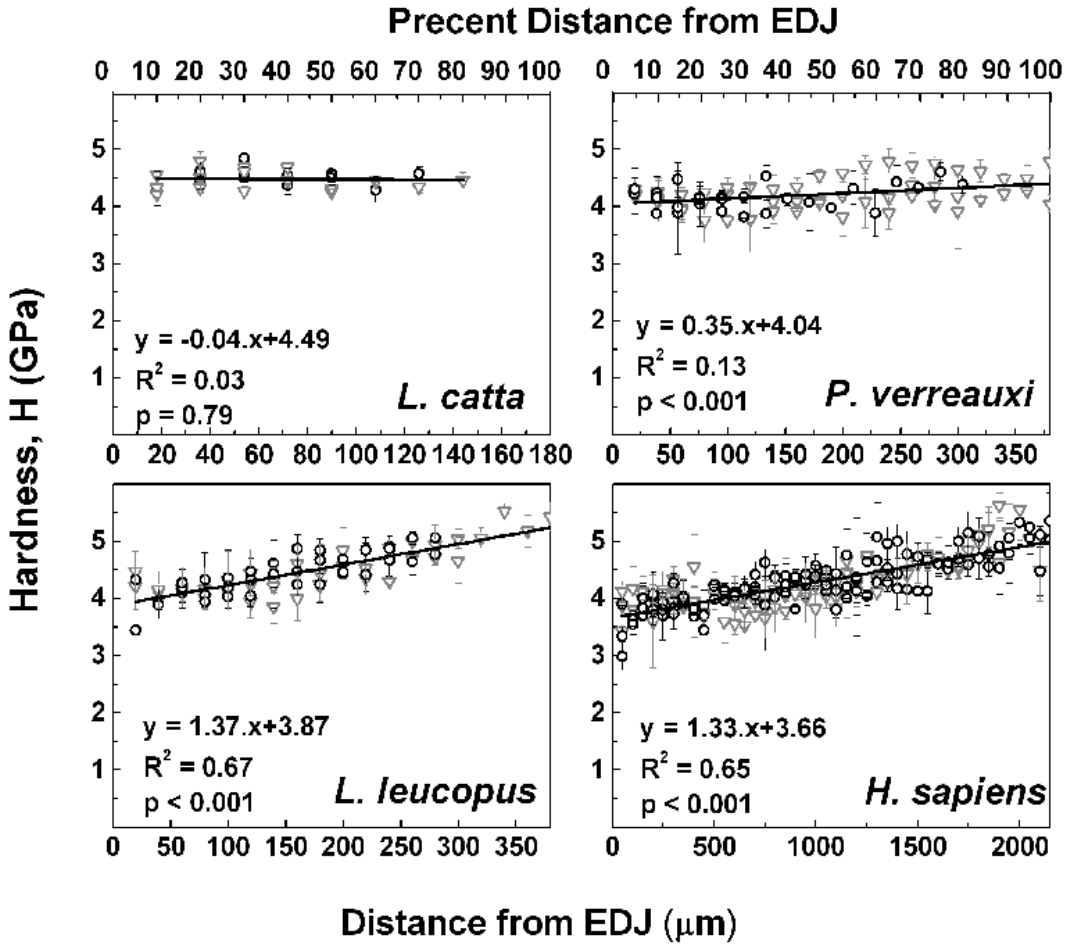

Figure 6.5: Nanoindentation hardness of dental enamel of three lemur species plus human. Open circles and triangles each represent an individual sample. Three indentation arrays were placed on each samples perpendicular to and covering the area from EDJ to occlusal surface. Each data point represents the mean ± standard deviation of four (3 for human sample) indentations taken in a row at equal distance from the EDJ (distance = 0) to OS. Rows were spaced 20 μm apart in lemur species and 50 μm in human sample. Linear fit equation for all data points are listed.

Table 6.3: Measured and literature values for RET and prism patterns (PP) indicating the presences of Hunter-Schreger bands (HSB). Additionally literature (lit.) values for the mass and observed diet of each species are listed. + Malagasy strepsirrhine taxa. a (Martin, 1985), b (Godfrey et al., 2005), c (Martin et al., 1988), d (Boyde and Martin, 1982), e (Maas, 1994), f (Fleagle, 1998), g (Kay, 1975), h (Harcourt and Thornback, 1990), i (Tattersall, 1982), j (Jolly, 1966), k (Rand, 1935), l (Shaw, 1879), m (Sussman, 1974), n (Hill, 1953), o (Forber, 1894), p (Nash, 1998), q (Schoeninger et al., 1998)

Taxon	**Observed RET mean (std)**	**RET Lit. Mean (n), Range**	**Observed PP (HSB)**	**Lit. PP (HSB)**	**PW (µm) mean(std)**	**Body Mass (g)**	**Diet**
H. sapiens	*H. sapiens* 1= 29.09 (0.18) *H. sapiens* 2= 25.92 (0.15)	22.4 (13)[a] 13.8 – 32.3	3 (HSB)	1, 2, 3 (HSB)[c,d]	6.33(0.62)	>40,000[f]	Processed foods
L. catta	*L. catta* 1= 4.09 (0.02) *L. catta* 2= 3.49 (0.08)	6.7 – 8.1[b]	3 (HSB)	1, 3 (HSB)[e]	4.47(0.37)	~2210 [f, g]	Fruit, wild figs, bananas, leaves, herbs, flowers [j, k, l, m]
P. verreauxi+	*P. verreauxi*1= 11.78 (0.09) *P. verreauxi* 2= 7.89 (0.56)	10.7 [b]	3 (HSB)	1, 3 (HSB)[e]	4.49(0.71)	~3000 [f, g]	Leaves, flowers, bark, some fruit [j, k, n, o]
L. leucopus	*L. leucopus*1= 16.47 (0.18) *L. leucopus*2= 15.23 (0.19)	N.A.	3 (no HSB)		3.87(0.33)	~540 [h, i]	Leaves, fruit, flowers, cecotroph [p, q]

species that displayed little to no wear. This general increasing trend corresponds with the general increase in mechanical properties seen for the EDJ to OS.

Additionally prism orientation varied from the EDJ with more randomly oriented prisms with Hunter-Schreger bands (HSB) to radially oriented prisms at the OS for all samples except Lepilemur (Figure 6.6). There was no evidence of HSB in the *L. leucopus* samples. Observed prism orientation and prism patterns for each species are reported in Table 6.3. Prism width was measured near the OS on one sample of each species and reported in Table 6.3. Prism width scaled with the mass of the species as Human enamel had the widest prisms and *L. leucopus*, the lightest species, had 48% reduction in prism diameter compared to humans. Prism diameters were similar to those previously reported ranging from 3.5 to 6 μm for a variety of lemur species (Maas, 1994).

6.3.3 Detection of micro-damage with Nanoindentation

Nanoindentation test sites within one indent width of a crack (category 3 & 4) had increased depth of penetration or permeant deformation evident in load-displacement curves (Figure 6.2A). Further, indentation testing within three indent widths of the testing site (category 2-4) resulted in reduced modulus and hardness values as grouped by species in Table 6.4. For all species there was an average decrease in modulus of 5% and hardness of 7% from category 1 to 2. Even larger differences were observed in category 3 and 4, where in group 4 an average 39% decrease in modulus and 49% decreases in hardness were observed compared to category 1.

Microcracks were visible on all samples and were primarily located near the EDJ except in *L. catta* (Figure 6.2B) where substantial cracking was also visible at the occlusal surface. Micro-cracks on *L. catta* were located at a distance of 70% of the enamel thickness from the EDJ compared to an average distance of 21% of the enamel distance in the other species (see Table 6.5). Additionally, *L. catta* samples had significantly more microcracks than other species, where 45% of all indentation test locations landing within three indent-widths of a

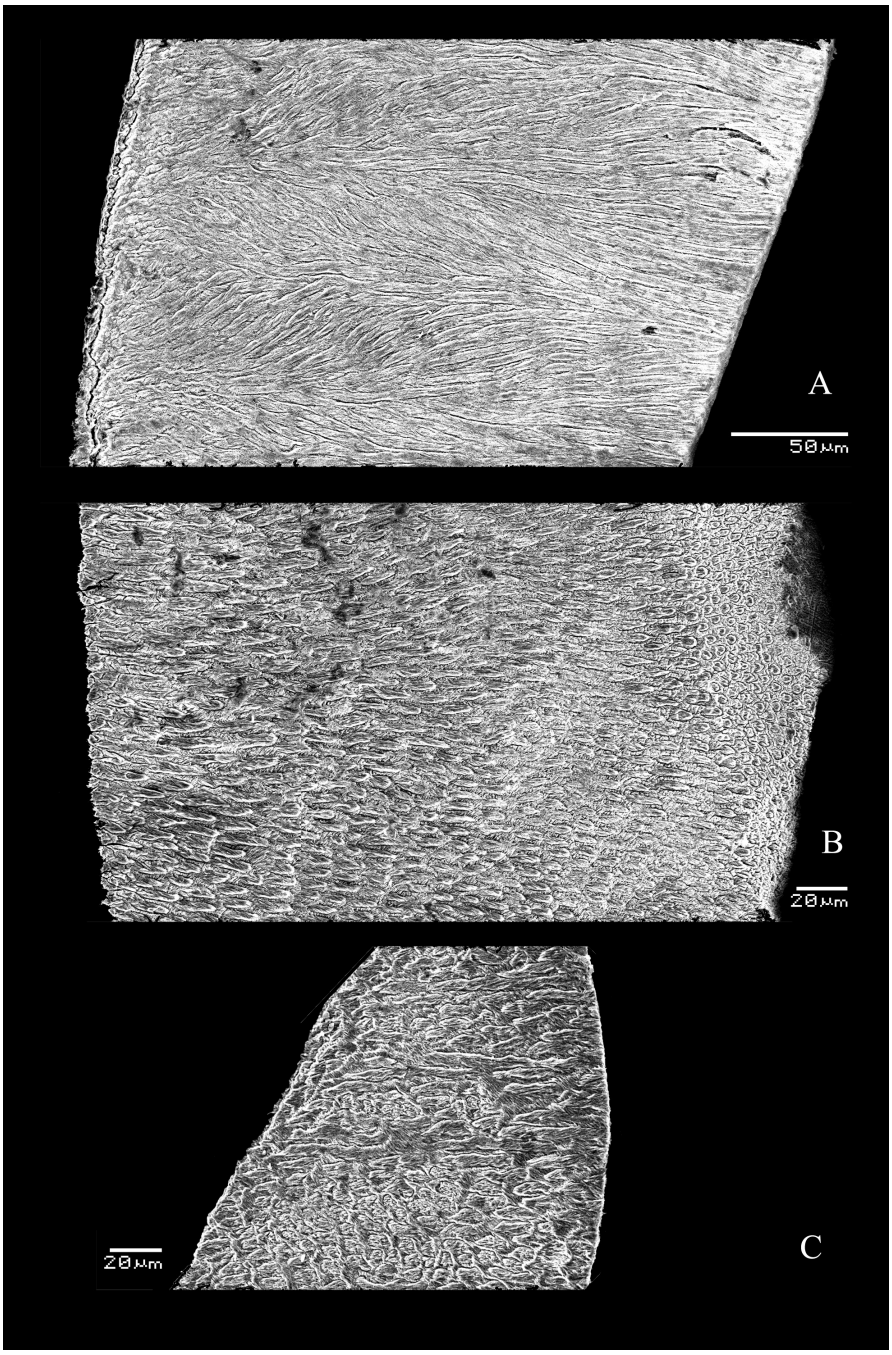

Figure 6.6: BSE images of etched enamel of A) *P. verreauxi*, B) *L. leucopus*, C) *L. Catta* with the OS on the right side of the image and EDJ on the left. Prism patterns are visible after 60 s of etching with 0.5 % H_3PO_4. Samples were coated with carbon.

Table 6.4: Nanoindentation data was classified into 4 groups based on location of indent test site to a micro crack. Categories represent: 1 = prefect indent location with no visible damage, 2 = crack distance greater than one to three indent widths away from indent location, 3 = crack located within one indent width for test site, 4 = indent on top of crack or visible damage. One-way ANOVA with a Bonferroni follow on test was used to compare difference between species on grouped data from the two samples with perfect (category 1) indent test. Significant difference between groups indicated for $p < 0.05$ where * = vs *H. sapien*, §= vs *P. verreauxi*, # = vs *L. catta*, %= vs *L. leucopus*.

Crack category (n)	H ± SD (GPa)	E'± SD (GPa)
H. sapien		
1 (578)	4.34 ± 0.48 ♯,%	92.73 ± 6.14 ♯,%,§
2 (35)	3.89 ± 0.40	82.88 ± 3.82
3 (11)	3.83 ± 0.36	80.74 ± 3.66
4 (6)	2.28 ± 1.53	53.97 ± 21.31
P. verreauxi		
1 (215)	4.26 ± 0.33 ♯,%	89.54 ± 3.98 %, *
2 (28)	3.97 ± 0.29	85.58 ± 3.14
3 (26)	3.92 ± 0.22	83.86 ± 2.41
4 (8)	2.07 ± 1.04	60.23 ± 15.26
L. catta		
1 (92)	4.48 ± 0.21 *, §	87.73 ± 5.36 *,%
2 (13)	4.43 ± 0.27	86.23 ± 7.95
3 (25)	3.88 ± 0.62	76.07 ± 14.16
4 (36)	2.71 ± 1.66	56.91 ± 30.14
L. leucopus		
1 (261)	4.57 ± 0.48 *, §	78.89 ± 5.87 ♯,*,§
2 (15)	4.08 ± 0.66	75.94 ± 9.65
3 (43)	3.98 ± 0.36	70.13 ± 5.99
4 (7)	2.00 ± 1.83	42.74 ± 22.41

crack (category 2-4) compared to an average of only 31% of testing site on the other samples.

6.4 Discussion

The complex functionality of primate teeth depend on mechanical and material characteristics as well as a number of morphological properties (i.e. size, shape, and enamel thickness) (Crompton and Sita-Lumsden, 1970; Gregory, 1922; Kay and Hiiemae, 1974; Maas and Dumont, 1999). While whole tooth morphology has been widely characterized in studies of primate diet and microwear, investigation of mechanical properties has been limited (Darnell et al., 2010). In this study, variation in enamel microstructure, mineralization, and mechanical properties were explored within single molars and between lemur species and humans. Comparison of enamel at the EDJ reveled similar mean properties between species. However significant intra-tooth variability was evident as the coefficient of variance (CV) within each sample ranged from 4.0 to 11.9% for H and E' indicating the fundamental heterogeneity of enamel. The numerous variations of mechanical properties of enamel within and between species are inherently linked to mineralization and microstructure that are altered by the destructive wear process.

6.4.1 Variations between species

Our reported mean values fit within the range of modulus and hardness of mammalian enamel previously measured by nanoindentation (Table 6.1). Further, our human data corresponds with previous studies of the nanomechanical properties of human enamel (Cuy et al., 2002; Habelitz et al., 2001; Zhou and Hsiung, 2007) (Table 6.1, 6.2). While variations in the mechanical properties of teeth of several species have been reported, meaningful comparison is difficult as these studies have low n-values and often only report a mean value for an entire tooth. As shown here and elsewhere (Cuy et al., 2002; Darnell et al., 2010), large variations in mechanical properties exist from the EDJ to the OS in primate enamel indicating that average mechanical values are not representative and are not an ideal way to compare be-

Table 6.5: Data from the two samples within each species were grouped to determine the precent cracking and location based on the % distance from the EDJ. The % cracking was calculated as the sum of all indents within three ident width or less of a crack (categorty 2, 3, 4) divided by the total number of indent sites [(cagtegory 2 + 3 + 4)/ (total # of indents)]. The % distatance from the EDJ, normalized to the length of each array, was calcluated for each indent sites classified as (2, 3, 4) to give an indication of the location of cracking.

Species	**% cracking**	**%distance**
L. catta	44.58	70.19
P. verreauxi	22.38	40.89
L. leucopus	19.94	32.12
H. sapien	19.93	21.46

tween species. Additionally, large variation in mechanical properties exists between different teeth within one animal (i.e. M^1 v.s. M^3, Table 6.1) (Darnell et al., 2010). An alternative comparison of mechanical properties between species might be made through values near the EDJ (Table 6.2), especially when considering samples that have been worn by mastication. Further, the mechanical properties of the OS in human enamel have previously been show to increase with aging and fluorination. In this study, comparison of the modulus of the EDJ set of data between species demonstrated little variation between samples, as the modulus was 88 $\pm$ 3 GPa for all of the species except *L. leucopus* which had a modulus of 78 GPa. Recently, Darnell et al. (2010) proposed a similar method of comparison between samples and reported *Alouatta palliata* (howler monkey) buccal cusp modulus values near the EDJ to have modulus values of 85 and 77 GPa for M^3 and M^1 respectively. While these values are in the range of our measured values a direct comparison is difficult as we sampled M^2 and large variations in mechanical properties clearly exist between different molars (Darnell et al., 2010).

In addition, the gradient in mechanical values from the EDJ to OS needs to be considered when comparing species. There was a general increase in mechanical properties from the EDJ to the OS in modulus and hardness for all species except *L. catta* (Figures 6.4, 6.5). The difference seen in *L. catta* is likely a result of the extreme wear and cracking present at the OS (further discussed later). A similar gradation in mechanical properties towards the OS has been observed in humans (Cuy et al., 2002), gorillas (Constantino et al., 2009), and howler monkeys (Darnell et al., 2010). Gradation of mechanical properties may help transmit load into the supporting dentin and possibly prevent crack formation. This gradation of nanomechanical properties is variable between the species as demonstrated by the percent difference in E and H between the EDJ and OS half (Table 6.2). The variations in the mechanical gradation magnitude and profile from the EDJ to OS likely has implications to the functional adaptations of different teeth based on diet and evolutionary trends. *H. sapiens* displayed the largest gradient of mechanical properties with 12.7% increases in hardness

and an 8% increase modulus from the EDJ to OS. Lemur species had smaller differences in mechanical properties, which may be linked, to thinner enamel or wear of the outer surface. Both *L. catta* and *P. verreauxi* 2 samples had the most severe wear and the smallest increase in mechanical properties suggesting that the hardest outer portion of the enamel surface had been removed though the wear process.

6.4.2 Variations in Mineralization and Microstructure

A general trend of increasing WMGL was present from the EDJ to the OS, which corresponds with the increase in mechanical properties in all species except *L. catta*. The human molars had the largest increase in WMGL, which corresponded with the largest increase in mechanical properties (Table 6.2). Our finding corroborate previous results which correlated increased mechanical properties to increased mineral content (Cuy et al., 2002; Robinson et al., 1995). In human enamel, weight percent mineral has shown to increase from 84% at the EDJ to 96% at the OS (Robinson et al., 1995). Variations in mineral composition have also been observed in *Alouatta palliata* (howler monkey) enamel where mineral content (P_2O_5 and CaO) measured by electron microprobe was highest at the hard occlusal surface and decreased toward the EDJ, corresponding with mechanical properties (Darnell et al., 2010).

While variation in mineralization can account for general mechanical property trends from the EDJ to the OS, the difference in WMGL between species was minimal and cannot explain lower modulus values in *L. leucopus*. The microstructure of enamel is also known to contribute to the measured mechanical properties though prism orientation (Jiang et al., 2005; Spears et al., 1997) and prism size (He et al., 2006). Prism orientation in all species except *L. leucopus*, was more random near the EDJ with the presence of HSB and radially oriented at the OS. It has been suggested that the majority of primates with a body mass less than 2000 g generally do not display HSB (Maas and Dumont, 1999) and *L. leucopus* is no exception. HSB are thought to help stop crack propagation and may provide

increased mechanical properties to the whole tooth. While the HA crystals that combine to create enamel prisms are inherently anisotropic there is much debate on the effect of this anisotropy on the mechanical properties of enamel. Nanoindentation tests in the occlusal direction were shown to have greater modulus and hardness values than those tested in the axial direction both, experimentally (Jiang et al., 2005) and through finite element analysis (Spears et al., 1997). However, another nanoindentation study (Braly et al., 2007) found no directional differences and attributes previous findings to variation in mineralization. As enamel prisms are anisotropic, prism orientation is likely to contribute to the mechanical response. However, nanoindentation is a multi-axial test (averaging properties in all three directions) and therefore less sensitive to measurement of anisotropy. Our data were averaged over several indentation points with variable prism orientations, effectively averaging out the effect of anisotropy in enamel containing HSB. However, *L. leucopus* enamel did not display HSB and all indentation test were made in the axial direction of the prisms. The reduced mechanical properties seen in *L. leucopus* as compared to the other species maybe a result of axial prism orientation with no HSB.

Additionally, prism size may contribute to the reduced mechanical properties seen in *L. leucopus*. Using AFM-based nannoindentation, Ge et al. (2005) has reported that the modulus and hardness of the prism sheaths were about 73.6% and 52.7% lower respectively than those of the prisms. In indentation testing the volume of deformed material increases with the depth of penetration of the indenter tip (Johnson, 1985). Thus a low depth indent, similar to those reported with atomic force microcopy (AMF) based indentation, when placed at the center of a prism will test only the crystals within that single prism. As the depth of the indent increases a larger volume may include both prisms and sheath and thus the resultant mechanical properties will be reduced compared to a test which only samples the prism. This concept has been demonstrated in human enamel where the mechanical properties have been shown to decrease with an increase in indentation depth (He et al., 2006; Zhou and Hsiung, 2007). In this study an indentation depth of about 800 nm results in an effective contact

radius of $\approx$ $5\mu m$, on the same order of the diameter of the enamel prisms. As indent sites were randomly placed with respect to prism boundaries most tests likely probed the combined mechanical properties of the prisms and sheaths. However, *L. leucopus* had the smallest prism diameter ($\approx$ $3.8\mu m$) indicating that every test, even when placed at the center of the prism, tested sheath material potentially leading to reduced modulus values compared to the other species with larger prism diameters. Further, the AFM study shows the sheath to experience a larger decrease in modulus than hardness values compared to the prism (Ge et al., 2005), which may also contribute to the fact that only modulus values and not hardness values were reduced in *L. leucopus* compared to the other species tested.

6.4.3 *Lemur catta* Micro-cracking and Wear

L. catta displayed severe wear in both samples as evident from reduced RET compared to non-worn samples (Table 6.3) and substantial cracking compared to other species (Table 6.5). The Beza Mahafaly *L. catta* population has been documented with extreme tooth wear and loss as a result of their extremely thin enamel and consumption of the hard-tough tamarind fruit (Cuozzo and Sauther, 2004; Cuozzo and Sauther, 2006; Sauther et al., 2002). It has been suggested that consumption of fallback foods, such as the tamarind fruit, contributes rapidly to evolutionary alterations of dentition (Kinzey, 1987; Lambert et al., 2004; Yamashita, 1998). Cuozzo and Sauther (2006) suggested that as the morphology of *L. catta* molars indicated adaptation to folivory (Seligsohn, 1977) then only recently has the tamarind fruit become a key fallback food to the ring-tailed lemurs in Beza Mahafaly. Our study collaborates this theory as the mechanical properties of *L. catta* are most similar to *P. verreauxi*, who possess a similar diet, indicating no evidence of mechanical property adaption to allow for consumption of the tamarind fruit.

Severe cracking present in the OS half (Table 6.5) corresponded to significantly reduced modulus and hardness values (Table 6.4) of the *L. catta* samples in this study and further points to the extreme wear and damage caused by consumption of the tamarind

fruit. It should be noted that all lemur tooth samples were found on the surface and thus subjected to unknown dehydration conditions which may contribute to cracking. However, the human samples were dehydrated in laboratory controlled conditions though a series of ethanol solutions, yet displayed similar cracking trends to *L. leucopus* and *P. verreauxi* with cracking along the EDJ. Therefore the substantial cracking present near the OS in *L. catta* (as depicted in Figure 6.2) is unlikely to be the result of dehydration. There was no change in WMGL within the cracked region indicating that reduced mechanical properties are not the result of demineralization from the acidic tamarind fruit, but rather mechanical abrasion. Cracking in enamel is cumulative process as no remodeling of the tissue occurs over the lifetime of the animal. The process of cracking likely accelerates the rate of wear as reduced mechanical properties were evident in testing sites near micro-cracks (Table 6.4, Figure 6.2).

6.5 Damaged Enamel Finite Element model

A finite element model of spherical indentation of enamel was developed to consider the effect of the proximity of cracking in dental enamel on the measured indentation moduli values. Experimentally measured modulus and hardness values were shown to decrease up to 50% when located within one indent width of a crack (Table 6.4). Cracking in enamel has commonly been observed to occur around the edge of prisms at the interface with the organic sheath or inter-rod region (see Figure 2.5). A stress concentration point occurs where the prism meets the organic sheath a direct result of the materials differing mechanical properties. Using AFM-indentation, at depths of 30-80 nm, the modulus of the enamel prisms (E_R= 83.4 GPa) and inter-prism regions (E_R = 39.5 GPa) have been measured (Ge et al., 2005). The smaller mechanical properties of the inter-prism region is a combined result of decreased mineral content and a less highly organized crystals than within the prism.

An axis-symmetric FEA model was created to evaluate the contribution of micro-cracking to the measured nanomechanical response of enamel. The proximity of indent site to a crack was explored assuming that the presence of a crack indicated no lateral connectivity

of the enamel prism to the surrounding material. As such the edge of the half-space can represent void space or crack. Alternatively in many experimental samples this void space may be filled with PMMA, thus providing some level of stability to the region. These two cracking cases were compared against an "intact region" of enamel that is surrounded by prism sheath.

6.5.1 Methods

The ABAQUS/Standard student edition finite element code with CAE was used to simulate nanoindentation of enamel. Contact between an analytically rigid spherical tip (R = 5 μm) and an elastic half-space was modeled using hard, frictionless contact along with large deformation theory. Finite element meshing used CAX4 (4 node, bilinear, axisymmetric) elements and was limited to 1000 nodes, as imposed by the student edition of ABAQUS. For each model the optimal use of the 1000 nodes resulted in variable element size between different models. Convergence of solution for the least dense mesh was verified through superposition of load-displacement curves and agreement of max load values with COV = 2.33% for the 15 x 15 node up to 30 x 30 node mesh. The half-space was meshed with the number of elements biased beneath the indenter tip. Boundary conditions were applied to the fix displacement of the bottom nodes. The axial symmetric model contained two material regions: an inner cylinder of enamel (radius = R') and a region of 50 μm of surrounding material (PMMA or inter-prism) as represented by the blue colored region in Figure 6.7. The total radius of the model R_t is the sum of the radius of the enamel portion R' plus the 50 μm of surrounding material. In the void case, no surrounding region was used and no boundary conditions were placed on that edge to allow outward deformation. The distance R' from the indent location to the crack or material interface was explored by holding H constant (100 μm) and varying R' from 1 to 100 μm. The material parameters are listed in Table 6.6 and all values used were measured experimentally using indentation testing.

The indentation process was simulated with two analysis steps (load and unload) in

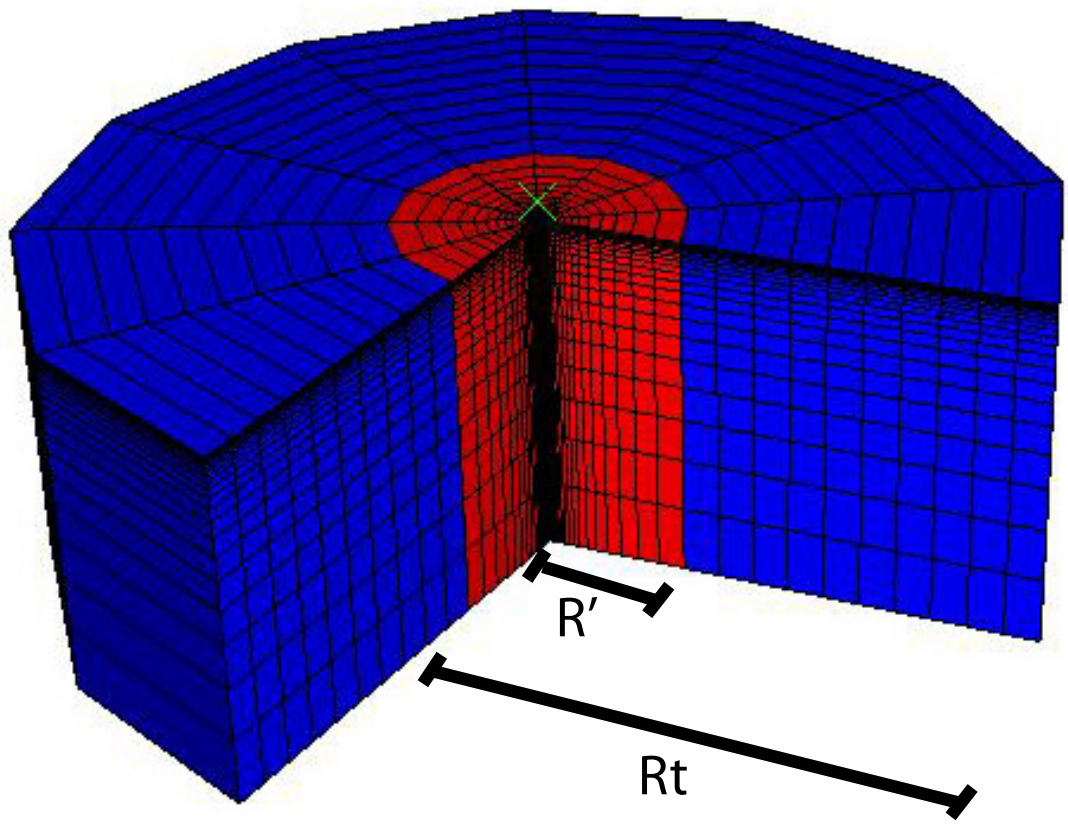

Figure 6.7: An axial symmetric model for indention near a crack or material boundary. A 5 μm spherical indenter tip is placed in the center of a region of enamel (E_R = 83.4 GPa) with radius R'. This is immediately surrounded by a 50 μm region of material to simulate void space (E_R = 0), void space infiltrated with PMMA (E_R= 3.5 GPa), or intact enamel prism surrounded by inter-prism (E_R = 39.5 GPa).

Table 6.6: Input FEA material properties.

Material	**E_R (GPa)**	**Poisson's Ratio (ν)**	**Reference**
Prism	83.4	0.25	(Ge et al., 2005)
Inter-prism	39.5	0.25	(Ge et al., 2005)
PMMA	3.5	0.35	(Bushby et al., 2004)

which the indenter tip was displaced downward 800 nm during loading and then returned to the original location during unload. The displacement boundary condition was applied to the indenter tip over one unit of time for both steps and does not consider any time-dependent properties. The data for the reaction force vs the displacement of the spherical tip was analyzed using the traditional Oliver-Pharr method (Oliver and Pharr, 1992) to extract the reduced modulus from the first 50% of the unloading curve. As this simulation only considered elastic properties the load and unload curve are coincident.

In order to consider the proximity of the indenter tip to material interface the contact radius (a) of the spherical tip must be considered. As discussed in section 3.2.1, the contact radius of a spherical tip is dependent on the contact depth (δ) given by:

$$a^2 = R\delta \tag{6.1}$$

Comparison of this contact radius to the dimension of interest (the distance to edge R') creates a scaled result that permits comparison between different tip sizes and indent depths. All indents in this model were made to 800 nm to allow for comparisons to experimental results, thus producing a contact radius a = 2 μm.

6.5.2 Results and Discussion

The load displacement plots for the enamel cracking axis symmetric model are seen in Figure 6.8. For all three cases (void, PMMA, and inter-prism) the stiffness of the load displacement curve decreased as the distance to the edge (R') decreased. For the void case,

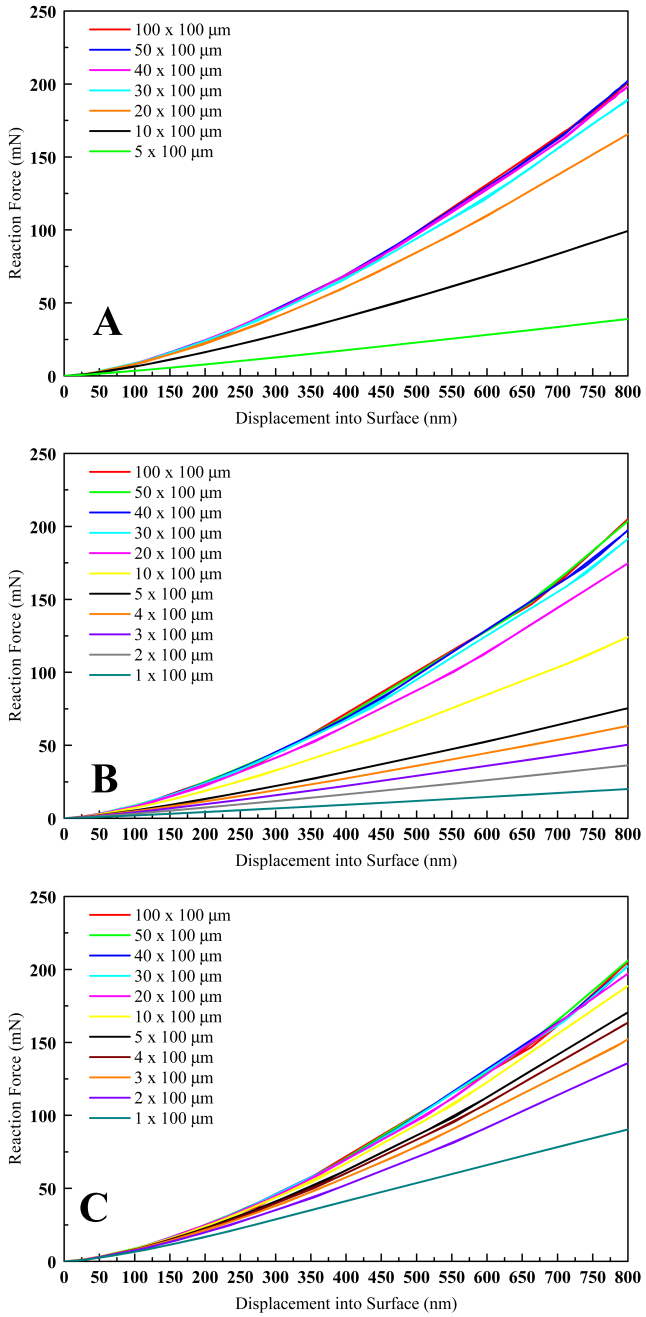

Figure 6.8: Reaction force vs displacement of the rigid spherical indenter tip displaced 800 nm into an enamel half-space of size R' x H with 50 μm of surrounding material made of A) void, B) PMMA, C) inter-prism.

in which no material surrounded the enamel region, an apparent change in the mechanical response was evident for indent locations with $R' \leq 20\mu m$. A similar response was apparent in the PMMA where an initial decrease is stiffness was seen at $R' \leq 20\mu m$, yet the decrease was less substantial for R' =10 and 5 μm away from the tip as compared to the void case. For the inter-prism case, a decrease in mechanical properties was not evident until $R' \leq 5\mu m$ a direct results of the significant higher modulus of the inter-prism material than PMMA.

The presence of a void space, even one filled with PMMA, played a significant role in the mechanical response of an indent test site upto 20 μm away. This distance is larger than expected using contact mechanics where the elastic stress field for bone has been approximated as a paraboloid of revolution of radius 3a and 5a in depth (Bushby et al., 2004). For these simulation the paraboloid would have a radius of 6 μm. Alternatively a common rule of thumb for spacing of indent array is generally 5-10 times the indent depth (in this case 4 to 8 μm). Thus, the use of either of these approximations (up to 8 μm) to space experimental indent arrays near cracks or material interface region could result in measurement errors. Measurements on "intact" enamel (simulation using surrounding inter-prism material) showed that a material interface up to 5 μm away contributes to the mechanical response. While, this distance agrees with contact mechanics approximations, caution should always be taken to provide sufficient indent spacing. Further, it is possible that subsurface cracks might be present at any given indention site and can unknowingly contribute to the measured mechanical response.

A significant advantage of this axial symmetric model is that it allows direct application of the Oliver-Pharr method (Oliver and Pharr, 1992) to extract reduced modulus values from unloading. The reduced modulus from FEA simulations is plotted vs the contact radius divided by the distance to edge (a/R') in Figure 6.9. Additionally, representative experimental value from each of the four cracking categories (see Table 6.4) are plotted for *L. catta*. The distance to crack was measured for each representative experimental indent site on an SEM image using Image J software package. For the indent with no cracks the

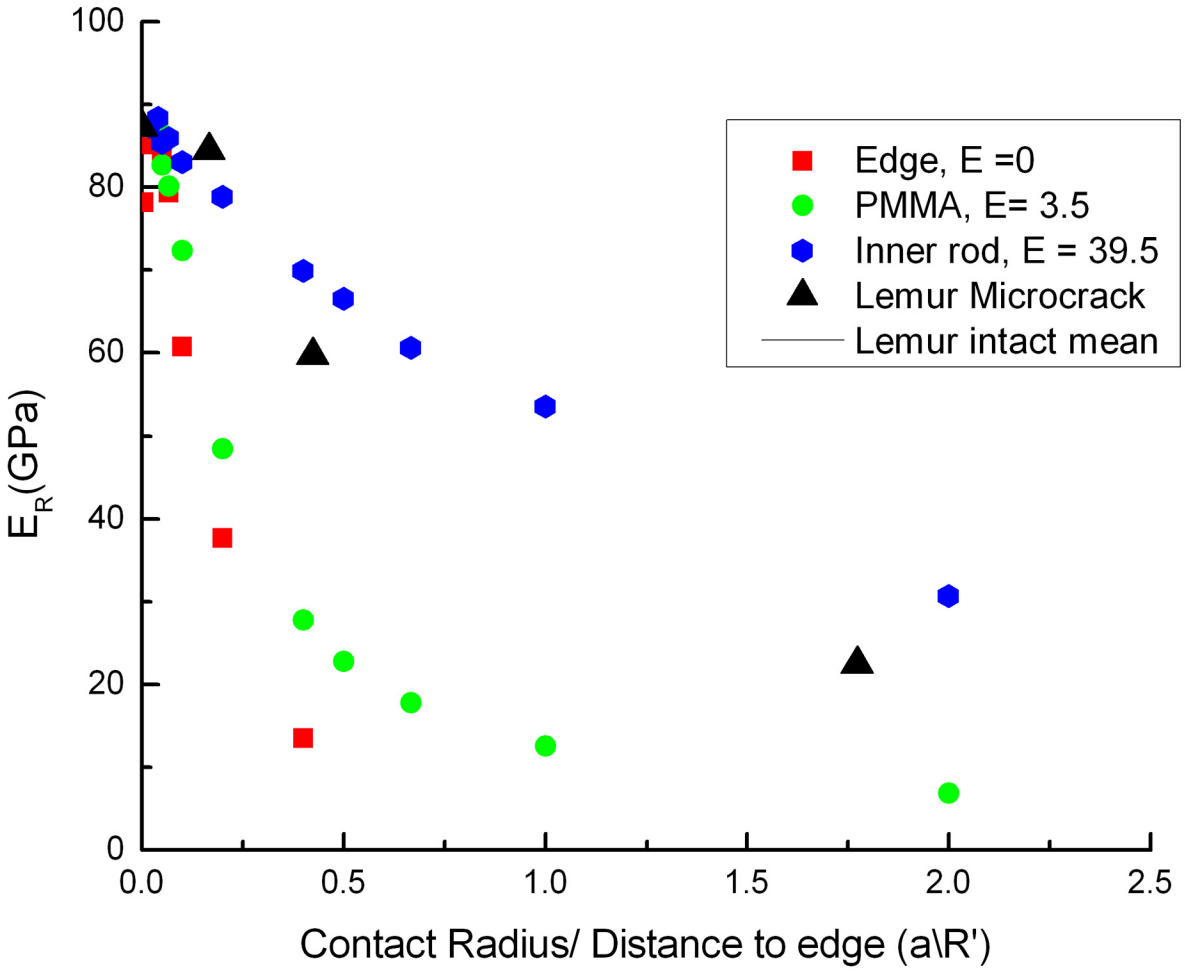

Figure 6.9: E_R values vs contact radius/ the distance to edge of material interface with either a void space, void space filled with PMMA, or inter-prism. Representative experimental data points are plotted from for indentations on Lemur *catta* near cracks.

distance to edge was assumed to be 20 μm as this was the spacing of the indent array. At low values of (a/R') the moduli of all data sets converged to the modulus of enamel at (80 to 90 GPa). As a/R' increases the measured modulus values decrease and asymptotically approached the mechanical properties of the second surrounding material. Both the PMMA and void simulation decreased more quickly with increasing a/R' values than the inter-prism simulations.

Nanoindentation of lemur enamel with micro-cracks followed a similar trend as the models, where increase values of a/R' resulted in decreased mechanical properties. This trend most closely resembling the inter-prism simulations, a likely results of the model's overestimation and assumption of the mechanical contribution of 360° crack. This model assumes that the presence of a crack indicates no connectivity to the surrounding material. In reality a crack would represent a single line of non-connectivity around which the material would remain intact due to the three dimensionality. Thus it is not surprising that the experimental values maintain some mechanical stability near a crack, at least more so than an infinite crack modeled in this FEA.

6.6 Enamel Prism Size Finite Element model

To further explore nanoindentation of enamel a two dimensional plane strain model was developed, which is not limited to circular symmetry as above. Specifically this model will look at the effect of enamel prism size on measured mechanical properties. As discussed above, the smallest lemur species studied, *L. leucopus*, had the smallest average enamel prism diameters ≈3 μm, as compared to 5-7 μm measured in human enamel measured in this study and in the literature (Ge et al., 2005; He and Swain, 2008). Further, *L. leucopus* had the lowest values of moduli compared to the other lemurs and human enamel. A wide number of complex factors could have contributed to these lower modulus values including prism orientation, the lack of decussation, or prism size. The use of FEA will allow isolation of the contribution of prism size to nanoindentation measurements.

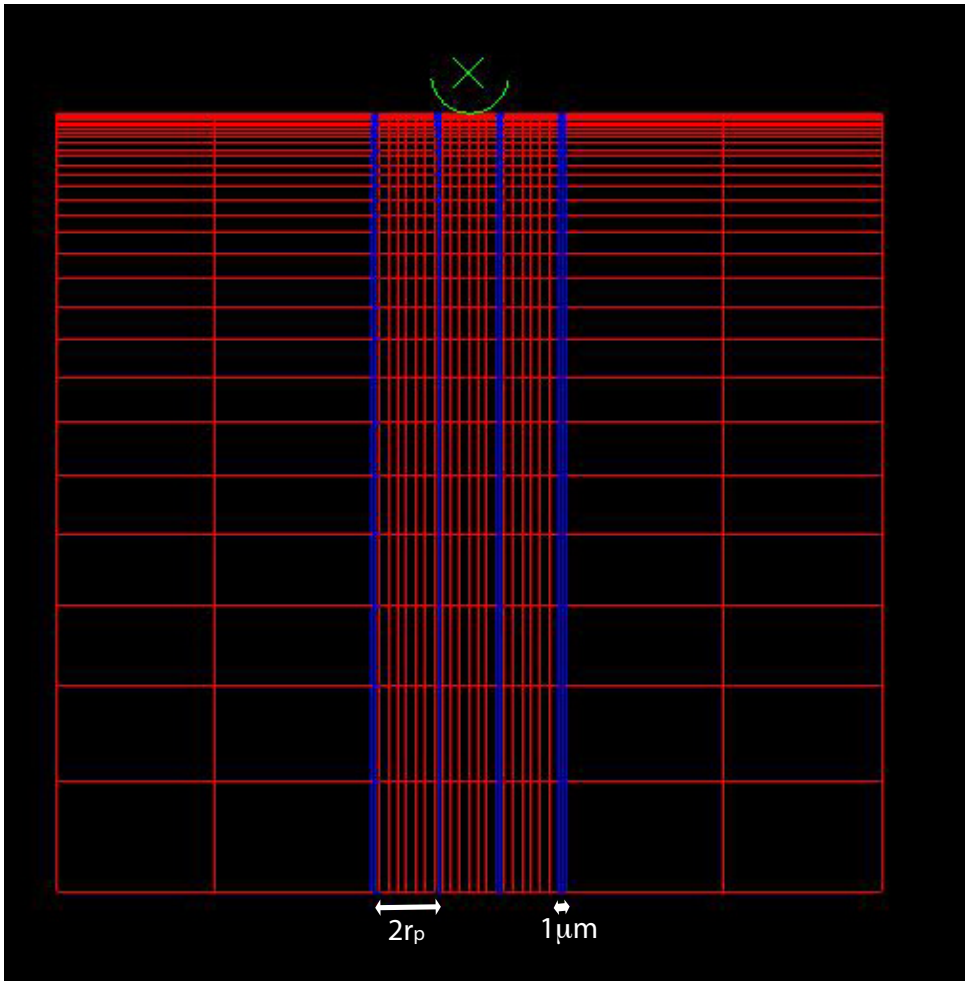

Figure 6.10: FEA mesh for prism model to explore the effect of the prism radius r_p on spherical nanoindentation test. Between each prism (red, E = 83.4 GPa) is a region of inter-prism (blue, E = 39.5) material. Three prism/ inter-prism regions were modeled surrounded by prism material and x-axis symmetrical boundary conditions to represent an infinite half-space.

6.6.1 Methods

In plane strain analyses, a two dimensional model is developed and extended into infinity in the third dimension. While the indenter and geometry are clearly not infinitely long, a relative measurements of modulus can be made by comparing models to a base case with stiffness (S_b). For the base case a 100 x 50 μm block of enamel (E = 83.4 GPa) was used. Boundary conditions of fixed bottom and x-symmetry on both edges was used to simulate an infinite half-space and to match the base case from the axial symmetric model above. For all plane strain models the stiffness (S) was determined from the slope of the load-displacement curve. An effective modulus (E_{eff}) can be determined as the ratio of the stiffness of the model (S) to the stiffness of the base case (S_b) multiplied by the input modulus of the base case (for enamel E = 83.4 GPa).

$$E_{eff} = \frac{S}{S_b} 83.4 \tag{6.2}$$

This two dimensional spherical indention model consists of three prisms/ inter-prism regions as seen in Figure 6.10. Each enamel prism (red, E = 83.4 GPa) was placed adjacent to a region of inter-prism material (blue, E = 39.5 GPa). The radius of the prism (r_p) was modeled for values of 1.5, 2.5, and 3.5 μm to correspond to values seen in lemur and human enamel. The inter-prism region has been measured to be 1 μm in human enamel (Ge et al., 2005) and was held constant for all simulations. Three prism/ inter-prism regions were modeled surrounded by prism material (E = 83.4 GPa) and x-axis symmetrical boundary conditions to represent an infinite half-space. The spherical indenter tip (R = 5 μm) was loaded into the material to a series of depths (0.6, 0.8, 1, 1.5, 2, 3 μm) to explore a wide range of contact volumes.

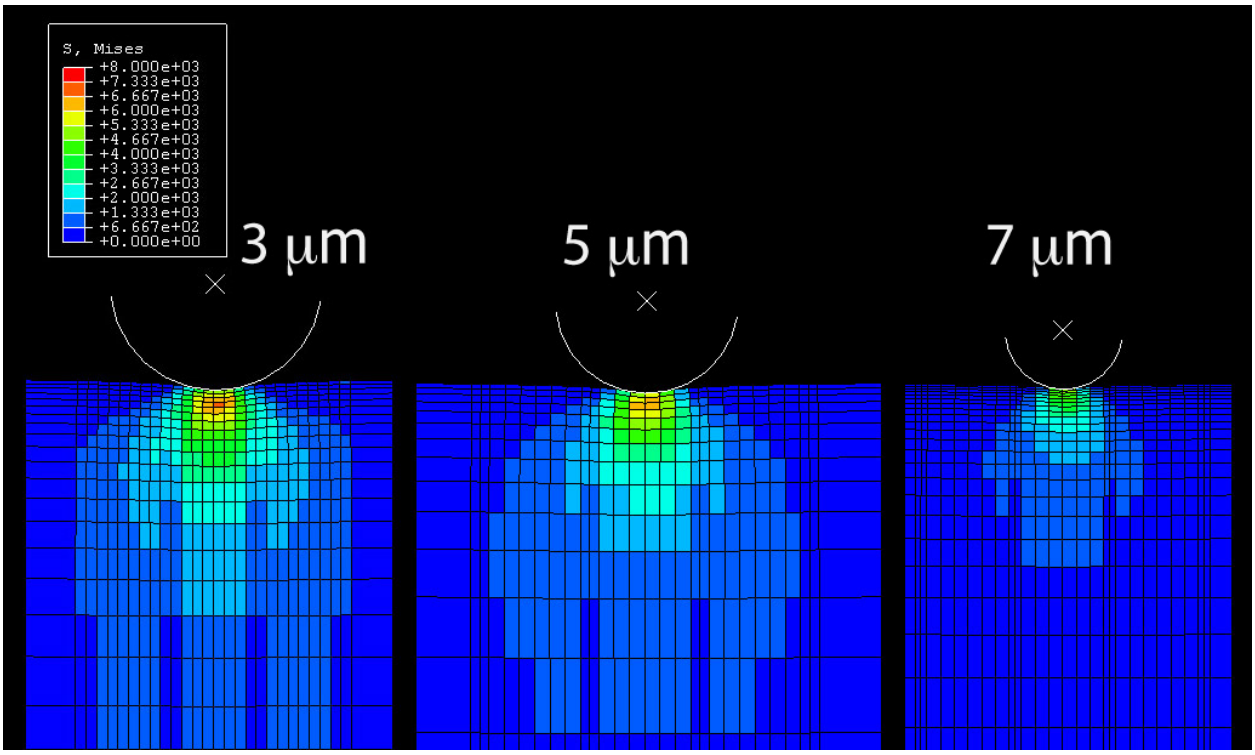

Figure 6.11: Stress fields for enamel prism model for prism diameter of 3, 5, and 7 μm. The 5 μm spherical tip was displaced into the half-space 800 nm. While the stress field remains primarily in the center prism for the 7 μm, it crosses over the inter-prism region transferring stress to the surrounding prisms in the 5 and 3 μm diameter prisms.

6.6.2 Results and Discussion

The stress fields for this enamel prism model is plotted for the 800 nm displacement case with the 5 μm radius tip in Figure 6.11. The the stress field remains primarily in the center prism for the 7 μm diameter, yet crosses over the inter-prism region transferring stress to the surrounding prisms in the 3 and 5 μm diameter prisms. The less stiff inter-prism region can support less load and results in the striping appearance in the stress plots. While, the Von Misses stress values in the figure are not representative of a true indentation test, they allow for direct comparison of the stress field between prisms sizes. While the inter-prism region supports less load than the prism region, this material plays a vital role in the transfer of stress to the surrounding prism. Damage to the inter-prism region can drastically alter the mechanical response as discussed above in the cracking model.

A decrease in the effective modulus was seen with an increase in contact radius and thus also the displacement of the indenter tip (Figure 6.12). At the deepest indent depths the effect of prism size was minimal as the effective modulus approached an average modulus of both the prism and the inter-prism regions. At larger values of contact radius (a), more inter-prism material is included in the the contact volume resulting in decreased E_{eff} as compared to shallow indents with low values of 'a' which primarily test only prism material. Only at indent depths of less than one micron (a $\leq$ 2.2 μm) is the contribution of prism size evident. At low contact depths (see Figure 6.11), the majority of the load is carried in a single prism resulting in higher effective modulus values for larger prism sizes. This corresponds with experimental results indicating that the smaller prism size of *L. leucopus* might contribute to the reduced mechanical properties as compared to the other species in the study.

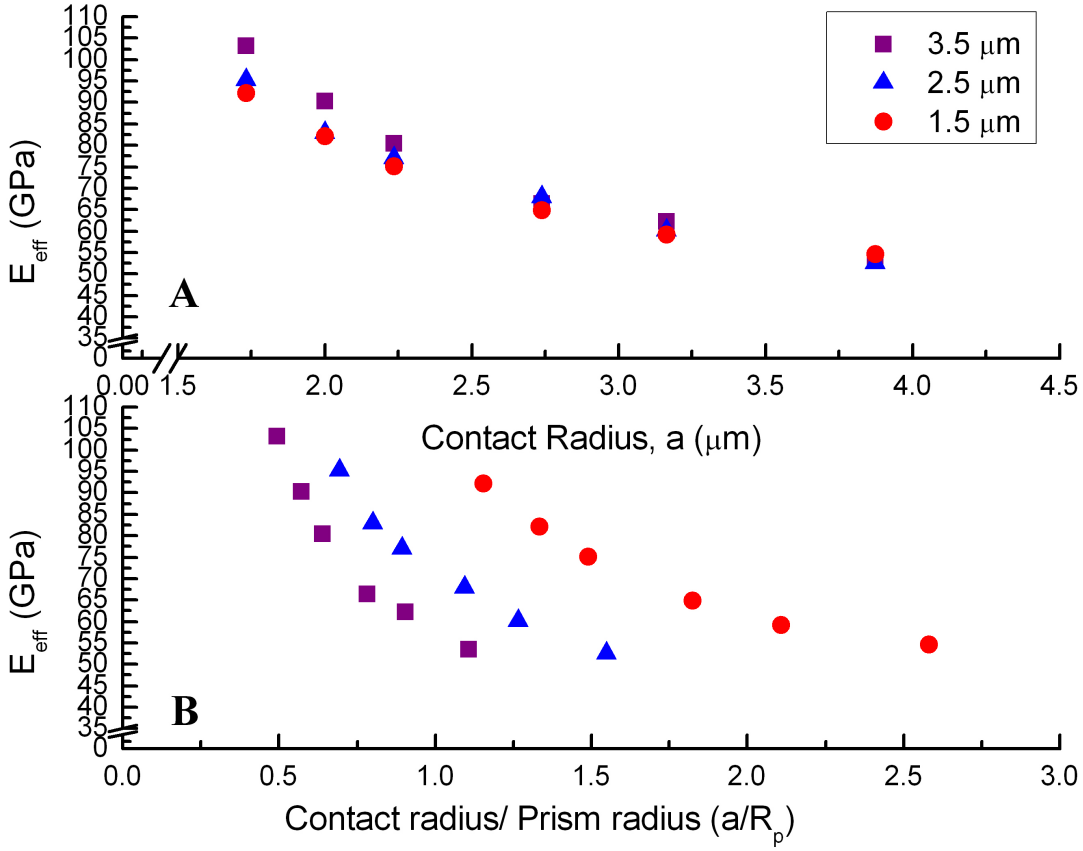

Figure 6.12: FEA enamel prism model values for effective modulus for three different values of prism radius. Increasing contact radius results in decreased mechanical properties as effective modulus approached an averaged value of the inter-prism and prism modulus values.

6.7 Conclusion

Nanoindentation is an ideal tool to investigate the link between nanomechanical properties, mineralization, and microstructure. While the morphology contributes significantly to the mechanical functionally of a tooth, so too must the mechanical an material properties of the enamel and dentin. A complete understanding functional adaptations of teeth requires investigation of the mechanical and material and property variations within and between species. Investigation of lemur and human molars reveled a similar property trend where mechanical properties and mineral content increased from the EDJ to the OS. This property gradient may allow for the transmission of load to the underlying dentin and further ensures that the hardest and stiffest enamel occurs at the occlusal chewing surface. Mechanical properties are further dependent on prism size and orientation where *L. leucopus* demonstrated reduced modulus values along with the smallest prism size and no decussation present. FEA reveled that at low contact radii measurements on small diameter prisms result in larger modulus values. The larger modulus values are a direct result of the larger volume of prism versus inter-prism material included in the test volume.

Further, nanoindentation can be utilized as a tool to detect micro-cracking and damage as in *L. catta* where reduced mechanical properties correlated with the distance from a micro-crack. The mechanical contribution of a microcracking was further explored using FEA, where cracking reduced mechanical properties from up to 20 μm away. Understanding of the contribution of microstructure and mineralization to the nanomechaincal properties of enamel will provide insignt in to the functional adapations of the tooth.

Chapter 7

Discussion and Future Work

The primary goal of this dissertation is to investigate the heterogeneity within the nanomechanical and material properties of naturally mineralized biocomposites. Specifically this work seeks to understand how the inherent variability in the mineral phase including fluctuations in mineral composition, crystallinity, and microstructure contribute to the nanomechanical properties measured by nanoindentation. The mineral phase, as the primary load bearing component, contains substantial heterogeneity in the amount, composition, size, shape, and orientation of the apatite crystals. In addition, numerous processes can alter the mineral phase including pathological states (e.g., osteoporosis), aging and gender, dental caries, damage accumulation, and even fossilization. In bone, pathological mineralization is poorly controlled and results in the formation several different calcium phosphates, thus increasing the heterogeneity of the mineral component. Alternatively, enamel has a more uniform composition associated with its well-controlled formation mechanisms, yet sufficient porosity permits fluid flow and allows acid dissolution or fluoridation to occur, thus altering the composition. Additionally, micro-cracking and damage in enamel accumulates over the lifetime of the tissue as enamel does not undergo the cellularly-controlled bone remodeling process. Nanoindentation, in combination with additional independent measures of the tissue, enable the detailed study of bone and enamel's poorly understood 3-D construction, material properties, and mechanical behavior at sub-micrometer scales. A full understanding of the mechanical properties of mineralized tissues, at multiple length scales, is essential

for a comprehensive understanding of the structure-property-function relationships within healthy and diseased tissues as well as for the ultimate success of implants and replacement materials.

An additional goal of this work is to utilize nanomechanical and material property measurements to elucidate the functional significance of mineralized tissues. Specifically, I applied material science techniques to investigate questions that are generally considered under an anthropological or paleontological setting. Understanding the mechanics and materials aspects of evolutionary, ecological, or taphonomy questions provides unique insight into the underlying mechanisms of these questions. I sought to understand diagenesis through alterations of material and mechanical properties of bone over time with changes in mineral content, composition, and crystallinity. Further, investigation of the mechanical and material properties of lemurs enamel under an ecological context provided insight into the evolutionary functional adaptation of teeth. Following is a review of how variations in the mineral phase composition, crystallinity, and microstructure contribute to the mechanical properties of mineralized tissues. The second part of this chapter will utilize a contact mechanics model to interpret the functionality of teeth during mastication.

7.1 Natural Variability of Mineralized Tissues

The heterogeneous and hierarchical structure of both bone and enamel (see Figure 2.1 and 2.5) contribute to the fundamental nanomechanical response. Variations in composition, crystallinity, and microstructure are evident with different tissues types, location, age, diet, gender, and disease state. Numerous forms of carbonated apatite crystals with substantial substitutions and vacancies (Elliott, 2002) are present in the mineral phase and are in part the result of the thermodynamically driven biomineralization process. In bone, heterogeneities exist in mineral content as a result of the cellularly-mediated remodeling process where new bone is continually being deposited alongside sites of removal of older bone. During the formation of a new osteon, rapid mineralization initially occurs as numerous ions flow freely.

Eventually this process slows as the density increases and the diffusion rate of the ions through the tissue declines. As a result secondary osteons are more highly mineralized near their core, at the blood vessel, and less mineralized at the periphery. Additionally, as bone ages it continues to mineralize resulting is a tissue with highly variable mineral content and composition (see Figure 4.5). Recently, the idea of "bone quality", while not well defined, has become common place in the literature as often relating to changes in the composition or crystallinity. This broad idea of changes in the "quality" of the bone rather than the amount of bone has been vital to investigation of pathological states where a substantial increase in the variability of composition or crystallinity is observed in conditions such as osteomalacia (Faibish et al., 2005) or osteoporosis (Paschalis et al., 2004). In enamel, while no remodeling occurs, the formation process results in variations in the prism and crystal orientation and size from the enamel dentin junction (EDJ) to the occlusal surface (OS). Further inherent variability in tissue microstructure contributes to the nanomechanical response in both bone (e.g., lamella, osteocyte lacuna) and in enamel (e.g., prism width and orientation).

Mineralized tissues, even in a healthy unaltered state, are extremely heterogeneous in mineral crystallinity, composition, content, connectivity, and microstructure. While the exact function of these heterogeneities is relatively unknown, it is likely to play an important role in crack propagation and damage accumulation. In any region of healthy bone, damage accumulates in the tissue until it is replaced through a remodeling process. This results in a tissue that contains a variable amount of damage in different regions. Damage accumulation is a normal response of composite materials to mechanical loading. This ability to accumulate damage and yet not fail contributes to the superior fatigue resistance and toughness of composite materials compared to monolithic ones (Reifsnider, 1991). In bone, microcracks are present in even healthy, normal bone and they may play a role in the turnover process or even adaptive behavior (Martin et al., 1982). Some previously proposed damage mechanisms include debonding of mineral-organic interface, collagen fibril shear, crosslink scission, denaturation and failure of collagen fibrils, crack formation and propagation, min-

eral displacement, deformation and structural phase transformation, viscous stretching of the organic component, and rupture of self-healing sacrificial bonds (Martin et al., 1982; Tai et al., 2005). Further, it has been suggested that the perimeter of the secondary osteon, where there is a cement sheath of different properties from the rest of the bone, acts as a crack propagation barrier (Yeni and Norman, 2000). In the tooth, there is no remodeling and any damage accumulated is permanent. However, to prevent cracks from the brittle enamel from spreading into the dentin, the EDJ provides a crack-barrier through gradation of mechanical properties. In a similar sense, nanoscale heterogeneities within bone and other mineralized tissues may also serve as crack-barriers. Heterogeneities may increase the ability of the tissues to functionally withstand or accumulate damage (crack propagation). Application of nanoindentation along with complimentary techniques allows investigation of how variations in mineral composition, crystallinity, and microstructure combine to create the heterogeneous mechanical response of mineralized tissues.

7.1.1 Variations in Mineral Composition

As mechanical properties generally increase with the amount of mineral in a tissue (Oyen et al., 2008; Currey, 1964; Katz, 1971), the quantification of the mineral volume fraction is vital to studies of heterogeneities in the mineral phase. In Chapter 4, novel glass standards were developed to quantify the mineral volume fraction using quantitative backscatter scanning electron (qBSE) microscopy. The qBSE technique is a powerful tool which allows for site matched measurements of mineral volume fraction and mechanical properties from nanoindentation. Visualization of mineral content heterogeneities can further indicate regions of interest for nanomechanical testing.

The relationship between the amount of mineral and the elastic response was examined in Chapter 4 over a wide range of mineralized tissues from cartilage to bone and enamel (see Figure 4.8). While there is a general increasing trend of modulus with mineral volume fraction, these widely variable tissues spanned the entire region between the Hashin-Shtrikman

composite bounds. These bounds describe a soft particle in a hard matrix at the upper limit and a hard particle in a soft matrix at the lower limit. The locations of various tissues between these bounds gives some indication of the connectivity of the mineral phase. Tissues with poorly-organized collagen networks (*i.e.*, carp dermal bone and whale bulla) tend to form a unorganized mineral matrix and fall near the lower bound. In fossilized bones, numerous data points even fell outside the upper Hashin-Shtrikman composite bound, yet were still within the Voigt-Reuss bound (see Figure 5.6). Removal of the collagen phase during diagenesis allows fossilized bones to form a highly connected mineral network dissimilar to that seen in biological mineralization. The connectivity of the mineral phase and not just the amount of mineral plays a vital role the mechanical response of mineralized tissues.

In addition to the amount and connectivity of the mineral phase, the composition also contributes to the mechanical response of mineralized tissues. Chapter 5 explored a uniquely large range of mineral volume fractions and compositions through investigation of fossilized samples. Mechanical properties generally increased with the age and density of the bone (see Figure 5.5) as a result of mineral infilling that can occur during diagenesis. However, large variations in mechanical properties and mineral content were evident even within one diagenetic environment (Olesiak et al., 2010b), reflecting the diversity of diagenesis. Variations in mineral composition were detected in over half of the fossilized bone samples using x-ray diffraction (XRD). The presence of quartz or calcite, in addition to hydroxyapatite, suggest that large pore spaces have been infilled with contaminant minerals. Further, infilling of nanoscale pore spaces between the mineral network is required to achieve the extremely high measured modulus values of the oldest fossilized bones ($\approx$ 98 GPa). The composition of the nanoscale mineral infilling is unknown as it possible that either locally dissolved apatite was re-precipitated or new minerals were introduced into the bone lattice. Future studies using energy-dispersive x-ray (EDX) spectroscopy could be used to site match measurement of chemical composition and nanomechanical properties within fossilized material.

Compositional variations must be considered at a length-scale that directly contribute

to the nanomechanical properties. In addition to EDX, micro-spectroscopy provides sufficiently small resolution required to investigate the contribution at the micro/nano length scale. Only recently have variations in bone composition (measured by FTIR) been linked to mechanical properties (Gadeleta et al., 2000; Busa et al., 2005, Boskey et al., 2005). In Chapter 4, modulus was shown to correlate with FTIR carbonate/phosphate ratio, suggesting that composition plays a role in mechanical properties. However, traditional FTIR has a spot size of hundreds of microns and little ability to select a specific region of interest (Boskey, 2006). The use of micro-FTIR shows great promise as it allows for scanning like measurements of composition with a spot size ≈ 6 μm in diameter (Miller, 2007). Further, micro-FTIR combined with qBSE and nanoindentation can provide a powerful arsenal of information of the contribution of mineral content and composition to mechanical properties.

7.1.2 Variations in Crystallinity and Microstructure

Another main goal of this work is to investigate how variations in mineral crystallinity and microstructure affect the nanomechanical properties of mineralized tissues. Wide variations in crystal size, shape, perfection, and orientation are seen in mineralized tissues that exist both in their native states (Boskey, 2006; Elliott et al., 2002) and in those altered by various biological and geological processes. The contribution of these variations to nanomechanical properties is poorly understood. The connectivity and thus also microstructure of the mineral phase contributes significantly to the nanomechanical response as shown in Chapter 4.

The concept of crystallinity encompasses the characteristics of the mineral crystals including their size, shape, orientation, and lattice perfection. Traditionally studies of crystallinity are primarily based on XRD measurements and also electron microscopy. Measurements using XRD are straightforward and cost effective. The widths of diffraction peaks give information about both the size and perfection (e.g. micro-strain) of the crystals (Elliott et all., 200; Cullity et al., 2001; Snyder et al., 1999). In principle, separation of this

information is possible if a large 2θ is considered as these factors have different angular dependencies (Snyder et al., 1999). However, this is rarely attempted for poorly crystallized biological apatites, thus the contribution of micro-strain to peak width is generally ignored. The size of the crystal can then be calculated from the Scherrer formula (equation 3.14), yet results in smaller than true physical dimension of the mineral as measured by electron microscopy (Snyder et al., 1999). Further, inhomogeneities in the chemical composition of the crystals may also cause peak broadening, yet little work has been done to understand this effect. Measurements of crystal size are limited to bulk analysis techniques such as XRD and microscopy where the bone is examined in powder form. To fully understand the contribution of crystallinity to mechanical properties site-match measurements need to be explored. Some techniques, such as micro-raman and EDX, can provide some crystallinity information but considerable work is still needed to separate out crystal size, perfection, and composition effects in these measurements. There is substantial future work in understanding diffraction patterns of various calcium phosphates and the role these phases play in bone. Improved ability to identify local variations in crystallinity changes may contribute to our fundamental understanding of the bone formation process in both healthy and diseased states.

A large range of crystallinity was considered using fossilized samples up to 50 million years in age. A general increase in crystallinity with the age of the bone was measured through XRD peak narrowing. The increase in crystallinity in the fossilized samples correlated with an increase in density along with geological age (Olesiak et al., 2008, 2010b). All bone samples were significantly less crystalline than synthetic hydroxyapatite indicative of the bone's small nano-crystals which contain very impure forms of carbonated apatite. During fossilization, the formation of new and the growth of existing crystals creates larger more perfect crystals (with less lattice strain) that directly increases the crystallinity over time. This increase primarily reflects the increase of crystal size and therefore also the density and connectivity of the sample resulting in increased mechanical properties. Nanoindentation modulus was correlated to XRD measurements of crystallinity over the wide range of

fossilized bone samples (R^2=0.73, p $<$ 0.001, Figure 5.5A) .

The contribution of microstructure to mechanical properties was considered in lemur enamel (in Chapter 6) where a relatively uniform mineral composition contributes little to the measured properties. Variations in prism size, orientation, and micro-cracking were considered to contribute to the nanomechanical response. To isolate these variations an FEA axial symmetric model (Section 6.5) of the indentation of enamel was created. FEA results indicate that a micro-crack up to a distance of 20 μm away can significantly decrease nanoindentation measured modulus value. These results corroborated experimental data measured in lemur enamel where substantial micro-cracking significantly reduced modulus values (see Table 6.4). Further FEA results demonstrate the contribution of prism size to the measured modulus only at indent depths less than 1000 nm. For enamel with small prisms the indentation contact volume contains a higher percentage of inter-prism material (E_R= 39.5 GPa) than prism material (E_R= 83.4 GPa) resulting in reduced mechanical properties as compared to enamel with large prisms. A similar results was evident in experimental result as the reduced mechanical properties of *L. leucopus* enamel is likely a result of its smaller prism size (diameter $\approx$ 3.8 μm) as compared to human enamel (diameter $\approx$ 6 μm).

Consideration of microstructure is important in the analysis of any single indentation site. The size, orientation, and geometry of a microstructural feature can substantially contribute to the mechanical response. In Paietta et al. 2011, we consider the contribution of lamellar bone structure to the mechanical response over a range of indenter tip sizes and indentation depths. Careful selection of tip location allows for targeted positioning to measure the modulus of specific structures such as lamellar bone (27.1 $\pm$ 2.9 GPa) that is approximately 30% greater than that of the interlamellar bone (20.9 $\pm$ 4.4 GPa) (Donnelly et al., 2005). Alternatively, a statistical grid sampling approach can be utilized to measure more averaged properties (Ulm et al., 2007). Further the use of a large indenter tip or large indent depth probes both lamellar and interlamellar bone and produces an averaged modulus value (Paietta, 2011). Microstructure, micro-cracking, and crystallinity all contribute to the

nanomechanical response of mineralized tissues.

7.2 Implications for enamel thickness, fracture, and wear

The functional mechanical advantage of thicker enamel has been suggested to provide greater wear potential during abrasion cause by mastication (Jolly, 1970; Macho and Spears, 1999) or to strengthen the crown and increase the resistance to fracture (Kay, 1981; Lucas et al., 2008). During the wear process, material is removed from the occlusal surface and the underlying tissue is damaged through cracking and yielding. In Chapter 6, tooth wear was evident within *Lemur catta* enamel where substantial micro-cracking was observed. Mastication can be considered under the context of contact mechanics where a food particle can be approximated as a sphere of a given radius that acts as an indenter upon the surface of enamel. Recently, Lucas et al. (2008), Lawn et al. (2009), and Lawn et al. (2010) considered the application of contact and fracture mechanics to determine failure mechanisms in enamel during mastication. However, oversimplification in these papers lead to inaccurate conclusions on tooth fracture, suggesting the common occurrence of cracking and whole tooth failure upon mastication of large nuts or seeds.

In Lucas et al. (2008) and Lawn et al. (2009), the food particle in contact with the tooth is assumed to be infinitely stiff (by using E in place of E_R). However, the moduli of consumed foods for orangutans and chimpanzees in the field range from 0.5 to 5.5 MPa (Vogel et al., 2008) and are substantially lower than the modulus of enamel ($\approx$ 90 GPa), invalidating the assumption of infinite stiffness. The mechanical properties of the food particle must inherently contribute to the contact mechanics of mastication, yet are ignored in the Lucas et al. (2008) and Lawn et al. (2009) analyses. Further, Lucas et al. (2008) assumed the enamel cusp to be flat, yet the radius of curvature of the surface can contribute substantially to the contact mechanics especially for large indenter or food particle radii (*e.g.*, seeds or nuts) that are comparable to the radius of curvature of the enamel cusp.

Additionally, Lucas et al. (2008) proposed a new form of crack initiation at the EDJ

(termed radial cracks) as a direct result of an induced flexure modes beneath a hard food particle. The prediction of radial cracking is based on plate bending equations and simplifies mastication as a point-load (representing the food particle) applied to a monolithic thin plate on a compliant substrate (representing the enamel). The assumption of a point load removes the contact mechanics from an indentation-like problem. Further the point load assumption is not valid when the radius of the particle approaches the thickness of the enamel, as is the case for mastication of large nuts or seeds with thin enamel. Further, whole tooth failure with evidence of radial cracking has never been reported *in vivo* in the literature, rather severe wear and surface damage is the predominate form of tooth failure (Lawn et al., 2009; Cuozzo and Sauther, 2006; Ungar and M'Kirera, 2003). The over-simplification of the stress states, loading conditions, and material properties of enamel during mastication led Lucas et al. (2008), Lawn et al. (2009), and Lawn et al. (2010) to questionable predictions of radial crack creation as a common failure mechanism in primates. Following is a review and analysis of the Lucas et al. (2008)'s contact mechanics and plate bending approach in consideration of the mechanics of mastication.

7.2.1 Methods of analysis

The application of contact mechanics to the problem of mastication is intuitive due to the similarities to an indentation problem. The contact of a food particle on thick layer of enamel allows us to only consider contact or near surface stresses associated with indentation and can be described by Hertzian contact mechanics (Johnson, 1985). There are two common forms of failure of brittle materials observed in contact problems, yielding and cone cracking (Lawn and Swain, 1975). Yielding occurs within the plastic damage zone present in indentation stress fields in Figure 3.3. Cone cracks are well documented from research on monolithic brittle solids. Cone cracks initially develop from the top surface outside the contact radius, where the tensile stress is maximum (Lawn and Swain, 1975; Lawn et al., 2002). The critical load (P) for the onset of cone cracks (C) and yielding (Y) from the

Table 7.1: Representative values from Lucas et al. (2008), used to predict cracking and yielding critical loads.

Material	**Modulus *E* (GPa)**	**Hardness *H* (GPa)**	**Strenght S (MPa)**	**Toughness T (MPa m^{-2})**
Human enamel	90	3.5	30	0.9
Human dentin	20	0.6		3.1
Macadamia shell	5.3	0.18	58	58
Macadamia kernel	0.003			0.04

contact of a sphere on a brittle solid has been well documented in the ceramics literature (Rhee et al., 2001) and is given in equation 7.1 and 7.2 respectively.

$$P_C = A\left(\frac{T^2}{E_R}\right)r' \tag{7.1}$$

$$P_Y = DH\left(\frac{H}{E_R}\right)^2 r'^2 \tag{7.2}$$

In the above equations, T is toughness (K_{IC}) and H is the hardness of the brittle material. E_R is the reduced modulus given by $E_R = 1/(1/E+1/E_i)$ where E_i is the modulus of the food particle or indenter in an experimental setting and E is the modulus of the enamel surface. Further, r' is the effective radius and in the case of curved surfaces $r' = 1/(1/r+1/r_i)$ where r_i is the radius of the food particle (or indenter) and r is the radius of curvature of the enamel cusp. Calibrated dimensionless values of A $= 8.5 \times 10^3$ and D $= 0.85$ have been measured on a range of ceramics (Rhee et al., 2001). Equation 7.1 and 7.2 are considered with the assumptions made in the literature (using table 7.1) and with new assumptions accounting for the radius of curvature of the enamel cusp and the modulus of the food particle.

A second approach in the literature which predicts the presence of radial cracking in enamel (Lucas et al., 2008) will be examined for appropriate application to mastication mechanics. Radial cracks are generally considered to initiate when an infinitely wide flat

brittle coating of thickness (d) and modulus E is bonded to a compliant substrate of modulus E_S. Radial cracks are induced by the flexural mode of the thin layer upon application of an approximate point load such the the radii of contact (a) is much less than the thickness (d). Radial cracking is thought to spontaneously initiate from a starting flaw in the lower coating surface at a critical load P_R given by equation 7.3 where B is a dimensionless constant equal to 2.04 as calibrated for glass substrate flat bilayers and S is the strength of the coating (Lawn et al., 2000).

$$P_R = \frac{BSd^2}{log(E/E_s)} \tag{7.3}$$

7.2.2 Results and Discussion

7.2.2.1 Mastication as a contact problem

Figure 7.1 plots equations 7.1 and 7.2 with the assumptions made in both Lucas et al. (2008) and Lawn et al. (2009) along with a set of representative materials values listed in Table 7.1. Additionally, these equations are plotted using both E_R and r' to correctly account for the modulus of the food particle and the radius of curvature of the tooth. The modulus of the food particle was taken to be that of the macadamia shell, $E = 5.3$ GPa, (Lucas et al., 2008) in-order to consider the extreme case for hard food particles.

In figure 7.1 it is clear that the radius of the tooth, r, does not contribute to the critical failure load until the radius of the food particle r_i approaches that of the tooth. However, within the range of radii for nuts and seeds, the critical load for the onset of both yielding and cone-cracking is lowered with increased radius of curvature of the tooth. This is a direct result of the decreased area of contact with a surface of high curvature, resulting in a higher force per area, suggesting that sharp cusps are more prone to yielding and cone-cracking.

By incorporating the correct modulus of the food particle the critical load for yielding and fracture increase substantially. When assuming a infinitely hard food particle a bite

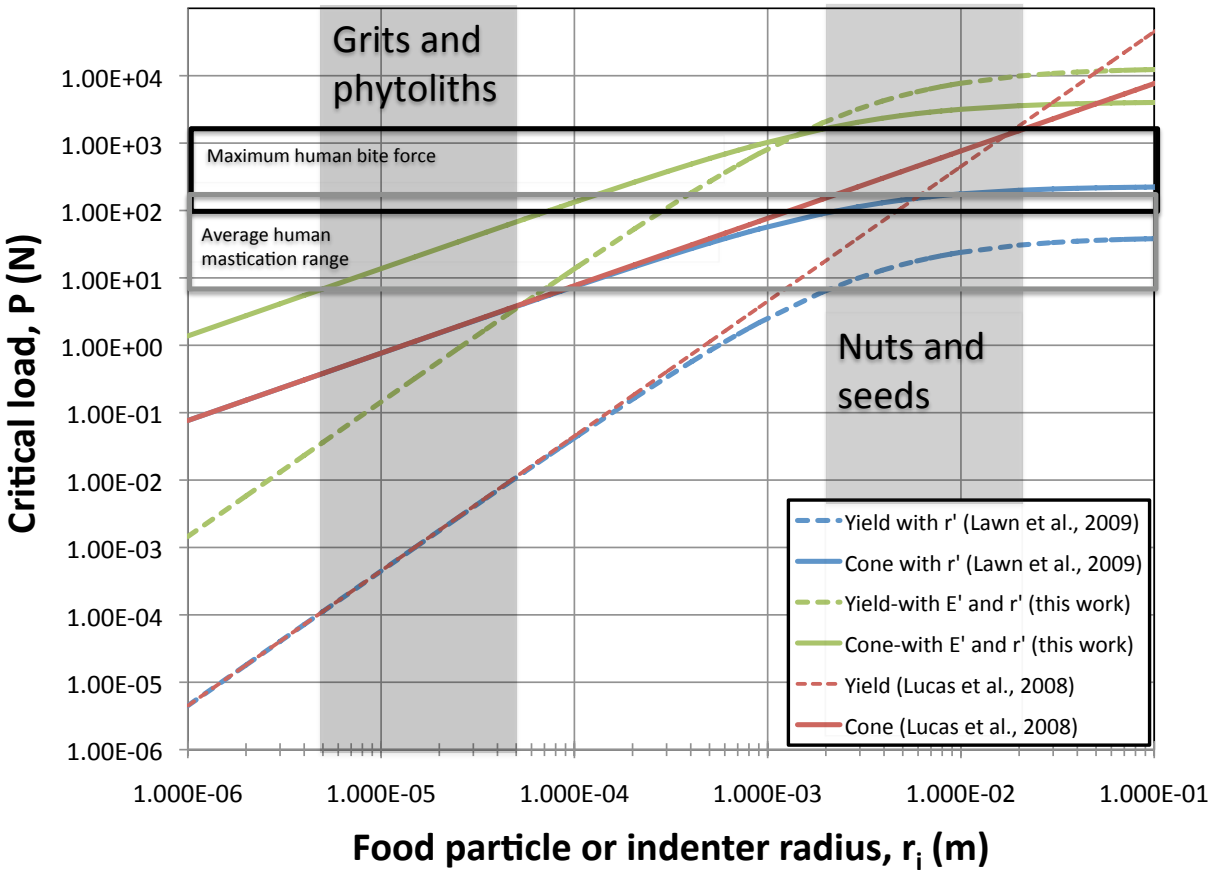

Figure 7.1: Critical loads for cone cracks (solid lines) and yield (dotted lines) for infinitely stiff foods using equation 7.1 and 7.2 with the assumptions made in both Lucas et al. (2008) and Lawn et al. (2009) using the representative materials values listed in Table 7.1. Additionally, critical load values are plotted using r' (assuming a radius of curvature of the tooth to be 0.003 m) and E' (assuming that E_i is that of the macadamia shell = 5.3 GPa). Gray shaded areas represent the radii of two common categories of consumed foods. The horizontal black rectangle represents the maximum occlusal forces (Burke, 1992; Kikuchi et al., 1997) measured in humans and the gray rectangle the average masticatory forces (DeLong and Douglas, 1983).

forces as low as 0.0001 to 0.01 N would cause yielding and 0.4 to 4 N would initiate cone cracking upon mastication of grits and phytoliths. For nuts and seeds loads of 15 to 31 N would cause yielding and 90 to 200 N would initiate cone cracking. Maximum human bite forces ranges from 100 to 1181 N (Hidaka et al., 1999; Burke, 1992; Kikuchi et al., 1997) with the average range within conditions of mastication from 9 to 180 N (DeLong and Douglas, 1983). Considering the above calculated critical loads with conditions applied in the Lucas et al. (2008) model, normal mastication would cause cracking in yielding with the majority of consumed food, which is clearly not the case.

The assumed modulus of the food particle contributes substantially to the critical load for both yielding and cone cracking. While numerous measurements on the hardness of foods consumed by primates exist (Yamashita, 1996; Vogel et al., 2008), very few measurement of the moduli of food are available. Recently, Agrawal and Lucas (2003) measured the modulus of a range of common food items from various cheeses to nuts and found that modulus varied from 0.15 to 33.84 MPa. Further, the average moduli of consumed foods for orangutans and chimpanzees in the field ranged from 0.5 to 5.5 MPa (Vogel et al., 2008). It should be noted that the assumed modulus by Lucas et al. (2008) of the macadamia shell = 5.3 GPa is high compared to their earlier measured value of 32.18 MPa by Agrawal and Lucas (2003). Figure 7.2 considers the effect of various food moduli by plotting equations 7.1 and 7.2 for low modulus food (E_i=0.15 MPa), high modulus foods such as nuts and seeds (E_i=5.5MPa), and enamel on enamel contact (E_i=90 GPa). Additionally, data points are emphasized for tooth to tooth contact assuming the same radius of curvature of each cusp of 3 mm. From Figure 7.2, it is unlikely that contact with even the hardest foods will initiate cone cracking or yielding as the critical loads are well above even the maximum human bite force. The majority of enamel cone cracking and yielding thus likely occurs in enamel-to-enamel contact possibly during normal mastication. The tooth-to-tooth critical load values are within the bite force range of humans, allowing yielding and then cone cracking to potentially occur.

Further, grit and phytoliths are often made of very hard materials such as silica and

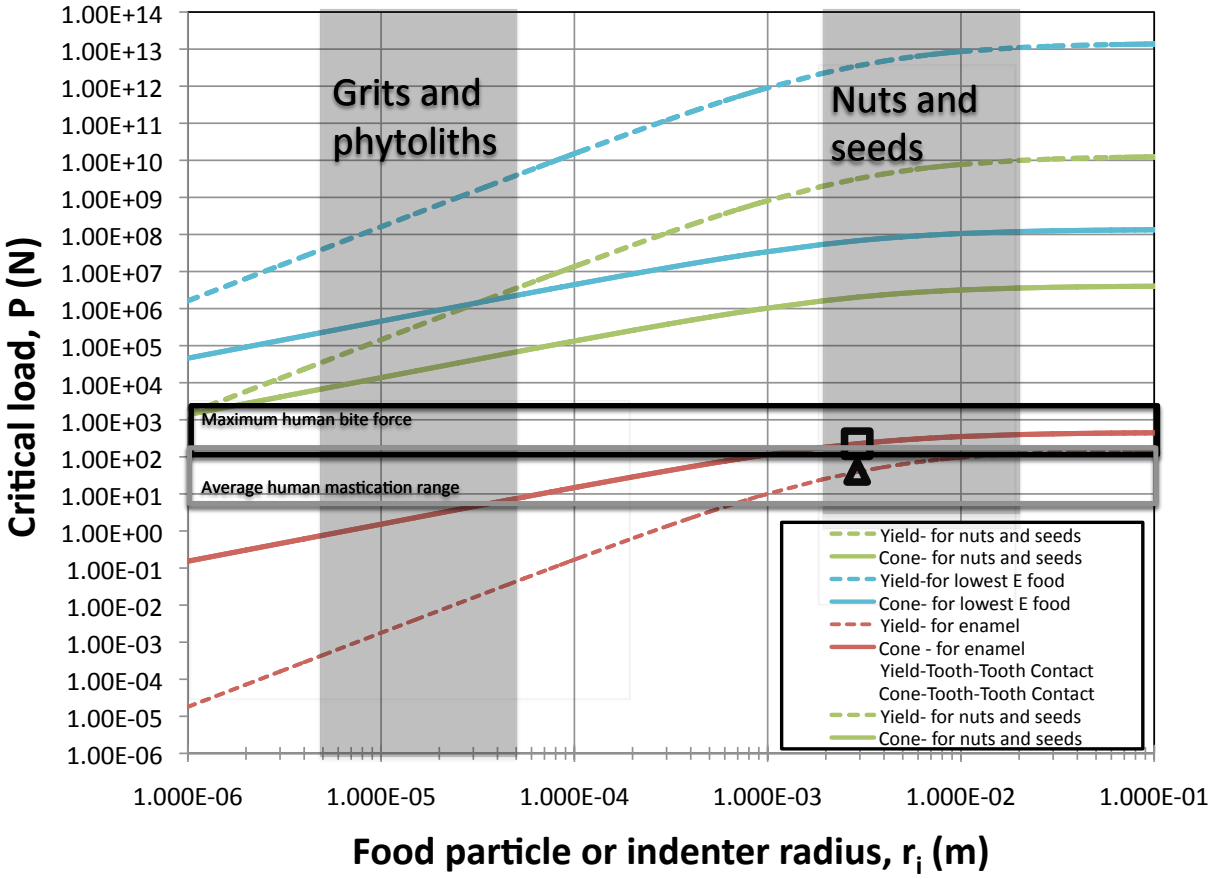

Figure 7.2: Critical loads for cone cracks (solid lines) and yield (dotted lines) for a range of food moduli using equation 7.1 and 7.2 with the radius of curvature of the tooth r'=0.003 m. Three sets of critical load values are plotted to consider the range of food moduli E_i. Data are plotted for: the minimum (E_i=0.000015 GPa) and maximum (E_i=0.005 GPa) modulus of average primate diet, and the modulus of enamel or grit E_i=90 GPa). Gray shaded areas represent the radii of two common categories of consumed foods. The black data points are emphasized for tooth to tooth contact assuming the same radius of curvature = 0.003 m for each surface. The horizontal black rectangle represents the maximum occlusal forces (Burke, 1992; Kikuchi et al., 1997) measured in humans and the gray rectangle the average masticatory forces (DeLong and Douglas, 1983).

quartz (E_i= 72 GPa). Contact with these hard particles gives critical load values almost identical to those plotted in Figure 7.2 for enamel-to-enamel contact. For the size range of grits and phytoliths yielding and cone cracking is likely to occur at normal masticatory loads leading to micro-wear ranging from $\approx$ 0.5 to 50 μm. This contact mechanics approach using equations 7.1 and 7.2 with the correct consideration of food moduli and radius of curvature of the tooth cusps is useful in predictions of surface cracking and yield damage accumulation. Specifically, large wear facets are likely only the results of tooth-to-tooth contact and smaller damage and micro-wear can also be the result of contact of grits and phytoliths.

7.2.2.2 Radial cracking predictions

Characteristics associated with laboratory testing and radial crack theoretical predictions are not consistent with normal masticatory experience *in vivo*. Traditional experimental load-to-failure testing commonly applies extremely high loads in order to initiate cracking often 1500 to 5000 N (Bortoluzzi et al., 2007; Kelly et al., 1990; Kelly, 1999) as compared to those measured during normal mastication and swallowing of 9 to 180 N (DeLong and Douglas, 1983). Further, traditional laboratory tests are suspect in that they generally use a hard metallic sphere or plate that are not representative of any food particle and often cause crushing damage accompanied by the formation of powder-like debris (Kelly, 1999). Simulated teeth, as represented by glass or ceramic domes (E $\approx$ 73 GPa) infiltrated with resin (E= 3.4 GPa), were loaded to failure with a tungsten carbide indenter (E=614 GPa) (Qasim et al., 2005). While the tests on glass domes (Qasim et al., 2005) are extremely poor approximations of occlusal conditions, they are continually cited as evidence for the existence of radial cracking in teeth (Lucas et al., 2008; Lawn et al., 2009, 2010). The use of monolithic materials in these experiments oversimplifies the material properties in enamel and dentin and their interface. Further, experimental measurement on domed surfaces has indicated a significant decrease in the critical load required to initiate cracking with decreased radius of curvature (Qasim et al., 2005). This suggests that cusp shape, specifically curvature, plays a

vital role in cracking modes and stress distribution within the tooth. Further, a simple dome does not accurately recreate the boundary condition of a tooth which has anchored ends and a complex dentin-enamel interface. Finite element analysis has indicated that a large majority of the skull experiences stresses during mastication (Strait et al., 2009) indicating that analysis of a simplified dome does not accurately represent the *in vivo* stress conditions. The use of glass domes to represent a tooth oversimplifies the true geometrical, materials, and stress conditions which all substantially contribute to the available cracking modes.

Equation 7.3 corresponds well with experimental data for flat ceramics and glasses on compliant substrates (Rhee et al., 2001; Lawn et al., 2000). However this does not imply applications of this equation to the complexities of the tooth in order to predict the existence of radial fractures, yet this has been recently published (Lucas et al., 2008; Lawn et al., 2009, 2010). There are numerous problems with the application of equation 7.3 to tooth fractures, primarily the assumed tensile stresses and plate bending mode within enamel which are thought to exist based on solely on overly simplified flat or even domed surface experimental measurement, described above (Qasim et al., 2005). In addition, the assumption of a point load which is infinitely stiff, does not apply to any normal mastication situation. As demonstrated above in section 7.2, it is clear the modulus and the mechanics of the food particle contribute significantly to mechanical analysis of mastication. Equation 7.3 is only valid when the radius of contact (a) is sufficiently smaller than the thickness of the brittle surface layer, as is the case for a point load. It was previously hypothesized using equation 7.3 that radial cracking would predominate when hard nuts or seed were consumed (Lucas et al., 2008). However in these cases the radius of contact approaches that of the thickness of enamel, thus invalidating the equation. While radial or deep fracture damage may occur within the tooth due to tensile stresses, analysis using equation 7.3 severely over-simplifies the problem and utilizes faulty assumptions. Therefore this approach is not suitable to predict failure within the tooth. Future work, likely involving FEA, is required to comprehend the true stress states involved in mastication within the tooth. Consideration

of the mechanics of the food particle and complex material properties of enamel and dentin must be included in this analysis in order to provide *in vivo* comparison.

7.2.2.3 Enamel thickness implications

In Chapter 6 severe wear and micro-fractures were observed in *Lemur catta* enamel as a direct result of consumption of a hard and tough fallback food, the tamarind fruit (Cuozzo and Sauther, 2004, 2006; Sauther et al., 2002). *Lemur catta* possesses relatively thin enamel as compared to other primates (see Table 7.2). Traditionally enamel thickness in primates has been linked to diets containing hard foods (Dumont, 1995; Kay, 1981) suggesting that *Lemur catta* with its thin enamel is ill-adapted to the tamarind fruit. Orangutan (*Pongo pygmaeus*) provides a good example of a consumption of hard fall back foods linked to thicker enamel as compared to Chimpanzee (*Pan troglodytes*). The chimpanzee's thinner enamel is linked to diet with an average modulus of 1.36 ± 0.23 MPa and toughness, R = 429 ± 121 Jm^{-2}. As compared to the orangutan's relatively thicker enamel (see Table 7.2) which is linked to a stronger (E=2.96 ± 0.2 MPa) and tougher diet (R= 1022 ± 22 Jm^{-2}). However, the relationship between thick enamel and hard object consumption is not direct (Maas and Dumont, 1999; Martin et al., 2003; Teaford and Ungar, 2000b). New World pitheciins have thin enamel with considerable prism decussation, yet are able to successfully consume hard objects, indicating that enamel microstructure plays a vital role in the function of the tooth (Macho and Shimizu, 2010, 2009; Martin et al., 2003).

Within the context of tooth wear, abrasion, and contact mechanics, thicker enamel is thought to provided a longer functional life of the tooth. As the tooth wears, molar cusps have been shown to maintain their shape throughout the process (Ungar and M'Kirera, 2003). Thus sharp molars, adapted for folivory, maintain the same angularity and are still able to functionally shear through tough leaves. This mechanism is similar to that seen in herbivorous ungulates that have complex infolding designed to form sharp edges with dentin exposure. Ungar and M'Kirera (2003) reasoned that as tooth cusp angularity was

Table 7.2: Measured and literature values for relative enamel thickness (RET) and average enamel thickness (AET). RET data are taken from current work (highlighted in yellow) and literature (Martin, 1985; Godfrey et al., 2005, 2006). AET are 3D measurements using microCT scans of the perpendicular distance from the occlusal surface to the EDJ averaged over the whole tooth surface. (Olejniczak et al., 2008).

Taxon	**AET (mm)** **Mean (Range)**	**RET** **Mean (Range)**
Loris gracilis	0.10 (0.09 – 0.1)	5.7 (4.85 – 6.33)
Varecia variegata		5.7
Lemur catta		7.3 (6.7 - 8.1)
Alouatta sp.	0.40 (0.26 - 0.53)	9.90 (7.23 - 13.77)
Gorilla gorilla	0.98 (0.67 - 1.25)	10.0 (6.8 - 13.4)
Pan troglodytes	0.75 (0.56 - 0.92)	10.1 (7.0 - 14.72)
Propithecus verreauxi		10.7
Lepilemur leucopus		15.85
Pongo pygmaeus	1.01 (0.81 - 1.42)	15.9 (11.3 - 20.5)
Cebus apella	0.65	19.2
Homo sapiens	1.43 (0.65 - 2.3)	22.4 (12.56 - 32.3)
Archaeolemur majori		28.3 (24.9 - 35.2)

maintained throughout the wear process and is likely a critical functional attribute linked to food fracture abilities. Thus thicker enamel may lengthen the life of the tooth while maintaing functionality.

Surface damage and wear slowly remove material from occlusal contact and it has been suggested that thicker enamel may extend the functional life of the enamel (Jolly, 1970; Macho and Spears, 1999). A secondary, non-exclusive hypothesis is that enamel thickness provides increased strength of the enamel surface by potentially preventing whole tooth failure (Kay, 1981; Lucas et al., 2008). Lucas et al. (2008) suggested that thick enamel provided greater resistance to formation of radial cracks. However these analyses are inaccurate as they are based on poor experimental evidence from glass domes (Qasim et al., 2005) and the use of equation 7.3, which both oversimplify the stress state and material properties within the tooth. While enamel thickness may play a functional role by increasing the resistance to fracture of the tooth, the analyses by (Lucas et al., 2008; Lawn et al., 2009, 2010) do not confirm this hypothesis.

7.2.3 Conclusion

Full understanding of the fracture and functional mechanics of the tooth must include the inherent heterogeneity of mineralized tissues considered in this dissertation. As covered in Chapter 6 variation in microstructure and mineralization within enamel contribute to the nanomechanical response. The gradient of mechanical properties and mineral content which exists across the thickness of enamel must inherently contribute to the macro-scale mechanical response. Further complications of the fracture mechanics of the tooth involve consideration of the complicated interface between the stiff enamel and more compliant dentin at the EDJ (Martin and Sharkey, 2001). The EDJ represents a superior interface, where naturally graded properties provide a crack propagation barrier and play a vital role in the fracture mechanics of the tooth (Kinney et al., 1996). The EDJ has a complex hierarchical scalloped structure containing convexities, where fibers of collagen transverse the

EDJ (Marshall et al., 2003). In addition, a chemical gradient has been observed with micro-Raman and FTIR spectroscopies (Tesch et al., 2001), creating a true interphase between a stiff and more compliant region. Consideration of fracture mechanics at the macro-scale requires understanding of the mechanics at this interface. Future work should consider how these interfaces mechanically interact to transmit load and prevent failure. Measurements of composition and microstructure with complementary techniques will allow for direct comparison of variations in nanomechanical, mineralization, chemical, and structural properties. Both nanoindentation and smaller-resolution techniques, such as AFM-based indentation, are necessary to investigate mechanics of this interface. Further, investigation of the EDJ will aid the development of biomimetic design principles to improve the interface between biology and engineering in applications such as dental restoration or bone implants.

7.3 Nanoindentation Testing of Mineralized Tissues

Nanoindentation of mineralized tissues has enabled the mechanical study of bone and teeth at the tissue-level. Researchers have long sought ways to evaluate bone and teeth at very small length scales, by mechanically testing individual microstructures which overcome limitations of larger scale testing methods. Recently, nanoindentation testing has become the most common approach to mechanical testing mineralized tissues at a length scale relevant to bone tissue's microstructural features (Bembey et al., 2005; Bushby et al., 2004; Cuy et al., 2002; Fan and Rho, 2003; Ferguson et al., 2003a; Guo and Goldstein, 2000; Gupta et al., 2006; Hengsberger et al., 2002; Hoffler et al., 2000b; Mahoney et al., 2000; Rho et al., 1999b,a, 1997; Zysset et al., 1999; Oyen et al., 2008; Oyen, 2006b; Oyen and Ko, 2008; Oyen and Cook, 2003; Constantino et al., 2009). Most of these studies utilize a Berkovich tip and the standard elastic-perfectly plastic indentation analysis (Oliver and Pharr, 1992). The widespread application of nanoindentation has allowed researchers to investigate variations in microstructure, mineral content, fracture toughness, and disease state in mineralized tissues. Because of the potential to collect large, statistically relevant populations of data by

indenting many sites within a small region, nanoindentation is an obvious choice for evaluation of precious samples that may exist only in small numbers or volumes of tissue such as human iliac crest biopsies (Boyde et al., 1999), fossil fragments (Olesiak et al., 2006, 2008, 2010a), howler monkey enamel (Darnell et al., 2010), or bones from space-flight missions (Ferguson, unpublished data 2009).

While nanoindentation has been widely adopted by the biological community for mechanically testing mineralized tissues numerous limitations still exist. Traditionally nanoindentation tests are analyzed using elastic and perfectly plastic analysis for conical/pyramidal tips (Oliver and Pharr, 1992) or spherical tips (Field and Swain, 1993; Bushby, 2001). These analyses assume that the sampled material is elastic, perfectly plastic, isotropic, and homogenous. Yet mineralized tissues are none of these, rather they are heterogeneous and display a time dependent, anisotropic mechanical response. Mineralized tissues can contain a significant amount of viscoelasticity especially *in vivo* or in wet conditions. The viscoelastic response of mineralized tissues is an important component of the overall mechanical behavior of the tissue. However, only recently have some researchers sought to analyze the time-dependent response rather that simply suppress it in order to measure elastic properties. Further, the Oliver-Pharr method essentially produces only one parameter as contact hardness (H_c) has been shown to be correlated to indentation modulus (E).

Recently, more advanced analytical approaches have been developed to directly extract viscoelastic properties from pyramidal indentation tests (Feng and Ngan 2002, Liu, et al. 2006, Oyen 2006, Oyen 2008, Oyen and Cook 2003, Sakai 1999, Zhang, et al. 2006, Zhang, et al. 2005). These analyses explicitly incorporate the time dependence by combining viscoelastic constitutive laws with expressions for displacement under elastic indentation to give the load-time response. In particular, a viscous-elastic-plastic (VEP) model for time-dependent indentation has been developed in terms of experimentally-derived variables of load, displacement, and time (Oyen and Cook 2003). The model is based on a simple set of mechanical elements in series, which describe the viscous, elastic, and plastic behavior

of indentation by sharp, geometrically similar tips (such as Vickers, Knoop, Berkovich, or conical indenter geometries). Improvement to the robustness of the VEP model has recently been made though the development of the full VEP solution for trapezoidal loading (Olesiak et al., 2010a), see appendix B. Further, the VEP model allows extraction of three independent parameters, including true hardness (H). While some advances in analysis methods has been made, numerous limitations sill exist as many analyses assume a linear creep rate and perfect plasticity. The creep rate of mineralized tissues would be more accurately modeled by a decaying, non-linear creep rate. Additionally, mineralized tissues do not display perfect plasticity and even the concept of "plastic deformation" is poorly defined as biological tissues do not undergo the traditional deformation mechanisms in more traditional materials (e.g., metals). Substantial future work is needed to fully understand the viscoelastic properties of mineralized tissues, a process that likely requires wet testing.

One significant advantage of nanoindentation testing is the ability to map mechanical properties across a region of material, which can help elucidate the functional significance of the tissue. For example, nanoindentation of human tooth enamel has demonstrated a gradation of mechanical properties with high values at the occlusal surface that decrease toward the dentin-enamel junction. This gradient in mechanical properties provides an effective transmittance of biting forces through the brittle enamel into the tough dentin (Cuy et al., 2002). Specifically this mapping ability can be used in combination with adjunctive techniques with similar resolution capabilities, such as micro-FTIR, micro-Raman (Akkus et al., 2004; Cardell et al., 2009; Colomban and Treppoz, 2001), and qBSE (Ferguson et al., 2003a, 2008; Oyen et al., 2008) to determine site specific changes in mineral composition an content and their contribution to nanomechanical properties. Nanoindentation, combined with adjunctive techniques, has and continues to prove its utility in revealing new insight into the microstructural and compositional characteristics across many types of mineralized tissues, in health and disease, in response to altered mechanical loading, and in experimentally altered conditions. There is also a tremendous potential for using nanoindentation to

evaluate the bone that forms in or adjacent to bone replacement materials and within small volumes of engineered bone tissue.

Bibliography

Agrawal, K. and Lucas, P. (2003). The mechanics of the first bite. **Proc. R. Soc. Lond. B**, 270:1277—1282.

Akkus, O., Adar, F., and Schaffler, M. (2004). Age-related changes in physicochemical properties of mineral crystals are related to impaired mechanical function of cortical bone. **Bone**, 34(3):443–453.

Alarcon, J. V., Engelmeier, R. L., Powers, J. M., and Triolo, P. T. (2009). Wear testing of composite, gold, porcelain, and enamel opposing a removable cobalt-chromium partial denture alloy. **J Prosthodont**, 18(5):421–6.

Alberts, B., Bray, D., Lewis, J., Raff, M., Roberts, K., and Watson, J. (1994). **Molecular Biology of the Cell**. Garland Publishing, New York, 3rd edition.

Ambrose, S., Butler, B., Hanson, D., Hunter-Anderson, R., and Krueger, H. (1997). Stable isotopic analysis of human diet in the marianas archipelago, western pacific. **American Journal of Physical Anthropology**, 104(3):343–361.

Amprino, R. (1958). Investigations on some physical properties of bone tissue. **Acta Anat (Basel)**, 34(3):161–86. 0001-5180 (Print) Journal Article.

Angker, L., Nockolds, C., Swain, M., and Kilpatrick, N. (2004). Correlating the mechanical properties to the mineral content of carious dentine a comparative study using an ultra-micro indentation system (umis) and sem-bse signals. **Archives of Oral Biology**, 49:369–378.

Antonio Ascenzi, E. B. (1967). The tensile properties of single osteons. **The Anatomical Record**, 158(4):375–386.

Arnal, F., Verdier, P., and Vincensi, P. (1969). Coefficient de retrodiffusion dans le cas d'electrons monocinetiques arrivant sur la cible sous une incidence oblique. **Compt rend Acad Sci B Phys**, 268:1526–1529.

Arsenault, A. L. (1989). A comparative electron-microscopic study of apatite crystals in collagen fibrils of rat bone, dentin and calcified turkey leg tendons. **Bone and Mineral**, 6(2):165–177.

Ascenzi, A. (1988). The micromechianics versus the macromechanics of bone - a comprehensive presentation. **Journal of biomechanical engineering- Transactions of the ASME**, 110(4):357–363.

Ascenzi, A., Boyde, A., Barbos, M., and Carando, S. (1987). Micro-biomechanics vs macro-biomechanics in cortical bone - a micromechanical investigation of femurs deformed by bending. **Journal of biomechanics**, 20(11-12):1045.

Badone, E. and Farquhar, R. M. (1982). Application of neutron-activation analysis of the study of element concentration and exchange in fossil bones. **Journal of Radioanalytical Chemistry**, 69(1-2):291–311.

Barbakadze, N., Enders, S., Gorb, S., and Arzt, E. (2006). Local mechanical properties of the head articulation cuticle in the beetle pachnoda marginata (coleoptera, scarabaeidae). **Journal of Experimental Biology**, 209(4):722–730.

Barthelat, F., Li, C., Comi, C., and Espinosa, H. (2006). Mechanical properties of nacre constituents and their impact on mechanical performance. **Journal of Materials Research**, 21(8):1977–1986.

Bartsiokas, A. and Middleton, A. P. (1992). Characterization and dating of recent and fossil bone by x-ray-diffraction. **Journal of Archaeological Science**, 19(1):63–72.

Bayraktar, H. H., Morgan, E. F., Niebur, G. L., Morris, G. E., Wong, E. K., and Keaveny, T. M. (2004). Comparison of the elastic and yield properties of human femoral trabecular and cortical bone tissue. **Journal of Biomechanics**, 37(1):27–35.

Bell, L. S., Skinner, M. F., and Jones, S. J. (1996). The speed of post mortem change to the human skeleton and its taphonomic significance. **Forensic Science International**, 82(2):129–140.

Bembey, A. K., Bushby, A. J., Boyde, A., Ferguson, V. L., and Oyen, M. L. (2006a). Hydration effects on the micro-mechanical properties of bone. **Journal of Materials Research**, 21(8):1962–1968.

Bembey, A. K., Bushby, A. J., Boyde, A., Ferguson, V. L., and Oyen, M. L. (2006b). Hydration effects on the micro-mechanical properties of bone. **Journal of Materials Research**, 21(8):1962–1968.

Bembey, A. K., Koonjul, V., Bushby, A. J., Ferguson, V. L., and Boyde, A. (2005). Contribution of collagen, mineral and water phases to the nanomechanical properties of bone. **Materials Research Society Symposium Proceedings**, 844:R\Y2.8.1–6.

Bembey, A. K., Oyen, M. L., Bushby, A. J., and Boyde, A. (2006c). Viscoelastic properties of bone as a function of hydration state determined by nanoindentation. **Philosophical Magazine**, 86(33-35):5691–5703.

Berna, F., Matthews, A., and Weiner, S. (2004). Solubilities of bone mineral from archaeological sites: the recrystallization window. **Journal of Archaeological Science**, 31(7):867–882.

Bloebaum, R., Skedros, J., Vajda, E., Bachus, K., and Constantz, B. (1997). Determining mineral content variations in bone using backscattered electron imaging. **Bone**, 20(5):485–490.

Boivin, G. Y., Chavassieux, P., Santora, A., Yates, J., and Meunier, P. (2000). Alendronate increases bone strength by increasing the mean degree of mineralization of bone tissue in osteoporotic women. **Bone**, 27(5):687–694.

Bortoluzzi, E. A., Souza, E. M., Reis, J. M. S. N., Esberard, R. M., and Tanomaru-Filho, M. (2007). Fracture strength of bovine incisors after intra-radicular treatment with mta in an experimental immature tooth model. **Int Endod J**, 40(9):684–691.

Boskey, A., DiCarlo, E., Paschalis, E., West, P., and Mendelsohn, R. (2005). Comparison of mineral quality and quantity in iliac crest biopsies from high-turnover and low-turnover osteoporosis: an ft-ir microspectroscopic investigation. **Osteoporos International**, 16:2031–2038.

Bowman, S. M., Zeind, J., Gibson, L. J., Hayes, W. C., and McMahon, T. A. (1996). The tensile behavior of demineralized bovine cortical bone. **J Biomech**, 29(11):1497–501.

Boyce, T., Bloebaum, R., Bachus, K., and Skedros, J. (1990). Reproducible method for calibrating the backscattered electron signal for quantitative assessment of mineral-content in bone. **Scanning Microscopy**, 4(3):591–603.

Boyde, A. (1989). Enamel. In Berkovizt, B., Boyde, A., Frank, R., Hohling, H., Moxham, B., Nalbandian, J., and Tonge, C., editors, **Handbook of Microscopic Anatomy**, volume 6, pages 309–473. Springer Verlag, Berlin.

Boyde, A. (1997). Dental enamel. In **CIBA Foundation Symposium Processings**, volume 205. John Wiley and Sons.

Boyde, A., Davy, K., and Jones, S. (1995). Standards for mineral quantitation of human bone by analysis of backscattered electron images. **Scanning**, 17(suppl V):V6–V7.

Boyde, A., ELLIOTT, J., and JONES, S. (1993). Stereology and histogram analysis of backscattered electron images– age changes in bone. **Bone**, 14(3):205–210.

Boyde, A. and Fortelius, M. (1986). Development, structure and function of rhinoceros enamel. **Zoological Journal of the Linnean Society**, 87(2):181–214.

Boyde, A. and Jones, S. (1983). Back-scattered electron imaging of skeletal tissues. **Metabolic bone disease & related research**, 5(3):145–50.

Boyde, A. and Martin, L. (1982). Enamel microstucture determination in hominoid and cercopithecoid primates. **Anatomy and Embryology**, 165(2):193–212.

Boyde, A., Travers, R., Glorieux, F. H., and Jones, S. J. (1999). The mineralization density of iliac crest bone from children with osteogenesis imperfecta. **Calcified Tissue International**, 64(3):185–190.

Brady, A. L., White, C. D., Longstaffe, F. J., and Southam, G. (2008). Investigating intra-bone isotopic variations in bioapatite using ir-laser ablation and micromilling: Implications for identifying diagenesis? **Palaeogeography, Palaeoclimatology, Palaeoecology**, 5(3-4):190–199.

Braly, A., Darnell, L., Mann, A., Teaford, M., and Weihs, T. (2007). The effect of prism orientation on the indentation testitng of human molar enamel. **Archives of Oral Biology**, 52(9):856–860.

Bres, E., Moebus, G., Kleebe, H.-J., Pourroy, G., Werkmann, J., and Ehret, G. (1993). High resolution electron microscopy study of amorphous calcium phosphate. **Journal of Crystal Growth**, 129:149–162.

Briscoe, B., Fiori, L., and Pelillo, E. (1998). Nano-indentation of polymeric surfaces. **Journal Physics D: Applied Physics**, 31:2395–2405.

Broz, J. J., Simske, S. J., Greenberg, A. R., and Luttges, M. W. (1993). Effects of rehydration state on the flexural properties of whole mouse long bones. **Journal of Biomechanical Engineering-Transactions of the Asme**, 115(4):447–449. Part A.

Broz, M., Cook, R., and Whitney, D. (2006). Microhardness, toughness, and modulus of mohs scale minerals. **American Mineralogist**, 91:135–142.

Bruet, B., Song, J., Boyce, M., and Ortiz, C. (2008). Materials design principles of ancient fish armour. **Nature Materials**, 7(9):748–756.

Budd, P., Montgomery, J., Barreiro, B., and Thomas, R. (2000). Differential diagenesis of strontium in archaeological human dental tissues. **Applied Geochemistry**, 15:687–694.

Burke, F. (1992). Tooth fracture invivo and invitro. **J Dent**, 20(3):131–139.

Burr, D., Miller, L., Grynpas, M., Li, J., Boyde, A., Mashiba, T., Hirano, T., and Johnston, C. (2003). Tissue mineralization is increased following 1-year treatment with high doses of bisphosphonates in dogs. **Bone**, 33(6):960–9.

Bushby, A. J. (2001). Nano-indentation using spherical indenters. **Nondestructive Testing and Evaluation**, 17(4):213 – 234.

Bushby, A. J., Ferguson, V. L., and Boyde, A. (2004). Nanoindentation of bone: Comparison of specimens tested in liquid and embedded in polymethylmethacrylate. **Journal of Materials Research**, 19(1):249–259.

Cardell, C., Guerra, I., Romero-Pastor, J., Cultrone, G., and Rodriguez-Navarro, A. (2009). Innovative analytical methodology combining micro-x-ray diffraction, scanning electron microscopy-based mineral maps, and diffuse reflectance infrared fourier transform spectroscopy to characterize archeological artifacts. **Analytical Chemistry**, 81(2):604–611.

Carden, A. and Morris, M. D. (2000). Application of vibrational spectroscopy to the study of mineralized tissues (review). **Journal of Biomedical Optics**, 5(3):259–268.

Casting, R. (1960). Electron probe microanalysis. **Advanced Electronics Electron Physics**, 13:317–386.

Cerling, T. E. and Sharp, Z. D. (1996). Stable carbon and oxygen isotope analysis of fossil tooth enamel using laser ablation. **Palaeogeography, Palaeoclimatology, Palaeoecology**, 126(1-2):173–186.

Chawla, K. (1987). **Composite Materials**. Springer-Verlag, New York.

Cheng, Y. T., Ni, W. Y., and Cheng, C. M. (2005). Relationships between initial unloading slope, contact depth, and mechanical properties for conical indentation in linear viscoelastic solids. **Journal of Materials Research**, 20(4):1046–1053.

Choi, K., Kuhn, J. L., Ciarelli, M. J., and Goldstein, S. A. (1990). The elastic moduli of human subchondral, trabecular, and cortical bone tissue and the size-dependency of cortical bone modulus. **Journal of Biomechanics**, 23(11):1103–1113.

Chudoba, T. and Richter, F. (2001). Investigation of creep behaviour under load during indentation experiments and its influence on hardness and modulus results. **Journal of Biomechanics**, 148(2-3):191–198.

Colomban, P. and Treppoz, F. (2001). Identification and differentiation of ancient and 593 modern european porcelains by raman macro- and micro-spectroscopy. **Journal of Raman Spectroscopy**, 32(2):93–102.

Constantino, P. J., Lee, J. J., Smith, T. M., Lucas, P. W., and Lawn, B. R. (2009). Mechanical properties of great ape tooth enamel. **American Journal of Physical Anthropology**, pages 108–108.

Cowin, S. C. (1999). Bone poroelasticity. **Journal of Biomechanics**, 32(3):217–238.

Cowin, S. C. (2007). The significance of bone microstructure in mechanotransduction. **Journal of Biomechanics**, 40(Suppl 1):S105–9.

Craig, R., Peyton, F., and Johnson, D. (1961). Compressive properties of enamel, dental cements, and gold. **Journal of Dental Research**, 40:936–945.

Croft, D. A. and Anderson, L. C. (2008). Locomotion in the extinct notoungulate protypotherium. **Palaeontologia Electronica**, 11(1):20.

Crompton, A. and Sita-Lumsden, A. (1970). Functional significance of therian molar pattern. **Nature**, 227(5254):197.

Cuozzo, F. and Sauther, M. L. (2004). Tooth loss, survival, and resource use in wild ring-tailed lemurs (lemur catta): implications for inferring conspecific care in fossil hominids. **Journal of Human Evolution**, 46:623–631.

Cuozzo, F. and Sauther, M. L. (2006). Severe wear and tooth loss in wild ring-tailed lemurs (lemur catta): A function of feeding ecology, dental structure, and individual life history. **Journal of Human Evolution**, 51(5):490–505.

Currey, J. (1964). Three analogies to explain the mechanical properties of bone. **Biorheology**, 2:1–10.

Currey, J. D. (1984). **The Mechanical Adaptations of Bone**. Princeton University Press, Princeton, NJ.

Currey, J. D. (1999). The design of mineralized hard tissues for their mehcanical functions. **Journal of Experimental Biology**, 202:3285–3294.

Currey, J. D. and Abeysekera, R. M. (2003). The microhardness and fracture surface of the petrodentine of lepidosiren (dipnoi), and of other mineralised tissues. **Archives of Oral Biology**, 48(6):439–447.

Cuy, J., Mann, A., Livi, K., Teaford, M., and Weihs, T. (2002). Nanoindentation mapping of the mechanical properties of human molar tooth enamel. **Archives of Oral Biology**, 47:281–291.

Daculsi, G., Legeros, R. Z., Legeros, J. P., and Mitre, D. (1991). Lattice-defects in calcium-phosphate ceramics - high-resolution tem ultrastructural-study. **Journal of Applied Biomaterials**, 2(3):147–152.

Dall'Ara, E., Ohman, C., Baleani, M., and Viceconti, M. (2007). The effect of tissue condition and applied load on vickers hardness of human trabecular bone. **J Biomech**, 40(14):3267–3270.

Darnell, L., Teaford, M., Livi, K., and Weihs, T. (2010). Variations in the mechanical properties ofalouatta palliatamolar enamel. **American Journal of Physical Anthropology**, 141:7–15.

Davy, K. (1994). Novel aromatic dimethacrylate esters as dental resins. **Journal of Material science materials in Medicine**, 5:350–352.

DeLong, R. and Douglas, W. (1983). Development of an artificial oral environment for the testing of dental restoratives: bi-axial force and movement control. **J Dent Res**, 62(3):2–6.

Donnelly, E., Baker, S. P., Boskey, A. L., and van der Meulen, M. C. H. (2006). Effects of surface roughness and maximum load on the mechanical properties of cancellous bone measured by nanoindentation. **Journal of Biomedical Materials Research Part A**, 77A(2):426–435.

Doube, M., Firth, E., and Boyde, A. (2005). Registration of confocal scanning laser microscopy and quantitative backscattered electron images for the temporospatial quantification of mineralization density in 18-month old thoroughbred racehorse articular calcified cartilage. **Scanning**, 27(5):219–26.

Dumont, E. (1995). Enamel thickness and dietary adaptation among extant primates and chiropterans. **Journal of Mammalogy**, 76(4):1127–1136.

El-Mowafy, O. and Watts, D. (1986). Fracture toughness of human dentin. **Journal of Dental Research**, 65:677–681.

Elliott, J. C. (2002). Calcium phosphate biominerals. In Kohn, M., Rakovan, J., and Hughes, J. M., editors, **Phosphates: Geochemical, Geobiological, and Materials Importance**, volume 48 of **Reviews in Mineralogy and Geochemistry**, pages 427–453. Mineralogical Society of America, Washington D.C.

Elliott, T. A. and Grime, G. W. (1993). Examining the diagenetic alteration of human bone material from a range of archaeological burial sites using nuclear microscopy. **Nuclear Instruments and Methods in Physics Research Section B**, 77(1-4):537–547.

Eppell, S. J., Tong, W. D., Katz, J. L., Kuhn, L., and Glimcher, M. J. (2001). Shape and size of isolated bone mineralites measured using atomic force microscopy. **Journal of Orthopaedic Research**, 19(6):1027–1034.

Evans, F. G. and Lebow, M. (1951). Regional differences in some of the physical properties of the human femur. **J Appl Physiol**, 3(9):563–572.

Everhart, T., Herzog, R.F. andChang, M., and DeVore, W. (1972). Computer-controlled resist exposure in scanning electron-microscope. **Proceedings of the 6th international conference on X-ray Optics and Microanalysis**, page 81.

Fan, Z., Swadener, J. G., Rho, J. Y., Roy, M. E., and Pharr, G. M. (2002). Anisotropic properties of human tibial cortical bone as measured by nanoindentation. **Journal of Orthopaedic Research**, 20(4):806–810.

Fan, Z. F. and Rho, J. Y. (2003). Effects of viscoelasticity and time-dependent plasticity on nanoindentation measurements of human cortical bone. **Journal of Biomedical Materials Research Part A**, 67A(1):208–214.

Fantner, G. E., Hassenkam, T., Kindt, J. H., Weaver, J. C., Birkedal, H., Pechenik, L., Cutroni, J. A., Cidade, G. A. G., Stucky, G. D., Morse, D. E., and Hansma, P. K. (2005). Sacrificial bonds and hidden length dissipate energy as mineralized fibrils separate during bone fracture. **Nature Materials**, 4(8):612–616.

Favre-Quattropani, L., Charlet, L., de Lumley, H., and Menu, M. (1999). Early palaeolithic bone diagenesis in the arago cave at tautavel, france. **Mineralogical Magazine**, 63(6):801–812.

Felicissimo, M., J.L.S., P., Tomasi, R., Azioune, A., J.J., P., Houssiau, L., and Rodrigues, U. (2004). X-ray photoemission spectroscopy and secondary-ion mass spectroscopy applied to the compositional study of pre-colonial pottery from pantanal, brazil. **Philosophical Magazine**, 84(32):34833496.

Feller, S., Lodden, G., Riley, A., Edwards, T., Croskrey, J., Schue, A., Liss, D., Stentz, D., Blair, S., Kelley, M., Smith, G., Singleton, S., Affatigato, M., Holland, D., Smith, M. E., Kamitoss, E. I., Varsamis, C. P. E., and Ioannou, E. (2010). A multispectroscopic structural study of lead silicate glasses over an extended range of compositions. **J Non-Cryst Solids**, 356(6-8):304–313.

Feng, G. and Ngan, A. H. W. (2002). Effects of creep and thermal drift on modulus measurement using depth-sensing indentation. **Journal Material Research**.

Ferguson, V., Bushby, A., Firth, E., Howell, P., and Boyde, A. (2008). Exercise does not affect siffness and mineralisation of third metacarpal condylar subarticular calicified tissues in 2 year old thoroughbred racehorse. **European Cells and Materials**, 16:40–46.

Ferguson, V. L., Ayers, R. A., Bateman, T. A., and Simske, S. J. (2003a). Bone development and age-related bone loss in male c57bl/6j mice. **Bone**, 33(3):387–398.

Ferguson, V. L., Boyde, A., and Bushby, A. J. (2005). Elastic modulus of dental enamel: effect of prism orientation and mineral content. **MRS Proceedings**, 841:R2.7.1–6.

Ferguson, V. L., Bushby, A. J., and Boyde, A. (2003b). Nanomechanical properties and mineral concentration in articular calcified cartilage and subchondral bone. **Journal of Anatomy**, 203(2):191–202.

Fernandes, C., Glantz, P., Svensson, S., and Bergmark, A. (2003). A novel sensor for bite force determinations. **Dental Materials**, 19(2):118–126.

Ferrario, V., Sforza, C., Zanotti, G., and Tartaglia, G. (2004). Maximal bite forces in healthy young adults as predicted by surface electromyography. **Journal of Dentistry**, 32(6):451–457.

Field, J. S. and Swain, M. V. (1993). A simple predictive model for spherical indentation. **Journal of Materials Research**, 8(2):297–306.

Finlay, J. B. and Hardie, W. R. (1994). Anisotropic contraction of cortical bone caused by dehydration of samples of the bovine femur in vitro. **Proceedings of the Institution of Mechanical Engineers, Part H: Journal of Engineering in Medicine**, 208(1):27–32.

Fischer-Cripps, A. (2002). **Nanoindentation**. Springer, New York.

Fleagle, J. (1998). **Primate Adaptation and Evolution**. Academic Press, New York.

Fong, H., Foster, B. L., Sarikaya, M., and Somerman, M. J. (2009). Structure and mechanical properties of ank/ank mutant mouse dental tissues-an animal model for studying periodontal regeneration. **Archives of Oral Biology**, 54(6):570–576.

Forber, H. (1894). **A handbook to the Primates**. Edward Lloyd Ltd., London.

Fujisaki, K. and Tadano, S. (2007). Relationship between bone tissue strain and lattic strain of hap crystals in bovine bone under tensile load. **Journal of Biomechanics**, 40:1832–1838.

Galli, M., Comley, K., Shean, T., and Oyen, M. (2009). Viscoelastic and poroelastic mechanical characterization of hydrated gels. **Journal of Materials Research**, 24(3):973–979.

Ge, J., Cui, F., Wang, X., and Feng, H. (2005). Property variations in the prism and the organic sheath within enamel by nanoindentation. **Biomaterials**, 26(16):3333–3339.

Gebhardt, W. (1906). Regarding the functionally important assembly techniques of the small scale and large scale building blocks of the vetebral bone ii: Special part: The building of the haversian lamellar system and its functional meaning. **Arch. Entwickl. Mech. Org.**, 20:187.

Godfrey, L. andSchwartz, G., Samonds, K., Jungers, W., and Catlett, K. (2006). The secrets of lemur teeth. **Evolutionary Anthropology**, 15:142–154.

Godfrey, L. R., Semprebon, G. M., and Schwartz, G. T. (2005). New insights into old lemurs: the trophic adaptations of the archaeolemuridae. **International Journal of Primatology**, 26(4):825–854.

Goldstein, J., Newbury, D., Echlin, P., Joy, D., Fiori, C., and Lifshin, E. (1981). **Scanning Electron Microscopy and X-ray Microanalysis**. Plenum Press, New York.

Gong, J. K., Arnold, J. S., and Cohn, S. H. (1964). Composition of trabecular and cortical bone. **Anatomical Record**, 149(3):325.

Goodship, A. E., Lanyon, L. E., and McFie, H. (1979). Functional adaptation of bone to increased stress. an experimental study. **Journal of Bone and Joint Surgery**, 61(4):539–46.

Gregory, W. (1922). **The Origin and Evolution of the Human Dentition**. Williams and Wilkins, Baltimore.

Grynpas, M. and Rey, C. (1992). The effect of fluoride treatment on bone-mineral crystals in the rat. **Bone**, 13(6):423–429.

Guidoni, G., Denkmayr, J., Schoberl, T., and Jager, I. (2006). Nanoindentation in teeth: influence of experimental conditions on local mechanical properties. **Philosophical Magazine**, 86(33-35):5705–5714.

Guidoni, G., Swain, M., and Jager, I. (1998). Wear behaviour of dental enamel at the nanoscale with a sharp and blunt indenter tip). **Wear**, 266(1-2):60–68.

Guo, X. E. and Goldstein, S. A. (2000). Vertebral trabecular bone microscopic tissue elastic modulus and hardness do not change in ovariectomized rats. **Journal of Orthopaedic Research**, 18(2):333–336.

Gupta, H. S., Stachewicz, U., Wagermaier, W., Roschger, P., Wagner, H. D., and Fratzl, P. (2006). Mechanical modulation at the lamellar level in osteonal bone. **Journal of Materials Research**, 21(8):1913–1921.

Habelitz, S., Marshall, G., Balooch, M., and Marshall, S. (2002). Nanoindentation and storage of teeth. **Journal of Biomechanics**, 35(7):995–998.

Habelitz, S., Marshall, S., Marshall, G., and Balooch, M. (2001). Mehcanical properties of human dental enamel on the nanometre scale. **Archives of Oral Biology**, 46:173–183.

Hackett, C. J. (1981). Microscopical focal destruction (tunnels) in exhumed human bones. **Medicine Science and the Law**, 21(4):243–265.

Hansma, P. K., Turner, P. J., and Fantner, G. E. (2006). Bone diagnostic instrument. **Review of Scientific Instruments**, 77(7).

Harcourt, C. and Thornback, J. (1990). **Lemurs of Madagascar and the Comoros**. IUCN, Gland, Switzerland.

Harris, J. and Vancouvering, J. (1995). Mock aridity and the paleoecology of volcanically influenced ecosystems. **Geology**, 23(7):593–596.

Harvey, S., Huang, H., Venkataraman, S., and Gerberich, W. (1993). Microscopy and microindentation mechanics of single-crystal fe- 3 wt% si: Part 1. atomic-force microscopy of small indentation. **Journal of Materials Research**, 8(6):1291–1299.

Hashin, Z. and Shtrickman, S. (1963). A variational approach to the theory of the elastic behaviour of multiphase materials. **Journal of Mechanics and Physics of Solids**, 11:127.

Hayes, W. (1991). Biomechanics of cortical and trabecular bone: implications for the assessment of fracture risk. In Mow, V. and Hayes, W., editors, **Basic Orthopaedic Biomechanics**. Raven Press, New York, 1st edition.

He, L. H., Fujisawa, N., and Swain, M. V. (2006). Elastic modulus and stress-strain response of human enamel by nano-indentation. **Biomaterials**, 27(24):4388–4398.

He, L. H. and Swain, M. V. (2008). Understanding the mechanical behaviour of human enamel from its structural and compositional characteristics. **Journal of the Mechanical Behavior of Biomedical Materials**, 1(1):18–29.

Hedges, R. E. M. (2002). Bone diagenesis: An overview of processes. **Archaeometry**, 44:319–328. Part 3.

Hedges, R. E. M. and Millard, A. R. (1995). Bones and groundwater - towards the modeling of diagenetic processes. **Journal of Archaeological Science**, 22(2):155–164.

Hengsberger, S., Kulik, A., and Zysset, P. (2002). Nanoindentation discriminates the elastic properties of individual human bone lamellae under dry and physiological conditions. **Bone**, 30(1):178–184.

Herakovich, C. (1997). **Mechanics of Fibrous Composites**. Wiley, New York.

Herrmann, R. and Reimer, L. (1984). Backscattering coefficient of multicomponent specimens. **Scanning**, 6(1):20–29.

Hidaka, O., Iwasaki, M., Saito, M., and Morimoto, T. (1999). Influence of clenching intensity on bite force balance, occlusal contact area, and average bite pressure. **J Dent Res**, 78(7):1336–1344.

Hill, W. (1953). **Primates: comparative anatomy and taxonomy. 1. Strepsirhini**. University Press, Edinburgh, UK.

Hoffler, C. E., Guo, X. E., Zysset, P. K., and Goldstein, S. A. (2005). An application of nanoindentation technique to measure bone tissue lamellae properties. **Journal of Biomechanical Engineering**, 127(7):1046–1053.

Hoffler, C. E., Moore, K. E., Kozloff, K., Zysset, P. K., Brown, M. B., and Goldstein, S. A. (2000a). Heterogeneity of bone lamellar-level elastic moduli. **Bone**, 26(6):603–9.

Hoffler, C. E., Moore, K. E., Kozloff, K., Zysset, P. K., and Goldstein, S. A. (2000b). Age, gender, and bone lamellae elastic moduli. **Journal of Orthopedic Research**, 18(3):432–7.

Hofmann, T., Heyroth, F., Meinhard, H., Franzel, W., and Raum, K. (2006). Assessment of composition and anisotropic elastic properties of secondary osteon lamellae. **Journal of Biomechanics**, 39(12):2282–2294.

Howell, P. and Boyde, A. (1998). Monte carlo simulation of electron backscattering from compounds with low mean atomic number. **Scanning**, 20(1).

Howell, P. and Boyde, A. (2003). Volumes from which calcium and phosphorus x-rays arise in electron probe emission microanalysis of bone: Monte carlo simulation. **Calcified Tissue Intnational**, 72(6):745–749.

Howell, P., Davy, K., and Boyde, A. (1997). Standards for low atomic number backscattered electron imaging: Correlations of experimental and theoretical results. **Scanning**, 19(3):179.

Huber, G., Orso, S., R., S., Wegst, U., Enders, S., Gorb, S., and Arzt, E. (2008). Mechanical properties of a single gecko seta. **International Journal of Materials Research**, 99(10):1113–1118.

Hubert, J., Panish, P., Chure, D., and Prostak, K. (1996). Chemistry, microstructure, petrology, and diagenetic model of jurassic dinosaur bones, dinosaur national monument, utah. **Journal of Sedimentary Research**, 66(3):531–547.

Imbeni, V., Kruzic, J., Marshall, G., Marshall, S., and Ritchie, R. (2005). The dentin-enamel junction and fracture of human teeth. **Nature of Materials**, 4:229–232.

Islam, M., Holland, D., and Scales, C. (2008). Chemical durability and conductivity of mixed borosilicate glasses for high level waste immobilisation. **Phys Chem Glasses-B**, 49(5):229.

Ivanova, T. I., Frank-Kamenetskaya, O. V., Kol'tsov, A. B., and Ugolkov, V. L. (2001). Crystal structure of calcium-deficient carbonated hydroxyapatite. thermal decomposition. **Journal of Solid State Chemistry**, 160(2):340–349.

Jager, I. and Fratzl, P. (2000). Mineralized collagen fibrils: A mechanical model with a staggered arrangement of mineral particles. **Biophys J**, 79(4):1737–1746.

Jiang, H., Liu, X., Lim, C., and Hsu, C. (2005). Ordering of self-assembled nanobiominerals in correlation to mechanical properties of hard tissues. **Appl Phys Lett**, 86(16):163901.

Johnson, K. (1985). **Contact Mechanics**. Cambridge University Press, Cambridge, UK.

Jolly, A. (1966). **Lemur Behavior**. Chicago University Press, Chicago.

Jolly, C. (1970). The seed eaters:a new model of hominid differentiation based on a baboon analogy. **Man**, 5:5–26.

Jongebloed, W., Molenaar, I., and Arends, J. (1975). Morphology and size distribution of sound and acid-treated enamel crystallites. **Calcif Tissue Int**, 19(2).

Joy, D. (1995). A database on electron-solid interactions. **Scanning**, 17(5):270–275.

Katz, E. P. and Li, S. (1973). Structure and function of bone collagen fibrils. **Journal of Molecular Biology**, 80(1):1–15.

Katz, J. L. (1971). Hard tissue as a composite material. i. bounds on the elastic behavior. **J Biomech**, 4(5):455–73.

Kay, R. and Hiiemae, K. (1974). Jaw movement and tooth use in recent and fossil primates. **American Journal of Physical Anthropology**, 40(2):227–256.

Kay, R. F. (1975). Functional adaptations of primate molar teeth. **American Journal of Physical Anthropology**, 43(2):195–215.

Kay, R. F. (1981). The nut-crackers-a new theory of the adatations of the ramapithecinae. **American Journal of Physical Anthropology**, 55(2):141–151.

Kazanci, M., Roschger, P., Paschalis, E. P., Klaushofer, K., and Fratzl, P. (2006). Bone osteonal tissues by raman spectral mapping: Orientation-composition. **Journal of Structural Biology**, 156(3):489–496.

Keenan, M., Hegsted, M., Jones, K., Delany, J., Kime, J., Melancon, L., Tulley, R., and Hong, K. (1997). Comparison of bone density measurement techniques: Dxa and archimedes' principle. **Journal of Bone Mineral Research**, 12(11):1903–1907.

Kelly, J. (1999). Clinically relevant approach to failure testing of all-ceramic restorations. **J Prosthet Dent**, 81(6):652–661.

Kelly, J., Giordano, R., Pober, R., and Cima, M. (1990). Fracture surface analysis of dental ceramics: clinically failed restorations. **Int. J. Prosthodont.**, 3:430–440.

Kikuchi, M., Korioth, T., and Hannam, A. (1997). The association among occlusal contacts, clenching effort, and bite force distribution in man. **J. Dent. Res.**, 76(6):1316–1325.

Kingsmill, V. and Boyde, A. (1999). Mineralization density and apparent density of bone in cranial and postcranial sites in the aging human. **Osteoporosis international: a journal established as result of cooperation between the European Foundation for Osteoporosis and the National Osteoporosis Foundation of the USA**, 9(3):260–8.

Kinney, J. H., Balooch, M., Marshall, S. J., Marshall, G. W., and Weihs, T. P. (1996). Atomic force microscope measurements of the hardness and elasticity of peritubular and intertubular human dentin. **J Biomech**, 118:133–135.

Kinzey, W. (1987). Comparative functional-morphology of the dentition of bearded saki and spider monkeys. **Anatomical Record**, 218(1):A72–A72.

Klein, C. and Dutrow, B. (2008). **Mineral Scince**. John Wiley and Sons, Hoboken, New Jersey.

Knothe Tate, M. (2001). Interstitial fluid flow. In Cowin, S. C., editor, **Bone Mechanics Handbook**, pages 1–29. CRC Press, New York, 2nd edition.

Koch, P. L. (1998). Isotopic reconstruction of past continental environments. **Annual Review of Earth and Planetary Sciences**, 26:573–613.

Kohn, M. J., Schoeninger, M. J., and Barker, W. W. (1999). Altered states: effects of diagenesis on fossil tooth chemistry. **Geochimica et Cosmochimica Acta**, 63(18):2737–2747.

Kotha, S. P. and Guzeslu, N. (2002). Modeling the tensile mechanical behavior of bone along the longitudinal direction. **J Theor Biol**, 219(2):269–79.

Lakes, R. (1993). Materials with structural hierarchy. **Nature**, 361(6412):511–515.

Lambert, J., Chapman, C., Wrangham, R., and Conklin-Brittain, N. (2004). Hardness of cercopithecine foods: Implications for the critical function of enamel thickness in exploiting fallback foods. **American Journal of Physical Anthropology**, 125(4):363–368.

Landis, W. J., Hodgens, K. J., Arena, J., Song, M. J., and McEwen, B. F. (1996). Structural relations between collagen and mineral in bone as determined by high voltage electron microscopic tomography. **Microscopy Research and Technique**, 33(2):192–202.

Lawn, B., Deng, Y., Miranda, P., Pajares, A., Chai, H., and Kim, D. (2002). Overview: Damage in brittle layer structures from concentrated loads. **J Mater Res**, 17(12):3019–3036.

Lawn, B. and Swain, M. (1975). Microfracture beneath point indentation in brittle solids. **J Mater Sci**, 10(1):113–122.

Lawn, B. R., Lee, J. J., Constantino, P. J., and Lucas, P. W. (2009). Predicting failure in mammalian enamel. **Journal of Mechanical Behavior Biomedical Materials**, 2(1):33–42.

Lawn, B. R., Lee, J. J. W., and Chai, H. (2010). Teeth: Among nature's most durable biocomposites. **Annu Rev Mater Res**, 40:55–75.

Lawn, B. R., Lee, J. J. W., Chai, H., and Pajares, A. (2000). Damage-resistant brittle coatings. **Adv. Eng. mater.**, 2(11):745–748.

Lee, D. and Glimcher, M. (1991). Three-dimensional spatial relationship between the collagen fibrils and the inorganic calcium phosphate crystals of pickerel (americanus americanus) and herring (clupea harengus) bone. **Journal of Molecular Biology**, 217:487–501.

Lee-Thorp, J. (2002). Two decades of progress towards understanding fossilization processes and isotopic signals in calcified tissue minerals. **Archaeometry**, 44(3):435–446.

Lee-Thorp, J. and Sponheimer, M. (2003). Three case studies used to reassess the reliability of fossil bone and enamel isotope signals for paleodietary studies. **Journal of Anthropological Archaeology**, 22(3):208–216.

Lees, S., Bonar, L. C., and Mook, H. A. (1984). A study of dense mineralized tissue by neutron-diffraction. **International Journal of Biological Macromolecules**, 6(6):321–326.

Lievers, W., Lee, V., Arsenault, S., Waldman, S., and Pilkey, A. (2007). Specimen size effect in the volumetric shrinkage of cancellous bone measured at two levels of dehydration. **Journal of Biomechanics**, 40(9):1903–1909.

Lloyd, G. (1987). Atomic-number and crystallographic contrast images with the sem - a review of backscattered electron techniques. **Mineral Mag**, 51(359):3–19.

Lloyde, G. (1987). Atomic-number and crystallographic contrast images with the sem- a review of backscattered electron techniques. **Mineral Magazine**, 51(359):3–19.

Loong, C. K., Rey, C., Kuhn, L. T., Combes, C., Wu, Y., Chen, S. H., and Glimcher, M. J. (2000). Evidence of hydroxyl-ion deficiency in bone apatites: An inelastic neutron-scattering study. **Bone**, 26(6):599–602.

Low, I., Duraman, N., and Mahmood, U. (2008). Mapping the structure, composition and mechanical properties of human teeth. **Materials Science and Engineering: C**, 28:243–247.

Lu, H., Campbell, C., Graham, D., and Ratner, B. (2000). Surface characterization of hydroxyapatite and related calcium phosphates by xps and tof-sims. **Analytical Chemistry**, 72(13):28862894.

Lu, W., Luk, K., Cheung, K., Gui-Xing, Q., Shen, J., Yuen, L., Ouyang, J., and Leong, Y. (2004). Microfracture and changes in energy absorption to fracture of young vertebral cancellous bone following physiological fatigue loading. **Spine**, 29:1196–1202.

Lubell, D., Jackes, M., Schwarcz, H., Knyf, M., and Meiklejohn, C. (1994). The mesolithic-neolithic transition in portugal: Isotopic and dental evidence of diet. **Journal of Archaeological Science**, 21(2):201–216.

Lucas, P., Constantino, P., Wood, B., and Lawn, B. (2008). Dental enamel as a dietary indicator in mammals. **Bioessays**, 30(4):374–385.

Lucas, P., Cook, R., and Lowrey, T. (2006). How baby plants avoid getting hurt and blossom into adulthood: The story of a tropical seed. **Materials Research Society Symposium Proceedings**, 975:DD08–07.

Maas, M. (1994). A scanning electron-microscopic study of in-vitro abrasion of mammalian tooth enamel under compressive loads. **Archives of Oral Biology**, 39(1):1–11.

Maas, M. C. and Dumont, E. R. (1999). Built to last: The structure, function, and evolution of primate dental enamel. **Evolutionary Anthropology**, 8(4):133–152.

Macho, G., Shimizu, D., Jiang, Y., and Spears, L. (2005). Australopithecus anamensis: A finite element approach to studying the functional adaptations of extinct hominins. **Anat Rec Part A**, 283A(2):310–318.

Macho, G. A. and Shimizu, D. (2010). Kinematic parameters inferred from enamel microstructure: new insights into the diet of australopithecus anamensis. **Journal of Human Evolution**, 58(1):23–32.

Macho, G. A. and Spears, I. R. (1999). Effects of loading on the biochemical behavior of molars of homo, pan, and pongo. **American Journal of Physical Anthropology**, 109(2):211–227.

Mahoney, E., Holt, A., Swain, M., and Kilpatrick, N. (2000). The hardness and modulus of elasticity of primary molar teeth: an ultra-micro-indentation study. **Journal of Dentistry**, 28(8):589–594.

Malek, S., Darendeliler, M., Rex, T., Kharbanda, O., Srivicharnkul, P., Swain, M., and Petocz, P. (2003). Physical properties of root cementum: Part 2. effect of different storage methods. **American Journal of Orthodontics and Dentofacial Orthopedics**, 124(5):561–570.

Marcondes, M., Paranhos, M., Spohr, A., Mota, E., da Silva, I., Souto, A., and Burnett, L. (2009). The influence of the nd:yag laser bleaching on physical and mechanical properties of the dental enamel. **Journal of Biomedical Materials Research B**, 90B(1):388–395.

Marotti, G., Lees, and Reeve (1993). A new theory of bone lamellation. **Calcified Tissue International**, 53:S47–S56. Suppl. 1.

Marshall, G. W., Balooch, M., Gallagher, R. R., Gansky, S. A., and Marshall, S. J. (2001). Mechanical properties of the dentinoenamel junction: Afm studies of nanohardness, elastic modulus, and fracture. **Journal of Biomedical Materials Research**, 54(1):87–95.

Marshall, S., Balooch, M., Habelitz, S., Balooch, G., Gallagher, R., and Marshall, G. (2003). The dentin-enamel junction - a natural, multilevel interface. **J Eur Ceram Soc**, 23(15):2897–2904.

Martin, L. (1985). Significance of enamel thickness in hominoid evolution. **Nature**, 314(6008):260–263.

Martin, L., Boyde, A., and Grine, F. (1988). Enamel structure in primates: A review of scanning electron microscope studies. **Scanning Microscopy**, 2(3):1503–1526.

Martin, L., Olejniczak, A. J., and Maas, M. C. (2003). Enamel thickness and microstructure in pitheciin primates, with comments on dietary adaptations of the middle miocene hominoid kenyapithecus. **Journal of Human Evolution**, 45(5):351–367.

Martin, R. and Sharkey, N. (2001). Mechanical effects of postmortem changes, preservation, and pllograft bone treatments. In Cowin, S., editor, **Bone Mechanics Handbook**, pages 20.1–4. CRC Press, New York.

Mcconnel, D., Termine, J., and Posner, A. (1967). Infrared absorption of carbonate apatite. **Science**, 155(3762):607–608.

McKee, M. D., Nanci, A., Landis, W. J., Gotoh, Y., Gerstenfeld, L. C., and Glimcher, M. J. (1991). Effects of fixation and demineralization on the retention of bone phosphoprotein and other matrix components as evaluated by biochemical analyses and quantitative immunocytochemistry. **Journal of Bone and Mineral Research**, 6(9):937–945.

Mencik, J., Rauchs, G., Bardon, J., and Riche, A. (2005). Determination of elastic modulus and hardness of viscoelastic-plastic materials by instrumented indentation under harmonic load. **Journal of Materials Research**, 20(10):2660–2669.

Mente, P. L. and Lewis, J. L. (1994). Elastic modulus of calcified cartilage is an order of magnitude less than that of subchondral bone. **Journal of Orthopedic Research**, 12(5):637–47.

Meredith, N., Sherriff, N., Setchell, D., and Swanson, S. (1996). Measurements of the microhardness and young's modulus of human eamel and dentin using an indentation technique. **Archives of Oral Biology**, 41(6):539–45.

Michel, V., Ilefonse, P., and Morin, G. (1996). Assessment of archeological bone and dentin preservation from lazaret cave (middle pleistocene) in france. **Palaeogeography, Palaeoclimatology, Palaeoecology**, 126:109–119.

Michel, V., P., I., and Morin, G. (1995). Chemical and structural changes in cervus elephas tooth enamels during fossilization (lazaret cave): a combined ir and xrd rietveld analysis. **Geochem. Appl.**, 10:145–159.

Mullins, L. P., Bruzzi, M. S., and McHugh, P. E. (2007). Measurement of the microstructural fracture toughness of cortical bone using indentation fracture. **Journal of Biomechanics**, 40(14):3285–3288.

Munro, L. E., Longstaffe, F. J., and White, C. D. (2008). Effects of heating on the carbon and oxygen-isotope compositions of structural carbonate in bioapatite from modern deer bone. **Palaeogeography, Palaeoclimatology, Palaeoecology**, 5(3-4):142–150. Munro, L. E. Longstaffe, F. J. White, C. D.

Myoung, S., Lee, J., Constantino, P., Lucas, P., Chai, H., and Lawn, B. (2009). Morphology and fracture of enamel. **J Biomech**, 42(12):1947–1951.

Nash, L. (1998). Vertical clingers and sleepers: Seasonal influences on the activities and substrate use of lepilemur leucopus at beza mahafaly special reserve, madagascar. **Folia Primatologica**, 69:204–217.

Neuman, W. F., Toribara, T. Y., and Mulryan, B. J. (1956). The surface chemistry of bone .9. carbonate-phosphate exchange. **Journal of the American Chemical Society**, 78(17):4263–4266.

Nielsen-Marsh, C. and Hedges, R. E. M. (2000). Patterns of diagenesis in bone i: The effects of site environments. **Journal of Archaeological Science**, 27(12):1139–1150.

Olejniczak, A., Tafforeau, P., Feeney, R., and Martin, L. (2008). Three-dimensional primate molar enamel thickness. **J Hum Evol**, 54(2):187–195.

Olesiak, S., Oyen, M., and Ferguson, V. (2010a). Viscous-elastic-plastic behavior of bone using berkovich nanoindentation. **Mechanics of Time-Dependent Materials**, In Press:DOI 10.1007/s11043–009–9098–5.

Olesiak, S., Oyen, M., Sponheimer, M., Eberle, J., and Ferguson, V. (2006). Ultrastructural mechanical and material characterization of fossilized bone. **Materials Research Society Symposium Proceedings**, 975:DD03–09.

Olesiak, S., Sponheimer, M., Eberle, J., and Ferguson, V. (2008). The contribution of crystallinity to tissue-level properties in modern and fossilized bone. **Materials Research Society Symposium Proceedings**, 1132:Z01–06.

Olesiak, S., Sponheimer, M., Eberle, J., Oyen, M., and Ferguson, V. (2010b). Nanomechanical properties of modern and fossil bone. **Palaeogeography, Palaeoclimatology, Palaeoecology**, 289(1-4):2532.

Oliver, W. C. and Pharr, G. M. (1992). An improved technique for determining hardness and elastic-modulus using load and displacement sensing indentation experiments. **Journal of Materials Research**, 7(6):1564–1583.

Oliver, W. C. and Pharr, G. M. (2004). Measurement of hardness and elastic modulus by instrumented indentation: Advances in understanding and refinements to methodology. **Journal of Materials Research**, 19(1):3–20.

Oyen, M. (2006a). Nanoindentation hardness of mineralized tissues. **Journal of Biomechanics**, 39(14):2699–2702.

Oyen, M. and Ko, C. (2008). Indentation variability of natural nanocomposite materials. **Journal of Material Research**, 23(3).

Oyen, M. L. (2005). Spherical indentation creep following ramp loading. **Journal of Materials Research**, 20(8):2094–100.

Oyen, M. L. (2006b). Analytical techniques for indentation of viscoelastic materials. **Philosophical Magazine**, 86(33-35).

Oyen, M. L. (2006c). Nanoindentation hardness of mineralized tissues. **Journal Biomechanics**, 39(14):2699–702.

Oyen, M. L. and Cook, R. F. (2003). Load-displacement behavior during sharp indentation of viscous-elastic-plastic materials. **Journal of Materials Research**, 18(1):139–50.

Oyen, M. L., Ferguson, V. L., Bembey, A. K., Bushby, A. J., and Boyde, A. (2008). Composite bounds on the elastic modulus of bone. **Journal of Biomechanics**, 41:2585.

Oyen, M. L. and Ko, C. C. (2005). Finite element modeling of bone ultrastructure as a two-phase composite. **Materials Research Society Symposium Proceedings**, 844:Y8.7.1–6.

Oyen, M. L. and Ko, C. C. (2007). Examination of local variations in viscous, elastic, and plastic indentation responses in healing bone. **Journal of Material Science Materials in Medicine**, 18(4):623–8.

Oyen, M. L., Ko, C. C., Bembey, A. K., Bushby, A. J., and Boyde, A. (2005). Nanoindentation and finite element analysis of resin-embedded bone samples as a three-phase composite material. **Materials Research Society Symposium Proceedings**, 874:L1.7.1–6.

Paschalis, E., DiCarlo, E., Betts, F., Sherman, P., Mendelsohn, R., and Boskey, A. (1996). Ftir microspectroscopic analysis of human osteonal bone. **Calcified Tissue Int**, 59(6):480–487.

Pegg, D. (2007). Principles of cryopreservation. **Methods in Molecular Biology**, 368:39–57.

Penel, G., Delfosse, C., Descamps, M., and Leroy, G. (2005). Composition of bone and apatitic biomaterials as revealed by intravital raman microspectroscopy. **Bone**, 36(5):893–901.

Person, A., Bocherens, H., Mariotti, A., and Renard, M. (1996). Diagenetic evolution and experimental heating of bone phosphate. **Palaeogeography, Palaeoclimatology, Palaeoecology**, 126(1-2):135–149.

Person, A., Bocherens, H., Saliege, J., Paris, F., Zeitoun, V., and Gerard, M. (1995). Early diagenetic evolution of bone phosphate: An x-ray diffractometry analysis. **Journal of Archaeological Science**, 22(2):211–221.

Petrtyl, M., Hert, J., and Fiala, P. (1996). Spatial organization of the haversian bone in man. **J Biomech**, 29(2):161–9.

Petruska, J. A. and Hodge, A. J. (1964). Subunit model for tropocollagen macromolecule. **Proceedings of the National Academy of Sciences of the United States of America**, 51(5):871.

Pidaparti, R. M., Chandran, A., Takano, Y., and Turner, C. H. (1996). Bone mineral lies mainly outside collagen fibrils: predictions of a composite model for osteonal bone. **J Biomech**, 29(7):909–16.

Pienkowski, D., Doers, T., MonierFaugere, M., Geng, Z., Camacho, N., Boskey, A., and Malluche, H. (1997). Calcitonin alters bone quality in beagle dogs. **J Bone Miner Res**, 12(11):1936–1943.

Posner, A. and Duyckaerts, G. (1954). Infra-red study of the carbonate in bone, teeth and francolite. **Experientia**, 10(10):424–425.

Price, T. D., Burton, J. H., and Bentley, R. A. (2002). The characterization of biologically available strontium isotope ratios for the study of prehistoric migration. **Archaeometry**, 44:117–135. Part 1.

Qasim, T., Bush, M., Hu, X., and Lawn, B. (2005). Contact damage in brittle coating layers: Influence of surface curvature. **J Biomed Mater Res B**, 73B(1):179–185.

Ramasamy, J. G. and Akkus, O. (2007). Local variations in the micromechanical properties of mouse femur: the involvement of collagen fiber orientation and mineralization. **J Biomech**, 40(4):910–918.

Rand, A. (1935). On the habits of some madagascar mammals. **Journal Mammalogy**, 16(2):89–104.

Rapoff, A. J., Rinaldi, R. G., Hotzman, J. L., and Daegling, D. J. (2008). Elastic modulus variation in mandibular bone: A microindentation study of macaca fascicularis. **American Journal of Physical Anthropology**, 135(1):100–109.

Reiche, I., Favre-Quattropani, L., Vignaud, C., Bocherens, H., Charlet, L., and Menu, M. (2003). A multi-analytical study of bone diagenesis: the neolithic site of bercy (paris, france). **Measurement Science and Technology**, 14(9):1608–1619.

Reiche, I., Vignaud, C., and Menu, M. (2002). The crystallinity of ancient bone and dentine: New insights by transmission electron microscopy. **Archaeometry**, 44(3):447–459. Part 3.

Reid, S. and Boyde, A. (1987). Changes in the mineral density distribution in the human-bone with age– image analysis using backscattered electrons in the sem. **Journal of Bone and Mineral Research**, 2:13–22.

Reifsnider, K. (1991). Damage and damage mechanics. In Reifsnider, K., editor, **Fatigue of Composite Materials**, pages 11–77. Elsevier, New York.

Reilly, D. T. and Burstein, A. H. (1975). The elastic and ultimate properties of compact bone tissue. **J Biomech**, 8(6):393–405.

Reilly, D. T., Burstein, A. H., and Frankel, V. H. (1974). Elastic-modulus for bone. **Journal of Biomechanics**, 7(3):271.

Rensberger, J. (1995). Determination of stresses in mammalian dental enamel and their relevance to the interpretation of feeding behaviors in extinct taxa. In Thomason, J., editor, **Functional Morphology in Vertebrate Paleontology**, pages 151–172. Cambridge University Press, Cambridge.

Rhee, Y., Kim, H., Deng, Y., and Lawn, B. (2001). Contact-induced damage in ceramic coatings on compliant substrates: Fracture mechanics and design. **J Am Ceram Soc**, 84(5):1066–1072.

Rho, J., Tsui, T. Y., and Pharr, G. M. (1997). Elastic properties of human cortical and trabecular lamellar bone measured by nanoindentation. **Biomaterials**, 18(20):1325–1330.

Rho, J. Y., Currey, J. D., Zioupos, P., and Pharr, G. M. (2001). The anisotropic young's modulus of equine secondary osteones and indterstitial bone determined by nanoindentation. **The Journal of Experimental Biology**, 204:1775–1781.

Rho, J.-Y., Kuhn-Spearing, L., and Zioupos, P. (1998). Mechanical properties and the hierarchical structure of bone. **Medical Engineering and Physics**, 20(2):92–102.

Rho, J. Y. and Pharr, G. M. (1999). Effects of drying on the mechanical properties of bovine femur measured by nanoindentation. **Journal of Materials Science-Materials in Medicine**, 10:485–488.

Rho, J. Y., Roy, M. E., Tsui, T. Y., and Pharr, G. M. (1999a). Elastic properties of microstructural components of human bone tissue as measured by nanoindentation. **Journal of Biomedical Materials Research**, 45(1):48–54.

Rho, J. Y., Zioupos, P., Currey, J. D., and Pharr, G. M. (1999b). Variations in the individual thick lamellar properties within osteons by nanoindentation. **Bone**, 25(3):295–300.

Rho, J. Y., Zioupos, P., Currey, J. D., and Pharr, G. M. (2002). Microstructural elasticity and regional heterogeneity in human femoral bone of various ages examined by nanoindentation. **Journal of Biomechanics**, 35(2):189–198.

Riches, P. E., Everitt, N. M., Heggie, A. R., and McNally, D. S. (1997). Microhardness anisotropy of lamellar bone. **J Biomech**, 30(10):1059–61.

Rink, W. J. and Schwarz, H. P. (1995). Tests for diagenesis in tooth enamel: Esr dating signals and carbonatecontents. **Journal of Archaeological Science**, 22:251–255.

Robinson, C., Kirkham, J., Brookes, S., Bonass, W., and Shore, R. (1995). The chemistry of enamel development. **International Journal of Developmental Biology**, 39(1):145–152.

Roschger, P., PLENK, H., Klaushofer, K., and ESCHBERGER, J. (1995). A new scanning electron-microscopy approach to the quantification of bone-mineral distribution - backscattered electron image grey-levels correlated to calcium k-alpha-line intensities. **Scanning Microscopy**, 9(1):75–88.

Rosen, V., Hobbs, L., and Spector, M. (2002). The ultrastructure of anorganic bovine bone and selected synthetic hyroxyapatites used as bone graft substitute materials. **Biomaterials**, 23(3):921–928.

Rubin, C. T. and Lanyon, L. E. (1984). Regulation of bone formation by applied dynamic loads. **Journal of Bone and Joint Surgery**, 66(3):397–402.

Rubin, C. T. and Lanyon, L. E. (1985). Regulation of bone mass by mechanical strain magnitude. **Calcified Tissue International**, 37(4):411–7.

Saito, H. and Yokoi, M. (1992). A c-13 nmr-study on collagens in the solid-state - hydration dehydration-induced conformational change of collagen and detection of internal motions. **Journal of Biochemistry**, 111(3):376–382.

Sasaki, N. and Enyo, A. (1995). Viscoelastic properties of bone as a function of water content. **Journal of Biomedical Materials Research**, 28(7):809–815.

Sauther, M. L. (1998). Interplay of phenology and reproduction in ring-tailed lemurs: Implications for ring-tailed lemur conservation. **Folia Primatol**, 69:309–320.

Sauther, M. L. and Cuozzo, F. P. (2009). The impact of fallback foods on wild ring-tailed lemur biology: A comparison of intact and anthropogenically disturbed habitats. **American Journal of Physical Anthropology**, 140(4):671–686.

Sauther, M. L., Sussman, R. W., and Cuozzo, F. (2002). Dental and general health in a population of wild ring-tailed lemurs: A life history approach. **American Journal of Physical Anthropology**, 117(2):122–132.

Schenk, R., Olah, A., and Herrmann, W. (1984). Preparation of calcified tissues for light microscopy. In Dickson, G., editor, **Methods of Calcified Tissue Preparation**. Elsevier, New York.

Schoeninger, M., Iwaniec, U., and Nash, L. (1998). Ecological attributes recorded in stable isotope ratios of arboreal prosimian hair. **Oecologia**, 113(2):222–230.

Seligsohn, D. (1977). Analysis of species-specific molar adaptations in strepsirhine primates. **Contributions to primatology**, 11:1–116.

Shaw, G. (1879). A few notes upon four species of lemurs (*lemur eatta, hapalemur simus, cheirogaleus milii, microcebus smithii*) specimens of which were brought alive to england in 1878. **Proceedings of the Zoological Society of London**, 168:132–136.

Shellis, R. P., Beynon, A. D., Reid, D. J., and HIIEMAE, K. M. (1998). Variations in molar enamel thickness among primates. **Journal of Human Evolution**, 35(4-5):507–522.

Shimizu, D. and Macho, G. A. (2008). Effect of enamel prism decussation and chemical composition on the biomechanical behavior of dental tissue: A theoretical approach to determine the loading conditions to which modern human teeth are adapted. **THE ANATOMICAL RECORD**, 291(2):175–182.

Shimizu, D., Macho, G. A., and Spears, I. R. (2005). Effect of prism orientation and loading direction on contact stresses in prismatic enamel of primates: Implications for interpreting wear patterns. **The Anatomical Record**, 126(4):427–434.

Sillen, A. (1989). Diagenesis of the inorganic phase of cortical bone. In Price, T. D., editor, **The Chemistry of Prehistoric Human Bones**, pages 221–229. Cambridge University Press, Cambridge.

Sillen, A. and Parkington, J. (1996). Diagenesis of bones from eland's bay cave. **Journal of Archaeological Science**, 23(4):535–542.

Simmen, B., Sauther, M., Soma, T., Rasamimanana, H., Sussman, R., Jolly, A., Tarnaud, L., and Hladik, A. (2006). Plant species fed on by lemur catta in gallery forests of the southern domain of madagascar. In Jolly, A., Sussman, R., Koyama, N., and Rasamimanana, H., editors, **Ring-Tailed Lemur Biology**, pages 55–68. Springer, New York.

Skedros, J., Bloebaum, R., Bachus, K., and Boyce, T. (1993). The meaning of graylevels in backscattered electron images of bone. **Journal of Biomedical Material Research**, 27(1):47–56.

Sneddon, I. (1948). Boussinesq's problem for a rigid cone. **Proceedings of Cambridge Philosophy Society**, 44:492–507.

Spears, I. (1997). A three-dimensional finite element model of prismatic enamel: A reappraisal of the data on the young's modulus of enamel. **Journal of Dental Research**, 76(10):1690–1697.

Spencer, P., Young, W., Katz, L., and Misra, A. (2005). Physicochemical interactions at the dentin/adhesive interface using ftir chemical imaging. **Journal of Biomedical Optics**, 10(3).

Sponheimer, M. and Lee-Thorp, J. (1999). Alteration of enamel carbonate environments during fossilization. **Journal of Archaeological Science**, 26:143–150.

Sponheimer, M. and Lee-Thorp, J. (2006). Enamel diagenesis at south african australopith sites: Implications for paleoecological reconstruction with trace elements. **Geochimica et Cosmochimica Acta**, 70:1644–1654.

Sponheimer, M., Passey, B., de Ruiter, D., Guatelli-Steinberg, D., Cerling, T., and Lee-Thorp, J. (2006). Isotopic evidence for dietary variability in the early hominin paranthropus robustus. **Science**, 314(5801):980–982.

Stanford, J. W., Paffenbarger, G. C., Kumpula, J. W., and Sweeney, W. T. (1958). Determination of some compressive properties of human enamel and dentin. **Journal of American Dental Association**, 57(4):487–95.

Stentz, D., Blair, S., Goater, C., Feller, S., and Affatigato, M. (2001). Analysis of the structure of lead borosilicate glasses using laser ionization time of flight mass spectroscopy. **J Non-Cryst Solids**, 293:416–421.

Straines, M., Robinson, W., and Hood, J. (1981). Spherical indentation of tooth enamel. **Journal of Materials Science**, 16:2551–2556.

Strait, D. S., Weber, G. W., Neubauer, S., Chalk, J., Richmond, B. G., Lucas, P. W., Spencer, M. A., Schrein, C., Dechow, P. C., Ross, C. F., Grosse, I. R., Wright, B. W., Constantino, P., Wood, B. A., Lawn, B., Hylander, W. L., Wang, Q., Byron, C., Slice, D. E., and Smith, A. L. (2009). The feeding biomechanics and dietary ecology of australopithecus africanus. **Proc Natl Acad Sci USA**, 106(7):2124–9.

Sudarsan, K. and Young, R. A. (1969). Significant precision in crystal structural details - holly springs hydroxyapatite. **Acta Crystallographica Section B-Structural Crystallography and Crystal Chemistry**, B25:1534. Part 8.

Sudarsanan, K. and Young, R. A. (1969). Significant precision in crystal structural details: Holly springs hydroxyapatite. **Acta Crystallographica Section B: Structural Science**, B25:1534–1543. Part 8.

Sussman, R. (1974). Ecological distinctions in sympatric species of lemur. In Martin, R., Doyle, G., and Walker, A., editors, **Prosimian Biology**, pages 75–80. Duckworth, London.

Svalbe, I., Chaudhri, M., Traxel, K., Ender, C., and Mandel, A. (1984). Microprobe profiling of fluorine and other trace elements to large depths in teeth. **Nuclear Instruments and Methods in Physics Research Section B: Beam Interactions with Materials and Atoms**, 3(1-3):648–650.

Swadener, J. G., Rho, J. Y., and Pharr, G. M. (2001). Effects of anisotropy on elastic moduli measured by nanoindentation in human tibial cortical bone. **Journal of Biomedical Materials Research**, 57(1):108–112.

Tabor, D. (1951). **The Hardness of Metals**. Clarendon Press, Oxford.

Tai, K. S., Qi, H. J., and Ortiz, C. (2005). Effect of mineral content on the nanoindentation properties and nanoscale deformation mechanisms of bovine tibial cortical bone. **Journal of Materials Science-Materials in Medicine**, 16(10):947–959.

Tattersall, I. (1982). **The Primates of Madagascar**. Columbia University Press, New York.

Teaford, M. F. and Ungar, P. S. (2000). Diet and the evolution of the earliest human ancestors. **Proceeding of the National Academy of Sciences**, 97(25):13506–13511.

Tesch, W., Eidelman, N., Roschger, P., Goldenberg, F., Klaushofer, K., and Fratzl, P. (2001). Graded microstucture and mechanical porperties of human crown dentin. **Calcif Tissue Int**, 69:147–157.

Trueman, C. N. G., Behrensmeyer, A. K., Tuross, N., and Weiner, S. (2004). Mineralogical and compositional changes in bones exposed on soil surfaces in amboseli national park, kenya: diagenetic mechanisms and the role of sediment pore fluids. **Journal of Archaeological Science**, 31(6):721–739.

Turner-Walker, G. and Jans, M. (2008). Reconstructing taphonomic histories using histological analysis. **Palaeogeography, Palaeoclimatology, Palaeoecology**, 266(3-4):227–235.

Ungar, P. and M'Kirera, F. (2003). A solution to the worn tooth conundrum in primate functional anatomy. **Proc Natl Acad Sci USA**, 100(7):3874–3877.

Vajda, E., Skedros, J., and Bloebaum, R. (1995). Consistency in calibrated backscattered electron images of calcified tissues and minerals analyzed in multiple imaging sessions. **Scanning Microscopy**, 9(3):741–755.

Vanleene, M., Mazeran, P. E., and Tho, M. (2006). Influence of strain rate on the mechanical behavior of cortical bone interstitial lamellae at the micrometer scale. **Journal of Materials Research**, 21(8):2093–2097.

Vogel, E. R., van Woerden, J. T., Lucas, P. W., Atmoko, S. S. U., van Schaik, C. P., and Dominy, N. J. (2008). Functional ecology and evolution of hominoid molar enamel thickness: Pan troglodytes schweinfurthii and pongo pygmaeus wurmbii. **J Hum Evol**, 55(1):60–74.

von Koenigswald, W., Rensberger, J. M., and Pretzschner, H. U. (1987). Changes in the tooth enamel of early paleocene mammals allowing increased diet diversity. **Nature**, 328(6126):150–2.

Wang, X., Yoon, Y. J., and Ji, H. (2007). A novel scratching approach for measuring age-related changes in the in situ toughness of bone. **Journal of Biomechanics**, 40(6):1401–1404.

Wang, Y. and Cerling, T. E. (1994). A model of fossil tooth and bone diagenesis: implications for paleodiet reconstruction from stable isotopes. **Palaeogeography, Palaeoclimatology, Palaeoecology**, 107:281–289.

Weatherell, J., Robinson, C., and Hallsworth, A. (1974). Variations in the chemical composition of human enamel. **Journal of Dental Research**, 53(2):179–192.

Weiner, S., Arad, T., Sabanay, I., and Traub, W. (1997). Rotated plywood structure of primary lamellar bone in the rat: Orientations of the collagen fibril arrays. **Bone**, 20(6):509–514.

Weiner, S. and Bar-Yosef, O. (1990). States of preservation of bones from prehistoric sites in the near-east - a survey. **Journal of Archaeological Science**, 17(2):187–196.

Weiner, S., Goldberg, P., and Bar-Yosef, O. (1993). Bone preservation in kebara cave, israel using on-site fourier-transform infrared spectrometry. **Journal of Archaeological Science**, 20(6):613–627.

Weiner, S. and Traub, W. (1992). Bone-structure - from angstroms to microns. **Faseb Journal**, 6(3):879–885.

Willems, G., Celis, J., Lambrechts, P., Braem, M., and Vanherle, G. (1993). Hardness and youngs modulus determined by nanoindenta- tion technique of ller particles of dental restorative materials compared with human enamel. **Journal of Biomedical Materials Research**, 27:747–755.

Wilson, E. E., Awonusi, A., Morris, M. D., Kohn, D. H., Tecklenburg, M. M. J., and Beck, L. W. (2006). Three structural roles for water in bone observed by solid-state NMR. **Biophysical Journal**, 90(10):3722–3731.

Xie, Z. H., Swain, M. V., Swadener, G., Munroe, P., and Hoffman, M. (2009). Effect of microstructure upon elastic behaviour of human tooth enamel. **J Biomech**, 42(8):1075–1080.

Xu, H., Smith, D., Jahanmir, S., Romberg, E., Kelly, J., Thompson, V., and Rekow, E. (1998). Indentation damage and mechanical properties of human enamel and dentin. **Journal of Dental Research**, 77(3):472–480.

Xu, J., Rho, J. Y., Mishra, S. R., and Fan, Z. (2003). Atomic force microscopy and nanoindentation characterization of human lamellar bone prepared by microtome sectioning and mechanical polishing technique. **Journal of Biomedical Materials Research Part A**, 67A(3):719–726.

Yamashita, J., Furman, B., Rawls, H., Wang, X., and Agrawal, C. (2001). The use of dynamic mechanical analysis to assess the viscoelastic properties of human cortical bone. **Journal of Biomedical Materials Research Part B**, 58(1):47–53.

Yamashita, N. (1996). Seasonality and site specificity of mechanical dietary patterns in two malagasy lemur families (lemuridae and indriidae). **International Journal of Primatology**, 17(3):355–387.

Yamashita, N. (1998). Functional dental correlates of food properties in five malagasy lemur species. **American Journal of Physical Anthropology**, 106(2):169–188.

Yamashita, N. (2002). Diets of two lemur species in different microhabitats in beza mahafaly special reserve, madagascar. **International Journal of Primatology**, 23(5):1025–1051.

Yamashita, N. (2003). Food procurement and tooth use in two sympatric lemur species. **American Journal of Physical Anthropology**, 121(2):125–133.

Zazzo, A., Mariotti, A., Lecuyer, C., and Heintz, E. (2002). Intra-tooth isotope variations in late miocene bovid enamel from afghanistan: paleobiological, taphonomic, and climatic implications. **Palaeogeography, Palaeoclimatology, Palaeoecology**, 186(1-2):145–161.

Zhang, C. Y., Zhang, Y. W., Zeng, K. Y., and Shen, L. (2005). Nanoindentation of polymers with a sharp indenter. **Journal of Materials Research**, 20(6):1597–1605.

Zhang, J., Michalenko, M., Kuhl, E., and Ovaert, T. (2010). Characterization of indentation response and stiffness reduction of bone using a continuum damage model. **Journal of the Mechanical Behavior of Biomedical Materials**, 3(2):189–202.

Zhang, J., Niebur, G., and Ovaert, T. (2008). Mechanical property determination of bone through nano- and micro-indentation testing and finite element simulation. **Journal of Biomechanics**, 41(2):267–75.

Zhou, J. and Hsiung, L. L. (2007). Depth-dependent mechanical properties of enamel by nanoindentation. **Journal of Biomedical Materials Research A**, 81A(1):66–74.

Ziv, V. and Weiner, S. (1994). Bone crystal sizes - a comparison of transmission electron-microscopic and x-ray-diffraction line-width broadening techniques. **Connective Tissue Research**, 30(3):165–175.

Zysset, P. K., Guo, X. E., Hoffler, C. E., Moore, K. E., and Goldstein, S. A. (1998). Mechanical properties of human trabecular bone lamellae quantified by nanoindentation. **Technol Health Care**, 6(5-6):429–32.

Zysset, P. K., Guo, X. E., Hoffler, C. E., Moore, K. E., and Goldstein, S. A. (1999). Elastic modulus and hardness of cortical and trabecular bone lamellae measured by nanoindentation in the human femur. **Journal of Biomechanics**, 32(10):1005–1012.

Appendix A

Publications, Abstracts, and Presentations

A.1 Journal Articles

(1) Paietta, R.C., Campbell, S.E., Ferguson, V.L."Influence of Nanoindentation Spherical Tip Radius, Contact Depth, and Contact Area on Properties in Lamellar Bone" Journal of Biomechanics (In preparation, 2010).

(2) Campbell, S.E., Geiss, R., Ferguson, V.L. Creation of lithium-rubidium borosilicate glass standards for quantitive backscatter electron imaging of mineralized tissues (In preparation)

(3) Campbell, S.E., Cuozzo, F.P., Sauther, M.L., Sponheimer, M., Ferguson, V.L. Nanoindentation of Lemur Enamel: Investigation of property variations within a single molar and between species American Journal of Physical Anthropology. (In preparation)

(4) Lloyd, S.A.J., Simske, S.J., Bogren, L.K., Olesiak, S.E., Bateman, T.A., Ferguson, V.L. "Insulin-like growth factor 1 and macrophage colony stimulating factor synergistically increase bone formation in mice." (In Review, 2010)

(5) Olesiak, S.E., Oyen, M.L., Ferguson, V.L. Viscous-Elastic-Plastic Behavior of Bone using Berkovich Nanoindentation Mechanics of Time-Dependent Materials. 14: 111-124, 2010.

(6) Olesiak, S.E., Sponheimer, M., Eberle, J.J., Oyen, M., Ferguson, V.L. Nanomechanical Properties of Modern and Fossil Bone Palaeogeography, Palaeoclimatology, Palaeoecology. 289 (1-4): 25-32, 2010.

A.2 Book Chapters

(1) Ferguson, V.L., Olesiak, S.E. Nanoindentation of Bone In Oyen, M.L., editor The Handbook of Nanoindentation with Biological Applications, World Scientific Inc. Press, 2010.

A.3 Refereed Conference Proceedings

(1) Olesiak, S.E, Oyen, M.L, Ferguson, V.L., Viscous Behavior in Berkovich Nanoindentation of Bone Society for Experimental Mechanics Annual Conference Proccedings. 451, 2009.

(2) Olesiak, S.E., Sponheimer, M., Eberle, J.J., Ferguson, V.L., The Contribution of Crystallinity to Tissue-level Properties in Modern and Fossilized Bone Materials Research Society Symposium Proceedings. 1132 (Z01-06), 2008.

(3) Olesiak, S.E., Oyen, M., Sponheimer, M., Eberle, J.J., Ferguson, V.L., Ultrastructural Mechanical and Material Characterization of Fossilized Bone, Materials Research Society Symposium Proceedings. 975 (DD03.09), 2006.

A.4 Conference Abstracts and Posters

(1) Olesiak, S.E., Cuozzo, F.P, Sauther, M.L, Sponheimer, M., Ferguson, V.L., Variations in Nanomechanical Properties of Lemur Enamel, American Society for Bone and Mineral Research (ASBMR) Annual Conference, Denver, CO, September, 2009. (poster)

(2) Olesiak, S.E., Oyen, M., Sponheimer, M., Eberle, J.J., Ferguson, V.L., Nanoindentation of modern and Fossilized Bone Graduate Engineering Annual Research Symposium (GEARS), University of Colorado, Boulder, CO, March, 2009. (Best Presentation award).

(3) Olesiak, S.E., Oyen, M., Sponheimer, M., Eberle, J.J., Ferguson, V.L., Nanoindentation: A new approach to understanding the Processes of Diagenesis Industrial Advisory Committee Meeting University of Colorado, Boulder, CO, October, 2008. (Invited talk)

(4) Olesiak, S.E., Oyen, M., Sponheimer, M., Eberle, J.J., Ferguson, V.L., Nanomechanical property dependence on crystallinity in modern and fossilized bone tissues, Society of Engineering Science (SES) annual technical meeting, University of Illinois, Champaign, IL, October, 2008.

(5) Olesiak, S.E., Oyen, M., Sponheimer, M., Eberle, J.J., Ferguson, V.L., Nanomechanical and Material Characterization of Fossilized Bone, Graduate Engineering Annual Research Symposium (GEARS), University of Colorado, Boulder, CO, March, 2008.

(6) Olesiak, S.E., Sponheimer, M., Ferguson, V.L., Preservation of Human Bone Remains at Joya de Ceren, American Society of Mechanical Engineering (ASME) Summer Bioengineering Conference, Keystone, CO, June, 2007. (poster)

(7) Olesiak, S.E., Oyen, M., Sponheimer, M., Ferguson, V.L., Diagenesis: Material and Mechanical Properties of Fossilized Bone, Graduate Engineering Annual Research Symposium (GEARS), University of Colorado, Boulder, CO, March, 2007.

(8) Olesiak, S.E., Ferguson, V.L., Mechanical Property Variation in Mouse Cortical Bone, Materials Research Society (MRS) Fall Meeting, Boston, MA, November, 2006.

(9) Olesiak, S.E., Ferguson, V.L., Bone Material Property Changes with Nerve Injury and Bisphosphonate Therapy, Graduate Engineering Annual Research Symposium (GEARS), University of Colorado, Boulder, CO, March, 2006. (poster)

Appendix B

Viscous-elastic-plastic behavior of bone using Berkovich nanoindentation

Viscous-elastic-plastic behavior of bone using Berkovich nanoindentation

Sara E. Olesiak · Michelle L. Oyen · Virginia L. Ferguson

Received: 30 June 2009 / Accepted: 28 September 2009 / Published online: 18 October 2009

Abstract A series viscous-elastic-plastic (VEP) indentation model was expanded to include analysis of the common trapezoidal testing condition, consisting of constant loading—and unloading—rates with an intervening creep hold period. This full VEP model was applied to analyze nanoindentation test of three polymers and five different types of bone. The full VEP solution allows for direct determination of the viscous term as calculated from the creep hold, while the elastic and plastic material parameters were determined from a non-linear curve-fit of the unloading displacement-time data. Additionally, the use of the trapezoidal loading procedure permitted analysis of the unloading load-displacement data with traditional Oliver-Pharr analysis; the material properties from this analysis compared well with those obtained with VEP analysis. Using the full VEP solution and fitted material constants the loading and creep hold displacement-time curves were simulated and matched well to both polymer and bone experimental data. The full VEP solution shows great promise in for obtaining material parameters for many viscoelastic materials such as hydrated bone, polymers, and other biological tissues.

Keywords Nanoindentation · Bone · Viscoelastic · Creep · Polymer

1 Introduction

Nanoindentation has become an increasingly popular technique to study a wide range of viscoelastic materials such as biological tissues and polymers. Nanoindentation with a Berkovich tip is well suited to study tissue-level mechanical properties and to investigate site specific variations within individual structures (e.g. lamellae) or bone types (osteonal versus interstitial) (Rho et al. 1999a, 1999b; Zysset et al. 1999). However, the ability to collect accurate material property measurements using nanoindentation is limited by the time

S.E. Olesiak · V.L. Ferguson
Department of Mechanical Engineering, University of Colorado, Boulder, CO, 80309, USA

M.L. Oyen (✉)
Department of Engineering, University of Cambridge, Trumpington Street, Cambridge CB2 1PZ, UK
e-mail: mlo29@cam.ac.uk

dependent nature of biological tissues, such as bone, as traditional analytical techniques often assume an elastic-perfectly plastic material with no viscous deformation component.

Biological materials possess inherently time-dependent behavior, yet conventional analyses, such as the "Oliver-Pharr" (OP) method (Oliver and Pharr 1992, 2004), are commonly applied to extract time-independent elastic (plane strain modulus, E') and plastic (contact hardness, H_c) material parameters. The use of the OP method of extracting material property measurements from viscoelastic materials and can lead to large errors by extracting material parameters from an unloading curve which assumes a purely elastic recovery, yet creep that occurs on initial portion of unloading can led to negative stiffness values (Oyen and Cook 2003). It is therefore common practice to eliminate viscous behavior through a rapid unloading rate (Cheng et al. 2005) or an extended creep hold (Briscoe et al. 1998; Chudoba and Richter 2001; Feng and Ngan 2002). However, the viscous material response is often of interest and more recent works have embraced nanoindentation as a tool to explore the viscoelastic behavior of biological tissues (Bembey et al. 2006; Oyen 2006a; Oyen and Cook 2003; Oyen and Ko 2007).

Recently, analytical approaches have been developed to directly extract viscoelastic properties from pyramidal indentation tests (Feng and Ngan 2002; Liu et al. 2006; Oyen 2006a, 2006b, 2008; Oyen and Cook 2003; Sakai 1999; Zhang et al. 2005, 2006). These analyses explicitly incorporate the time dependence by combining viscoelastic constitutive laws with expressions for displacement under elastic indentation to give the load-time response. In particular, a viscous-elastic-plastic (VEP) model for time-dependent indentation has been developed in terms of experimentally-derived variables of load, displacement, and time (Oyen and Cook 2003). The model is based on a simple set of mechanical elements in series, which describe the viscous, elastic, and plastic behavior of indentation by sharp, geometrically similar tips (such as Vickers, Knoop, Berkovich, or conical indenter geometries).

To date, the VEP model has only been solved for two loading conditions: the triangular test profile with a constant loading and unloading rate, and exponential loading. The VEP model has not been utilized for the very common test profile of trapezoidal loading, which uses constant loading—and unloading—rates with an intervening hold period to allow for creep. The trapezoidal testing profile is commonly used for OP analysis of viscoelastic material and seeks to "eliminate" the viscous component, thus allowing for semi-elastic unloading due to a steady-state creep rate near the end of the hold period (Feng and Ngan 2002). The development of the full VEP model (for trapezoidal loading) will allow for retroactive analysis of numerous nanoindentation studies in order to extract a complete set of material properties including viscosity. Additionally, the full VEP solution allows for direct extraction of the viscous component from the creep hold, which is not possible with the simple triangular loading profile. This full VEP solution will also allow for comparison of material parameters obtained from both OP and VEP analyses, which may not directly correlate in extremely viscous materials such as biological tissues.

In this work, substantial improvement to the robustness of the VEP model is made though the development of the full VEP solution for trapezoidal loading. We apply the full VEP model to extract the viscous, elastic and plastic properties of three polymer controls, and then use the model to examine five different types of bone. Parameters obtained from the full VEP solution to the load-hold-unload data of the different types of bone compared well with parameters from a traditional OP analysis.

2 Analytical solutions

2.1 VEP model background

The VEP model combines, in series, three extensive quadratic elements, viscous, elastic, and plastic, to create a time-dependent indentation model. Equal loads (P) are distributed in the three elements leading to a total displacement that is equivalent to the sum of the displacement of the individual elements (Oyen and Cook 2003).

$$h = h_v + h_e + h_p. \tag{1}$$

The VEP constitutive differential equation is given by the sum of the displacement rates of each of the three elements (Oyen and Cook 2003):

$$\begin{aligned} \frac{dh}{dt} &= \frac{dh_v}{dt} + \frac{dh_e}{dt} + \frac{dh_p}{dt} \\ &= \frac{P^{1/2}}{(\alpha_3 \eta_Q)^{1/2}} + \frac{1}{P^{1/2}} \frac{dP}{dt} \frac{1}{2(\alpha_2 E')^{1/2}} + \frac{1}{P^{1/2}} \frac{dP}{dt} \frac{1}{2(\alpha_1 H)^{1/2}} \end{aligned} \tag{2}$$

where η_Q, E', and H are the parameters indentation viscosity, plane strain modulus, and resistance to plastic deformation, respectively. The dimensionless geometric constants are defined for a Berkovich tip as: $\alpha_1 = 24.5$ and $\alpha_2 = \alpha_3 = 4.4$ (Oyen and Cook 2003). The plane strain modulus (E') can be related to elastic modulus (E) with a know Poisson's ratio by:

$$E' = \frac{E}{1 - \upsilon^2}. \tag{3}$$

2.2 VEP solution for trapezoidal loading

The VEP constitutive equation can be solved for various loading histories given the initial conditions. Trapezoidal loading can be seen in Fig. 1, where t_R = rise time and t_c = creep

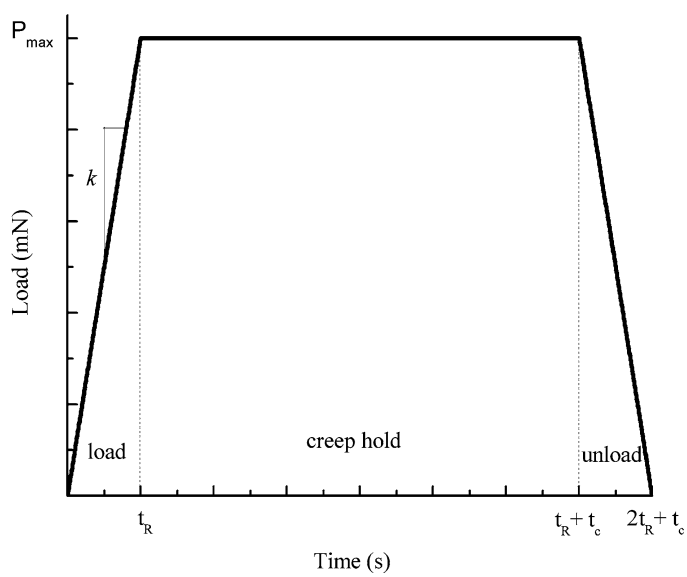

Fig. 1 A general trapezoidal load-time (P–t) input function for indentation experiments. Depicted in the figure is the constant load and unload rate (k) over the rise time (t_R) with a creep hold time (t_c). The total time of the test is equal to $2t_R + t_c$

hold time. Loading at a constant rate (k) to a max load ($P_{\max}$) over rise time t_{R}, gives the initial conditions:

$$\begin{aligned} P(t) &= kt \\ \frac{dP}{dt} &= k; \quad 0 \le t \le t_R. \end{aligned} \tag{4}$$

The VEP constitutive equation for loading is given by:

$$\frac{dh}{dt} = \frac{(kt)^{1/2}}{(\alpha_3 \eta_Q)^{1/2}} + \frac{1}{(kt)^{1/2}} \frac{k}{2(\alpha_2 E')^{1/2}} + \frac{1}{(kt)^{1/2}} \frac{k}{2(\alpha_1 H)^{1/2}} \tag{5}$$

which is solved for (Oyen and Cook 2003):

$$h^{\mathrm{LOAD}}(t) = (kt)^{1/2} \left(\frac{2t}{3(\alpha_3 \eta_Q)^{1/2}} + \frac{1}{(\alpha_2 E')^{1/2}} + \frac{1}{(\alpha_1 H)^{1/2}} \right). \tag{6}$$

During the creep hold at max load, $P(t) = P_{\max}$, the VEP constitutive equation gives:

$$\frac{dh}{dt} = \frac{(P_{\max})^{1/2}}{(\alpha_3 \eta_Q)^{1/2}}; \quad t_{\mathrm{R}} \le t \le t_{\mathrm{c}} + t_{\mathrm{R}} \tag{7}$$

which is solved for:

$$h^{\mathrm{CREEP}}(t) = \frac{(P_{\max})^{1/2}}{(\alpha_3 \eta_Q)^{1/2}} (t - t_{\mathrm{R}}) + h^{\mathrm{LOAD}}(t_{\mathrm{R}}). \tag{8}$$

For unloading, at time $t_{\mathrm{R}} + t_{\mathrm{c}}$, with an unloading rate $-k$, the input values are given by:

$$\begin{aligned} P(t) &= kt_{\mathrm{R}} - k(t - t_{\mathrm{R}} - t_{\mathrm{c}}) = k(2t_{\mathrm{R}} + t_{\mathrm{c}} - t) \\ \frac{dP}{dt} &= -k; \quad t_{\mathrm{R}} + t_{\mathrm{c}} \le t \le 2t_{\mathrm{R}} + t_{\mathrm{c}}. \end{aligned} \tag{9}$$

The assumption of perfect plasticity forces the plastic element to be suppressed on unloading as $dh_p/dt = 0$. Thus the unloading constitutive equation is:

$$\frac{dh}{dt} = \frac{[k(2t_{\mathrm{R}} + t_{\mathrm{c}} - t)]^{1/2}}{(\alpha_3 \eta_Q)^{1/2}} - \frac{1}{[k(2t_{\mathrm{R}} + t_{\mathrm{c}} - t)]^{1/2}} \frac{k}{2(\alpha_2 E')^{1/2}} + 0, \tag{10}$$

which is solved to give:

$$h^{\mathrm{UNLOAD}}(t) = (k)^{1/2} \left(\frac{t_{\mathrm{R}}^{3/2} - (2t_{\mathrm{R}} + t_{\mathrm{c}} - t)^{3/2}}{3/2(\alpha_3 \eta_Q)^{1/2}} + \frac{(2t_{\mathrm{R}} + t_{\mathrm{c}} - t)^{1/2} - t_{\mathrm{R}}^{1/2}}{(\alpha_2 E')^{1/2}} \right) + h^{\mathrm{CREEP}}(t_{\mathrm{R}} + t_{\mathrm{c}}) \tag{11}$$

Equations (6), (8), and (11) form the full displacement-time response for a VEP material under trapezoidal loading.

3 Methods and materials

3.1 Materials

In total five types of bone were prepared for nanoindentation testing: porcine jaw plexiform bone, adult bovine femur osteonal and interstitial bone, and immature porcine tibia osteonal

and interstitial bone. Porcine plexiform bone sample was prepared for nanoindentation testing in a previous study (Chang et al. 2003). Briefly, the 4th premolar was surgically removed and replaced with a titanium dental implant in the alveolar ridge seven months post extraction. The implants were shielded from bite force and left in place for one month prior to animal sacrifice. Plexiform bone around the implant was sectioned and embedded in polymer resin (PL-1, Vishay Micro-Measurements, Raleigh, NC) (Chang et al. 2003). Adult bovine femur was obtained from an abattoir (Arapahoe Packing, Lafayette, CO) as fresh frozen and was then sectioned and dehydrated in a series of ethanol solution. Young porcine dried tibia (∼3 yr, with a non-fused growth plate) was obtained from the museum of the University of Colorado at Boulder. Porcine tibia and bovine femur cortical bone was tested in both interstitial (int.) and osteonal (ost.) sites. All samples were sectioned and polished to a 0.05 μm finish for indentation testing. Additionally three polymer samples: polycarbonate (PC), polymethymethacrylate (PMMA), and high-density polyethylene (HDPE), were prepared for nanoindentation testing in order to validate the full VEP model across a wide range of viscoelastic material responses.

Nanoindentation tests were performed using a Nanoindenter XP (MTS Systems Corp, Oak Ridge, TN) with a diamond pyramidal Berkovich tip. Tests were run with a trapezoidal loading scheme (Fig. 1) with a constant loading/unloading rate (k) to a max load ($P_{\max}$) of 100 mN, with a creep hold of time (t_c). All bone indentation test were conducted at a constant loading rate of 5 mN s^{-1} with a creep hold $t_c = 120$ s. Six indentations were placed in each type of bone. Indentation in polymer samples were conducted at a constant load rate of 4 mN s^{-1} with creep holds ranging from $t_c = 370$ to 450 s.

The load-displacement-time data was exported for each test and analyzed using both the OP method (Oliver and Pharr 2004) and the full solution VEP model (Sect. 2). In both analytical methods a "perfect" (non-blunted) Berkovich tip shape and a constant Poisson's ratio for bone ($\nu = 0.3$) were assumed to permit comparison between the two methods.

3.2 Viscous-elastic-plastic model

The displacement time (h–t) curve from each indent was fitted to the full VEP model in order to extract material parameters of each sample. In this two-step process, the indentation viscosity (η_Q) was first calculated from the creep hold segment and (8), which assumes a linear creep response that is averaged over the entire creep hold period. Secondly, while the indentation viscosity (η_Q) was held constant, the unloading (h–t) curve was fit to (11) in order to extract elastic (E') and plastic (H) material parameters. Equation (11) accounts for the initial total displacement (at time $t_c + t_R$) from both loading and creep hold which is dependent on the material properties of the material and therefore fitting to the unloading curve alone can allow for the extraction of both (E') and plastic (H) parameters. The nonlinear curve-fit function in OriginPro 8 (OriginLab, Northampton, MA) was used with Levenberg-Marquardt iterations. Loading rate (k), rise time (t_R), and creep hold time (t_c) were fixed from experimental parameters.

Additionally, the contact hardness (H_{c_VEP}) was calculated for comparison to OP analysis, based on the definition of contact hardness and using the VEP material parameters (E', H, and η_Q) as follows (Oyen 2006a; Oyen and Ko 2007; Sakai 1999):

$$H_c = \frac{P_{\max}}{24.5(h_v + h_e + h_p)^2} = \frac{1}{\alpha_1((\alpha_2 E')^{-1/2} + (\alpha_1 H)^{-1/2} + (2t_R/3)(\alpha_3 \eta_Q)^{-1/2})^2}. \quad (12)$$

3.3 Oliver-Pharr analysis

Using the OP method (Oliver and Pharr 2004), the modulus (E_{OP}) and contact hardness ($H_{\mathrm{c\_OP}}$) was calculated from the unloading load-displacement (P–h) curve. The stiffness (S) was determined as the slope of the first 80% of the unloading curve and the tip contact area, A_{c}, was assumed to be that of a perfect Berkovich ($A_{\mathrm{c}} = 24.5h_{\mathrm{c}}^2$, where h_{c} is the contact depth). The reduced modulus (E_{r}) is calculated from S and A_{c} (Oliver and Pharr 2004):

$$E_{\mathrm{r}} = \frac{\sqrt{\pi}}{2}\frac{S}{\sqrt{A_{\mathrm{c}}}}. \tag{13}$$

The reduced modulus is a result of the combined elastic response of the indenter (given by the Young's modulus and Poisson's ratio of diamond: 1140 GPa and 0.07, respectively) and the test surface (given by the Poisson's ratio (ν_{s}) and modulus E_{OP}).

$$\frac{1}{E_{\mathrm{r}}} = \frac{1-\nu_{\mathrm{s}}^2}{E_{\mathrm{OP}}} + \frac{1-\nu_i^2}{E_i}. \tag{14}$$

The elastic modulus obtained from the VEP model (E_{VEP}) did not include a correction for the material properties of the diamond tip. For materials substantially less stiff than the diamond tip ($\sim E < 30$ GPa), this correction has little effect (<3%) on the calculated modulus (see (14)). For example, a bone with a reduced modulus ($E_{\mathrm{r}} = 30$) and Poisson's ratio ($\nu_{\mathrm{s}} = 0.3$) the $E_{\mathrm{OP}} = 28.03$ GPa when accounting for diamond's material properties as compared to 27.30 GPa without the correction. Additionally, contact hardness $H_{\mathrm{c\_OP}}$ is defined at max load as:

$$H_{\mathrm{c\_OP}} = \frac{P_{\max}}{A_{\mathrm{c}}}. \tag{15}$$

4 Results and analysis

4.1 VEP of polymers

The VEP model was fit to the experimental unloading data for three polymers: PC, PMMA, and HDPE (Fig. 2). The fitted material parameters (Table 1) of these three polymers were used along with (6) and (8) to simulate the loading and creep hold response of the materials. The simulated VEP load and creep hold curves closely matched the experimental data (Fig. 2), indicating that indentation of the three polymers was well described by the full VEP model. Further, E_{VEP} and H_{VEP} values reasonably corresponded with data published by other investigators (Briscoe et al. 1998; Oyen and Cook 2003), further validating the full VEP model.

In this study, indentation viscosity was determined from the average displacement rate during the creep hold at max load. The viscosity parameter could have also been determined by fitting the unloading curve using the same method that was used to determine E_{VEP} and H_{VEP}. However, the unloading response is less sensitive to changes in the viscosity value, while the creep segment is solely affected by viscosity. As such the best-fit values for viscosity were obtained when the creep-hold segment was used for calculation, and this also improved the quality of the E_{VEP} and H_{VEP} parameters (obtained from the unloading response).

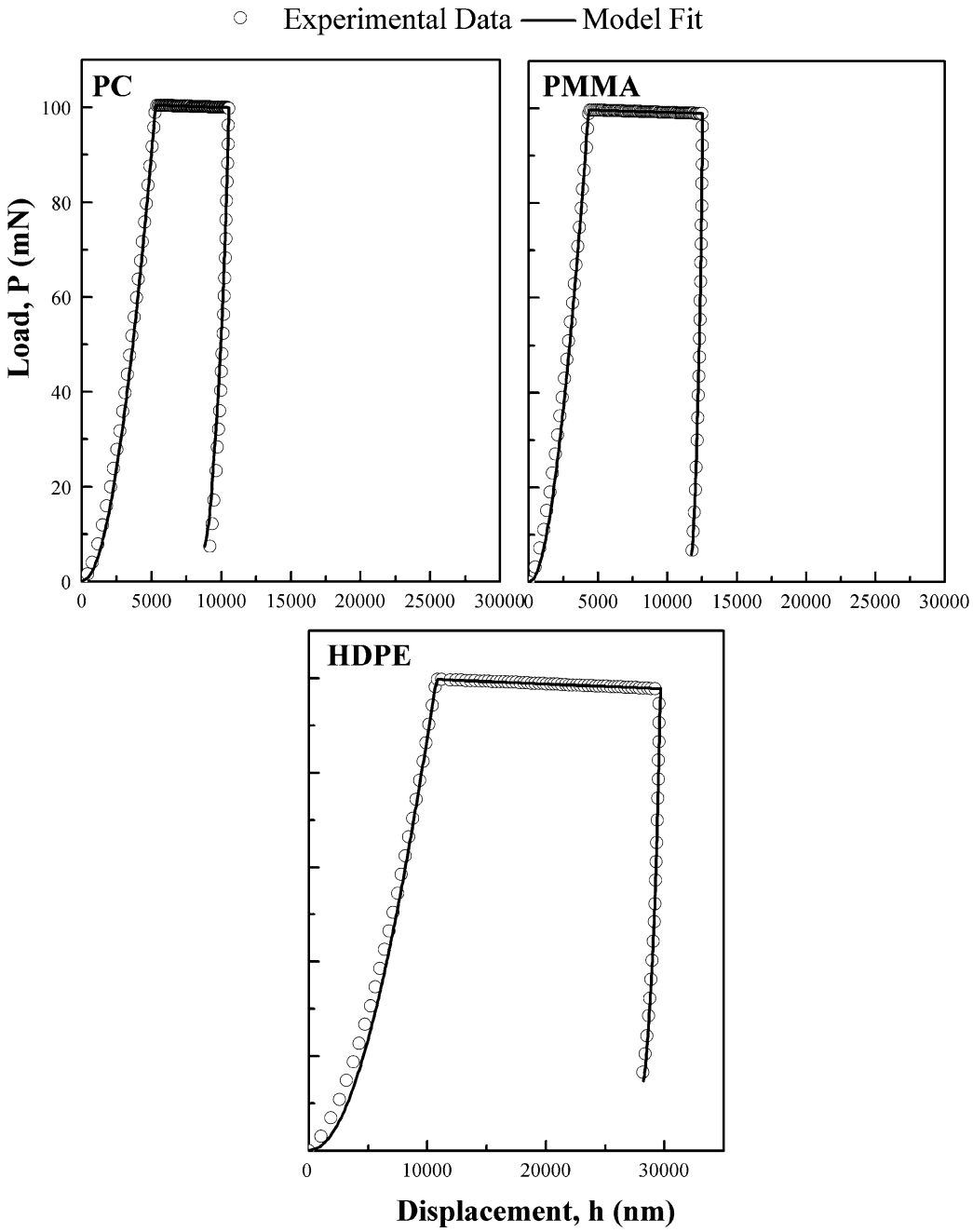

Fig. 2 Indentation load-displacement (P–h) responses for three different polymeric materials under trapezoidal loading to a max load of 100 mN. *Black line* is VEP simulated indentation response using fitted material parameters

In the order of PC, PMMA, and then HDPE, there is an increasing tendency towards viscous creep, as seen in Fig. 2 and reflected by the decrease in the viscosity term (η_Q, Table 1). A similar decrease in the viscosity term between the three polymers was observed under triangle loading with VEP analysis (Oyen and Cook 2003). However, the values of η_Q found with triangle loading (Oyen and Cook 2003) were several orders of magnitude higher than our η_Q values, indicating less observed creep. This result is likely produced from the

assumption of a linear creep rate for the entire hold period. The initial portion of the creep hold has a higher displacement rate, which eventually decelerates to reach a steady state rate. Thus the average creep rate would tend to be overestimated, which in turn would result in an underestimation of the viscosity term. Even with the simplified assumption of a linear creep rate, the full VEP model was able to accurately predict the load-hold-unload response of three different polymers with distinctly different viscoelastic responses.

4.2 Nanoindentation of bone

Representative indentation traces from the three bone samples (porcine jaw, porcine cortical bone, and bovine cortical bone) tested are shown in Fig. 3. The unloading portion of the time-displacement (t–h) experimental data (Fig. 3A) was fit to (11) in order to obtain material constants (E_{VEP} and H_{VEP}). The full VEP displacement-time (h–t, Fig. 3A) and load-displacement (P–h, Fig. 3B) simulated curves are plotted along with experimental data. Good correspondence with experimental data and model predictions demonstrate that the full VEP model accurately models Berkovich indentation of bone.

The mean E_{VEP} values ranged from 17.82 to 24.78 GPa for each of the five different types of bone (Table 2), which is in good agreement with previously reported values for dry bone despite the difference in analysis techniques (Bembey et al. 2006; Oyen and Ko 2007; Rho et al. 1999a). While there was no statistical difference between porcine and bovine cortical bone, the porcine pelixform bone demonstrated a statistically significant lower modulus and hardness values than both types of cortical bone ($p < 0.001$, Table 2).

Interstitial (int.) bone is commonly reported as having a higher modulus than osteonal (ost.) bone (Rho et al. 1999a), yet we found no significant difference between in either the porcine or bovine bone (Table 2). However variations, or lack there of, between the different the types of bone in this study needs to be interpreted with caution as large indentation depths (~3000 nm) and small sample size ($n = 6$) may mask any differences between the types of bone. The large indentation depths were chosen to allow for the assumption of a perfect Berkovich tip area function for both VEP and OP analysis. Further, bone is heterogeneous

Table 1 VEP model fit parameter for polymers tested to a max load $P_{\max} = 100$ mN, using trapezoidal loading with constant load and unload rate ($k = 4$ mN s^{-1})

	Plane Strain modulus, E' (GPa)	Plastic deformation resistance, H (GPa)	Viscosity term, η_Q (Pa s^2)
PC	4.80	0.49	1.15×10^{14}
PMMA	8.56	0.73	1.06×10^{13}
HDPE	1.79	0.05	2.05×10^{12}

Table 2 Mean ± STD of material parameters calculated using the full VEP model fit to unloading data and OP analysis

	Porcine jaw	Bovine int.	Bovine ost.	Porcine int.	Porcine ost.
$\eta_Q (\times 10^{15})$ (Pa s^2)	6.29 ± 3.01	9.45 ± 1.01	9.24 ± 1.08	4.90 ± 0.98	5.53 ± 1.24
H_{VEP} (GPa)	1.41 ± 0.45	2.21 ± 0.27	2.44 ± 0.19	1.54 ± 0.33	2.04 ± 0.38
E_{VEP} (GPa)	17.82 ± 2.71	24.78 ± 3.07	22.62 ± 2.77	22.97 ± 1.80	22.79 ± 2.63
$H_{\mathrm{c\_VEP}}$ (GPa)	0.51 ± 0.08	0.79 ± 0.06	0.80 ± 0.06	0.61 ± 0.10	0.72 ± 0.06
$H_{\mathrm{c\_OP}}$ (GPa)	0.47 ± 0.07	0.66 ± 0.06	0.70 ± 0.03	0.48 ± 0.07	0.55 ± 0.04
E_{OP} (GPa)	16.55 ± 1.41	25.55 ± 1.18	23.93 ± 3.68	22.97 ± 1.80	23.99 ± 1.39

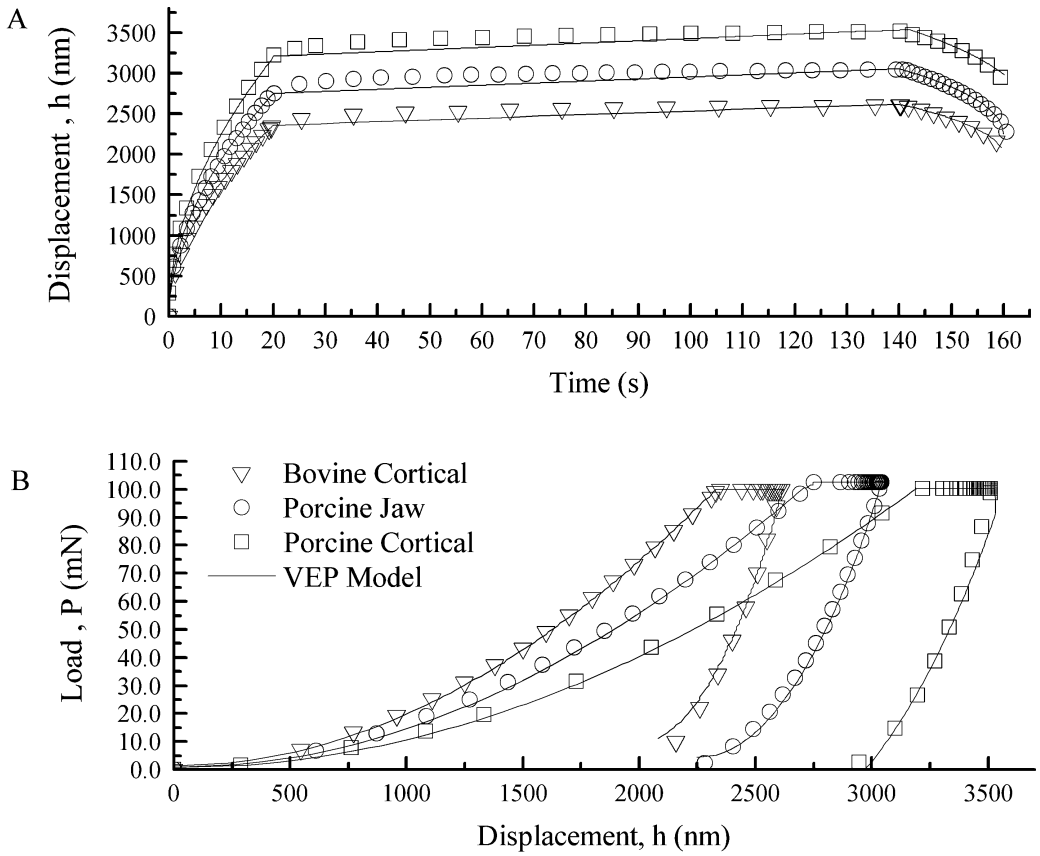

Fig. 3 (**A**) Representative displacement-time (h–t) traces from bone indentation experiments. Unloading data was fit with the full VEP model to obtain material constants. (**B**) Experimental load-displacement (P–h) curves from same experiments above (*open symbols*). *Open symbols* are experimental data and *black lines* are fits to (6) and (8). The *black line* are simulated from the full VEP and from fitted material constants found in (**A**)

in composition, structure, and mineral volume fraction, which leads to variations in material properties, such as E and H (Ferguson 2009; Ferguson et al. 2003; Oyen 2008). It is possible that for the limited range of mineral volume fraction in these samples, relationships between material parameters may be obscured.

A relatively small range of average indentation viscosity values were observed across the five types of bone, with values that varied from 4.90×10^{15} to 9.45×10^{15} (Pa s^2). Bovine cortical (both ost. and int.) bone had significantly higher viscosity values ($p < 0.001$, Table 2) than porcine cortical and jawbone indicating that less viscous creep occurred at max load. While the exact ages of the animals are not known, the bovine cortical sample was from a mature specimen as the growth plate was fully fused, where as the porcine cortical sample, lacking a fused growth plate, was from an immature specimen. The mature bovine cortical bone exhibited significantly less creep than the porcine cortical bone sample, potentially caused by the difference in age of the sample or by variations between species. It is well know that increasing mineralization with age results in increased E and H values (Ferguson 2009), however it is not known how viscoelastic properties vary with an animal's age. Clearly, further investigation of the viscoelastic properties of bone is warranted.

Indentation viscosity was an independent parameter of E_{VEP} but was found to correlated to H_{VEP} (Fig. 4). A previous study using the VEP analysis, without a creep hold, found that

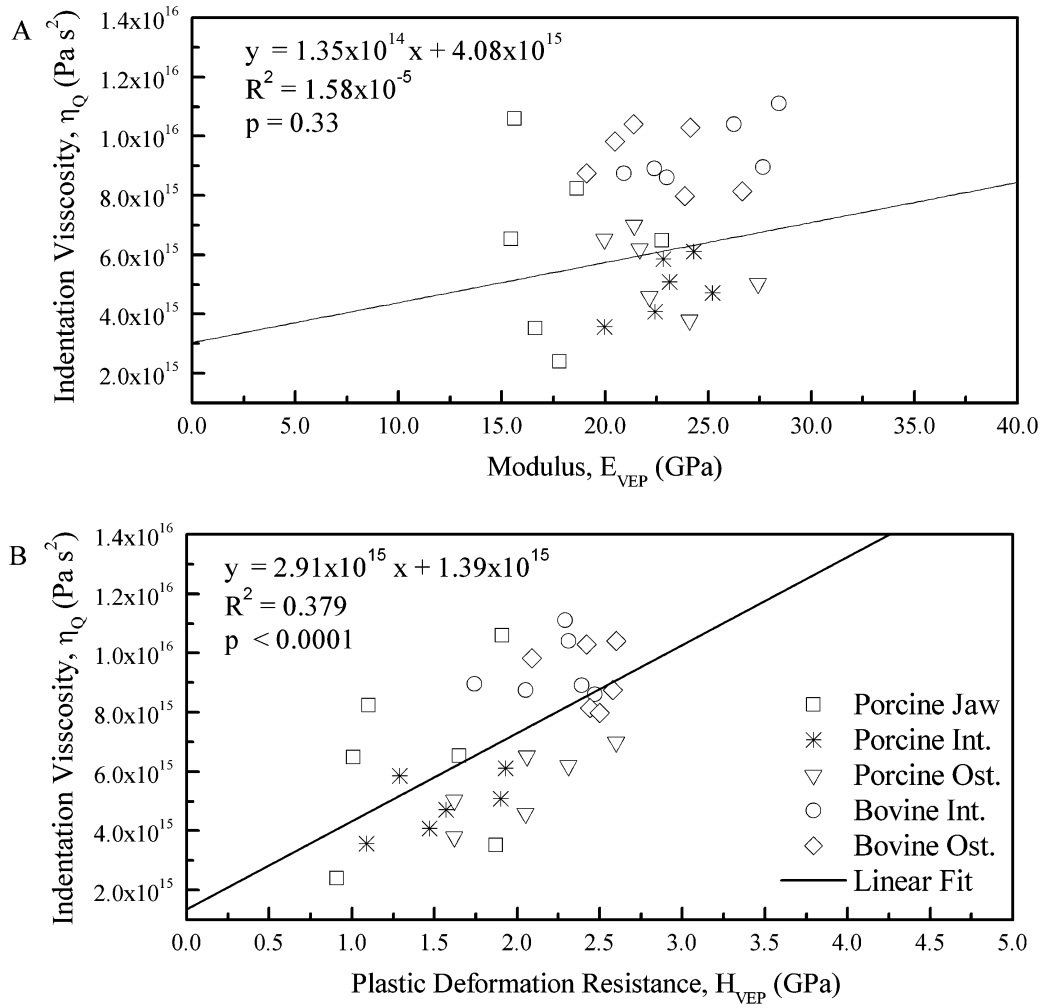

Fig. 4 Indentation viscosity of the five different bone samples is independent of modulus (**A**) but is dependent on the resistance to plastic deformation (**B**). Linear fit values are given in the upper left hand corner with along with R^2, a measure of how well the regression fits the data, and p, the probability that the non-zero slope is not derived by chance

the indentation viscosity, from unloading VEP curve fit, was not an independent parameter but was rather approximately the square of the elastic modulus (Oyen and Ko 2007). In contrast, we found that modulus was independent of viscosity (Fig. 4A, $p = 0.33$), a result of our method of determining the viscosity from the creep hold rather than unloading curve. It is likely that the correlation of viscosity and modulus was affected by the triangle-wave test being less sensitive to creep, as noted above—the modulus and creep were determined from the same unloading fit, and could have thus varied proportionally and fits may not have been unique. The lack of correlation here likely reflects a more accurate and independent determination of the modulus and viscosity parameters. The relationship between H_{VEP} and the viscosity likely suggests common underlying physical mechanisms for time-dependent deformation with significantly different time-scales, since of course there is no true "plastic" (dislocation-associated) deformation in a biological composite.

The VEP resistance to plastic deformation (H_{VEP}), was independent of modulus (Fig. 5A). However, the more commonly reported indentation contact hardness ($H_{\mathrm{c\_VEP}}$)

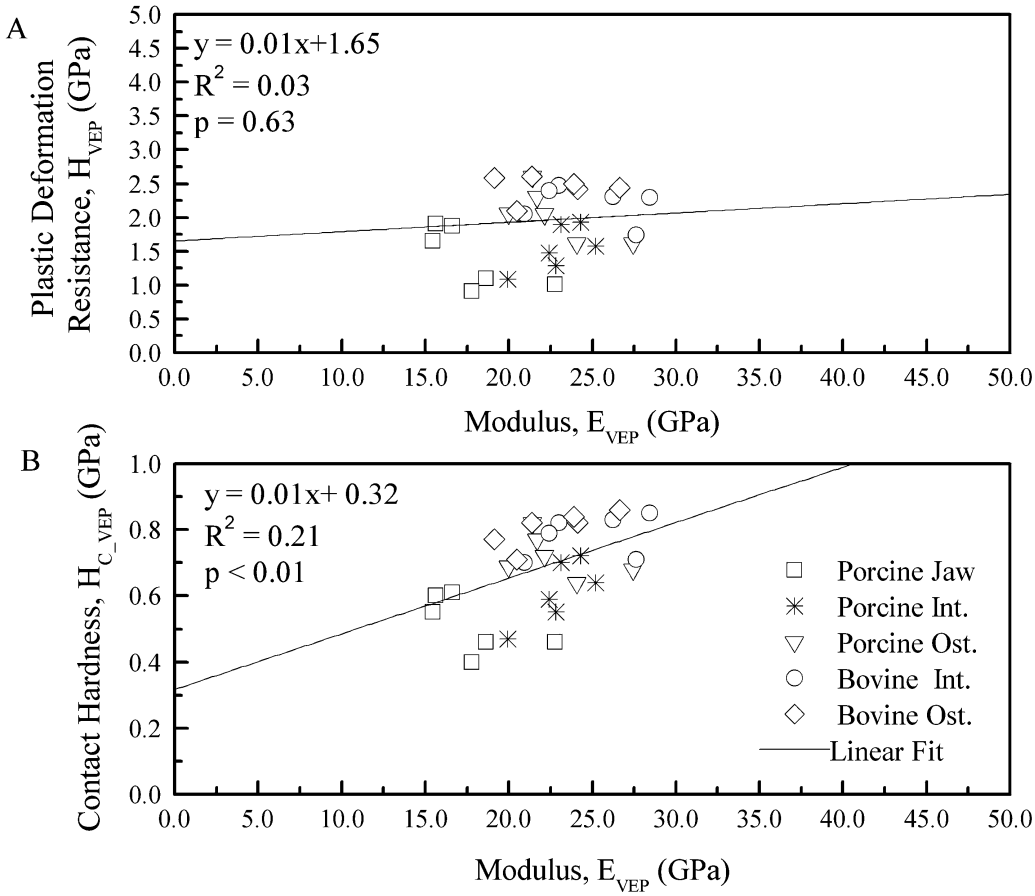

Fig. 5 Resistant to plastic deformation of the five different bone samples is independent of modulus (**A**) obtained from VEP fit. Calculated contact hardness is correlated to the modulus of the five bone samples (**B**). Linear fit values are given in the upper left hand corner

was correlated ($p < 0.01$) to modulus (Fig. 5B). It has been previously observed the contact hardness is not an independent parameter, but rather scales with elastic modulus (Chang et al. 2003; Ferguson 2009; Oyen and Ko 2007; Sakai 1999; Zysset et al. 1999) since it is a measure of the total, not just plastic, deformation. The independent nature of H_{VEP} further impresses the importance of using the full VEP solution over the OP analysis which only produces one truly independent material property E_{OP}.

The OP analysis method produced comparable results to the VEP method with no significant difference between the material parameters from each method (Table 2). OP modulus (E_{OP}) and contact hardness ($H_{\mathrm{c\_OP}}$) were highly correlated ($p < 0.0001$) to their VEP counterparts, modulus (E_{VEP}) (Fig. 6) and contact hardness ($H_{\mathrm{c\_VEP}}$) (Fig. 7) respectively. As both methods are based on the same contact mechanics this agreement is to be expected. The improvement in using VEP approaches thus stems from the increase in information that results from obtaining more than one property value per indentation location; future studies will aim to identify specific correlates between the VEP properties and tissue composition (e.g. mineral content) and microstructural features (e.g. lamellae).

While the full VEP solution allows extraction of visco-elastic-plastic material parameters from trapezoidal loading, there are some notable limitations to this approach. The full VEP solution assumes a linear creep rate, which would be more accurately modeled by a decay-

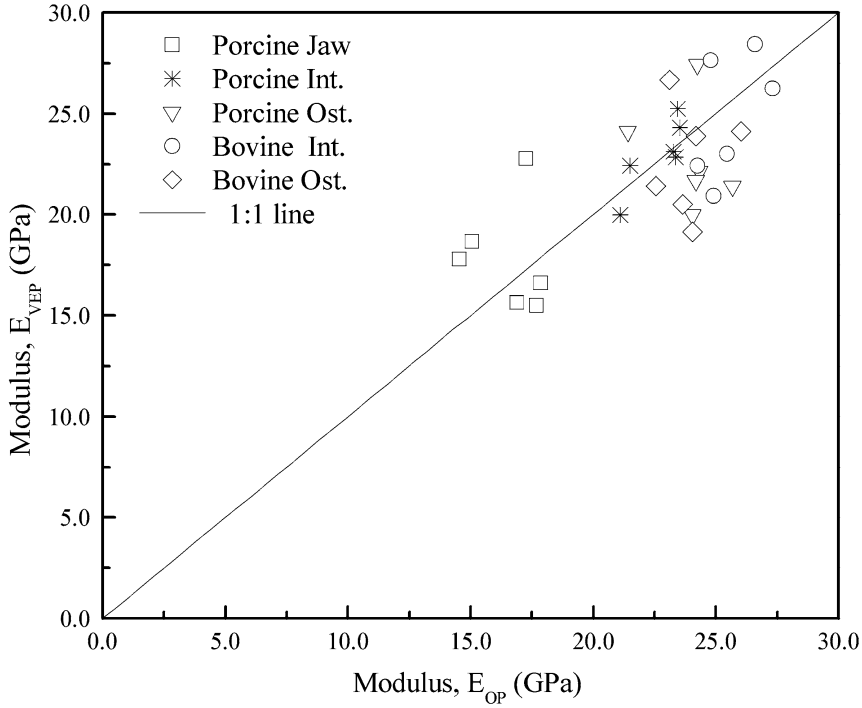

Fig. 6 Modulus values of all bone samples obtained from VEP and OP analysis shows a strong one to one correlation (*solid line*). Linear fit (not shown) gives strong correlation ($p < 0.0001$)

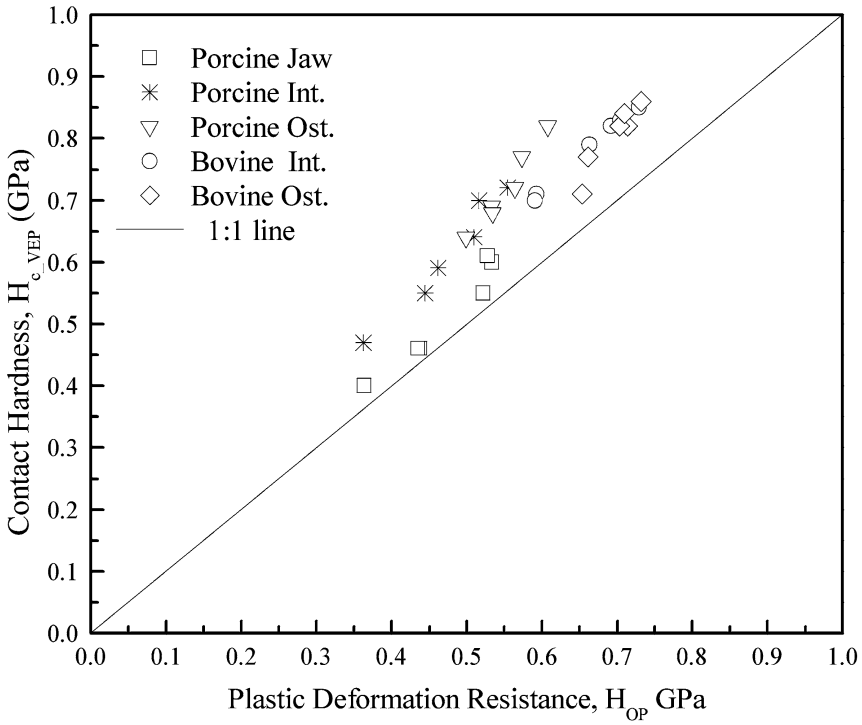

Fig. 7 VEP contact hardness versus OP hardness values of all bone samples. A linear fit (not shown) gives strong correlation ($p < 0.00001$), yet samples do not have a perfect one to one ratio (*solid line in graph*)

ing, non-linear creep rate. Further, the viscosity component need be extracted from the creep hold, requiring a two-step fitting procedure to obtain the three VEP parameters. Additionally, indentation test control systems require explicit time-displacement-load data and true load- or displacement-control. Future work will seek to extend the application of the full VEP solution to materials displaying a larger range of material properties with increased time-dependence such as soft biological tissues or hydrated bone.

4.3 Summary and conclusion

In this study we develop the full VEP solution, which substantially improves the robustness of the original VEP model by providing the trapezoidal loading solution. The full VEP solutions accurately modeled nanoindentation test of the three test polymers, thus validating the full VEP solution for a wide range of viscoelastic responses. Analysis of the five different types of bone produced E_{VEP} and $H_{\mathrm{c\_VEP}}$ values that corresponded well with values calculated from the traditional OP method as well as previous experimental data. Using the full VEP solution the viscous, elastic, and plastic material parameters of the five different types of bone were extracted from indentation test. While there were no significant variations in the modulus (E_{VEP}) between the different types of bone, variations in creep and resistance to plastic deformation were present. Thus indicating the value of the VEP model in its ability over the OP method to analyze more than one material parameter. A complete understanding of the viscous, elastic, and plastic material properties of bone can further our ability to understand many research and clinical problems and advance our understanding of the complex heterogeneous nanomechanical properties of bone. Further, the mechanical properties of polymers and other biological tissues is of great importance to a wide range of fields and application of the VEP model can further the understanding of these materials.

Acknowledgements We thank Jaelyn J. Eberle from the CU Museum and Department of Geological Sciences at the University of Colorado at Boulder for access to the porcine cortical bone samples. This work was performed in part at the University of Colorado's Nanomaterials Characterization Facility. S.E.O. is supported through an NFS Graduate Research Fellowship.

References

Bembey, A.K., Oyen, M.L., Bushby, A.J., Boyde, A.: Viscoelastic properties of bone as a function of hydration state determined by nanoindentation. Philos. Mag. **86**(33–35), 5691–5703 (2006)

Briscoe, B.J., Fiori, L., Pelillo, E.: Nano-indentation of polymeric surfaces. J. Phys. D, Appl. Phys. **31**(19), 2395–2405 (1998)

Chang, M.C., Ko, C.C., Liu, C.C., Douglas, W.H., DeLong, R., Seong, W.J., Hodges, J., An, K.N.: Elasticity of alveolar bone near dental implant-bone interfaces after one month's healing. J. Biomech. **36**(8), 1209–1214 (2003)

Cheng, Y.T., Ni, W.Y., Cheng, C.M.: Determining the instantaneous modulus of viscoelastic solids using instrumented indentation measurements. J. Mater. Res. **20**(11), 3061–3071 (2005)

Chudoba, T., Richter, F.: Investigation of creep behaviour under load during indentation experiments and its influence on hardness and modulus results. Surf. Coat. Technol. **148**, 191–198 (2001)

Feng, G., Ngan, A.H.W.: Effects of creep and thermal drift on modulus measurement using depth-sensing indentation. J. Mater. Res. **17**(3), 660–668 (2002)

Ferguson, V.L.: Deformation partitioning provides insight into elastic, plastic, and viscous contributions to bone material behavior. J. Mech. Behav. Biomed. Mater. **2**(4), 364–374 (2009)

Ferguson, V.L., Bushby, A.J., Boyde, A.: Nanomechanical properties and mineral concentration in articular calcified cartilage and subchondral bone. J. Anat. **203**(2), 191–202 (2003)

Liu, C.-K., Lee, S., Sung, L.-P., Nguyen, T.: Load-displacement relations for nanoindentation of viscoelastic materials. J. Appl. Phys. **100**(3), 033503 (2006)

Oliver, W.C., Pharr, G.M.: An improved technique for determining hardness and elastic-modulus using load and displacement sensing indentation experiments. J. Mater. Res. **7**(6), 1564–1583 (1992)

Oliver, W.C., Pharr, G.M.: Measurement of hardness and elastic modulus by instrumented indentation: Advances in understanding and refinements to methodology. J. Mater. Res. **19**(1), 3–20 (2004)

Oyen, M.L.: Analytical techniques for indentation of viscoelastic materials. Philos. Mag. **86**(33–35), 5625–5641 (2006a)

Oyen, M.L.: Nanoindentation hardness of mineralized tissues. J. Biomech. **39**(14), 2699–2702 (2006b)

Oyen, M.L.: Relating viscoelastic nanoindentation creep and load relaxation experiments. Int. J. Mater. Res. **99**(8), 823–828 (2008)

Oyen, M.L., Cook, R.F.: Load-displacement behavior during sharp indentation of viscous-elastic-plastic materials. J. Mater. Res. **18**(1), 139–150 (2003)

Oyen, M.L., Ko, C.: Examination of local variations in viscous, elastic, and plastic indentation responses in healing bone. J. Mater. Sci. Mater. Med. **18**(4), 623–628 (2007)

Rho, J.Y., Roy, M.E., Tsui, T.Y., Pharr, G.M.: Elastic properties of microstructural components of human bone tissue as measured by nanoindentation. J. Biomed. Mater. Res. **45**(1), 48–54 (1999a)

Rho, J.Y., Zioupos, P., Currey, J.D., Pharr, G.M.: Variations in the individual thick lamellar properties within osteons by nanoindentation. Bone **25**(3), 295–300 (1999b)

Sakai, M.: The Meyer hardness: A measure for plasticity? J. Mater. Res. **14**(9), 3630–3639 (1999)

Zhang, C.Y., Zhang, Y.W., Zeng, K.Y., Shen, L.: Nanoindentation of polymers with a sharp indenter. J. Mater. Res. **20**(6), 1597–1605 (2005)

Zhang, C.Y., Zhang, Y.W., Zeng, K.Y., Shen, L.: Characterization of mechanical properties of polymers by nanoindentation tests. Philos. Mag. **86**(28), 4487–4506 (2006)

Zysset, P.K., Guo, X.E., Hoffler, C.E., Moore, K.E., Goldstein, S.A.: Elastic modulus and hardness of cortical and trabecular bone lamellae measured by nanoindentation in the human femur. J. Biomech. **32**(10), 1005–1012 (1999)